

**NANO EMITTERS: FLUORIMETRIC ANALYSIS OF SINGLE-WALLED
CARBON NANOTUBES IN BIO-OXIDATION**

by

Cheuk Fai CHIU

B.S. Chemistry, Temple University, 2010

Submitted to the Graduate Faculty of
The Dietrich School of Arts and Sciences in partial fulfillment
of the requirements for the degree of
Doctor of Philosophy

University of Pittsburgh

2017

UNIVERSITY OF PITTSBURGH
THE DIETRICH SCHOOL OF ARTS AND SCIENCES

This dissertation was presented

by

Cheuk Fai Chiu

It was defended on

August 30th, 2017

and approved by

Dr. Renã A. S. Robinson, Associate Professor, Department of Chemistry

Dr. Haitao Liu, Associate Professor, Department of Chemistry

Dr. Mohammad F. Islam, Professor, Department of Materials Science and Engineering,

Carnegie Mellon University

Dissertation Advisor: Dr. Alexander Star, Professor, Department of Chemistry

Copyright © by Cheuk Fai Chiu

2017

**NANO EMITTERS: FLUORIMETRIC ANALYSIS OF SINGLE-WALLED
CARBON NANOTUBES IN BIO-OXIDATION**

Cheuk Fai Chiu, PhD

University of Pittsburgh, 2017

ABSTRACT

Carbon nanotubes have remarkable electrical, mechanical and optical properties. They have been employed for applications such as electronics, sensors, composite materials and solar cells. One developing application is biomedical imaging and nanomedicine. For these in vivo applications, the interactions between carbon nanotubes and biomolecules are particularly important.

This dissertation will guide the reader through the recent studies of bio-oxidations of single-walled carbon nanotubes (SWCNTs). The enzyme-catalyzed oxidation of SWCNTs will be examined using photoluminescence spectroscopy. The analysis of photoluminescence data will extend the understanding of enzymatic oxidation of SWCNTs to include CNTs of different diameters and geometries. The mechanism of these processes will be discussed. The enzyme-shortened SWCNTs may find application in cellular imaging and drug delivery systems. Furthermore, the effect of CNT coatings on bio-oxidation will be studied. Surfactants and biomolecules that protect SWCNTs from enzymatic degradation will be identified. The findings will provide an important insight into the mechanism of bio-degradation of coated-nanotubes, and can be applied and extended to other nanomaterials and nano-emitters.

Finally, reaction between SWCNTs and polyunsaturated fatty acids will be examined. Reaction mechanism will be established and products identified. The reaction of interest will provide a new understanding of SWCNT-lipid interactions, and can be potentially used for in vivo lipid peroxidation detection.

TABLE OF CONTENTS

1.0	INTRODUCTION.....	1
1.1	CHAPTER PREFACE.....	1
1.2	CARBON NANOTUBES	1
1.2.1	Structure of Carbon Nanotubes	2
1.2.2	Properties and Applications of Carbon Nanotubes.....	4
	1.2.2.1 Mechanical Properties and Applications	4
	1.2.2.2 Electronic Properties and Applications	4
	1.2.2.3 Biological Applications	6
1.2.3	Synthesis of Carbon Nanotubes	7
1.2.4	Post-synthesis Treatments of Carbon Nanotubes.....	10
	1.2.4.1 Separation from Impurities.....	11
	1.2.4.2 Suspension of Carbon Nanotubes.....	12
	1.2.4.3 Separation of Metallic vs. Semiconducting and Single-Chirality Isolation	15
1.3	CHARACTERIZATION OF CARBON NANOTUBES	18
1.3.1	Transmission Electron Microscopy (TEM).....	18
1.3.2	X-ray Photoelectron Spectroscopy (XPS).....	20
1.3.3	Raman Spectroscopy	20

1.3.4	Absorption Spectroscopy	25
1.3.5	Fluorescence Spectroscopy	26
1.3.5.1	Bandgap Luminescence of Semiconducting SWCNTs	26
1.3.5.2	Defect-Induced Photoluminescence.....	29
1.4	TOXICITY OF CARBON NANOTUBES AND THEIR BIODEGRADATIONS	32
1.4.1	Toxicity of Carbon Nanotubes.....	32
1.4.1.1	Metal Impurity	33
1.4.1.2	Size and Length	34
1.4.1.3	Aggregation.....	35
1.4.1.4	Functionalization.....	36
1.4.2	Biodegradation of Carbon Nanotubes	40
1.4.2.1	Horseradish Peroxidase (HRP).....	41
1.4.2.2	Myeloperoxidase (MPO).....	44
2.0	CHIRALITY STUDIES ON ENZYMATIC BIOOXIDATION.....	50
2.1	CHAPTER PREFACE.....	50
2.2	ENZYME-CATALYZED OXIDATION FACILITATES THE RETURN OF FLUORESCENCE FOR SINGLE-WALLED CARBON NANOTUBES	51
2.2.1	Preface	51
2.2.2	Introduction	52
2.2.3	Results.....	53
2.2.4	Discussion	57
2.2.5	Conclusion	67

2.2.6	Experimental.....	68
2.2.6.1	Chemical Oxidation	68
2.2.6.2	Enzymatic Oxidation of SWCNTs Using HRP.....	68
2.2.6.3	Enzymatic Oxidation of SWCNTs Using MPO.....	69
2.2.6.4	Raman Spectroscopy.....	69
2.2.6.5	TEM Imaging and Histogram Determination.....	70
2.2.6.6	HRTEM Imaging	70
2.2.6.7	UV–Vis–NIR Spectroscopy and PL Mapping.....	70
2.2.6.8	DFT Calculations	71
2.2.6.9	Modified Boehm’s Titration.....	71
2.3	NANO EMITTERS AND INNATE IMMUNITY: THE ROLE OF SURFACTANTS AND BIO-CORONAS IN MYELOPEROXIDASE-CATALYZED OXIDATION OF PRISTINE SINGLE-WALLED CARBON NANOTUBES.....	73
2.3.1	Preface	73
2.3.2	Introduction	74
2.3.3	Results.....	76
2.3.4	Discussion	87
2.3.5	Conclusion	91
2.3.6	Experimental.....	91
3.0	DEFECT-INDUCED NEAR-INFRARED PHOTOLUMINESCENCE OF SINGLE-WALLED CARBON NANOTUBES TREATED WITH POLYUNSATURATED FATTY ACIDS.....	95
3.1	CHAPTER PREFACE.....	95

3.1.1	Introduction	96
3.1.2	Result	98
3.1.3	Discussion	106
3.1.4	Conclusion	110
3.1.5	Experimental.....	110
4.0	STATISTIC AND REPRODUCIBILITY	114
5.0	OUTLOOK AND FUTURE DIRECTIONS.....	115
5.1	CHAPTER PREFACE.....	115
5.1.1	Real Time in vivo Imaging of SWCNTs	116
5.1.2	Thin-film SWCNT Luminescence and Chemical Detection	118
6.0	PUBLICATIONS	122
	APPENDIX A	123
	APPENDIX B	134
	APPENDIX C	142
	BIBLIOGRAPHY	151

LIST OF FIGURES

Figure 1. (a) Single-walled carbon nanotube rolled from a sheet of graphene. (Reproduced with permission from Ref 6. © 2007 Nature Publishing Group) (b) Chiral indices of CNTs with metallic (red) and semiconducting (black) ones identified. (Reproduced with permission from Ref 7. © 2009, Springer-Verlag) (c) Models of single-walled and multi-walled carbon nanotube. (Reproduced with permission from Ref 15 © 2002 John Wiley and Sons, and Ref 13 © 2002 Elsevier)	3
Figure 2. Density of States diagrams of (a) semiconducting and (b) metallic SWCNTs. Electronic transitions between the van Hove singularities are labeled as S_{11} and S_{22} for first and second transition for the semiconducting and M_{11} for the metallic. (Reproduced with permission from Ref 19. © 2008 Royal Society of Chemistry).....	5
Figure 3. Schemes for carbon nanotube synthesis methods: (a) the electric arc-discharge method; (b) the pulsed laser vaporization method; (c) the chemical vapor deposition method and (d) combustion synthesis method by co-flow and counter-flow flame set-up. (Reproduced with permission from Ref 38. © 2010 Elsevier).....	9
Figure 4. Scheme for various purification stages, starting from as produced SWCNT. (Reproduced with permission from Ref 45. © 2010 Cambridge University Press)	10
Figure 5. Molecular structures of (a) sodium dodecyl sulfate (SDS) and (b) dodecyl benzene sulfonate (SDBS). (c) Scheme of micelle formation between SWCNTs and SDS. (Reproduced	

with permission from Ref 56. © 2002 The American Association for the Advancement of Science). Molecular structures of (d) sodium cholate (SC) and (e) sodium deoxycholate (SDC).

..... 13

Figure 6. (a) 1-Pyrenebutanoic acid, succinimidyl ester adsorbing onto the sidewall of a SWCNT via π - π stacking. (Reproduced with permission from Ref 62. © 2001 American Chemical Society). (b) A pair of stereoisomers (R and S) of chiral diporphyrin nanotweezers 1 and 2 used in CNT enantiomer separation. (Reproduced with permission from Ref 66. © 2008 American Chemical Society). (c) Schematic of DNA wrapping on SWCNT. (Reproduced with permission from Ref 69. © 2009 Nature Publishing Group). 14

Figure 7. Scheme for various isolation processes. (a) Hydrophilic and hydrophobic phases used in partition separation by partition. (b) Semiconducting SWCNTs are collected in the top PEG phase, and metallic SWCNTs are in the dextran phase. (Reproduced with permission from Ref 72. © 2013 American Chemical Society). 16

Figure 8. (a) Scheme for gel chromatography. (b) Photograph of separated metallic and semiconducting SWCNT fractions. (Reproduced with permission from Ref 41. © 2011 Nature Publishing Group). (c) Initial density gradient setup for density differentiation centrifugation. (d) Separation of SWCNTs by chirality (Reproduced with permission from Ref 76. © 2006 Nature Publishing Group) and (e) by enantiomer. (Reproduced with permission from Ref 77. © 2010 Nature Publishing Group). 17

Figure 9. (a) Cross-sectional view of a SWCNT bundle. (Reproduced with permission from Ref 81. © 1998 Springer-Verlag). (b) TEM image of SWCNT and the fitting performed to obtain the CNT diameter from TEM line profiles. (Reproduced with permission from Ref 82. © 2016 Nature Publishing Group). 19

Figure 10. AC-HRTEM images of SWNTs. (a) (18,8) SWCNT and (b) (28,0) SWCNT. (c) Higher magnification shows the full atomic structure of the SWCNT and reveals a slight bending. (Reproduced with permission from Ref 83. © 2011 Nature Publishing Group) 19

Figure 11. HRXPS of (a) carbon and (b) oxygen peaks of the as-produced MWCNTs. (Reproduced with permission from Ref 48. © 2008 Elsevier) 20

Figure 12. (a) Raman spectrum of carbon nanotubes (Reproduced with permission from Ref 86. © 2007 John Wiley and Sons) (b) Schematic of Z-translational motion of graphene folded into the RBM of carbon nanotube (Reproduced with permission from Ref 87. © 2000 Taylor & Francis) (c) G' peak of various layers of graphene. (Reproduced with permission from Ref 88. © 2007 Springer) 21

Figure 13. Schematic of Stokes scattering under (a) non-resonance and (b) resonance condition. (Reproduced with permission from Ref 89. © 2006 Springer-Verlag Berlin/Heidelberg) GS (ES) refers to the ground (excited) state of the material. Dashed line refers to the virtual state. Under resonance condition, the signal is enhanced as indicated at the bottom. (c) RBM Raman measurements of HiPco SWCNTs using 76 different laser lines (Reproduced with permission from Ref 94. © 2004 American Physical Society) 24

Figure 14. UV-vis-NIR absorption spectra of (A) pristine and (B) covalently functionalized HiPco SWCNTs. Electronic transition between the S₁₁, S₂₂, and M₁₁ regions are marked, respectively. (Reproduced with permission from Ref 91. © 2003 American Chemical Society) 26

Figure 15. Photoluminescence of (a) HiPco SWCNTs dispersed in SDS and deuterium oxide in EE map (Reproduced with permission from Ref 5. © 2002 The American Association for the Advancement of Science), and (b) CoMoCAT SWCNTs dispersed CMC in 3D-plot. (Reproduced with permission from Ref 71. © 2006 AIP Publishing LLC) 27

Figure 16. (a) EE map of SWCNs with transitions marked with solid circles (E_{11}), diamonds (E_{22}), and triangles (E_{33} and E_{44}). Open circles and diamonds are phonon sidebands. Solid crosses are exciton energy transfer (EET) between SWCNTs. (Reproduced with permission from Ref 98. © 2007 American Physical Society) Decomposed EE maps for (b) collinear and (c) perpendicular dipoles. Peaks for I_{\perp} spectrum are indicated by arrows. (Reproduced with permission from Ref 100. © 2006, American Physical Society)..... 28

Figure 17. (a) Defect-induced photoluminescence (E_{11}^{-}) by diazonium reaction. (b) Emission intensity of E_{11} and E_{11}^{-} photoluminescence from (6,5) SWCNTs as a function of defect density. (Reproduced with permission from Ref 112. © 2013 Nature Publishing Group). (c) Defect-induced photoluminescence (E_{11}^{-}) by ozonation treatment. (d) Computation model of the E_{11} band split into E_{11}^{-} and E_{11}^{+} energy states. (Reproduced with permission from Ref 111. © 2010 The American Association for the Advancement of Science)..... 31

Figure 18. Properties of CNTs influencing cell uptake and responses. (Reproduced with permission from Ref 120. © 2013 American Chemical Society)..... 33

Figure 19. Inflammatory response induced by CNTs of different size and shape in vivo. C57BL/6 mice were intraperitoneally injected with 50 μg CNTs (M1, M2, M3, and S4). After 24 h post-exposure, the abdominal lavage fluid was harvested and the total cell number was determined to evaluate inflammatory responses induced by CNTs. (Reproduced with permission from Ref 124. © 2010 Springer) 34

Figure 20. TEM images show the (a) tangled and (b) long fiber examined in mice after 7 days. Haematoxylin and eosin histology sections of the diaphragms show the presence of granulomatous inflammation (GI) in mice exposed to long fibers. (Reproduced with permission from Ref 125. © 2008 Nature Publishing Group) 35

Figure 21. Body weight of nude mice following injection of SWCNTs. Mean and standard deviation of body weight of nude mice injected intravenously with non-covalently PEGylated SWCNTs (black diamonds), oxidized, covalently functionalized SWCNTs (black triangles) or PBS control (white squares) show no statistically significant differences over a period of 4 months. (Reproduced with permission from Ref 135. © 2008 Nature Publishing Group) 38

Figure 22. (a) Optical image of a mouse bearing a 4T1 tumor on the right shoulder. (b-d) NIR-II (950-1400 nm) fluorescent time course imaging 12, 24, and 48 h post-injection, from left to right, showing clear SWCNTs accumulation in the 4T1 tumor. All mice were injected with 0.254 mg/kg of SWCNTs and emission collected from 0.9 to 1.4 μm after excitation at 808 nm at a laser power density of 0.14 W/cm^2 . The scale bar on the right corresponds to all NIR images of 4T1 tumor-bearing mice. (Reproduced with permission from Ref 137. © 2013 American Chemical Society)..... 39

Figure 23. (a) Oxidation states of horseradish peroxidase. (Reproduced with permission from Ref 151. Copyright 2002 Nature Publishing Group) (b) Structure of HRP and possible binding position with carboxylated SWCNTs (Reproduced with permission from Ref 156. © 2009 American Chemical Society) 42

Figure 24. (a) Peroxidase cycle of MPO (solid black line) and the formation of OCl^- from Cl^- by MPO-Compound I (dashed blue line). (Reproduced with permission from Ref 151. © Copyright 2002 Nature Publishing Group) (b) Structure of MPO and possible binding position with carboxylated SWCNTs. (Reproduced with permission from Ref 143. © 2010 Nature Publishing Group)..... 45

Figure 25. (a) Photographs of carboxylated SWCNTs incubated with or without degradative reagents after 24 h. (b) Dynamic light scattering data of different samples showing decreasing

sizes of degraded nanotubes. (c) Raman spectra of SWCNTs before and after 24 h of MPO degradation. (d) Visible-near infrared (Vis-NIR) absorption spectra of SWCNTs being degraded during 24 h. (Reproduced with permission from Ref 143. © 2010 Nature Publishing Group).... 47

Figure 26. Photoluminescence (PL) maps of SWCNTs (a) before and (b) after acid oxidation, and of the acid-oxidized SWCNT sample from (b) after treatment with (c) HRP/H₂O₂ or (d) MPO/H₂O₂/NaCl. Before PL mapping, sodium cholate (1 wt %) was added, and the samples were sonicated for 2 h. Literature values were employed to assign the SWCNT chirality.⁵ 54

Figure 27. Enlarged radial breathing mode (RBM) sections and the full Raman spectra of SWCNTs treated with (a) HRP/H₂O₂ and (b) MPO/H₂O₂/NaCl at various experimental stages [before oxidation (black, dotted), after acid oxidation (red), and after enzymatic reaction (blue)]. The SWCNT chirality was assigned according to the literature.¹² The RBM sections have been offset for clarity..... 55

Figure 28. UV-vis-NIR absorption spectra of SWCNTs treated with (a) HRP/H₂O₂ and (b) MPO/H₂O₂/NaCl at various experimental stages [before oxidation (black, dotted), after oxidation (red), and after enzymatic reaction (blue)]. 56

Figure 29. Transmission electron microscopy (TEM) micrographs of SWCNT bundles (a) before and (b) after acid oxidation. (c) High-Resolution TEM (HRTEM) of the acid-treated SWCNTs bundles. TEM micrographs of the acid-treated SWCNT bundles (d) after treatment with MPO/H₂O₂/NaCl and (e) after treatment with HRP/H₂O₂. (f) HRTEM micrograph of the HRP/H₂O₂ treated sample. Insets depict histograms of the length distributions for the SWCNT bundles at various experimental stages..... 57

Figure 30. (a) Top view of the COOH functionalized (14,0) SWCNT. (b) Reaction energy profile for decarboxylation of a (14,0) pristine SWCNT functionalized with a carboxyl and a ketone

group. Side views of selected parts of the SWCNT are also shown for the initial, transition and final configurations during the decarboxylation process. The potential energy surface near the final state is very flat due to small energy barrier for the rotation of $-OH$ group around the $O-C$ bond, as can be seen by inspecting the inset images. Panel (c) and (e) show initial and final configurations for the decarboxylation process of a defective (14,0) CNT functionalized with $-COOH$ and two ketone groups. This process is exothermic with 1.75 eV per CO_2 molecule. Panel (d) shows the structure of a possible intermediate transition state where the hydrogen of $-COOH$ group is transferred to the ketone group forming an $-OH$ group with the release of CO_2 in the gas phase. Carbon atoms are turquoise, oxygen is red, and hydrogen is white. 62

Figure 31. Electrochemical potentials of SWCNTs with different diameters plotted against the oxidation-reduction potentials of HRP, MPO and $HOCl$ (black dashed line). The dependence of electrochemical potentials of SWCNTs on their diameter was modeled in Ref 196 with experimental data adapted from Ref 197 (squares). The green region indicates the diameter range of SWCNTs studied in this work (HiPco). The pink region indicates the larger diameter SWCNTs utilized in earlier work.145,156 HRP, MPO and $HOCl$ potentials were adapted from Ref 184. Structures of HRP and MPO possible binding positions with carboxylated SWCNTs (right) were adapted from Ref 156 and Ref 143, respectively. The density of states diagrams (left) was adapted from Ref 19, indicating the valence and conduction band of the semiconducting and metallic SWCNTs. 66

Figure 32. a) Crystal structure of MPO (Reproduced with permission from Ref 210. © 2009 American Society for Biochemistry and Molecular Biology). b) Peroxidase and halogenation cycles of MPO. (Reproduced with permission from Ref 151. Copyright 2002 Nature Publishing Group). c) Molecule structures of the surfactants, sodium cholate (SC) and deoxycholate (SDC),

used in this study. d) Chiralities of SWCNTs investigated in this work are highlighted in yellow.

..... 76

Figure 33. The excitation-emission (EE) maps of SC-SWCNTs a) before activation of the halogenation cycle of MPO and b) after five additions of H₂O₂ into the reaction mixture (MPO/NaCl). c) EE map for SC-SWCNTs treated with H₂O₂/NaCl (without MPO). d)

Calculated rate constants of different SWCNTs versus their diameters..... 77

Figure 34. Raman spectra of SWCNT before and after the reaction. Inset shows the change of D/G ratio over H₂O₂ additions..... 79

Figure 35. Complete degradation of SC-SWCNTs by NaOCl. EE maps of SC-SWCNTs a) before the addition of NaOCl, b) 1 day, and c) 3 days after. d) Raman spectra and TEM images of SC-SWCNTs e) before and f) after the reaction..... 82

Figure 36. EE maps of a) CpG DNA-SWCNTs, b) BSA-SWCNTs, c) PL-PEG-SWCNTs, and d) PS-SWCNTs after oxidation with MPO/H₂O₂/NaCl. Inserts are EE maps before the reactions. 83

Figure 37. Normalized intensity of (7,6) SWCNTs after incubation with MPO, neutrophils, and MEF..... 85

Figure 38. EE maps of (6,5) purified HiPco SWCNTs (a) before and (b) after reaction with linoleic acid. (c) Spectral changes over 60 min (spectra taken every 5 min). (d) UV-vis absorption spectra showing the presence of lipid hydroperoxide (235 nm) and its concentration decreasing after reaction with SWCNTs. SWCNTs vis-NIR absorptions were unshifted. (e)

Emission intensities of E₁₁⁻ and E₁₁ of CoMoCAT SWCNTs reacted with linoleic acid over 6 h. 99

Figure 39 (a) Normalized E₁₁⁻ intensities of the reaction illuminated at different wavelengths (235, 366, 466, 566, and 666 nm). All data points were collected with 566 nm excitation and

efficiency was corrected to photon flux. UV-vis absorption of SWCNTs suspension is shown on the right axis. (b) Effect of LA-OOH concentration on the SWCNT NIR emission. Samples were stored in the dark for 3 days and then activated with 566 nm illumination for 1 h. 102

Figure 40. (a) Raman, (b) XPS survey and (c) high-resolution spectra of the oxygen peak. (d) DRIFTS spectra of LA-OOH/SWCNTs after (top) and before (bottom) illumination. 103

Figure 41. (a) Schematic of the hyperspectroscopy method using supercontinuum light source. (b) Spatial extent of the excitation source at the sample focus. The 600-1000 nm excitation range covers a 1 mm width. (c) Four PLE maps taken from a time series, where F4-TCNQ is successively added to a SWCNT dispersion after 2, 6, 10, and 14 min. Integration time was 200 ms, averaged over four frames. (Reproduced with permission from Ref 253. © 2016 American Chemical Society)..... 116

Figure 42. (a) Schematic of NIR II imaging setup. Anesthetized mice are illuminated from above with 808-nm light. NIR fluorescence (1,100–1,700 nm) is filtered and imaged onto a 2D InGaAs array. (b) Fluorescence spectrum of functionalized SWNTs excited at 808 nm showing several emission peaks. (Adapted from Ref 136. © 2011 National Academy of Sciences)..... 118

Figure 43. SWCNTs dispersed in sodium carboxymethylcellulose (a) as a solution, and (b) drop casted on quartz slide. (c) Peak ratio of $E_{22\rightarrow11} / E_{33\rightarrow11}$ of (7,6) SWCNTs in CMC film exposed to different humidity. (d) CMC/SWCNTs film drop-casted on Si/SiO₂ chip with printed gold electrodes. (e) Free standing CMC/SWCNTs film. 121

Figure 44. Raman RBM section of the pristine SWCNTs fitted with reported literature values using Lorentzian function.¹² The Raman shift in wavenumbers can be corresponded to the chiral indices of SWCNTs (in parentheses). The major components of the peaks are highlighted in blue. 125

Figure 45. Control Experiments with acid oxidized SWCNTs.....	127
Figure 46. PL maps of the oxidized SWCNTs incubated with (a) 0.1 mg of HRP and (b) 1.5 mg of HRP for 35 days. (c) Raman spectra of the oxidized SWCNTs (black, dotted), 0.1 mg HRP treated SWCNTs (blue) and 1.5 mg HRP treated SWCNTs (red).....	128
Figure 47. Photoluminescence (PL) maps of SWCNTs (a) before oxidation and (b) non-oxidized sample after treatment with HRP/H ₂ O ₂ . (c) UV-vis-NIR absorption and (d) Raman spectrum of non-oxidized HiPco SWCNTs (black, dotted) after HRP/H ₂ O ₂ treatment (blue). Inset depicts enlarged Raman spectrum of the D and G peak region. Additional control experiments: Pristine SWCNTs dispersed in (e) HRP and (f) 1% wt sodium cholate. Results from 47e, 47f, and Figure 45 demonstrated HRP could not individualize SWCNTs. Sodium cholate-wrapped SWCNTs (g) before and (h) after the addition of HRP, showing that HRP is not an enhancer in SWCNT luminescence.....	129
Figure 48. (a) Raman and (b) UV-vis-NIR absorption spectra of the non-oxidized HiPco SWCNTs (black, dotted) after MPO/H ₂ O ₂ /NaCl treatment (blue). (c) TEM micrograph of the pristine SWCNTs after MPO/H ₂ O ₂ /NaCl treatment.....	130
Figure 49 (a) Photoluminescence map of the pristine SWCNTs after NaOCl treatment. (b) Raman and (c) UV-vis-NIR absorption spectra of the non-oxidized HiPco SWCNTs (black, dotted) after NaOCl treatment (blue). (d) TEM micrograph of the pristine SWCNTs after NaOCl treatment.	131
Figure 50. (a) Defective CNT (14,0) functionalized with two ketone and two carboxyl groups. (b) Partially decarboxylated CNT associated with a release of one CO ₂ molecule in the gas phase. Compared to (a), the energy of this structure is lower by 1 eV. (c) Full decarboxylation of	

the CNT with the release of two CO₂ molecules in the gas phase. This process is exothermic by 1.8 eV compared to (a)..... 132

Figure 51. AFM image of the surfactant-wrapped, oxidized SWCNTs that were treated with HRP/H₂O₂ for 35 days (from Figure 26c)..... 133

Figure 52. EE maps and relative intensity plots for control experiments: (a, b) MPO/NaCl without H₂O₂, and (c, d) NaCl without neither MPO nor H₂O₂. 135

Figure 53. 3D plot for MPO/H₂O₂/NaCl treated SC-SWCNTs EE maps a) before and b) after 14 additions of H₂O₂ in MPO/H₂O₂/NaCl oxidation. c) Intensity values from the EE maps, and d) Relative emission intensity plot. Animated EE map is available as gif file. Data from (7,6) SWCNTs were fitted to (e) zero, (f) first, and (g) second order rate law. h) First order reaction equation applied to all SWCNTs 136

Figure 54. EE maps of SDC-SWCNTs a) before and b) after oxidation with MPO/H₂O₂/NaCl. EE maps for controls, c) with MPO/NaCl (without H₂O₂), and d) with H₂O₂/NaCl (without MPO)..... 137

Figure 55. EE maps for SC-SWCNTs a) before dialysis, b) after dialysis, and c) dialyzed in the presence of MPO. EE maps for SDC-SWCNTs d) before dialysis, e) after dialysis, and f) dialyzed in the presence of MPO. 138

Figure 56. EE maps a) before and b) after NaOCl oxidation of SC-SWCNTs. 138

Figure 57. Intensity plot for a) CpG DNA-SWCNTs, b) BSA-SWCNTs, c) PL-PEG-SWCNTs, and d) PS-SWCNTs during oxidation with MPO/H₂O₂/NaCl..... 139

Figure 58. Controls for CpG DNA-SWCNTs oxidation with MPO/H₂O₂/NaCl: (a) MPO/NaCl without H₂O₂, and (b) H₂O₂/NaCl without MPO. Controls for MPO-catalyzed oxidation of BSA-SWCNTs: (c) MPO/NaCl without H₂O₂, and (d) H₂O₂/NaCl without MPO. 140

Figure 59. EE maps of SDC-SWCNTs (top), CpG DNA-SWCNTs (middle) and BSA-SWCNTs (bottom) subjected to non-activated neutrophils (left), activated neutrophils (center) and mouse embryonic fibroblasts (right). Inserts are EE maps before the reactions..... 141

Figure 60. EE maps of CoMoCAT SWCNTs a) before and b) after reaction with linoleic acid. Panel c) shows the spectral changes over 60 mins (spectra taken every 5 mins). d) vis-NIR absorption spectra of SWCNTs before and after the reaction. 143

Figure 61. Control reactions with a) only SWCNTs and linoleic acid (no surfactant), b) SWCNTs and sodium cholate (no linoleic acid), and c) sodium cholate and linoleic acid (no SWCNTs). d) Linoleic acid pretreated with morin (250 $\mu\text{g} / \text{mL}$) to inhibit the autoxidation by terminating the radical chain reactions. SWCNTs exposed to pretreated linoleic acid showed no increase in E_{11}^- emission. 144

Figure 62. Spectra of SWCNTs / LA-OOH reaction using different surfactants. Sodium cholate (SC) at a) 0.1 wt % and b) 1 wt %, sodium dodecyl sulfate (SDS) at c) 0.1 wt % and d) 1 wt %, and dodecylbenzene sulfonate (SDBS) at e) 0.1 wt % and f) 1 wt %..... 145

Figure 63. HRXPS spectra of carbon peak of the SWCNTs (a) before and (b) after LA-OOH reaction..... 146

Figure 64. a) The absorption spectra of the pristine and the oxygen-doped CNTs. Optimum adsorption configuration of the CNT with b) ether-perpendicular c) epoxide-parallel, d) O_2 -parallel, e) O_2 -perpendicular, and f) O_3 -perpendicular. 147

Figure 65. Emission spectra of SWCNTs reacted with a) γ -linolenic acid (18:3), b) stearic acid (18:0), and c) stearyl-cardiolipin (14:0)..... 147

Figure 66. Emission spectra of SWCNTs reacted with a) autoxidized cardiolipin (18:2), and b) non-oxidized cardiolipin (18:2). 148

Figure 67. Emission spectra of SWCNTs treated with linoleic acid before, after illumination, and in the presence of diethylenetriaminepentaacetic acid (DTPA). 148

Figure 68. SWCNTs treated with antioxidants, a) ascorbic acid (250 mM) and b) morin (250 $\mu\text{g} / \text{mL}$), before subjected to linoleic acid hydroperoxide and 566 nm excitation light for one hour. No evolvment of the E_{11}^- emission was observed. 149

Figure 69. Reaction control and product isolation. SWCNTs were a) reacted with LA-OOH, and b) analyzed again after being stored in the dark for 1 week. Another sample was c) reacted with LA-OOH, and d) dialyzed to remove linoleic acids and surfactants, and re-dispersed in bovine serum albumin (1 wt %) in water. 149

Figure 70. Emission spectra of sodium cholate coated SWCNTs/LA taken after sonication for 0, 10 and 60 minutes under normal laboratory lighting conditions. 150

Figure 71. EE maps of raw a) (6,5) purified HiPco and b) CoMoCAT (6,5) SWCNTs. 150

LIST OF TABLES

Table 1. Transition Wavelength of Semiconducting SWCNTs (Reproduced with permission from Ref 12. © 2003 American Chemical Society)	24
Table 2. Transition Wavelength of Metallic / Semimetal SWCNTs, (Reproduced with permission from Ref 12. © 2003 American Chemical Society)	25
Table 3. Biodegradation of Carbon Nanomaterials by Horseradish Peroxidase-Catalyzed Oxidation.....	43
Table 4. Biodegradation of Carbon Nanomaterials by Myeloperoxidase-Catalyzed Oxidation ..	48
Table 5. Reaction Progression (ΔE_{11^-} Intensity) with Different Surfactants at Two Concentrations*	101
Table 6. Computation of Electronic Properties of Undoped and Oxygen-Doped (6,5) SWCNTs	105
Table 7. Calculated Rate Constant of Different SWCNTs for MPO/H ₂ O ₂ /NaCl Reaction.....	137
Table 8. Reaction Conditions and Calculations for Wavelength-Dependence Experiment.	146

LIST OF SCHEMES

- Scheme 1. Proposed Reaction between Polyunsaturated Fatty Acids/Lipids and SWCNTs 106
- Scheme 2. Experimental Procedure for the Enzymatic Oxidations of Oxidized SWCNTs 124

PREFACE

I would first like to express my sincerest gratitude to my research advisor, Professor Alexander Star, from whom I have learned so much: everything from conducting research, to story-telling, to picking a color-scheme for cover-art. This has been a great journey and it would not be possible without him. Thank you for believing in me before I believed myself. And thank you for spoiling me with your research funding. It has been a true honor to work and learn from you.

I would also like to express my appreciation to the members of my committee, Professor Renã A. S. Robinson, Professor Haitao Liu, and Professor Mohammad F. Islam. Their time and valuable advice throughout the years have helped me to mature as a scientist. Thank you.

Special thanks to all my collaborators, from whom I have learned a great deal of science through our efforts. In particular, I would like to thank Professor Valerian Kagan, Dr. Oleksandr Kapralov, Dr. Haider Dar, for their knowledge in biochemistry and their assistance in performing cell studies. To Dr. Wissam Saidi, for performing computation modeling. To Professor Stéphane Petoud and Dr. Kristy Gogick, I would not know where to start without your help. To Dr. Christopher Andolina, thank you for always going the extra mile and the 300+ miles to Edison, New Jersey. Much appreciation is owed to Tom Harper from the Department of Biological Science for his assistance with electron microscopy, and Dr. Susheng Tan from NCFE.

Furthermore, I am very grateful to my former and current group members, Dr. Gregg Kotchey, Dr. Yong Zhao, Dr. Yanan Chen, Dr. Mengning Ding, Dr. Yifan Tang, Dr. Harindra

Vedala, Dr. Nadine Kraut, Dr. Haifeng Dong, Dr. Uri Green, Dr. Pingping Gou, Dr. Wanji Seo, Ian Feigel, Brian Barth, James Gaugler, Gregory Morgan, Philip Fournier, Hao Bai, Zachary Michael, Seth Burkert, James Ellis, Sean Hwang, Michael Chido, David White, Wenting Shao, Long Bian, and Xiaoyun He. You have made our lab not only a place for the exchange of scientific ideas, but also of politics, go, fantasy football, and everything around the world. It has been productive, fruitful, and fun. It has been a pleasure working together and I wish you the best of luck with your future endeavors.

Special thanks to technology, particularly Google, Web of Science, Endnote, PowerPoint, Mendeley and email. This dissertation would not be possible without you. To those who completed a Ph.D. before the Internet, I admire you.

This dissertation would not be possible without the support from friends and family. To Dr. Sara Smith, Dr. Karen Ricardo, Amanda Leavitt, and Zach Michael, this group has been through comprehensive exams, dissertations, weddings, babies... You guys hold a special place in my heart. To my parents and my younger brother, Jacky, thank you for your love and support, and bearing with the fact that I was still in school. Finally, I would like to thank my better half, Ka Po, for bearing with me on a daily basis, waiting seemingly endlessly for my graduation. Without her, I would not have been able to do this, or anything really.

Dedicated to the memories of my Grandparents. I am sorry I did not make this any sooner.

1.0 INTRODUCTION

1.1 CHAPTER PREFACE

The goal of this dissertation is to guide the readers through recent efforts on enzymatic degradation of carbon nanotubes. The first chapter will provide an introduction to carbon nanotubes, their synthesis methods, methods for their characterization and studies of their toxicity. Research on the enzymatic degradation of carbon nanomaterials using horseradish peroxidase (HRP) and myeloperoxidase (MPO) will be summarized. An extended discussion on fluorescence spectroscopy on carbon nanotubes will be included, as it will be the primary tool to investigate the enzymatic degradation of single-walled carbon nanotubes.

1.2 CARBON NANOTUBES

Until the 1980s, there were only two known allotropes of carbon, the sp^2 -hybridized graphite, and the sp^3 -hybridized diamond. The situation changed when the soccer-ball-shaped fullerenes were discovered in 1985,¹ and soon followed by the discovery of carbon nanotubes (CNTs) in 1991.² The findings continued with the isolation of graphene in 2004.³ However, CNT family is by far the most complex material among the carbon allotropes. Like fullerenes and graphene, their properties change after the chemical functionalizations. However, unlike the other two,

carbon nanotubes can be both single-walled and multi-walled.⁴ Their physical and electronic properties are also strongly influenced by their roll-up structure.⁵ The following sections will provide a review of the structure of carbon nanotubes and their synthesis methods.

1.2.1 Structure of Carbon Nanotubes

Carbon nanotubes can be visualized as a sheet of graphene rolled into a tube as depicted in Figure 1a.⁶ The roll-up vector (C_h) can be resolved into two unit vectors, a_1 and a_2 , as indicated in Figure 1b.⁷ Different CNTs can be constructed by having various ratios of unit vectors, a_1 and a_2 , where

$$C_h = n a_1 + m a_2 \quad (1)$$

given that n and m are integrals.⁸ CNTs are often described by these values known as the chiral indices in the form of (n,m) .⁹ The diameter of any CNTs can also be computed from the indices, using the equation

$$d_t = \frac{a}{\rho} \sqrt{n^2 + m^2 + nm} \quad (2)$$

where a represents the length of 0.246 nm of the unit vectors a_1 and a_2 .¹⁰

While the hybridized p-orbitals on a graphene sheet enjoy a 2-dimensional degree of freedom and have zero bandgap, the rolled-up nanotubes have a curvature which induces partial σ - π hybridization.¹¹ This property leads to 1-dimensional quantum confinement along the diameter of the nanotubes and determines their electronic structures.¹² The electronic structure of a nanotube can be predicted by the rolling factor integrals n and m . Nanotubes are metallic when $n - m = 3k$ where k is an integer; otherwise, they are semiconductors with a geometry dependent bandgap.¹² Briefly, small diameter nanotubes have a larger bandgap due to the resulting

curvature and confinement. Interband transition values from theoretical models and experimental data have been widely used in the interpretation of experiments.¹²

Nanotubes can be comprised of a single tube, known as single-walled carbon nanotubes (SWCNTs), or multiple concentric tubes, named as multi-walled carbon nanotubes (MWCNTs).¹³ The diameter of SWCNTs ranges from 0.4 nm to 5 nm, whereas of MWCNTs ranges from 2 to 50 nm.¹¹ Their lengths are commonly in the micrometer ranges, though CNTs as long as 55 centimeters have been reported.¹⁴

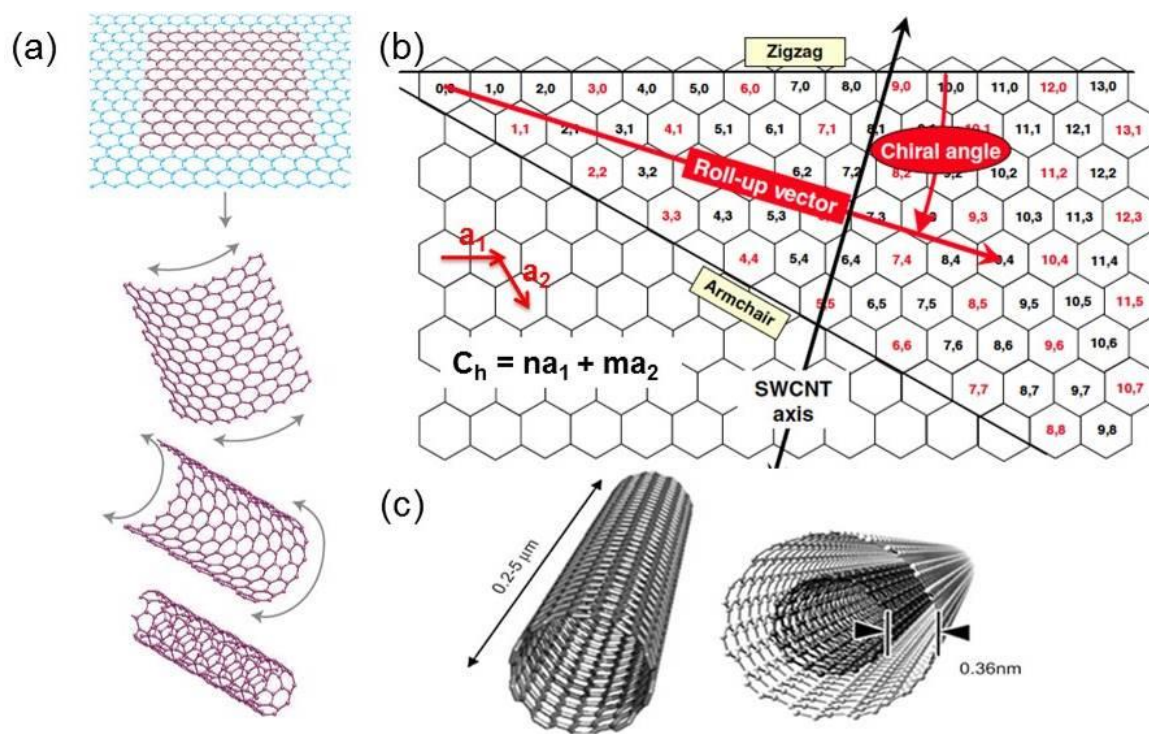


Figure 1. (a) Single-walled carbon nanotube rolled from a sheet of graphene. (Reproduced with permission from Ref 6. © 2007 Nature Publishing Group) (b) Chiral indices of CNTs with metallic (red) and semiconducting (black) ones identified. (Reproduced with permission from Ref 7. © 2009, Springer-Verlag) (c) Models of single-walled and multi-walled carbon nanotube. (Reproduced with permission from Ref 15 © 2002 John Wiley and Sons, and Ref 13 © 2002 Elsevier)

1.2.2 Properties and Applications of Carbon Nanotubes

1.2.2.1 Mechanical Properties and Applications

The sp^2 -hybridized structure of carbon nanotubes endows these materials with unique properties. CNTs have Young's modulus and tensile strength higher than those of diamond and steel.¹⁶ Young's modulus is a measure of stiffness, and CNTs have a value of about 1 TPa comparing to 0.21 TPa of steel.¹⁷ Tensile strength (i.e., the capacity of a material to resist tension) of CNTs ranges from 50 to 150 GPa and is about 20 times stronger than steel.¹⁶ These properties make CNTs a good filler for materials reinforcement. The enhancements depend on CNT diameter, aspect ratio, alignment, dispersion, and interfacial interaction with the matrix. Materials with CNT loadings from 0.1 to 20 wt % are available from different manufacturers.¹⁸ CNT-reinforced products include tennis racquets, baseball bats, and bicycle frames.

1.2.2.2 Electronic Properties and Applications

As discussed in section 1.2.1, about one-third of the CNTs are metallic and two third of them are semiconducting. The electronic density of states of CNTs has well-defined electronic transitions known as van Hove singularities.¹⁹ These transitions can be optically excited and are labeled as E_{ii} , where E is either M for metallic CNTs or S for semiconducting, and $_{ii}$ represents $_{11}, _{22}, _{33}, \dots$ for the first, second and third electronic transitions and so forth. Figure 2 depicts the density of states diagrams for metallic and semiconducting CNTs with their M_{11} , S_{11} and S_{22} transitions labeled.¹⁹ As this energy difference is defined by the one-dimensional quantum confinement along the diameter of the CNTs, the bandgap decreases as the diameter increases. The bandgap transitions for CNTs are important properties in characterization techniques including ultraviolet-

visible-near-infrared (UV-vis-NIR) absorption, resonance Raman spectroscopy and fluorescence spectroscopy, which will be discussed in Section 1.3.

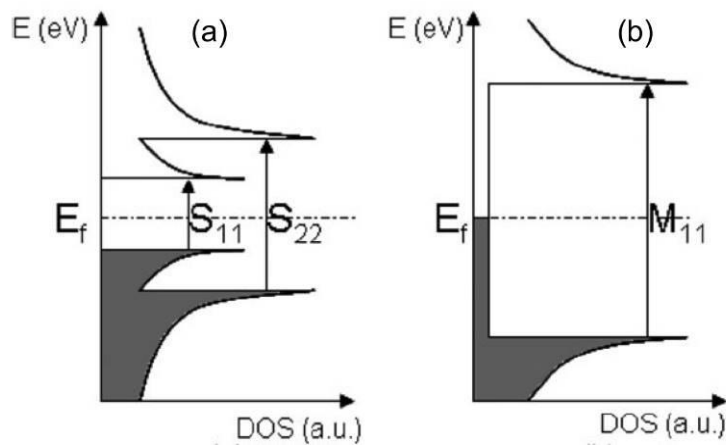


Figure 2. Density of States diagrams of (a) semiconducting and (b) metallic SWCNTs. Electronic transitions between the van Hove singularities are labeled as S_{11} and S_{22} for first and second transition for the semiconducting and M_{11} for the metallic. (Reproduced with permission from Ref 19. © 2008 Royal Society of Chemistry)

Metallic nanotubes, due to their high conductivity, are preferred for the production of conducting films and nanotube electrodes. Other applications include electrostatic dissipation and electro-magnetic interference (EMI) shielding.¹⁸

Semiconducting CNTs are favorable in sensors and optical applications. Semiconducting SWCNTs have been shown to have significant conductance changes in response to different gases.²⁰ Other field-effect transistor (FET)-based sensors were fabricated to detect proteins, antibody, DNA, and enzymatic reactions.²¹ The large bandgap of semiconducting CNTs provides unique intrinsic optical properties such as NIR photoluminescence and resonant Raman signatures for biological detection and imaging. SWCNTs with ~ 1 nm diameter are of particular interest for in vivo imaging as their excitation (λ_{ex}) and emission (λ_{em}) wavelengths lay within the near-infrared window in biological tissue (650 nm to 1350 nm).²² The NIR photoactivity of SWCNTs has minimal photobleaching,²³ and avoids autofluorescence from biological molecules,

which are typically excited by ultraviolet-visible light coinciding with small molecule dyes. The in-vivo imaging of tumors has been heavily studied because of its medical values. The “search and destroy” approaches are of particular interest by coupling imaging with thermal destruction or drug-release to target cancer cells.²⁴⁻²⁶ The intensity of the emitted luminescence from SWCNTs is critical for imaging, as well as for in-vivo chemical sensing.²⁷

1.2.2.3 Biological Applications

Apart from in-vivo imaging and sensing, CNTs are also widely explored as drug delivery vehicles^{28,29} and bone regeneration scaffolds.^{30,31} Fluorescent dyes and anti-cancer drugs can be functionalized with CNTs through covalent linkage or non-covalent π - π stacking.²⁹ A cancer chemotherapy drug, doxorubicin, was loaded onto polyethylene glycol-coated (PEGylated) SWCNTs.³² Binding and release of the drug were controlled by pH which favors release in tumor with acidic pH. Drug release can also be triggered by NIR radiation.²⁶ While most of the drug loadings happen on the outer surface of the CNTs, the encapsulations of fullerenes³³, metal complex, and DNA suggest that drug loading inside the hollow structure may also be possible.²⁹

Carbon nanotubes are also used for tissue engineering and bone regeneration scaffolds.^{30,31} CNTs have been functionalized with collagen and fibroblast growth factor (FGF) to promote cell growth. Newly-formed bones were observed from FGF-MWCNTs, suggesting that MWCNTs accelerated new bone formation.³⁰ It has been proposed by the Haddon’s group that negatively charged functionalized CNTs can attract calcium ions and promote the formation of mineralized bone.³⁴ It has also been shown that CNTs promote cell adhesion.³¹

Other applications of CNTs include CNT-based membranes for water filtration.³⁵ The CNT membranes were reported to impede bacterial adhesion and resist biofilm formation. The antifouling properties of CNTs were also utilized in ship hull coatings.¹⁸

1.2.3 Synthesis of Carbon Nanotubes

Nowadays carbon nanotubes are commercially available. The majority of carbon nanotubes on the market are produced using arc-discharge, laser ablation, or chemical vapor deposition (CVD) methods. Of the CVD-produced SWCNTs, High-Pressure Carbon Monoxide Reaction (HiPco®)³⁶ and cobalt and molybdenum catalyzed process (CoMoCAT®)³⁷ are of particular interest. Nanotube syntheses through combustion are also reported.³⁸ In 2015, carbon nanotubes were found inside airways of Parisian children, raising concerns that CNTs might be produced from vehicle exhausts.³⁹

CNTs were first produced and discovered using the electric arc-discharge method.² Figure 3a shows the configuration of a typical electric arc-discharge set-up. Two graphitic electrodes (6–12 mm in diameter) that are separated by a short distance (1–4 mm) inside a chamber.¹⁶ A voltage of 20-25 V and a continuous electric current of 50-120 A is passed through the electrodes, evaporating the carbon atoms in the anode. Products are collected at the cathode, which includes soot, fullerenes, and CNTs. Product ratio can be optimized by the choice of carrier gases and catalysts. Both MWCNTs and SWCNTs can be synthesized, and SWCNT production can be favored by using catalysts such as Ni, Co, and Fe.³⁸ The produced SWCNTs have diameters of 1-5 nm.¹⁶

The laser ablation method was first introduced by Smalley and co-workers in 1995.⁴⁰ In the laser ablation method, a powerful pulsed laser beam is focused on a graphite target (Figure 3b). The target is vaporized in a hot helium (He) or argon (Ar) atmosphere (~1200 °C).¹⁶ The vaporized carbon atoms condense into CNTs on a water-cooled collector. The SWCNT diameters can be controlled by adjusting the temperature, gas flow rate, and catalyst composition.¹⁶ Unfortunately, the laser ablation produced SWCNTs are not common, as they are

expensive due to the use of high-purity graphite rods and high-power laser, as well as the limited scale of production.³⁸

Chemical vapor deposition (CVD) method is used to mass produce CNTs due to its large-scale and high-quality production at a relatively low cost.¹⁶ For this approach, hydrocarbon source is injected into a pre-heated furnace at high temperature (700-1200 °C) as illustrated in Figure 3c. The hydrocarbons decompose inside a quartz tube and form CNTs on the surface of catalysts, which can be introduced in the gas phase or as a solid on a substrate.¹⁶ Substrate-supported CVD is also unique because it can produce ordered arrays of vertically aligned CNTs.¹⁶ The growth of CNTs can be controlled by adjusting the reaction parameters such as the catalyst, temperature, type of hydrocarbon, and the flow rate of the gases. Of all the variations of CVD processes, High-Pressure Carbon Monoxide Reaction (HiPco) and cobalt and molybdenum catalyzed process (CoMoCAT) methods are of particular interest due to their ability to produce small diameter SWCNTs. They are also suitable for large-scale production, making them widely available.

The HiPco method was developed in 1999.³⁶ This method is an example of gas phase catalyzed production in which flowing iron pentacarbonyl, $\text{Fe}(\text{CO})_5$, is mixed with carbon monoxide (CO) in a heated reactor. Iron clusters are produced in the gas phase on which SWCNTs are nucleated and grown. As both catalysts and carbon source are in the gas phase, the reaction can be operated continuously and thus suitable for large-scale synthesis. HiPco SWCNTs are typically between 0.8 nm to 1.2 nm, which contain ~20 (n,m) species in a given sample.⁴¹

The CoMoCAT® method was developed in 2000.³⁷ Cobalt and molybdenum catalysts are embedded onto silica support and carbon monoxide is used as carbon source at 700°C -

950°C. Different CNT species can be produced by altering the Co:Mo ratio and temperature.⁴² The CoMoCAT process is known to be more selective for chirality and diameter than alternative methods. Under certain conditions, the diameter distribution can be as narrow as 0.2 nm (0.7 - 0.9 nm) with the majority of the SWCNTs being a single chirality (6,5).⁴²

Nanotubes and other nanostructures can be fabricated by flame.^{38,43} Figure 3d shows the co-flow and the counterflow diffusion burner configurations used in combustion synthesis.³⁸ Although this method is more consistent in producing fullerenes and MWCNTs than SWCNTs, there are promising advances for this process to be used in large-scale production.⁴⁴

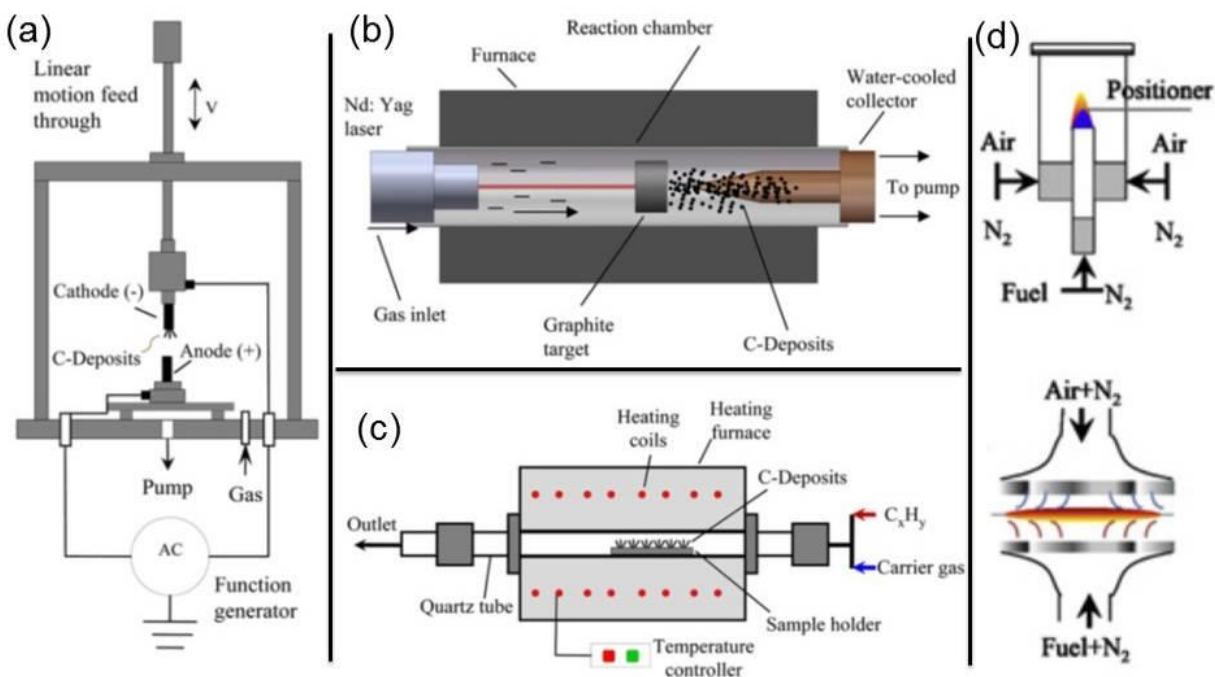


Figure 3. Schemes for carbon nanotube synthesis methods: (a) the electric arc-discharge method; (b) the pulsed laser vaporization method; (c) the chemical vapor deposition method and (d) combustion synthesis method by co-flow and counter-flow flame set-up. (Reproduced with permission from Ref 38. © 2010 Elsevier)

1.2.4 Post-synthesis Treatments of Carbon Nanotubes

As-produced CNTs suffer from four problems that hinder their applications. First, as-prepared CNTs are often contaminated with impurities such as amorphous carbon and metal catalysts. Second, nanotubes have strong van der Waals interactions with each other that result in bundling and aggregation. Third, CNTs have poor solubility in aqueous media due to their sp^2 hybridized surfaces, and in organic media due to their bundling. Finally, as-produced CNTs contain a variety of diameter, length, and chirality distribution of nanotubes. Figure 4 shows the different levels of purifications to be achieved. Separation from impurities, the formation of stable suspensions, and isolation of single chirality will be discussed in this section.

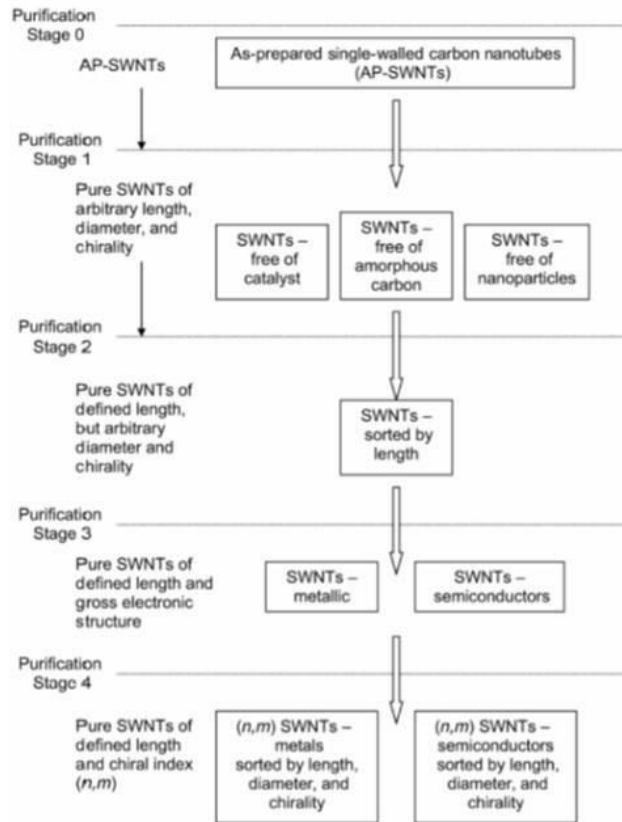


Figure 4. Scheme for various purification stages, starting from as produced SWCNT. (Reproduced with permission from Ref 45. © 2010 Cambridge University Press)

1.2.4.1 Separation from Impurities

The first stage of the purification is to remove soot and metal catalysts. Soot can be removed by air oxidation at 350°C and catalysts can be removed by washing with nitric or hydrochloric acids.⁴⁶⁻⁴⁸ For SWCNTs, the oxidative purification first requires the removal of metal particles as they catalyze the low-temperature oxidation of carbons indiscriminately, destroying the SWCNTs.⁴⁵ The process begins with long (18 h), low-temperature (225°C) oxidation to crack open the carbonaceous shells encapsulating the metal particles.^{49,50} The solution is stirred in concentrated HCl to dissolve the iron nanoparticles. The sample is filtered and dried. The oxidation and acid extraction cycle are repeated at 325 °C for 1.5 h and 425 °C for one hour.^{49,50} Other methods include refluxing or sonicating CNTs in nitric acid⁴⁵, a mixture of concentrated sulfuric and nitric acids (3:1, vol/vol H₂SO₄/ HNO₃)⁵¹, hydrogen peroxide (H₂O₂) and HCl⁵², or other mixture of acids.⁵³ While acid treatments are efficient at removing impurities, they also introduce structure defects (mainly carboxyl groups) on the sidewalls of CNTs.⁴

The introduction of functional groups on CNT sidewalls has its pros and cons. On the pro side, groups like carboxyl, carbonyl and hydroxyl can improve the hydrophilicity of CNTs, increasing their solubility in water. Stable suspensions of oxidized CNTs can be produced by sonication, where the oxygen-containing functional groups prevent the CNT from aggregating. The functional groups are also useful reaction sites for other chemical reactions, such as esterification or amidization.⁴ Reactions using fluorine, ozone, and diazonium have been demonstrated with CNTs to tailor their properties.^{4,54,55} However, the covalent modification of CNTs has its drawbacks as it disturbs the sp² hybridization of the CNT surfaces. The term “defect sites” is sometimes used when these functional groups are not desired. Their presence

can disturb the electronic properties of CNTs and diminish the unique band-gap fluorescence, which we will discuss in details in Section 1.3.5.

1.2.4.2 Suspension of Carbon Nanotubes

Surfactant-stabilization offers an alternative method of making CNT suspensions without sacrificing their electronic properties or sidewall integrity. Dispersants of CNTs can be divided into four categories: (a) surfactants, (b) polycyclic aromatic compounds, (c) biomolecules, and (d) polymers.

The most convenient and frequently used dispersant for CNTs in aqueous media is surfactant, such as sodium dodecyl sulfate (SDS, Figure 5a)⁵⁶ and sodium dodecyl benzene sulfonate (SDBS, Figure 5b).⁵⁷ The suggested mechanism for individual dispersion is the encapsulation of CNTs through the formation of micelles (Figure 5c). Biological surfactants, such as bile salts, are also used as CNTs solubilizers. Sodium cholate (SC, Figure 5d), sodium deoxycholate (SDC, Figure 5e) and other cholate derivatives are commonly used for stabilizing CNTs.^{58,59} The typical concentration of surfactants is applied at 1 wt %. Surfactant wrapping has shown selectivity towards CNTs with specific chirality, and diameters. The selective interaction is key for the isolation of CNTs by gel chromatography.^{41,60}

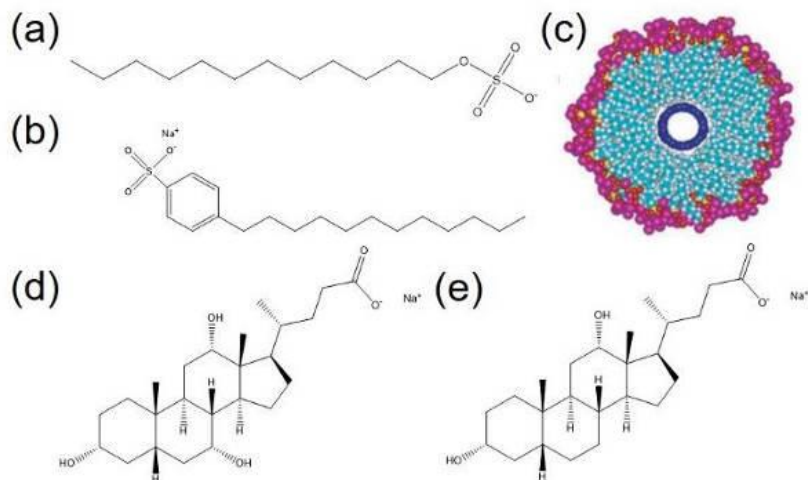


Figure 5. Molecular structures of (a) sodium dodecyl sulfate (SDS) and (b) dodecyl benzene sulfonate (SDBS). (c) Scheme of micelle formation between SWCNTs and SDS. (Reproduced with permission from Ref 56. © 2002 The American Association for the Advancement of Science). Molecular structures of (d) sodium cholate (SC) and (e) sodium deoxycholate (SDC).

CNTs can be stabilized through π - π interactions with polycyclic aromatic compounds.⁶¹ Dai and co-workers stabilized SWCNTs with pyrene derivatives to attach proteins (Figure 6a).⁶² Other pyrene-based, anthracene-based, and porphyrin-based dispersants have been examined.⁶³ Porphyrin-based compounds are of particular interest for their ability to capture metal ions in the center of the porphyrin ring allowing the study of CNT-metal complexes.⁶⁴ Other interesting phenomena includes charge transfer⁶⁴ and separation of optically active SWCNTs.⁶⁵ An optically active porphyrin dimers were used to recognize and enrich SWCNTs with specific diameters and right- or left-handed helicity structures (Figure 6b).⁶⁶

To increase the biocompatibility of CNTs, biomolecules can be applied as CNT dispersants. The benefit of using lipids or proteins is that they can mediate bioactivity. Phosphatidylserine (PS) coated SWCNTs have shown to be recognizable by macrophages, promoting biodegradation of SWCNTs.⁶⁷ Bovine serum albumin (BSA) coated SWCNTs have also shown increased uptake by both human mesenchymal stem cells (hMSC) and HeLa cells.⁶⁸

DNA sequences are also utilized for making CNT dispersions (Figure 6c). DNA sequences can be selective to specific nanotube chirality, enabling the purification of a particular nanotube species from the as-produced mixture.⁶⁹

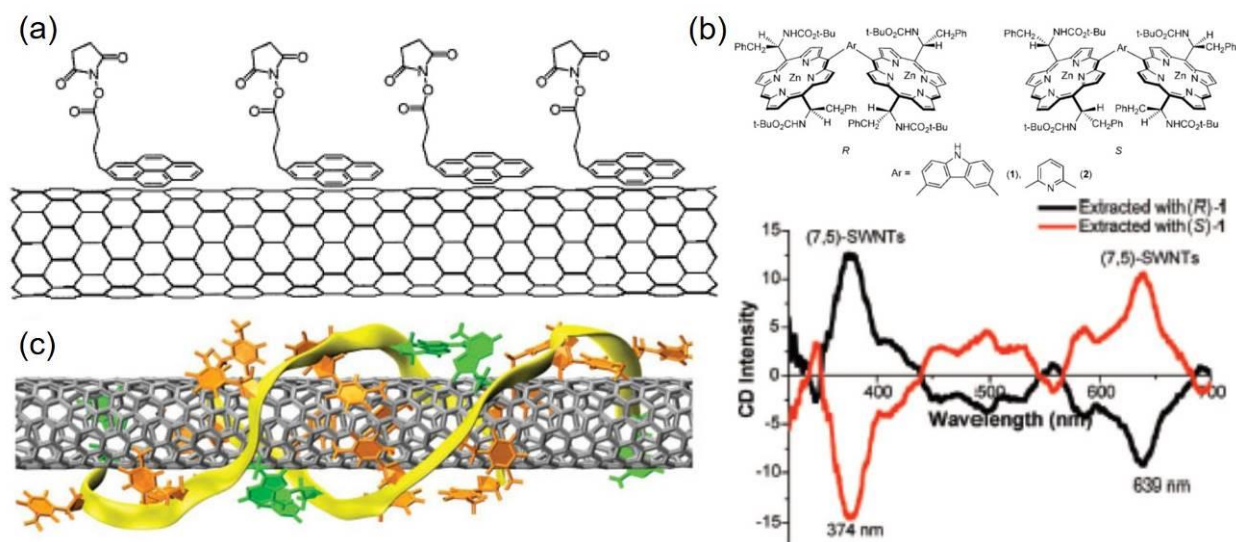


Figure 6. (a) 1-Pyrenebutanoic acid, succinimidyl ester adsorbing onto the sidewall of a SWCNT via π - π stacking. (Reproduced with permission from Ref 62. © 2001 American Chemical Society). (b) A pair of stereoisomers (R and S) of chiral diporphyrin nanotweezers 1 and 2 used in CNT enantiomer separation. (Reproduced with permission from Ref 66. © 2008 American Chemical Society). (c) Schematic of DNA wrapping on SWCNT. (Reproduced with permission from Ref 69. © 2009 Nature Publishing Group).

Polymers can also wrap around CNTs. Polyethylene glycol (PEG)^{32,70}, polyvinylpyrrolidone (PVP)⁶¹, tween⁶¹, and carboxymethyl cellulose (CMC)⁷¹ are examples of polymers used in CNT dispersions. Dai and co-workers have shown PEG-coated SWCNTs for loading and delivery of the drug doxorubicin (DOX).³² SWCNT thin films can be produced by casting CMC-coated SWCNTs on quartz substrates. The resulting thin films showed the alignment of tubes by mechanical stretching.⁷¹

1.2.4.3 Separation of Metallic vs. Semiconducting and Single-Chirality Isolation

Suspension of SWCNTs allows individual nanotubes to be isolated from bundles and be processed for separation. SWCNTs are often sonicated to be dispersed individually and are separated from bundles by centrifugation.⁵⁶ However, more advanced separations are needed for research and electronic/optical applications.

Early methods were specific for separating metallic vs. semiconducting nanotubes.^{53,72,73} In addition to the removal of carbon impurities and metal particles, acid oxidation for nanotube separation has been demonstrated.⁵³ Lee and co-workers reported the removal of metallic SWCNTs using a combination of nitric and sulfuric acids (HNO_3 and H_2SO_4).⁵³ Other selective reactions have also been reported using nitric acid, ozone, and hydrogen peroxide.⁷³ In some cases, reactions can be diameter-selective.^{74,75} Smalley et al. have demonstrated the selective oxidation of small diameter SWCNTs by piranha solution (4:1, vol/vol 96% H_2SO_4 /30% H_2O_2) at high temperature.⁷⁵

While oxidative methods tend to destroy part of the samples, separation by partition can spontaneously isolate pristine metallic and semiconducting SWCNTs.⁷² Using a hydrophobic PEG-rich phase and a hydrophilic dextran-rich phase (Figure 7a), Khripin and co-workers demonstrated both metallic/semiconductor and diameter separation. For arc-discharged SWCNTs (~1.4 nm), metallic tubes were partitioned in the hydrophilic phase, whereas semiconducting tubes were in the hydrophobic phase (Figure 7b). For CoMoCAT SWCNTs (0.6-1.0 nm), the smaller diameter tubes (6,4) were in the dextran-rich phase, whereas the larger diameter tubes (7,5) and (8,4) were in the PEG-rich phase. The difference was explained by two regimes of partition behavior. One for larger diameter SWCNTs, which separates by

polarizability and the other for smaller CoMoCAT SWCNTs, which separation is determined by curvature.⁷²

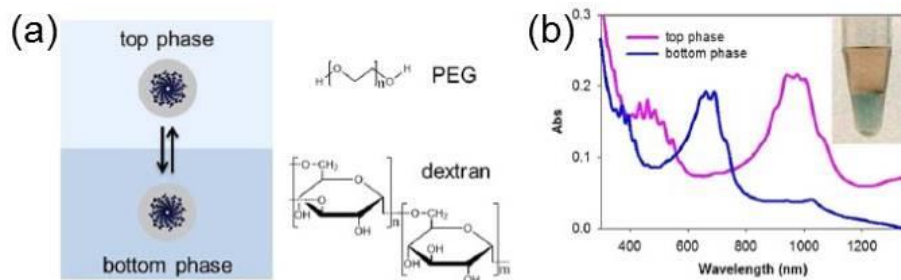


Figure 7. Scheme for various isolation processes. (a) Hydrophilic and hydrophobic phases used in partition separation by partition. (b) Semiconducting SWCNTs are collected in the top PEG phase, and metallic SWCNTs are in the dextran phase. (Reproduced with permission from Ref 72. © 2013 American Chemical Society).

Similar metallic/semiconducting separation can also be achieved by electrophoresis.⁷³ The method utilizes the polarizability of different SWCNTs under an electric field. SWCNTs have to be dispersed individually using a surfactant before being separated.⁷³

SWCNTs by individual chiralities are important for electronic and biomedical applications. Several methods have demonstrated promising results in achieving this goal. DNA-dispersed SWCNTs can also be isolated by ion exchange chromatography (IEX).⁶⁹ Specific DNA sequences have been shown to recognize a particular nanotube species from a mixture. The proposed mechanism was the DNA structure minimizing interaction with the IEX resin, allowing the selected SWCNTs to be eluted first.⁶⁹

Gel chromatography also showed efficient separation of CNTs by chirality.^{41,60} Kataura and co-workers reported a multicolumn gel chromatography method using SDS (Figure 8a). The method is based on the structure-dependent interaction with the allyl dextran-based size-exclusion (Sephacryl S-200). The isolation of 13 semiconducting species was demonstrated by trapping the specific SWCNTs in the gel and later releasing them by high concentration SDS

wash (Figure 8b). Metallic SWCNTs were also collected as they have the lowest interaction with the gel.⁴¹ Modification and improvements were made using the addition of alcohol.⁶⁰

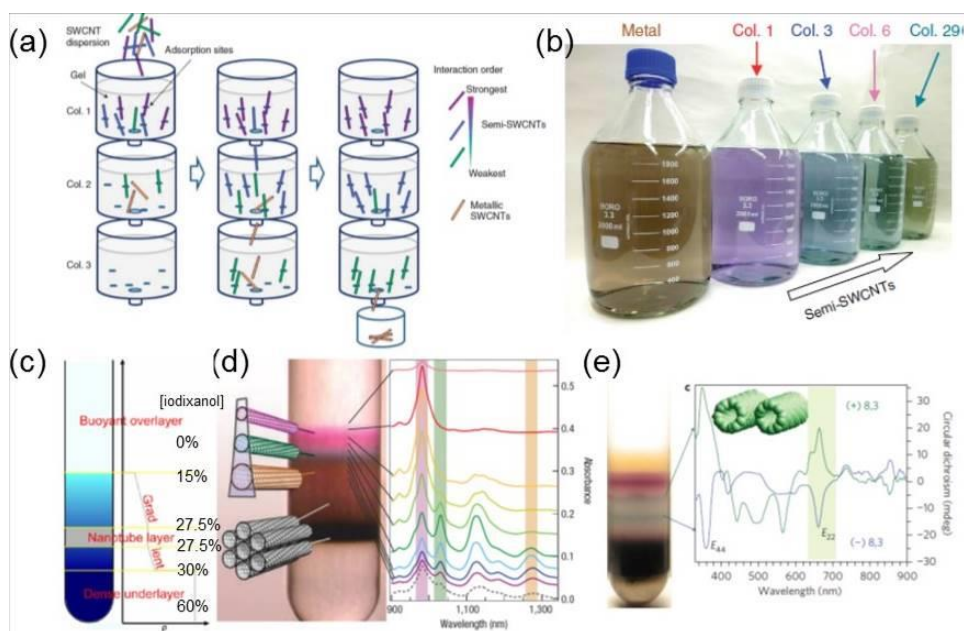


Figure 8. (a) Scheme for gel chromatography. (b) Photograph of separated metallic and semiconducting SWCNT fractions. (Reproduced with permission from Ref 41. © 2011 Nature Publishing Group). (c) Initial density gradient setup for density differentiation centrifugation. (d) Separation of SWCNTs by chirality (Reproduced with permission from Ref 76. © 2006 Nature Publishing Group) and (e) by enantiomer. (Reproduced with permission from Ref 77. © 2010 Nature Publishing Group).

Density-differentiation centrifugation is another scalable approach for separating SWCNTs. Isolation by diameter, bandgap, and electronic property had been demonstrated.⁷⁶ This method exploits the difference in the buoyant densities of different SWCNTs. Isolation is induced by centrifugation in aqueous non-ionic density gradient medium, iodixanol (Figure 8c and 8d).⁷⁶ Furthermore, minor variations of the method allow separation of the enantiomers (Figure 8e)⁷⁷ and by length fractionation.⁷⁸

1.3 CHARACTERIZATION OF CARBON NANOTUBES

1.3.1 Transmission Electron Microscopy (TEM)

CNTs were first identified by transmission electron microscopy (TEM).² Electrons are fired from a tungsten or lithium hexaboride filament at a sample, and the transmitted electrons are captured to form the images. CNTs samples are often prepared by casting on TEM grids. To avoid aggregation during solvent evaporation, samples are prepared by sonication at low concentration. The field of view in the TEM images is relatively small. The section under analysis may not be representative of the entire sample.⁷⁹

High-resolution transmission electron microscopy (HRTEM) uses a combination of brightfield and lattice imaging to form a high-resolution image of the sample.⁷⁹ HRTEM can be utilized to identify the number of walls on a MWCNT, the inter-wall distance, and the diameter of each wall. Different imaging modes and spectroscopies have been developed and applied to characterize CNTs. For example, dark field imaging is beneficial for studying CNT-metal complex,⁸⁰ electron diffraction for determining the atomic structure of crystal or CNTs,¹⁰ and electron energy loss spectroscopy (EELS) for elemental analysis.

Diameter determination can be performed using TEM. Direct measurement had been conducted on a single CNTs and cross-sectional view of a SWCNT bundle (Figure 9a).⁸¹ To image the cross-section of a bundle, CNT sample was affixed to the TEM sample rod and wetted by a drop of methanol. As the methanol evaporates, the surface tension curls the sample. Some of these curved tubes provide images useful for diameter measurement.⁸¹ Diameter analysis can also be performed by fitting the intensity profile with Gaussian function as shown in Figure 9b.⁸²

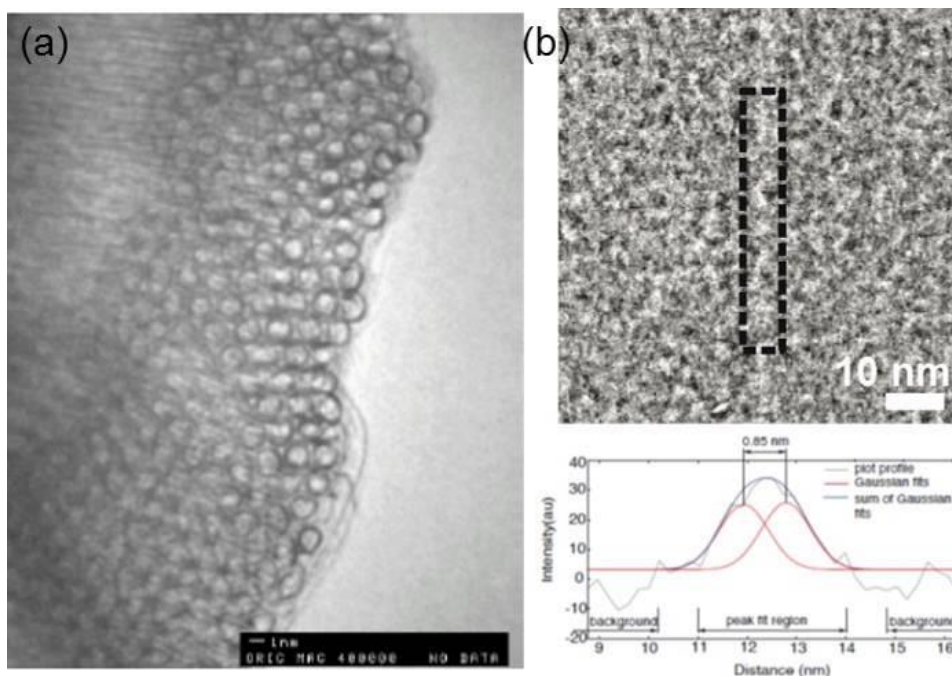


Figure 9. (a) Cross-sectional view of a SWCNT bundle. (Reproduced with permission from Ref 81. © 1998 Springer-Verlag). (b) TEM image of SWCNT and the fitting performed to obtain the CNT diameter from TEM line profiles. (Reproduced with permission from Ref 82. © 2016 Nature Publishing Group)

Determination of the chiral indices (n,m) of carbon nanotubes has been demonstrated using electron diffraction, though this method is not widely used in research.¹⁰ The atomic structure of CNTs has been visualized using aberration-corrected high-resolution transmission electron microscopy (AC-HRTEM).⁸³ The strain and bending can be analyzed in two dimensions. Figure 10 shows the AC-HRTEM images of an $(18,8)$ and a $(28,0)$ SWCNT. Atomic structures and bending angle are revealed.⁸³

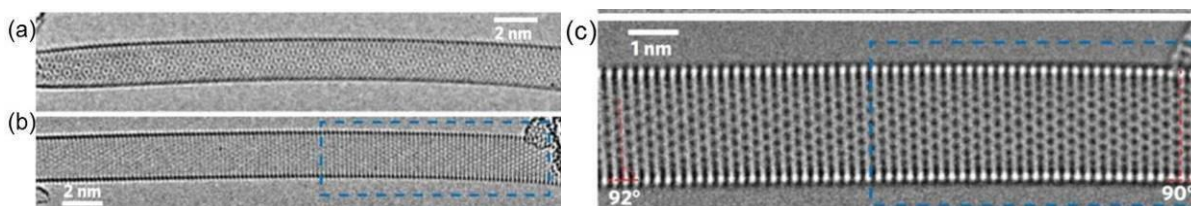


Figure 10. AC-HRTEM images of SWCNTs. (a) $(18,8)$ SWCNT and (b) $(28,0)$ SWCNT. (c) Higher magnification shows the full atomic structure of the SWCNT and reveals a slight bending. (Reproduced with permission from Ref 83. © 2011 Nature Publishing Group)

1.3.2 X-ray Photoelectron Spectroscopy (XPS)

X-ray photoelectron spectroscopy (XPS) is a quantitative spectroscopic technique for elemental analysis. The solid sample is placed inside a high vacuum and is irradiated by a beam of X-rays, typically from a monochromatic Al $K\alpha$ source. XPS spectrum is obtained by recording the number of electrons ejected and their kinetic energy. This technique also produces the chemical state of the elements, making this a valuable tool for chemical structure analysis. XPS has been widely applied in CNT characterization. High-resolution spectra of carbon and oxygen are of particular interest. Figure 11 shows the high resolution-XPS (HR-XPS) spectra of MWCNTs. The spectra were deconvoluted into different peaks and their associated chemical states had been assigned.⁴⁸

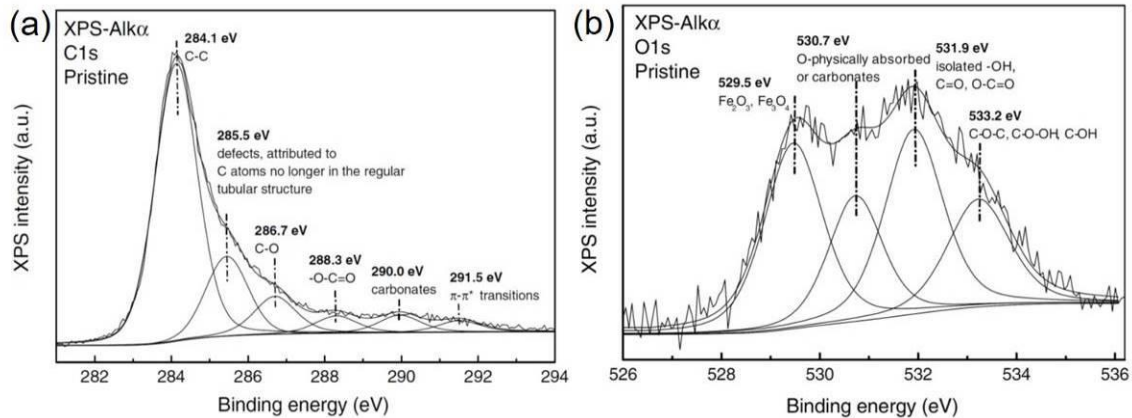


Figure 11. HRXPS of (a) carbon and (b) oxygen peaks of the as-produced MWCNTs. (Reproduced with permission from Ref 48. © 2008 Elsevier)

1.3.3 Raman Spectroscopy

Raman spectroscopy is valuable for CNT characterization in many ways. Raman spectroscopy can be applied for diameter evaluation, defect determination and layers analysis.⁸⁴ It also has the

advantages of detecting both metallic and semiconducting tubes, as well as individually dispersed and bundled CNTs. Samples can be measured as solid or in solution. A typical Raman spectrum is shown in Figure 12 and can be divided into four sections: the radial breathing mode (RBM), the defect band (D-band), the graphitic band (G-band), and the G'-band.

The radial breathing mode (RBM), located between 120 and 350 cm^{-1} , is a result of symmetric vibration of carbon atoms in the radial direction. The RBM frequencies (ω_{RBM}) are inversely proportional to the diameter giving the equation,

$$\omega_{RBM} = \frac{A}{d_t} + B \quad (3)$$

where $A = 223.5 \text{ cm}^{-1} \text{ nm}$, $B = 12.5 \text{ cm}^{-1}$ and d_t is the diameter.⁵ Constants A and B here are also known as environmental factors.⁵⁴ As the RBM in nanotubes is essentially a translational mode of graphene (Figure 12b),⁸⁵ the RBM is only present in cylindrical objects, making a good indicator for the presence of CNTs.

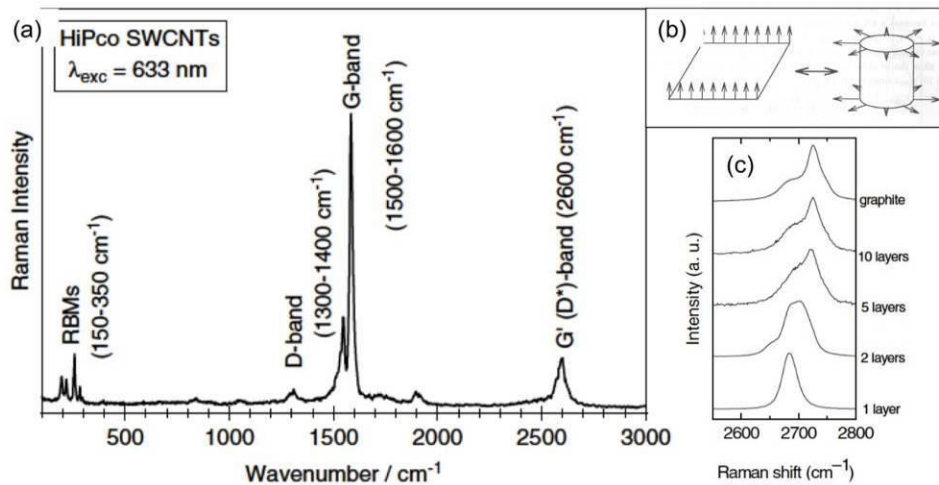


Figure 12. (a) Raman spectrum of carbon nanotubes (Reproduced with permission from Ref 86. © 2007 John Wiley and Sons) (b) Schematic of Z-translational motion of graphene folded into the RBM of carbon nanotube (Reproduced with permission from Ref 87. © 2000 Taylor & Francis) (c) G' peak of various layers of graphene. (Reproduced with permission from Ref 88. © 2007 Springer)

The graphitic band (G-band) is the most intense line between 1500~1600 cm^{-1} . The G mode originates from the tangential vibration of carbon atoms in a sp^2 lattice and is also presented in the Raman spectrum of graphite.⁸⁹ The G-band of CNTs can be deconvoluted into two components; one peaked at 1590 cm^{-1} (G+) and the other peaked at about 1570 cm^{-1} (G-). The G+ peak is associated with carbon atom vibrations along the nanotube axis. The G- peak is related to carbon atom vibrations along the circumferential direction of the CNTs. The line shapes of these peaks are sensitive to the electronic properties of the CNTs and their peak frequencies are sensitive to electron doping.⁹⁰

The defect-induced band (D-band) at $\sim 1350 \text{ cm}^{-1}$ is a result of disruption in the sp^2 hybridized carbon network.⁸⁶ The intensity of D band is more intense when the CNT surface is being covalently functionalization.⁹¹ The intensity ratio between the D-band and the G-band, D/G ratio, is often employed as an indicator for the defectiveness of the graphitic surface at low defect density.⁹⁰ At high defect density, Strano et al. have demonstrated that both the D- and G-band would decrease, resulting in an overall decline in D/G ratio.⁵⁴ Such observation was attributed to the accumulation of defects disrupting the electronic structure of the CNTs. Covalent functionalization is known to disrupt the sp^2 network and the electronic transition of CNTs. The breakdown of the electronic transitions prevented the resonance Raman condition to be matched, resulting in reduced intensity of both the D- and G-bands.⁵⁴ Similar non-linear relation between defect density and D/G ratio was reported in graphene monolayers.⁹²

The G'-band is located around 2500-2800 cm^{-1} and has been associated with the number of graphene layers in a sample (Figure 12c).⁹³ The G'-band is often analyzed as a ratio between the G'-band and the G-band (G'/G ratio). Monolayer, bilayers, and up to 5 layers can be distinguished using this G'/G ratio, as the relative intensity reduces with increasing graphene

layers. The position of the G'-band is also subjected to shift to higher wavenumber in multilayer samples.⁹³

As mentioned in Section 1.2.2.2, CNTs have electronic transitions that can be probed by optical excitation. When incoming light matches the transition energy of the CNT, a resonance occurs and the Raman signal intensity increases strongly. Figure 13a and b show the schematic of the Raman scattering processes under resonance and non-resonance conditions. Under resonance conditions, the Raman signal can be enhanced up to 3 orders of magnitude.⁸⁶ Resonance Raman spectroscopy is considered a non-uniform characterization technique due to this enhancement effect, but selective towards those CNTs at resonance with the excitation wavelength. The use of multiple laser wavelength is recommended to probe CNTs with different transition energy.⁵ Figure 13c shows the RMB of HiPco SWCNTs using 76 different laser lines. Various species are enhanced at different wavelengths, and hence provide a chirality analysis method of a bulk sample.⁸⁹ However, this technique requires a continuous laser excitation source to match the resonance energy of all nanotubes.⁹⁴ CNTs chiral indices, transition energy, and their RBM wavelength are listed in Table 1 and 2.

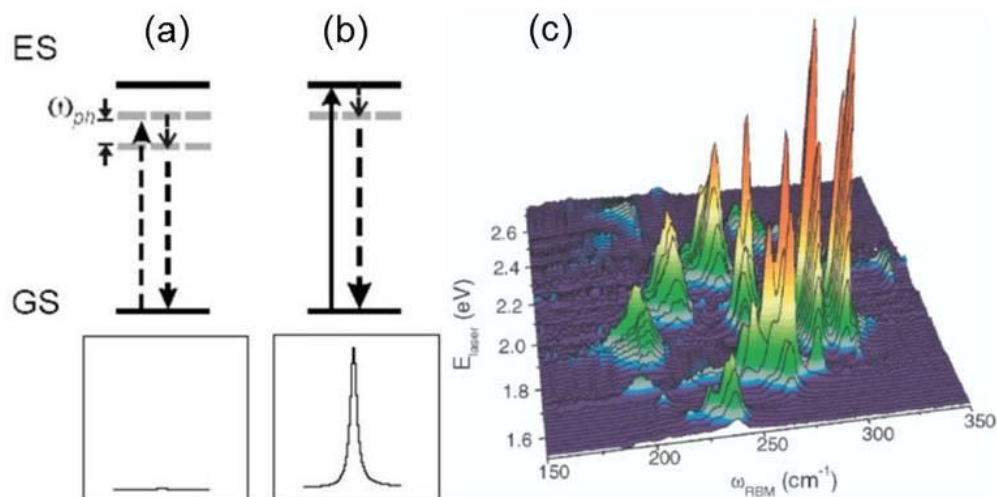


Figure 13. Schematic of Stokes scattering under (a) non-resonance and (b) resonance condition. (Reproduced with permission from Ref 89. © 2006 Springer-Verlag Berlin/Heidelberg) GS (ES) refers to the ground (excited) state of the material. Dashed line refers to the virtual state. Under resonance condition, the signal is enhanced as indicated at the bottom. (c) RBM Raman measurements of HiPco SWCNTs using 76 different laser lines (Reproduced with permission from Ref 94. © 2004 American Physical Society)

Table 1. Transition Wavelength of Semiconducting SWCNTs (Reproduced with permission from Ref 12. © 2003 American Chemical Society)

Chirality (n,m)	Diameter (nm)	Transition wavelength E ₁₁ (nm)	Transition wavelength E ₂₂ (nm)	RBM Peak center (cm ⁻¹)
(6,5)	0.757	974.3	566.4	307.61
(7,5)	0.829	1018.0	641.8	282.14
(8,4)	0.840	1114.9	589.4	278.51
(7,6)	0.895	1115.7	643.7	262.31
(9,4)	0.916	1097.9	719.8	256.61
(12,1)	0.995	1168.0	798.7	237.17
(17,1)	1.391	1755.6	892.8	173.17
(16,3)	1.405	1760.7	905.4	171.62

Table 2. Transition Wavelength of Metallic / Semimetal SWCNTs, (Reproduced with permission from Ref 12. © 2003 American Chemical Society)

Chirality (n,m)	Diameter (nm)	Transition wavelength E ₁₁ (+) (nm)	Transition wavelength E ₁₁ (-) (nm)	RBM Peak center (cm ⁻¹)
(7,4)	0.766	478.3	448.4	304.42
(6,6)	0.825	476.3	476.3	283.39
(9,3)	0.859	526.1	474.7	272.76
(13,7)	1.396	734.0	710.8	172.65
(18,0)	1.429	767.3	707.7	168.90

1.3.4 Absorption Spectroscopy

Ultraviolet-visible-near-infrared (UV-vis-NIR) absorption spectroscopy measures the optical absorption of CNTs from the electronic transitions of the van Hove singularity.⁴⁷ Figure 14 shows the adsorption spectra of pristine and covalently functionalized HiPco SWCNTs.⁹¹ Depending on the CNT structure, the E₁₁ and E₂₂ transitions of semiconducting nanotubes vary from 700-2800 nm and 600-1600 nm respectively.¹² Metallic CNTs have an M₁₁ singularity to be probed, typically ranging from 380-1150 nm.¹² Table 1 and 2 show examples of these transitions for many SWCNTs. As the band-gap varies inversely with the diameter of the tube, large diameter SWCNTs absorb at a higher wavelength for the same band. For example, the S₁₁ transition of a SWCNT with a diameter of 1.4 nm is at ~1700 nm whereas a 0.8 nm SWCNT has its S₁₁ transition at ~1000 nm.

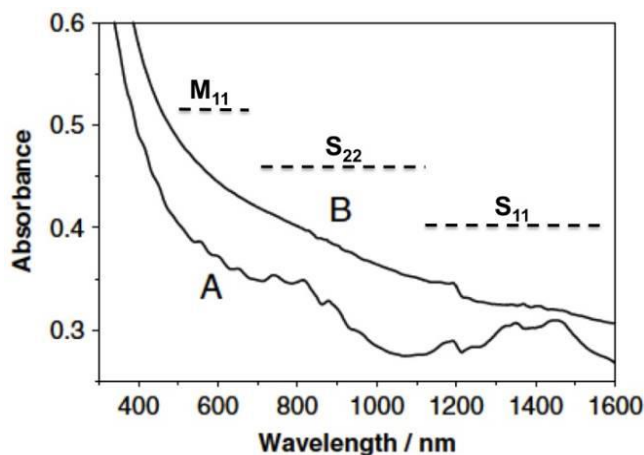


Figure 14. UV-vis-NIR absorption spectra of (A) pristine and (B) covalently functionalized HiPco SWCNTs. Electronic transition between the S_{11} , S_{22} , and M_{11} regions are marked, respectively. (Reproduced with permission from Ref 91. © 2003 American Chemical Society)

While the absorption spectroscopy has the advantage of detecting both metallic and semiconducting SWCNTs, the superpositions of multiple bands can occur, resulting in broad bands instead of distinct peaks. The overlapping of peaks makes the spectra deconvolution tough. As shown in Table 1, the difference can be as small as within 1 nm, as for (8,4) and (7,6) SWCNTs. Furthermore, the absorption peaks are perturbed by covalent functionalization as defect sites disrupt electronic property of the CNTs. Absorption spectroscopy is less useful for functionalized CNTs than for pristine CNTs.

The high absorbance in the UV region (200-350 nm) is attributed to the π - π^* transition and related to CNT diameters.⁹⁵

1.3.5 Fluorescence Spectroscopy

1.3.5.1 Bandgap Luminescence of Semiconducting SWCNTs

The electronic transitions of the CNTs can be probed by fluorescence spectroscopy and was first demonstrated by O'Connell et al.⁵⁶ The photoluminescence (PL) of individual semiconducting

SWCNTs can be excited at their high energy transition (S_{22} or S_{33}) and fluorescence is emitted at their S_{11} band after internal conversion.⁷ Data from fluorescence spectroscopy is often presented as an excitation-emission map (EE map, Figure 15a) or as a 3D plot (excitation wavelength vs. emission wavelength vs. intensity, Figure 15b). As the pair of S_{22} and S_{11} energies depend on the nanotube structure, no spectrum deconvolution is needed for chirality analysis and the abundance of each species is related to their emission intensity.⁷ This method of characterization is widely adopted for nanotubes with diameters between 0.7 to 1.0 nm. For larger diameters, like the ~1.4 nm nanotubes by arc-discharge synthesis, the transitions for S_{22} and S_{11} fall into the NIR range at 900 and 1850 nm respectively. Detection at this NIR range would require a tunable Ti:sapphire laser (700-1055 nm range) and IR-enhanced InGaAs detector, and the experiment would require being done in deuterium oxide to avoid optical absorption by water.^{96,97}

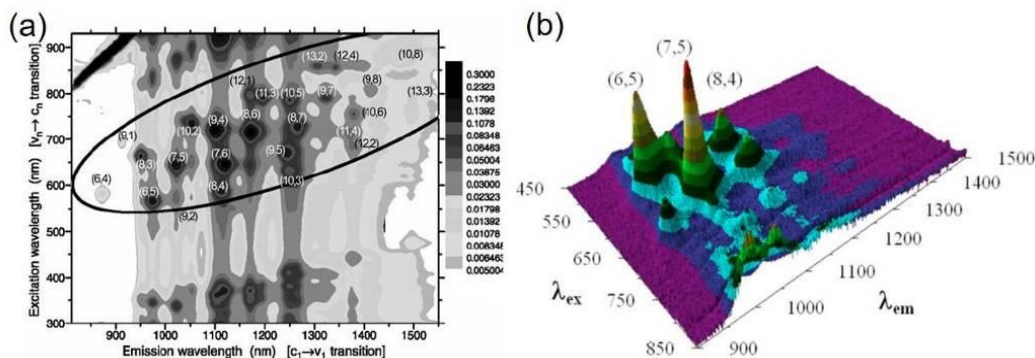


Figure 15. Photoluminescence of (a) HiPco SWCNTs dispersed in SDS and deuterium oxide in EE map (Reproduced with permission from Ref 5. © 2002 The American Association for the Advancement of Science), and (b) CoMoCAT SWCNTs dispersed CMC in 3D-plot. (Reproduced with permission from Ref 71. © 2006 AIP Publishing LLC)

Only individually dispersed semiconducting SWCNTs exhibit PL as the bundled SWCNTs could contain metallic tubes that quench the fluorescence. Thus the PL observation is a good indicator of individually solubilized SWCNT in solutions and polymer thin films.^{56,71} Aggregation is known to generate sidebands on the EE map by exciton energy transfer

(EET).^{98,99} Figure 16a shows the bandgap transitions of SWCNTs and the EET between different tubes. The solid cross indicates the interaction of two semiconducting SWCNTs. EET occurs when individualized CNTs bundle together in which the larger gap CNTs act as exciton donors and the smaller gap tubes act as acceptors.⁹⁸

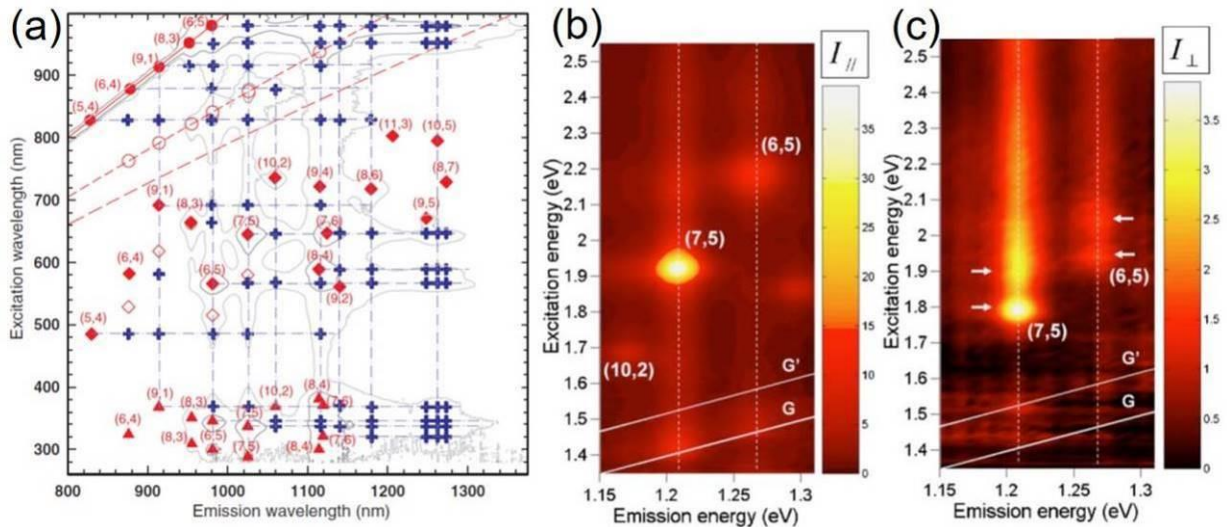


Figure 16. (a) EE map of SWCNTs with transitions marked with solid circles (E_{11}), diamonds (E_{22}), and triangles (E_{33} and E_{44}). Open circles and diamonds are phonon sidebands. Solid crosses are exciton energy transfer (EET) between SWCNTs. (Reproduced with permission from Ref 98. © 2007 American Physical Society) Decomposed EE maps for (b) collinear and (c) perpendicular dipoles. Peaks for I_{\perp} spectrum are indicated by arrows. (Reproduced with permission from Ref 100. © 2006, American Physical Society)

Maruyama and co-workers analyzed the PL of SWCNTs using polarized excitation light (Figure 16b and c).¹⁰⁰ They reported distinct peaks from SWCNTs corresponding to excitation light perpendicular to the tube axis. This excitation causes a blue-shifted intensity tail above the distinct peaks when plotted in eV, which would be below the distinct peaks if plotted in nanometer.

The excitation and emission wavelengths of the SWCNTs can be up- and down-shifted by solvent,^{101,102} chemical environment,¹⁰³ and the choice of surfactant^{57,104}. Haggenueller et al. reported the shift of PL emissions by up to 15 nm in different surfactant dispersions.¹⁰⁴

The photoluminescence of semiconducting SWCNTs can be diminished by structure defects and covalent functionalizations.¹⁰⁵ Weisman described the defect sites as exciton recombination sites, which is more accessible in short pristine nanotubes during the exciton lifetime.¹⁰⁵ Weisman and co-workers concluded that the average PL emission of HiPco SWCNTs is only 40% of their near-pristine values due to structural defects.¹⁰⁵ The NIR emission intensity is proportional to CNT length according to both direct and fractional measurement studies.^{105,106} Hobbie et al. determined that shorter nanotubes are more defective than longer tubes within the same batch, which would also explain the lower quantum yield in the shorter CNTs.¹⁰⁶ Chiral- and diameter-selective reactions have been demonstrated by the protection via the use of surfactants, resulting with selective PL quenching of the SWCNTs.^{58,107,108}

Recent advances allow NIR detection in three-dimensional tracking. PL from a single SWCNT was tracked in solution and in HeLa cells using orbital tracking microscopy.¹⁰⁹ Orbital microscopy utilizes an orbiting excitation beam and a real-time feedback control system to keep the particle in focus, whereas the z-displacement is detected by the deviation of two, off-focus detection planes.¹⁰⁹ An alternative approach was demonstrated by Dai and co-workers.¹¹⁰ Using a gold substrate as a plasmonic ruler to probe ~10 nm of z-displacement, the Dai group observed the single nanotube endocytosis in three dimensions.¹¹⁰

1.3.5.2 Defect-Induced Photoluminescence

Recent studies have been focusing on slightly functionalized semiconducting SWCNTs. A new emission band from semiconducting SWCNTs was reported upon a small degree of defects.^{108,111–113} This new emission band, named E_{11}^- or E_{11}^* , has been demonstrated by diazonium reaction (Figure 17a)¹¹², ozonation (Figure 17c)¹¹¹, hydrogen peroxide oxidation¹⁰⁸, and alkylcarboxylation¹¹³. Wang and co-workers have demonstrated that the relation between

defect density and band emissions.¹¹² Upon functionalization, the bandgap emission (E_{11}) was diminished, whereas the E_{11}^- band appears at low defect density, beyond which it is completely lost (Figure 17b).¹¹² The mechanism of this emission has been proposed by Ghosh et al.¹¹¹ In short, defect sites create local exciton traps that have a locally reduced bandgap. As the defect density is low, the majority of the tubes have the properties of pristine CNTs, including a nearly unchanged absorption. Excitons, generated by light absorption at the pristine CNTs' S_{11} or S_{22} bandgap, are mobile and may diffuse along the SWCNTs. The excitons are stabilized at the defect sites and give the E_{11}^- emission through radiative recombination (Figure 17d).¹¹¹ Wang et al. used density functional theory (DFT) to calculate the effect of diazonium functionalization on (6,5) SWCNTs.¹¹² Their calculation showed that resulting defect site breaks the symmetry of the nanotube structure and split the E_{11} absorption into two dipole-allowed optical transitions, E_{11}^- and E_{11}^+ . The lower energy E_{11}^- was 181 meV below the E_{11} transition, whereas the E_{11}^+ was 225 meV above the E_{11} . They reported that the calculated E_{11}^- transition matches the E_{11}^- photoluminescence energy observed experimentally.¹¹²

Despite the different nature of ether and diazonium functionalization, the resulting E_{11}^- emission can emit at similar wavelengths and has been attributed to the same localized trap states generated by oxygen or diazonium defects.¹¹⁴ It is important to note that ethers on SWCNTs does not break the sp^2 hybridization of the neighboring carbons.¹¹¹ Moreover, ether-perpendicular to CNT axis can stabilize the CNT by rupturing of the C-C bond and releasing the curvature strain at the circumference of the tube.¹¹⁵ On the contrary, diazonium reaction does not break the C-C network, but induces sp^3 defects in the sp^2 lattice of carbon nanotubes.¹¹² With diazonium, the new E_{11}^- peak position can be shifted by changing the substituents on the aryl group.¹¹²

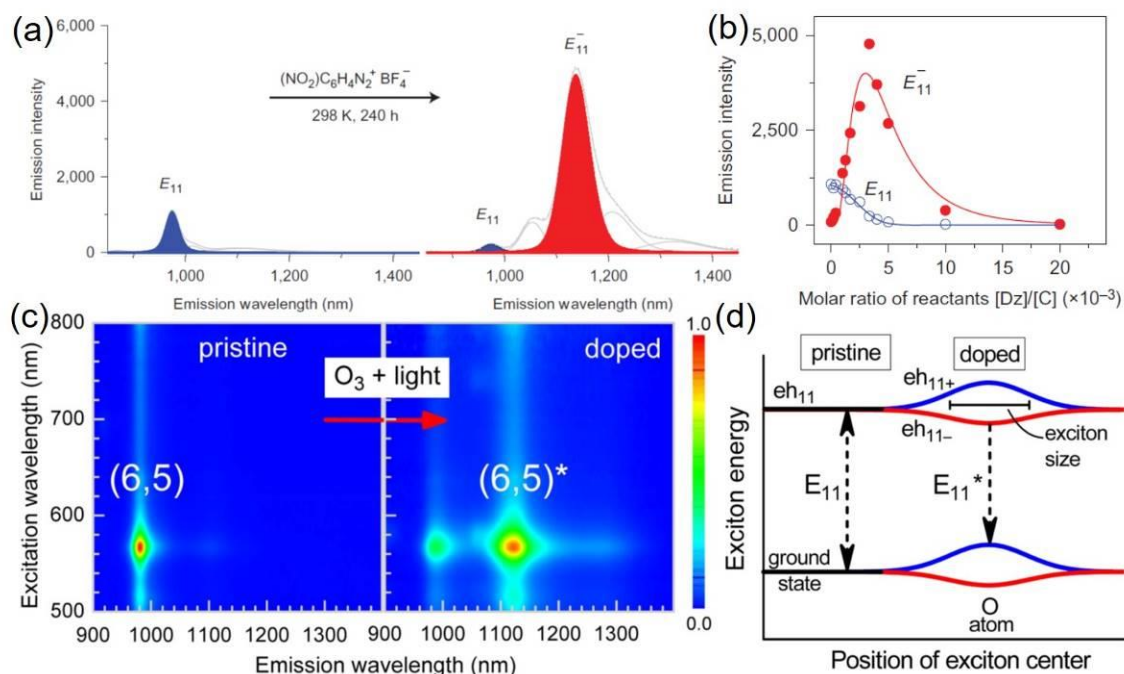


Figure 17. (a) Defect-induced photoluminescence (E_{11}^-) by diazonium reaction. (b) Emission intensity of E_{11} and E_{11}^- photoluminescence from (6,5) SWCNTs as a function of defect density. (Reproduced with permission from Ref 112. © 2013 Nature Publishing Group). (c) Defect-induced photoluminescence (E_{11}^-) by ozonation treatment. (d) Computation model of the E_{11} band split into E_{11}^- and E_{11}^+ energy states. (Reproduced with permission from Ref 111. © 2010 The American Association for the Advancement of Science)

In a recent paper, Wang et al. have utilized this defect-induced E_{11}^- photoluminescence for sensor applications.¹¹⁶ SWCNTs were functionalized by aminoaryl functional groups to generate sp^3 defect sites. Defect photoluminescence of N,N-dimethylamino- and N,N-diethylamino- benzene functionalized SWCNTs are strongly dependent on pH, and emission peaks can be red-shifted by 18 nm from pH 9 to pH 4 through the protonation of tertiary amines. Temperature sensing was achieved by monitoring the ratio between the E_{11}^- and E_{11} emissions.¹¹⁶

1.4 TOXICITY OF CARBON NANOTUBES AND THEIR BIODEGRADATIONS

Although CNTs show promising applications for in vivo imaging and drug delivery application, there are two fundamental questions that need to be addressed. First, safety is the first priority for any material used in medicine. Toxicity of CNTs has to be carefully studied before any CNTs are administered to patients. Second, the fate of these nanomaterials administered has to be understood, whether they are degraded through biooxidation or eliminated through biliary and renal pathways. This section will cover the toxicity of carbon nanotubes and review recent efforts on the biodegradation of nanomaterials.

1.4.1 Toxicity of Carbon Nanotubes

Early studies focused on the pulmonary toxicity of CNTs after intratracheal instillation.^{117,118} These results suggest that aerosol exposure of raw CNTs in the workplace should be avoided.²⁹ However, some attributed the toxicity to the metal catalyst or CNTs aggregation in the lungs, arguing that the toxicology should be different for those administered through other routes such as intraperitoneal (IP) and intravenous (IV) injections.^{29,119} Systematic examinations of different aspects of CNTs have been conducted. The toxicity of CNTs can be summarized into four categories: metal impurity, size and length of the CNTs, aggregation and functionalization (Figure 18).

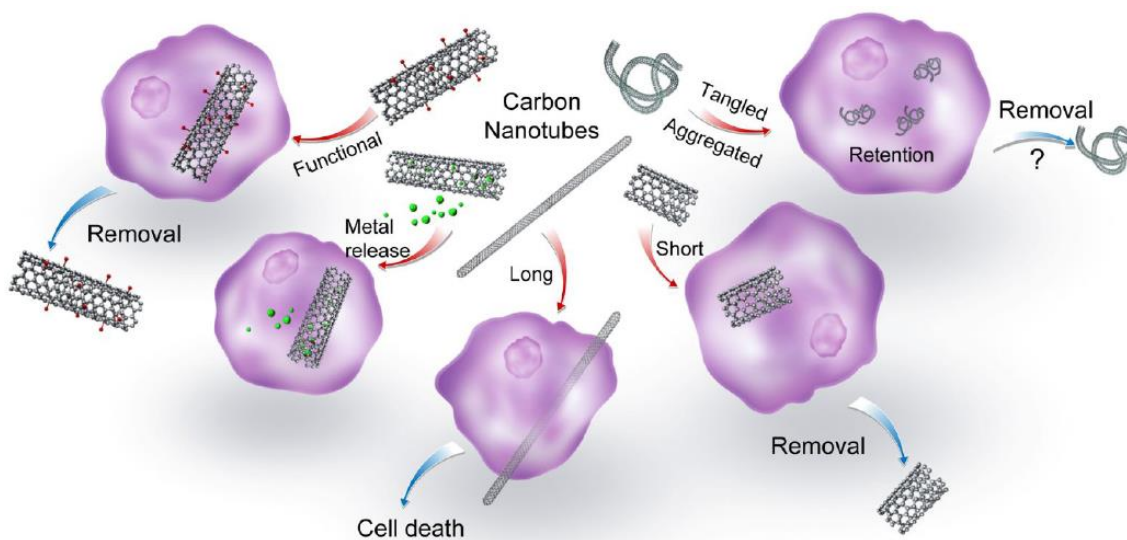


Figure 18. Properties of CNTs influencing cell uptake and responses. (Reproduced with permission from Ref 120. © 2013 American Chemical Society)

1.4.1.1 Metal Impurity

Metal catalysts are employed in CNTs synthesis and can be removed by acid treatments discussed in Section 1.4.1.1. The presence of these metal particles can be toxic to cells by inducing oxidative stress.¹²⁰ Kagan and co-workers compared the toxicity of SWCNTs containing different iron concentrations in RAW 264.7 macrophages.¹²¹ They reported that iron-rich SWCNTs (26 wt % Fe) were more effective in generating hydroxyl radicals than the purified SWCNTs (0.23 wt % Fe). The antioxidant concentration was reduced due to the oxidative stress generated by iron-rich SWCNTs.¹²¹ Similar result was reported by Pulskamp et al., in which purified CNTs did not induce any inflammatory mediators in rat macrophages (NR8383) and human A549 lung cells.¹²² However, intracellular reactive oxygen species were detected when cells were incubated with metal-containing non-purified CNTs. Pulskamp et al. concluded that metal traces associated with the commercial nanotubes are responsible for the biological effects.¹²²

1.4.1.2 Size and Length

Experimental data indicate that long CNTs are more toxic than the shorter ones.^{123–125} Sata et al. compared MWCNTs of 220 nm and 825 nm long and studied their effects in human cells and in rats.¹²³ They reported a stronger inflammation response with the longer CNTs than the shorter ones and attributed this observation to the ability of macrophages to envelop shorter CNTs.¹²³ In another report by Tsutsumi and co-workers, their results indicated that long MWCNT (5–15 μm) caused more DNA damage and more severe inflammatory effects than short MWCNTs (1–2 μm), though long SWCNTs (5–15 μm) caused little effects (Figure 19).¹²⁴ Length-dependent inflammation and formation of granulomas were also observed in mice.¹²⁵

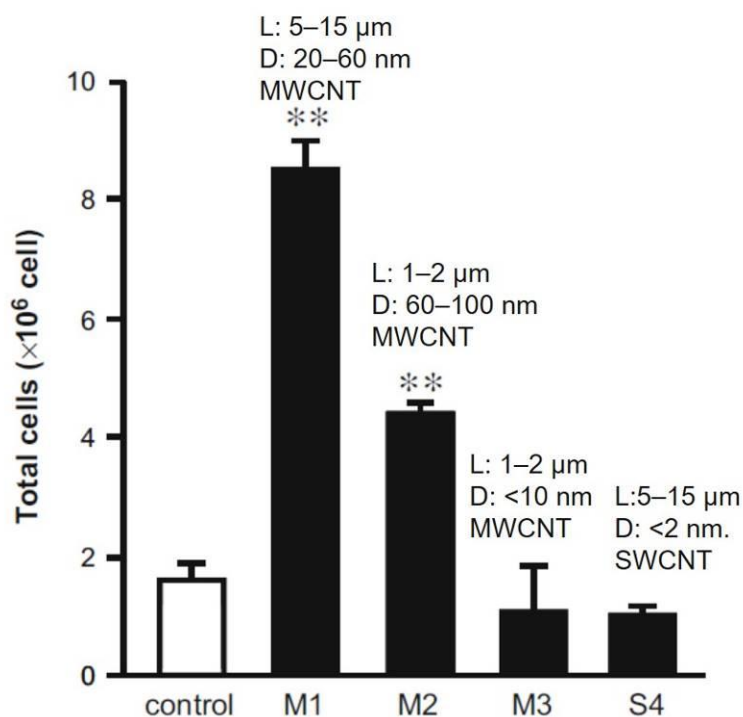


Figure 19. Inflammatory response induced by CNTs of different size and shape in vivo. C57BL/6 mice were intraperitoneally injected with 50 μg CNTs (M1, M2, M3, and S4). After 24 h post-exposure, the abdominal lavage fluid was harvested and the total cell number was determined to evaluate inflammatory responses induced by CNTs. (Reproduced with permission from Ref 124. © 2010 Springer)

1.4.1.3 Aggregation

Aggregation status can also affect the toxicity of CNTs.^{125–127} Tightly packed spherical agglomerates, central tangled agglomerates, rope/needle-like fibers were reported to produce different inflammation responses in mice with the long fibers produced the most severe response (Figure 20).¹²⁵ Similar results were reported by Palomäki et al. in which different nanomaterials were examined in human primary macrophages.¹²⁶ They observed a CNT-induced NLRP3 inflammasome activation only from long needle-like CNT. Minimal inflammatory responses were observed from carbon black, short CNT, and long-tangled CNT.¹²⁶ Study on SWCNTs was performed using human MSTO-211H cells.¹²⁷ Using the same SWCNT materials, Wick et al. reported that suspended SWCNTs were less toxic than rope-like agglomerates.¹²⁷

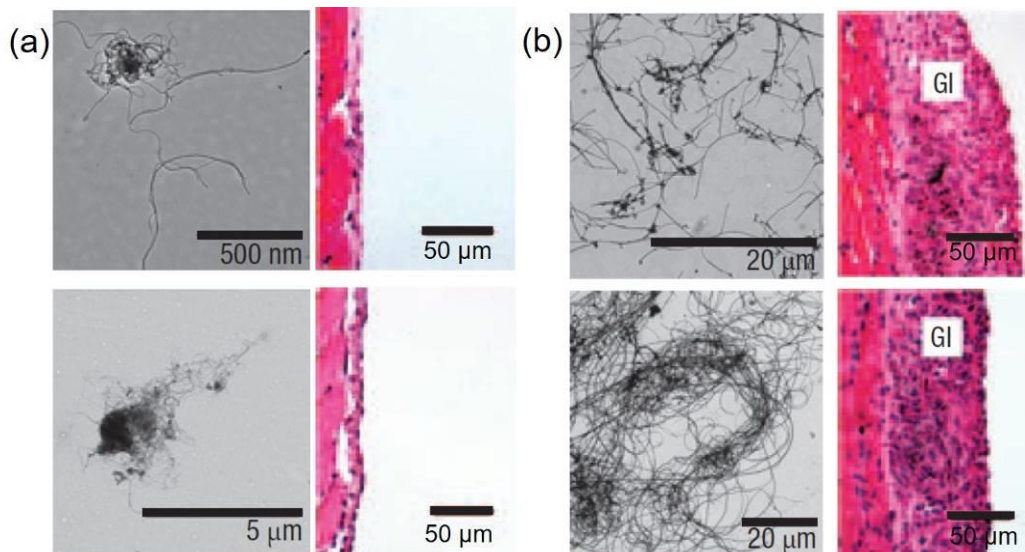


Figure 20. TEM images show the (a) tangled and (b) long fiber examined in mice after 7 days. Haematoxylin and eosin histology sections of the diaphragms show the presence of granulomatous inflammation (GI) in mice exposed to long fibers. (Reproduced with permission from Ref 125. © 2008 Nature Publishing Group)

1.4.1.4 Functionalization

There are conflicting reports on the effects of functionalizations of CNTs and their toxicity. Bottini et al. concluded that oxidized MWCNTs were more toxic than their pristine counterparts from their studies on human T cells.¹²⁸ On the other hand, the Welland group reported that acid-treated SWCNTs with sidewall defects were nontoxic in human monocyte-derived macrophages.¹²⁹ One problem with comparing pristine and functionalized CNTs is that multiple parameters are often changed in the functionalization process. As mentioned, acid treatments can remove the metal particles, shorten tube lengths, and the additions of functional groups can improve solubility in water, which in turn reduce the degree of aggregation. While acid treatments generate simple hydrophilic groups such as hydroxyl, carboxyl and carbonyl sites, Dai argued that these functional groups cannot make CNTs soluble in most biological solutions as the media contain a high content of salt, which can precipitate out the SWCNTs by charge screening effects.²⁹ However, specific functionalizations through covalent attachments of molecules and non-covalent coating can be tailored to improve the biocompatibility of the nanomaterials.

Covalent Functionalization

Oxygen-containing-functional groups can be further modified with polyethylene glycol (PEG) to yield CNT-polymer conjugates that are stable in biological environments.³² PEG can be attached to the carboxylic groups on SWCNTs through amidation.³² Other covalent attachments include biotin,¹³⁰ fluorescein molecules¹³⁰ and peptide nucleic acid (PNA)¹³¹.

Colvin and co-workers studied the cytotoxic response of cells on the phenyl functionalized SWCNTs.¹³² SWCNTs were prepared at three phenyl densities and were

incubated with human dermal fibroblasts (HDF). Their result revealed that as the degree of sidewall functionalization increases, the SWCNTs sample becomes less cytotoxic.¹³²

Although covalent functionalization can improve the biocompatibility of CNTs, the induced defect sites disrupt the nanotube structures and destroy their intrinsic physical properties. Photoluminescence and resonance Raman scattering are often diminished as the result of the disrupted electronic structures. This reduces the potential for optical applications.

Non-covalent Functionalization

Section 1.2.4.2 covered a variety of CNTs suspensions through the non-covalent coating. However, not all of them are suitable for biological applications. Surfactants, such as SDS and sodium cholate, are typically not stable unless they are at high concentrations. However, large amounts of surfactants may lyse cell membranes and denature proteins.²⁹

Toxicity of non-covalently functionalized SWCNTs has been examined in cell culture and animal studies. Nontoxic suspension of SWCNTs was prepared by Pluronic F-108 (Polyethylene glycol-block-polypropylene glycol-block-polyethylene glycol) to study the uptake of SWCNTs in phagocytic cells.¹³³ Uptake of pristine SWCNTs was demonstrated by the detection of their intrinsic NIR fluorescence. Macrophage population was unaffected by the exposure to SWCNTs.¹³³

Tween 80 dispersed SWCNTs were intravenously (tail vein) injected into mice and studied for three months.¹³⁴ Accumulation of SWCNTs was detected in liver, lung, and spleen with slight inflammation and inflammatory cell infiltration occurred in the lung. The toxicity of SWCNTs was attributed to oxidative stress.¹³⁴ In another work, SWCNTs non-covalently functionalized by PEG were injected to mice through intravenous injection and were monitored for four months (Figure 21).¹³⁵ The accumulation of SWCNTs was detected in the liver and

spleen four months after injection. Necropsy and tissue histology showed age-related changes only and revealed no SWCNTs related toxicity. From these results, Gambhir and co-workers concluded that “*water-soluble, (non-covalently) functionalized, pristine nanotubes to be less cytotoxic than non-functionalized or oxidized tubes*”.¹³⁵

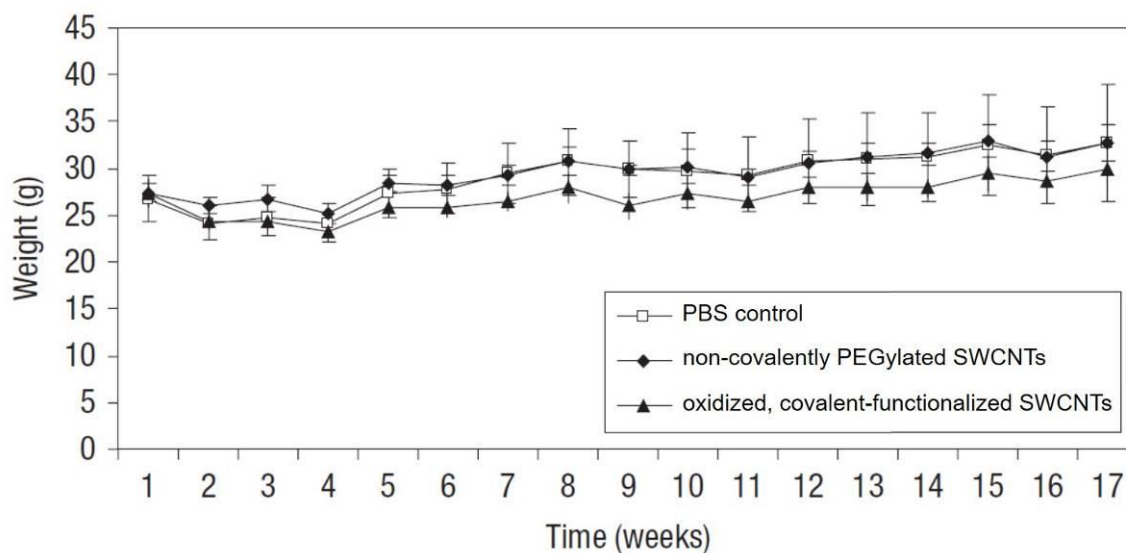


Figure 21. Body weight of nude mice following injection of SWCNTs. Mean and standard deviation of body weight of nude mice injected intravenously with non-covalently PEGylated SWCNTs (black diamonds), oxidized, covalently functionalized SWCNTs (black triangles) or PBS control (white squares) show no statistically significant differences over a period of 4 months. (Reproduced with permission from Ref 135. © 2008 Nature Publishing Group)

Non-covalently functionalized pristine SWCNTs maintain their intrinsic electronic structures and have allowed the use of semiconducting SWCNTs as fluorophores for in-vivo imaging, molecular tag, and cell detections. Using dynamic contrast-enhanced imaging, the circulation of dispersed SWCNTs can be followed frame by frame during intravenous injection.^{136,137} Organs can be observed in real-time as SWCNTs pass through and image resolution can be improved by principal component analysis (PCA).¹³⁶ Accumulation of SWCNTs in the tumor was reported using 90 kDa amphiphilic poly(maleic anhydride-alt-1-octadecene)-

methoxy polyethylene glycol (C18-PMH-mPEG) as CNT dispersant.¹³⁷ Using isolated (6,5) SWCNTs, the photoluminescence is six-fold brighter than HiPco SWCNTs of the same mass. Photothermal tumor ablation was performed with the (6,5) SWCNTs accumulated inside the tumor cells after 48 hours (Figure 22).¹³⁷

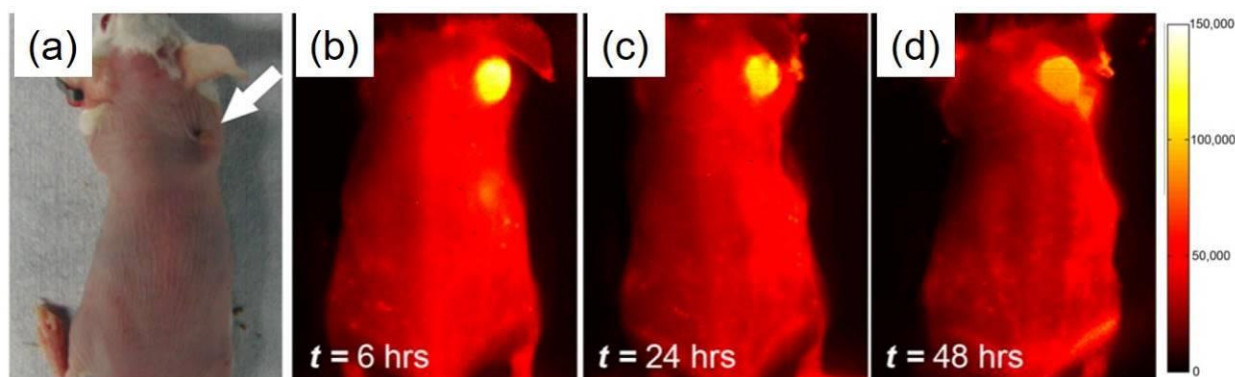


Figure 22. (a) Optical image of a mouse bearing a 4T1 tumor on the right shoulder. (b-d) NIR-II (950-1400 nm) fluorescent time course imaging 12, 24, and 48 h post-injection, from left to right, showing clear SWCNTs accumulation in the 4T1 tumor. All mice were injected with 0.254 mg/kg of SWCNTs and emission collected from 0.9 to 1.4 μm after excitation at 808 nm at a laser power density of 0.14 W/cm². The scale bar on the right corresponds to all NIR images of 4T1 tumor-bearing mice. (Reproduced with permission from Ref 137. © 2013 American Chemical Society)

SWCNTs can be prepared by non-covalent functionalization with PEGylated phospholipids.¹³⁸ The prepared SWCNTs are also NIR active and can be utilized as fluorescent tags for selective probing of cell surface receptors and cell imaging. Selectivity was achieved through the conjugation of antibodies to the polymers. Herceptin conjugation to SWCNTs showed promising results in recognizing breast cancer cells with high NIR fluorescence.¹³⁸ Arginine–glycine–aspartic acid (RGD) peptide ligands were linked to the amine residue on the aminated PEGylated phospholipids chain to bind to $\alpha_v\beta_3$ -integrin positive U87 MG cells selectively.¹³⁹

1.4.2 Biodegradation of Carbon Nanotubes

Coated-pristine SWCNTs have been shown to accumulate in the spleen and liver suggesting that the clearance of SWCNTs is via the biliary and renal pathways.¹⁴⁰ Using Raman spectroscopy, PEGylated phospholipids-coated SWCNTs were detected in intestines, kidneys, and bladders of mice. No toxicity from SWCNTs was observed in necropsy and blood measurements. The length of PEG chains was compared at 2 kDa, 5 kDa, and 7 kDa. Increased PEG length is associated with longer circulation time of CNTs in the blood.¹⁴⁰ Pristine SWCNTs coated with Tween 80 have shown similar accumulation of SWCNTs in the organs, especially in the lungs.¹⁴¹ Two pathways were suggested by Sun et al. One is that nanotubes are removed by alveolar macrophages as mucus through mucociliary transport to leave the lungs. The other is by the interstitial transfer of CNTs to the spleen through the lymph nodes.¹⁴¹

For the non-suspended or oxidized SWCNTs, inflammation responses are often observed.¹²³⁻¹²⁶ Unusual inflammatory and fibrogenic pulmonary responses were seen from mice exposed to raw SWCNTs through pulmonary aspiration.¹⁴² These studies inspired later investigations on understanding the reaction between innate immunity and CNTs.^{143,144} The enzymatic biodegradation of SWCNTs was first demonstrated by the plant-derived enzyme, horseradish peroxidase (HRP).¹⁴⁵ Other enzymes examined include eosinophil peroxidase (EPO)¹⁴⁶, lactoperoxidase (LPO)¹⁴⁷, lignin peroxidase (LiP)^{148,149}, manganese peroxidase (MnP)¹⁴⁹, and myeloperoxidase (MPO).¹⁴³

1.4.2.1 Horseradish Peroxidase (HRP)

Introduction to the Enzyme

Horseradish peroxidase (HRP) is obtained from the roots of horseradish plant. It contains 308 amino acid residues and one iron (III) protoporphyrin IX heme active site. The functions of the peroxidase enzyme in plants include the removal of hydrogen peroxide, oxidation of toxic reductants, biosynthesis and degradation of lignin, and defensive responses to wounds.¹⁵⁰ In the presence of hydrogen peroxide (H_2O_2), this enzyme demonstrates the ability to oxidize organic substrates. Figure 23a shows the oxidation states of the HRP enzyme. After reacting with H_2O_2 , the oxidation state of the iron atom in the heme group is increased from (III) to (IV), and a porphyrin-based cation radical is formed. The iron (IV) porphyrin cation radical state of the enzyme, known as Compound I, oxidizes a substrate by two consequent one-electron-oxidation-steps, whereby Compound I is reduced to Compound II and subsequently back to the native iron (III) form of HRP; this is referred as the peroxidase cycle (Figure 23a).¹⁵¹ In the excess amount of hydrogen peroxide, Compound II can further react with H_2O_2 to form Compound III.¹⁵² Compound III formation is reported to be accompanied by the oxidation of aromatic amino acid groups on the protein.¹⁵² The self-oxidation of the enzyme through the formation of Compound III is in agreement with reported HRP inactivation when the enzyme is over-exposed to excess peroxide. At high concentration ($>1 \text{ M}$), the inactivation mechanism was proposed as the disruption of the heme site configuration through the oxidation of a certain amino acid residue nearby.¹⁵³ Such inactivation was not observed at low H_2O_2 concentration, where Compound III formation is negligible.¹⁵³ The ability for HRP to react with H_2O_2 has drawn attentions in using the enzyme for H_2O_2 detection. Amperometric sensors for H_2O_2 have been demonstrated through the immobilization of HRP enzymes on polymer nanochannels and SWCNTs.^{154,155}

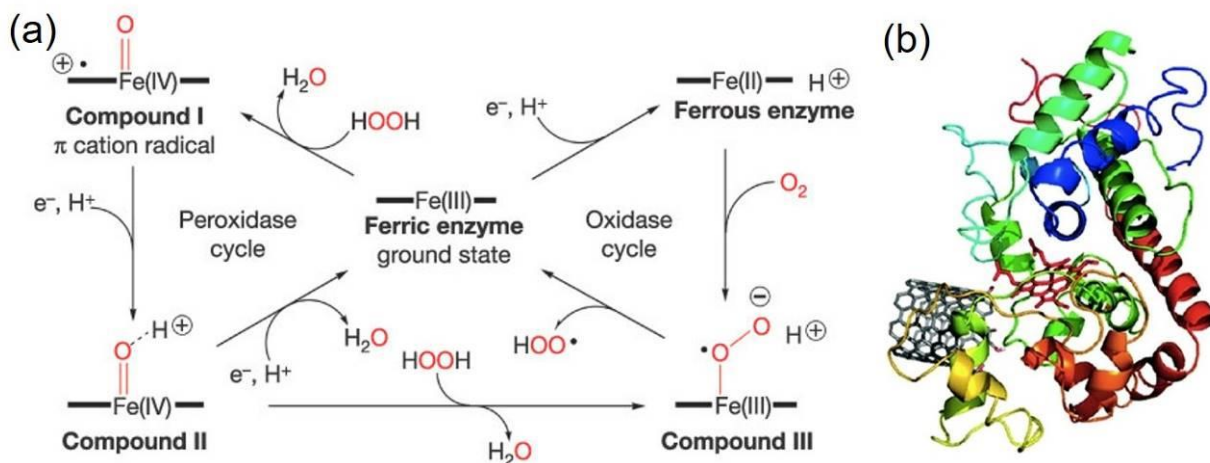


Figure 23. (a) Oxidation states of horseradish peroxidase. (Reproduced with permission from Ref 151. Copyright 2002 Nature Publishing Group) (b) Structure of HRP and possible binding position with carboxylated SWCNTs (Reproduced with permission from Ref 156. © 2009 American Chemical Society)

HRP-catalyzed Biodegradation of Carbon Nanomaterial

Degradation of SWCNTs has been demonstrated by Star and co-workers.¹⁴⁵ Oxidized SWCNTs, synthesized via arc-discharge method, were incubated at 4 °C in the presence of H₂O₂ and HRP. Deformation of SWCNTs was observed over 12 weeks. Pristine SWCNTs were examined in the following mechanistic investigation and showed no degradation over the same period.¹⁵⁶ These findings demonstrated that oxygen-containing functional groups are essential for degradation of SWCNTs via HRP-catalyzed biodegradation. It has been proposed that the attractive electrostatic interactions between the negatively-charged oxygen functional groups on the surface of a SWCNT and the positively-charged arginine residues of HRP may decrease the distance between the SWCNT and the reactive heme site of HRP, thereby permitting oxygen-functionalized SWCNTs (Figure 23b) but not pristine SWCNTs (which do not possess these negatively charged functional groups) to undergo further oxidation.¹⁵⁶

Biodegradation of nanomaterials has been extended to oxidized SWCNTs of smaller diameters¹⁵⁷, oxidized MWCNTs^{157,158}, nitrogen-doped nanocups¹⁵⁸, and graphene oxides¹⁵⁹. For MWCNTs, a layer-by-layer mechanism was revealed by TEM and Raman spectroscopy.¹⁵⁸ The biooxidation of HRP degraded the defective outer wall of the oxidized MWCNTs, exposing the pristine inner walls to HRP oxidation. MWCNTs with reduced diameters and their Raman signal were still be observed over 80 days of incubation, suggesting that the pristine inner walls are more resistant to HRP oxidation.¹⁵⁸ In the case of graphene oxides, the biooxidation of graphene oxide resulted in the formation of holes on its basal plane.¹⁵⁹ Similar inefficiency in the degradation of pristine sp² surfaces was reported through the study of reduced graphene oxide.¹⁵⁹

Table 3. Biodegradation of Carbon Nanomaterials by Horseradish Peroxidase-Catalyzed Oxidation

Material	Functionalization	Degradation	Ref
SWCNTs	Oxidized	Yes	145,156,157
SWCNTs	Pristine	No	156
MWCNTs	Oxidized	Yes	157,158,160
MWCNTs	N-doped (stacked-cup)	Yes	158
MWCNTs	Coumarin-functionalized	Yes	160
MWCNTs	Catechol-functionalized	Yes	160
RGO	Pristine	No	159
GO	Carboxylated	Yes (hole formation)	159

SWCNTs: single-walled carbon nanotubes; MWCNTs: multi-walled carbon nanotubes; RGO: reduced graphene oxide; GO: graphene oxide

1.4.2.2 Myeloperoxidase (MPO)

Introduction to the Enzyme

Myeloperoxidase (MPO) is a heme-containing enzyme stored in immense amounts in neutrophils and macrophages.¹⁶¹ The enzyme is a 146 kDa dimer with a single disulfide bridge (Cys153) between symmetry-related halves (73 kDa), each of which contains two polypeptides of 14.5 and 58.5 kDa.¹⁶² The small polypeptide is composed of 106 and the large of 467 amino acids. Each half of the enzyme have a covalently-linked heme, which contains one iron ion.¹⁶² MPO can undergo both peroxidase and halogenation cycles, both start by reaction of the ground state peroxidase with hydrogen peroxide to form Compound I. In the peroxidase cycle, as described above, the Compound I is reduced by two successive one-electron steps via Compound II, oxidizing two substrates into their corresponding radicals. In the presence halide, MPO can undergo halogenation cycles similar to eosinophil peroxidase (EPO) and lactoperoxidase (LPO). In the halogenation cycle, Compound I is reduced back to the ferric resting state by directly oxidizing halides to hypohalous acids through a two-electron process (Figure 24a). The ease of oxidation of halide ions is in order of $I^- > Br^- > Cl^-$, and all heme peroxidases can oxidize iodide.¹⁶² However, only MPO Compound I can oxidize chloride to hypochlorous acid (HOCl) at pH 7.0 at reasonable rates, EPO and LPO mainly use bromide and iodide ions as their substrate.¹⁶² Using chloride ion, the net equation can be written as:



HOCl has a pKa of 7.5 at 30°C, so it exists as a mixture of HOCl and OCl form at neutral pH.¹⁶³ The formation of hypohalous acid is important in the immune system to carry out their antimicrobial activity.¹⁶¹

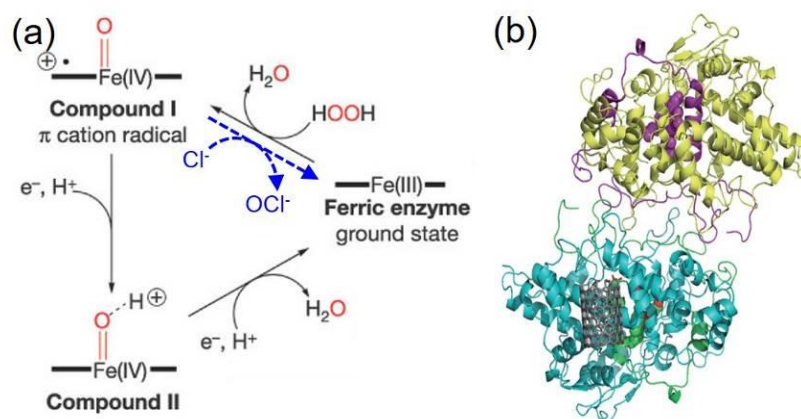


Figure 24. (a) Peroxidase cycle of MPO (solid black line) and the formation of OCl⁻ from Cl⁻ by MPO-Compound I (dashed blue line). (Reproduced with permission from Ref 151. © Copyright 2002 Nature Publishing Group) (b) Structure of MPO and possible binding position with carboxylated SWCNTs. (Reproduced with permission from Ref 143. © 2010 Nature Publishing Group)

MPO-catalyzed Biodegradation of Carbon Nanomaterial

Kagan and co-workers first demonstrated the degradation of SWCNTs by human myeloperoxidase.¹⁴³ Carboxylated SWCNTs were incubated with MPO and in the presence of both H₂O₂ and Cl⁻ for 24 h. The degradation of SWCNTs was evidenced by the reduction in sizes by dynamic light scattering, and the disappearance of Raman and UV-vis-NIR absorption signals (Figure 25). In the absence of Cl⁻, MPO can still degrade carboxylated SWCNTs via peroxidase cycle, although the degradation rate was markedly slower than the rate by halogenation cycle, or by direct addition of sodium hypochlorite.¹⁴³ Pristine nanotubes did not degrade, but showed signs of oxidation and was attributed to HOCl oxidation. It was suggested that HOCl would trigger and initially accumulate carboxylated sites on the sidewall of CNTs, which MPO can bind onto and further degrade the CNTs via both halogenation and peroxidase cycles.¹⁴³ Binding energy between MPO and CNTs have been calculated by computational modeling. The simulation pointed to a strong interaction between the positively charged residues

on MPO and the carboxyl groups on the nanotubes (Figure 24b).¹⁴³ The importance of hypochlorite was emphasized by Vlasova et al.¹⁴⁷ In their study, MPO-generated hypochlorite was more effective in degrading carboxylated SWCNTs than exogenous hypochlorite or through MPO peroxidase cycle.¹⁴⁷ Their experiments also revealed that CNTs bind to proteins in blood plasma, preventing direct interaction between MPO and CNTs. They suggested that only hypochlorite from MPO can cause the biodegradation of carbon nanotubes in blood.¹⁴⁷ Kotchey et al. studied the effect of antioxidants on MPO-catalyzed biodegradation of SWCNTs, and showed that the presence of antioxidants, L-ascorbic acid, and L-glutathione, can suppress the enzymatic oxidation.¹⁶⁴ Two protection mechanisms were proposed. First hypochlorite production can be limited through the reduction of MPO-Compound I by L-ascorbic acid or reduction of H₂O₂ by L-glutathione. Second, both L-ascorbic acid and L-glutathione can be oxidized by HOCl at very rapid rates, which outcompete the CNTs.¹⁶⁴

MPO-catalyzed biodegradation has been demonstrated on polymer-coated and drug-loaded SWCNTs.^{70,165} Bhattacharya et al. compared the molecular weight (MW) of PEG chains and its effect on MPO biodegradation of CNTs.⁷⁰ SWCNTs were covalently functionalized with PEG chains of 2, 5 and 10 kDa. Their results show that the efficiency of MPO-driven degradation of SWCNTs decreased with PEG chain MW.⁷⁰ Carboxylated SWCNTs were coated with PEGylated phospholipids and loaded with a chemotherapeutic drug, doxorubicin (DOX), before subjected to MPO biooxidation.¹⁶⁵ The CNT-drug conjugates were shown to be degradable and provided protection to the loaded cargo. DOX in the CNT-drug conjugates was degraded slower than free DOX under the same oxidative conditions.¹⁶⁵

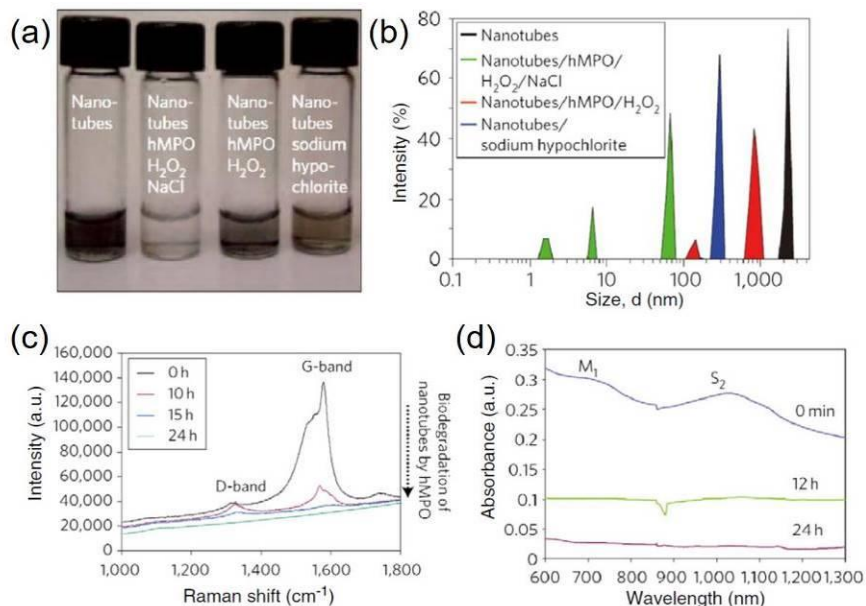


Figure 25. (a) Photographs of carboxylated SWCNTs incubated with or without degradative reagents after 24 h. (b) Dynamic light scattering data of different samples showing decreasing sizes of degraded nanotubes. (c) Raman spectra of SWCNTs before and after 24 h of MPO degradation. (d) Visible-near infrared (Vis-NIR) absorption spectra of SWCNTs being degraded during 24 h. (Reproduced with permission from Ref 143. © 2010 Nature Publishing Group)

Other carbon nanomaterials are also subjected to the MPO-catalyzed biodegradation including graphene oxide¹⁶⁶, carbon nanotube cups¹⁶⁷, and carbon nanohorns¹⁶⁸. For gold-corked carbon nanotube cups, MPO biooxidation can “open” the closed vesicles for a potential release of their cargos. The separated nanocups were gradually degraded within 20 days, providing a pathway for the clearance of this potential drug delivery vehicles.¹⁶⁷

Table 4. Biodegradation of Carbon Nanomaterials by Myeloperoxidase-Catalyzed Oxidation

Material	Functionalization	Degradation	Ref
SWCNTs	Carboxylated	Yes	143,147,164
SWCNTs	Pristine	No (oxidized)	143
SWCNTs	Carboxylated (coated with PL-PEG)	Yes	165
SWCNTs	Carboxylated (coated with PL-PEG and DOX)	Yes	165
SWCNTs	Pristine (non-covalent PL-PEG (2kDa))	No	70
SWCNTs	Carboxylated (covalent 2 / 5 / 10 kDa PEG)	Yes	70
GO	Carboxylated (dispersed)	Yes	166
GO	Carboxylated (aggregated)	No	166
Nanocups	Oxygen- and nitrogen-containing groups	Yes	167
Nanohorns	Carboxylated and carbonylated	Yes (~60%)	168

SWCNTs: single-walled carbon nanotubes; GO: graphene oxide

PL-PEG: PEGylated phospholipids; DOX: doxorubicin

Cells (Neutrophils) and Animal Studies

Myeloperoxidase-rich neutrophils can also degrade carbon nanotubes. In the early study by Kagan et al., neutrophils were subjected to carboxylated SWCNTs and activated by N-formylmethionyl-leucyl-phenylalanine (fMLP) and cytochalasin B to trigger the release of MPO.¹⁴³ SWCNTs were coated with immunoglobulin G (IgG) to increase cellular uptake. Raman microscopy confirmed that IgG-SWCNTs were completely degraded by the neutrophils after 12 hours of incubation, whereas only 30% of the non-IgG-coated nanotubes were degraded.¹⁴³ Recently, Vlasova et al. demonstrated that PEGylated SWCNTs could activate isolated human neutrophils to produce HOCl. Furthermore, in whole blood sample, both carboxylated and PEGylated SWCNTs were shown to activate neutrophils.¹⁶⁹ Similar result was

reported by Lu and co-workers.¹⁷⁰ SWCNTs bound to human serum albumin (HSA) showed enhanced cellular uptake and stimulated MPO release and HOCl generation in neutrophils.¹⁷⁰

Bhattacharya et al. have reported that the degradation of PEGylated SWCNTs in neutrophil was independent of the molecular weight of the PEG chain.⁷⁰ Instead, the covalently attached PEG chains were defunctionalized from the CNTs.⁷⁰ Similar detachment of PEG chains was reported in the liver of the intravenously injected mice by Yang et al.¹⁷¹

Biooxidation and clearance of SWNTs from lungs of mice have been demonstrated by Shvedova et al.¹⁴⁴ Upon pulmonary exposure to SWCNTs, wild-type mice showed more severe inflammatory response than myeloperoxidase knockout (MPO k/o) mice. Oxidation and clearance of SWCNTs were also more effective in wild-type mice than their MPO knockout counterparts.¹⁴⁴ Intraperitoneal injection of PEG-SWCNTs into mice also showed an inflammatory response.¹⁶⁹ An increase concentration neutrophils and their activation was detected in the peritoneal cavity.¹⁶⁹

2.0 CHIRALITY STUDIES ON ENZYMATIC BIOOXIDATION

2.1 CHAPTER PREFACE

Section 1.4.2 discussed recent developments in enzymatic degradation of carbon nanotubes. While most of the research focused on the role of functional groups in the oxidation process, the differences in tube diameters and chiralities have not been systematically studied. In this chapter, we present two original research that address the difference reactivity of nanotube chiralities in biooxidations. Chapter 2.2 will focus on oxidized SWCNTs in HRP oxidation, and Chapter 2.3 on pristine-coated SWCNTs in MPO-catalyzed reaction.

2.2 ENZYME-CATALYZED OXIDATION FACILITATES THE RETURN OF FLUORESCENCE FOR SINGLE-WALLED CARBON NANOTUBES

2.2.1 Preface

In this section, we extended our knowledge on enzymatic degradation by HRP and MPO to oxidized HiPco SWCNTs and focused on the effect of CNT chiralities. While oxidation via strong acids introduced defect sites on SWCNTs and suppressed their near-infrared (NIR) fluorescence, our results indicated that the fluorescence of certain types of SWCNTs was restored upon enzymatic oxidation, providing new evidence that the reaction catalyzed by horseradish peroxidase (HRP) in the presence of H_2O_2 is mainly a defect-consuming step. In contrast, upon treatment with myeloperoxidase (MPO), H_2O_2 , and NaCl, the oxidized HiPco SWCNTs underwent complete oxidation (i.e., degradation). The shortened, NIR-fluorescent SWCNTs resulting from HRP-catalyzed oxidation of acid-cut HiPco SWCNTs may find applications in cellular NIR imaging and drug delivery systems.

The material contained within Chapter 2.2 was published as an original research paper in the journal, *Journal of the American Chemical Society*, and the figures have been reproduced with permission from Ref ¹⁷². This article was selected as cover art for the September 11, 2013 issue of the *Journal of the American Chemical Society*.

List of Authors: C. F. Chiu, B. A. Barth, G. P. Kotchey, Y. Zhao, K. A. Gogick, W. A. Saidi, S. Petoud, and A. Star.

2.2.2 Introduction

Because of the unique properties of carbon nanotubes (CNTs), such as their small size, large surface area, high strength, the ability to transport electrons, and inert chemical nature, this carbon based nanomaterial has been incorporated in a wide array of applications, including building composites, electronics, and medical therapeutics.^{173–175} The full implementation of CNTs in consumer goods, however, may be hindered as a result of emerging evidence that this nanomaterial can induce cytotoxic effects such as inflammation, epithelioid granulomas, fibrosis, and oxidation stresses that stem from both the chemical / electronic properties and the fibrous, anisotropic geometry of CNTs.^{176,177} Moreover, CNTs that are engulfed by cells during endocytosis may rupture the cell membrane as a result of their length; therefore, there is a direct correlation between cytotoxic response and CNT length.¹⁷⁷ A recent study by Ali-Boucetta et al. has also demonstrated that the toxicity of CNTs is dependent on both their lengths and surface functionalities imparted to this nanomaterial.¹⁷⁸ For this reason and as a result of better circulation,^{179,180} shortened CNTs, which are generally fabricated through chemical oxidation, have been employed for in vitro and in vivo drug delivery applications.^{32,181} The primary shortcomings of employing harsh chemical oxidation methods to shorten (i.e., “cut”) the length of semiconducting single-walled carbon nanotubes (s-SWCNTs) entails damaging the sp^2 lattice and creating oxygen functionalities, both of which result in the loss of the nanotubes’ intrinsic near-infrared (NIR) fluorescence.^{182,183}

Recently, we and others have demonstrated that peroxidases such as the plant-derived enzyme horseradish peroxidase (HRP)^{145,156–159,184} and myeloperoxidase (MPO),^{143,144,147,184} an enzyme expressed by inflammatory cells in humans, can oxidatively degrade CNTs and graphene oxide. The presence of oxygen functionalities on the carbon nanomaterials may

influence the ability of HRP to oxidize the substrate. It has been proposed that the attractive electrostatic interactions between negatively charged carboxyl groups on SWCNTs and positively-charged arginine residues of HRP may decrease the distance between the two.¹⁵⁶ MPO is known to react with H₂O₂ and Cl⁻ to yield hypochlorite (OCl⁻), which is the major oxidant responsible for the degradation of nanomaterials.^{143,147}

In this work, we extended our study of enzymatic oxidation to SWCNTs synthesized by the high-pressure carbon monoxide (HiPco) method because the small diameter of these nanotubes enables one to probe the material's electronic properties and chirality distribution using photoluminescence (PL) mapping.⁵ While oxidation via strong acids introduces defect sites on SWCNTs and suppresses their NIR fluorescence, our results indicated that the NIR fluorescence of certain types of SWCNTs is restored upon enzymatic oxidation, providing new evidence that the oxidation reaction catalyzed by HRP in the presence of H₂O₂ occurs at the defect sites. When acid oxidation followed by HRP-catalyzed enzyme oxidation was employed, shortened (<300 nm in length) and NIR-fluorescent SWCNTs were produced. The resulting products could find applications in NIR imaging and drug delivery systems.

2.2.3 Results

Figure 26 presents PL maps of SWCNTs at various stages of oxidation. The typical characteristic band-gap luminescence was assigned to SWCNT chirality according to the literature.⁵ The emissions were disrupted upon acid oxidation (Figure 26a,b);^{181,182} upon HRP/H₂O₂ treatment, however, the fluorescence returned to the SWCNTs with certain chiralities (i.e., (9,4), (10,2), and (7,6); Figure 26c). This spectral change was not observed for the MPO/H₂O₂/NaCl system (Figure 26d).

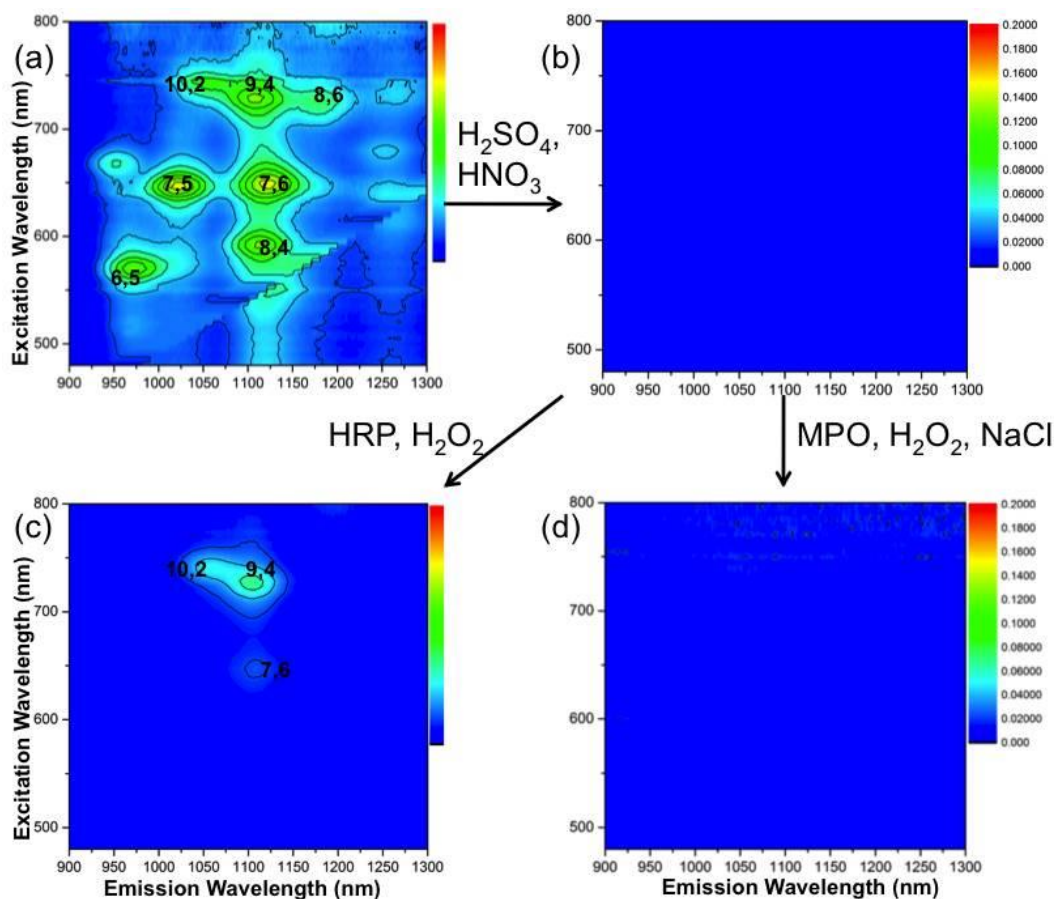


Figure 26. Photoluminescence (PL) maps of SWCNTs (a) before and (b) after acid oxidation, and of the acid-oxidized SWCNT sample from (b) after treatment with (c) HRP/H₂O₂ or (d) MPO/H₂O₂/NaCl. Before PL mapping, sodium cholate (1 wt %) was added, and the samples were sonicated for 2 h. Literature values were employed to assign the SWCNT chirality.⁵

For pristine SWCNTs, four major peaks were determined in the radial breathing mode (RBM) section of the Raman spectra (i.e., at 196, 217, 258, and 283 cm⁻¹). Upon acid oxidation, the 283 cm⁻¹ peak was fully suppressed (Figure 27a, left). A similar result was also reported by Yang et al., who attributed the loss of signal to the destruction of smaller-diameter SWCNTs during the acid oxidation.⁵³ The D-band/G-band (D/G) ratio decreased from 0.51 for acid-oxidized SWCNTs to 0.24 for acid-oxidized SWCNTs treated with HRP/H₂O₂ (Figure 27a, right). Likewise, a decrease in the D/G ratio was observed for the MPO/H₂O₂/NaCl-treated

SWCNTs (Figure 27b, right); this decrease to 0.27, however, was likely the result of nanotube degradation. Further evidence of degradation was provided by the decrease in the RBM and G-band signals, which possibly stemmed not only from the loss of resonance as the sp^2 surface was damaged but also from a high fluorescence background arising from organic fragments.^{159,185}

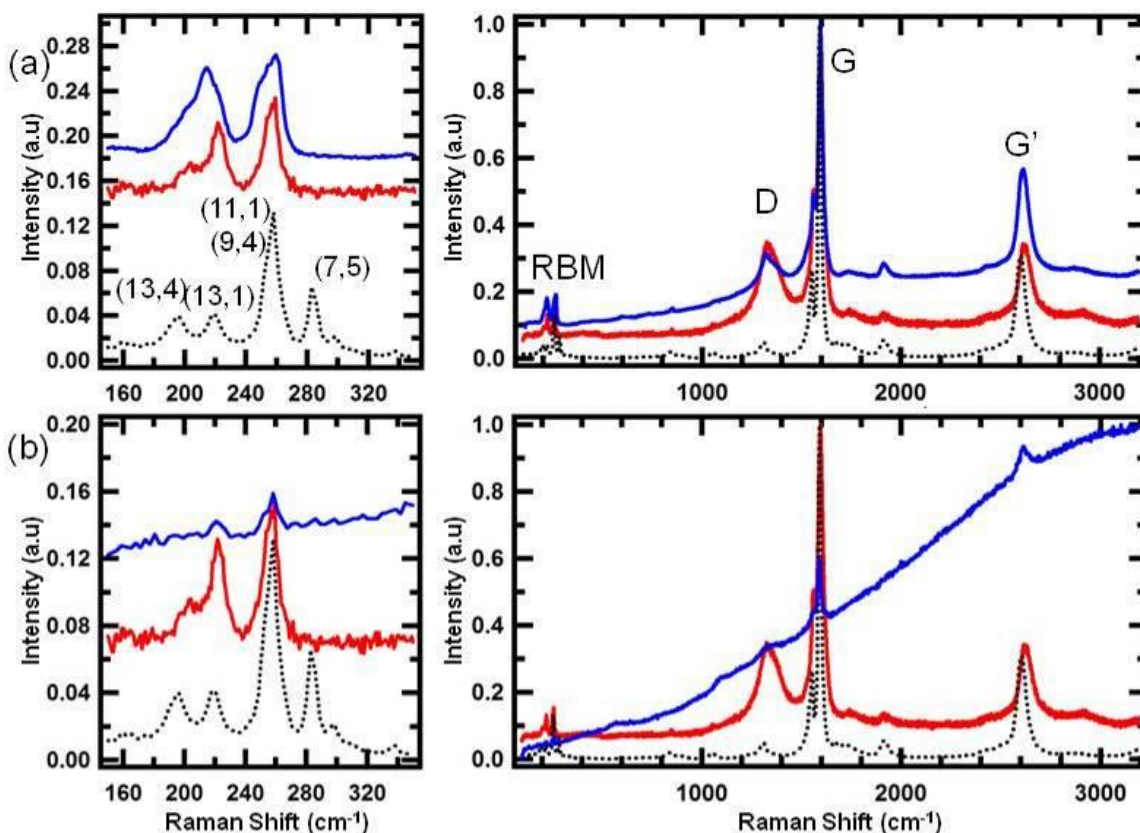


Figure 27. Enlarged radial breathing mode (RBM) sections and the full Raman spectra of SWCNTs treated with (a) HRP/ H_2O_2 and (b) MPO/ H_2O_2 /NaCl at various experimental stages [before oxidation (black, dotted), after acid oxidation (red), and after enzymatic reaction (blue)]. The SWCNT chirality was assigned according to the literature.¹² The RBM sections have been offset for clarity.

UV-vis-NIR absorption spectra of the samples before oxidation, after acid oxidation, and after enzymatic treatment are presented in Figure 28. The S_{11} (900–1200 nm) and S_{22} (600–900 nm) optical transitions for the semiconducting nanotubes, which were clearly present before oxidation, disappeared after acid oxidation and then reappeared after HRP/ H_2O_2 treatment

(Figure 28a), which is all in agreement with the PL results. On the other hand, upon MPO/H₂O₂/NaCl treatment, the overall absorbance of the SWCNTs decreased by ~50% (Figure 28b); such a loss in absorbance can be attributed to the loss of carbon content.¹⁴³

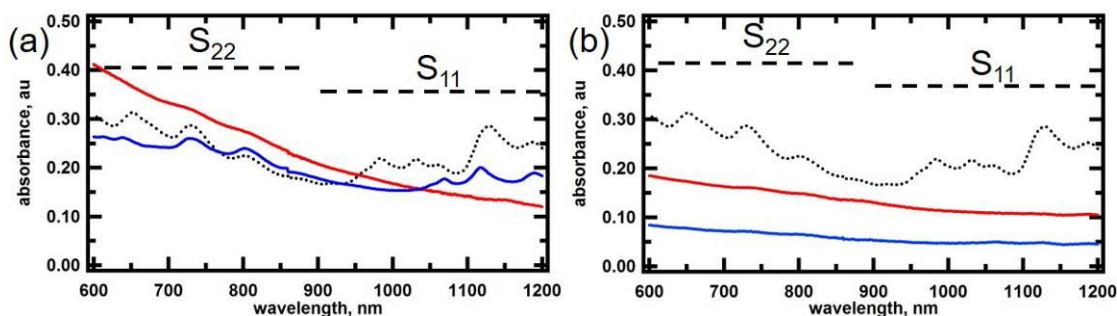


Figure 28. UV-vis-NIR absorption spectra of SWCNTs treated with (a) HRP/H₂O₂ and (b) MPO/H₂O₂/NaCl at various experimental stages [before oxidation (black, dotted), after oxidation (red), and after enzymatic reaction (blue)].

The spectroscopy results were further supported by transmission electron microscopy (TEM) images of the SWCNT samples. Figure 29 indicates that the SWCNT bundles were shortened by 35% during the acid treatment (Figure 29b). High-resolution TEM (HRTEM) imaging of the acid-oxidized SWCNTs (Figure 29c) revealed both significant bundling of SWCNTs and a rough/defective sidewall structure. The TEM image of the acid-oxidized SWCNTs treated with MPO/H₂O₂/NaCl (Figure 29d) revealed only carbonaceous fragments, which are the typical products of the degradation process.^{143,145,158,159,164} As tubular objects were not present in the image, a histogram for this sample was not recorded. In contrast, after HRP/H₂O₂ treatment (Figure 29e), a 30% reduction in bundle length was observed. The average length of the HRP/H₂O₂-treated SWCNT bundles was 215 ± 125 nm. In the HRTEM image (Figure 29f), this sample appeared to be less bundled and demonstrated a more defined CNT sidewall structure.

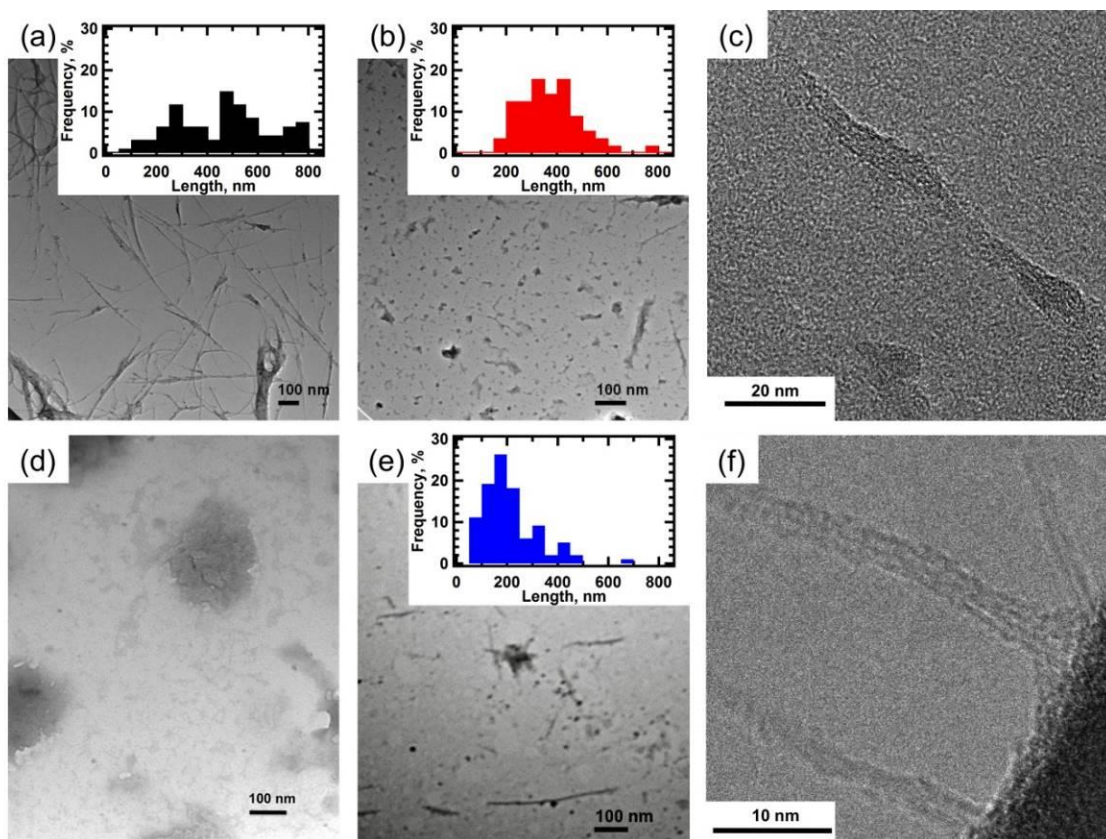


Figure 29. Transmission electron microscopy (TEM) micrographs of SWCNT bundles (a) before and (b) after acid oxidation. (c) High-Resolution TEM (HRTEM) of the acid-treated SWCNTs bundles. TEM micrographs of the acid-treated SWCNT bundles (d) after treatment with MPO/H₂O₂/NaCl and (e) after treatment with HRP/H₂O₂. (f) HRTEM micrograph of the HRP/H₂O₂ treated sample. Insets depict histograms of the length distributions for the SWCNT bundles at various experimental stages.

2.2.4 Discussion

The enzyme-catalyzed oxidation of acid-treated SWCNTs revealed some interesting chiral selectivity, as demonstrated in Figure 26c. To identify the chiralities of these nanotubes, PL results were cross-examined with the Raman RBM data. From our PL maps (Figure 26c), the (10,2), (7,6), and (9,4) nanotubes were identified, but the Raman spectra demonstrated an absence of the (10,2) species (Figure 27). We hypothesize that these seemingly contradictory

results stemmed from the fact that the S₂₂ absorbance bands of (10,2) s-SWCNTs, which have corresponding wavelengths of 733 nm, were out of resonance with the excitation laser (i.e., 633 nm), thereby resulting in the absence of their Raman signal.¹² From the Raman RBM spectrum of the pristine SWCNTs, four major peaks were located at ~196, 217, 258, and 283 cm⁻¹ (Figure 27, black dotted trace). Further fitting of the RBM data utilizing Lorentzian functions revealed that the four peaks corresponded mainly to (13,4), (13,1), (11,1), and (7,5) SWCNTs, respectively, of which the former two are metallic and lack PL properties, whereas the latter two are semiconducting.⁷ It is also interesting to note that the RBMs for the metallic SWCNTs were upshifted by ~10 cm⁻¹ upon acid oxidation; such an upshift, however, was not observed for the semiconducting SWCNTs at 258 cm⁻¹. While the possible causes of this upshift are still debatable, with reasons ranging from bundling-induced redshifts of transition energies^{186,187}, to charge transfer from SWCNTs to -COOH groups,¹⁸⁸ the fact that metallic SWCNTs shifted more than their semiconducting counterparts agrees with previous report that metallic tubes are more reactive than semiconducting SWCNTs in the 0.9–1.1 nm diameter range.⁵³ The observed upshift was reversed upon HRP/H₂O₂ treatment, which is similar to what has been reported for oxidized SWCNTs upon annealing.¹⁸⁹

Meanwhile, the Raman signal for the (7,5) SWCNTs was absent after the acid treatment, and their fluorescence did not return after incubation with HRP/H₂O₂ (Figure 26c), suggesting that the (7,5) nanotubes were destroyed during the acid treatment process.⁵³

The observed decreases in the Raman D/G ratio appeared similar to the data obtained for enzyme-catalyzed oxidation of multi-walled CNTs.¹⁵⁸ While a decline in the D/G ratio can be interpreted as a reduction in defect density, as demonstrated by Strano and co-workers,⁵⁴ this change could also result from decreases in both the D and G bands at high degrees of

functionalization due to the loss of resonance enhancement. Therefore, a reduction in the D/G ratio alone is not a conclusive way to show a decrease in defect density.⁸⁶ As a result, UV–vis–NIR and PL spectroscopy were also utilized to provide insight into the defect density of oxidized SWCNTs. Such a degradation-induced decrease in the D/G ratio was exhibited by the oxidized SWCNTs upon MPO/H₂O₂/NaCl treatment and will be discussed later.

Functionalized SWCNTs are known to exhibit a flattened UV–vis–NIR absorbance spectrum⁹¹ and no NIR fluorescence emission⁷ as the introduced defect sites disrupt the electronic structure of the nanotubes. Such behavior was demonstrated by the acid-treated SWCNTs (Figures 26b and 28). The opposite trend, however, was observed upon enzymatic oxidation via HRP/H₂O₂, where the NIR fluorescence and UV–vis–NIR signal were restored (Figure 26c and 28a); these results are similar to those reported for Ar annealing.⁵⁰ Our PL map for the acid-treated SWCNT sample after the HRP/H₂O₂ reaction revealed the presence of (10,2), (7,6), and (9,4) nanotubes; their corresponding absorption bands were also present in the UV–vis–NIR absorption spectrum (Figure 28a, blue trace). Combining our Raman and optical results, we concluded that the HRP/H₂O₂ reaction specifically attacked defect sites and restored the sp² lattice.

In Figure 26c, the emission wavelength (λ_{em}) for oxidized (7,6) SWCNTs that were treated with HRP/H₂O₂ was blue-shifted by ~14 nm (i.e., from ~1122 to ~1108 nm). In contrast, when a duplicate experiment was performed, acid oxidized SWCNTs that were treated with HRP/H₂O₂ did not demonstrate any blue shift (Figure 45 in Appendix A). We attribute these apparently contradictory results to differences in the local environments.¹⁰⁴ For both sets of data, the same restoration of emission was observed for (9,4), (8,6), and (7,6) chiralities with the removal of (6,5), (7,5), and (8,4) species (Figure 45), which is consistent with previous studies

showing that acid treatment removes SWCNTs with diameters smaller than 0.88 nm [i.e., (8,6) SWCNTs have a diameter of 0.966 nm].^{12,53} Finally, the peak due to (8,6) SWCNTs was more intense in the duplicate experiment.

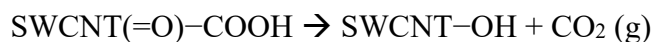
We attributed these results to the removal of defect sites (most likely oxygen-containing functional groups) from the surfaces of SWCNTs. The data presented herein indicate that HRP/H₂O₂ oxidized the functionalized SWCNTs through reactive intermediates of the peroxidase cycle, thereby removing oxygen groups and restoring the sp² lattice, possibly through decarboxylation.^{145,158,159,190} As suggested by Kane and colleagues, the removal of a carboxyl group involves breaking only the one intact bond connecting it to the CNT backbone, whereas removal of hydroxyl, epoxide, and peroxides groups requires breaking three backbone bonds.¹⁹¹ Therefore, decarboxylation would be more energetically favorable than oxidation and eventual removal of other oxygen-containing functional groups.¹⁹¹ This work, however, does not suggest any further oxidation of the graphitic lattice of the nanotube after the enzymatic reaction. Instead, our Raman D/G ratio, UV-vis-NIR absorbance, and PL map data all indicate a reduction in the number of defect sites and a restoration of the sp² lattice.

Defunctionalization of CNTs with hydrogen peroxide has been reported in the literature.^{192,193} Hou et al. showed that hydroxyl radical (\bullet OH) from H₂O₂ could photoreact with carboxylated SWCNTs to form CO₂. The SWCNTs products aggregated and precipitated, and was attributed to the removal of amorphous carbon and functional groups on SWCNTs, resulting in the reduction of carboxyl groups and hence aqueous dispersibility.¹⁹² In this work, the dispersibility issue is addressed by re-sonication with surfactants. Results from PL and absorption spectroscopy unambiguously focus on surface functionalization of SWCNTs. Our result also indicates defunctionalization of nanotubes. Decarboxylation of MWCNTs had been

demonstrated by Qu et al. in the presence of H₂O₂ under UV light irradiation.¹⁹³ In our control, SWCNTs were incubated with H₂O₂ in the absence of HRP, and defunctionalization was not observed (Figure 45h).

To exclude the possibility that the return of the PL emission resulted from the reduction of oxygen functional groups via the oxidase cycle of HRP,¹⁵¹ a control experiment was performed wherein oxidized SWCNTs were incubated in the absence of H₂O₂ for 35 days. Under our experimental conditions, no PL emission characteristic of SWCNTs was observed (Figure 46 in Appendix A), thereby indicating that oxidation via the peroxidase cycle rather than reduction via the oxidase cycle is the likely mechanism for the return of fluorescence.

Density functional theory (DFT) calculations were performed to estimate the overall energy change for decarboxylation of a SWCNT containing both a carboxyl group and an adjacent ketone group (Figure 30). To estimate the overall energy for decarboxylation of a (14,0) SWCNT functionalized with both a carboxyl group and a ketone group, the nudged elastic band (NEB) method was used to determine the minimum energy path for the following reaction:



The reactant has a -COOH group and the oxygen of the ketone group adsorbed on a neighboring site of a sidewall ring, as shown schematically in the upper left inset in Figure 30b. The functionalization locally disrupts the π -orbital network of the tube. The products correspond to the complete decarboxylation of the oxidized SWCNT, resulting in the formation of a hydroxyl group on the nanotube and carbon dioxide in the gas phase.¹⁴⁵ As can be seen in Figure 30b, the decarboxylation process proceeds with a small energy barrier of 0.15 eV. In the transition state (upper right inset in Figure 30b), the hydrogen of the -COOH group rotates from the optimum position towards the oxygen of the ketone group. It is also noteworthy that the decarboxylation

process is exothermic and thermodynamically very favorable, with an energy release of ~ 2.9 eV per desorbed CO_2 molecule in the gas phase.

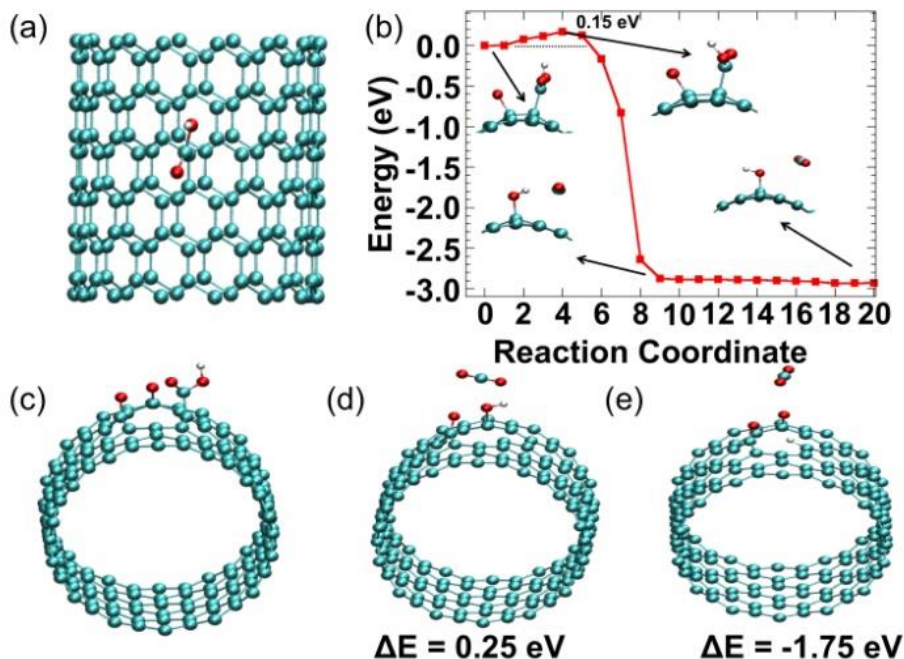


Figure 30. (a) Top view of the COOH functionalized (14,0) SWCNT. (b) Reaction energy profile for decarboxylation of a (14,0) pristine SWCNT functionalized with a carboxyl and a ketone group. Side views of selected parts of the SWCNT are also shown for the initial, transition and final configurations during the decarboxylation process. The potential energy surface near the final state is very flat due to small energy barrier for the rotation of $-\text{OH}$ group around the $\text{O}-\text{C}$ bond, as can be seen by inspecting the inset images. Panel (c) and (e) show initial and final configurations for the decarboxylation process of a defective (14,0) CNT functionalized with $-\text{COOH}$ and two ketone groups. This process is exothermic with 1.75 eV per CO_2 molecule. Panel (d) shows the structure of a possible intermediate transition state where the hydrogen of $-\text{COOH}$ group is transferred to the ketone group forming an $-\text{OH}$ group with the release of CO_2 in the gas phase. Carbon atoms are turquoise, oxygen is red, and hydrogen is white.

Although the employed SWCNT model is idealized, as it ignores the presence of defects, it nevertheless reveals that the decarboxylation is thermodynamically very favorable under the experimental conditions. To show that this is also the case even in the presence of CNT defects,

we examined the energetics of possible initial and final structures in the decarboxylation process. This is shown in Figure 30c,e for a (14,0) SWCNT with a carbon vacancy that is functionalized with a -COOH group and two ketone groups. As in the case of the pristine SWCNT, the decarboxylation process for the CNT with the defect is also exothermic by ~ 1.75 eV per desorbed CO_2 molecule in the gas phase. The configuration shown in Figure 30d is a potential transition state for this process that is only 0.25 eV higher in energy than the initial structure. In the presence of a solvent, as is the case in the experiments, this transition state would be expected to have a lower energy because a proton could be transferred from solution to passivate the dangling bond of the CNT that is left by the desorbed CO_2 molecule.

The decarboxylation process was also evidenced in a control experiment wherein pristine HiPco SWCNTs were subjected to HRP/ H_2O_2 oxidation. They demonstrated an improved UV-vis-NIR and NIR fluorescence signal as well as a decrease in the Raman D/G ratio (Figure 47 in Appendix A). Recent research has suggested that defect sites are present in pristine HiPco SWCNTs, constraining the fluorescence to $\sim 40\%$ of its maximum brightness.¹⁰⁵ Therefore, HRP/ H_2O_2 oxidation may remove defect sites on pristine SWCNTs just as this enzymatic system removes defect sites on the oxidized samples.

The MPO/ H_2O_2 / NaCl reaction is known to produce hypochlorite (OCl^-), which is the strongest oxidant of the MPO system.^{143,147} OCl^- oxidizes the sidewalls of SWCNTs, which in turn damages the sp^2 network and results in loss of the resonance condition for the Raman and fluorescence responses. In comparison with the HRP/ H_2O_2 reaction, the MPO/ H_2O_2 / NaCl system demonstrated no return of fluorescence, suggesting a different oxidation mechanism that does not involve the restoration of the sp^2 surfaces. Therefore, the acid-treated SWCNTs were likely degraded by the MPO/ H_2O_2 / NaCl system, as evidenced by the fragment-induced fluorescence in

the Raman spectrum (Figure 27b),^{159,185} the loss of overall UV–vis–NIR absorption (Figure 28b),^{143,147} and the fragmented byproducts visualized by TEM (Figure 29d).

Pristine SWCNTs were also subjected to the MPO/H₂O₂/NaCl system. After the five day treatment, however, no degradation was observed for the pristine SWCNTs (Figure 48 in Appendix A); we believe this observation to be a consequence of the insufficient production of OCl⁻ with the current experimental setup. In a different control experiment (Figure 49 in Appendix A), pristine SWCNTs were incubated with 0.20 M NaOCl; the SWCNTs were destroyed within 1 day, thereby providing evidence that high concentrations of OCl⁻ can degrade even pristine SWCNTs.

In comparison with earlier work on HRP/H₂O₂ oxidation of larger diameter SWCNTs,^{145,156} the smaller-diameter HiPco SWCNTs degraded at a lower rate. The complete degradation of CNTs by the HRP/H₂O₂ system after ~30 days at room temperature has been reported.^{145,158,159} Since oxygen-containing defects were found to be essential for this enzymatic oxidation,^{145,158,159} one might expect the defect density to be higher for the larger diameter SWCNTs than the SWCNTs used in this work, where the lower defect density would be responsible for the lower reaction rate. To test this hypothesis, the defect density was determined by the acid titration method following a published procedure.^{158,194} The density of oxygen-containing defects for the SWCNTs used in this work was calculated to be 7.8 ± 0.5 $\mu\text{mol}/\text{mg}$, versus 3.4 ± 0.2 $\mu\text{mol}/\text{mg}$ for the larger diameter SWCNTs used before. This affirmed that the defect density was not the reason for the difference in the degradation rates as the smaller-diameter SWCNTs had both a higher defect density and a lower rate than their larger diameter counterparts. Although this defect density of 7.8 ± 0.5 $\mu\text{mol}/\text{mg}$ is an average value for SWCNTs of all chiralities in the sample and it is likely that some SWCNTs (e.g., metallic tubes) are more

defective than others, as reported in the literature,⁵³ the difference in our results cannot be solely explained by defect density.

Selectivity by the redox potential of SWCNTs has been suggested and utilized by O'Connell et al.¹⁹⁵ Similar reasoning was constructed by us to explain the oxidation by HRP, MPO, and HOCl.¹⁸⁴ Recently, the redox potentials of SWCNTs with different chiralities and diameters were modeled¹⁹⁶ and experimentally measured¹⁹ via electrochemistry coupled with spectroscopy. Figure 31 shows the electrochemical potentials of various bands of SWCNTs as functions of nanotube diameter (red and blue curves) along with the redox potentials of HRP, MPO, and HOCl (black dashed lines).^{184,195} The electrochemical potential of the s-SWCNT valence band (V1s) has been shown to increase as the nanotube diameter decreases (Figure 31). In this model, electron transfer takes place from the top of the valence band to the oxidizing species. The redox potential of HRP/H₂O₂ is ~0.95 V, which is higher than that of the V1s band of the larger diameter SWCNTs (pink-shaded region in Figure 31) but similar to that of the smaller diameter SWCNTs (green-shaded region). As a result of this difference in the redox potential, larger diameter SWCNTs are more favorably oxidized than smaller diameter SWCNTs, in agreement with the shortened degradation time that we observed for larger SWCNTs.^{156,158} For the MPO/H₂O₂/NaCl system, HOCl is produced; it has a redox potential of 1.48 V,¹⁸⁴ which represents a much higher oxidizing capacity than for HRP. At this potential, HOCl has a significant potential difference even with smaller-diameter SWCNTs and therefore oxidizes them, as evidenced by the degradation of the acid treated HiPco SWCNTs by the MPO/H₂O₂/NaCl system. Furthermore, the fact that smaller-diameter pristine SWCNTs, which cannot be degraded by HRP/H₂O₂ (Figure 47 in Appendix A), were degraded by hypochlorite ions (Figure 49 in Appendix A) also supports the electrochemical potential argument.

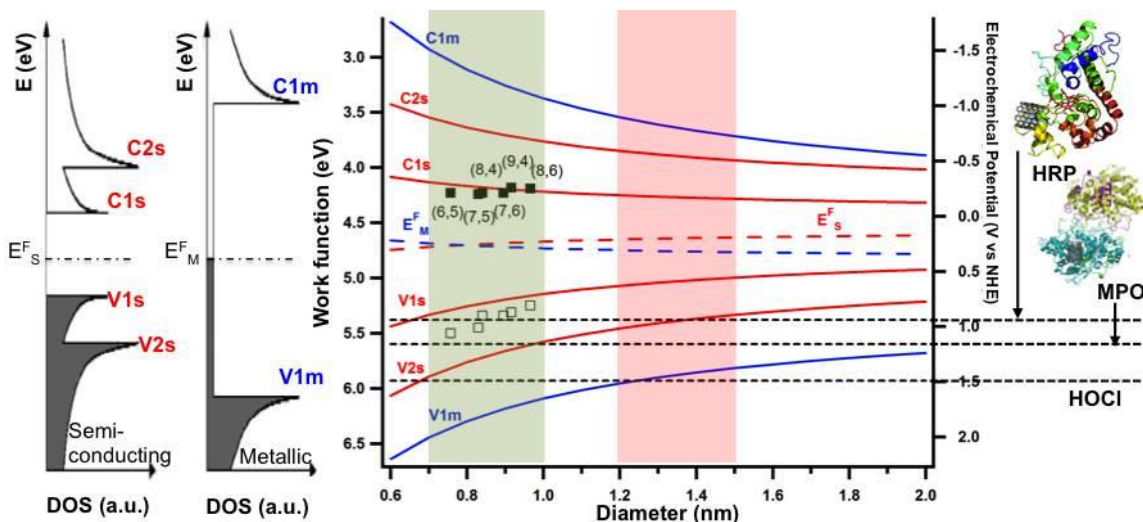


Figure 31. Electrochemical potentials of SWCNTs with different diameters plotted against the oxidation-reduction potentials of HRP, MPO and HOCl (black dashed line). The dependence of electrochemical potentials of SWCNTs on their diameter was modeled in Ref 196 with experimental data adapted from Ref 197 (squares). The green region indicates the diameter range of SWCNTs studied in this work (HiPco). The pink region indicates the larger diameter SWCNTs utilized in earlier work.^{145,156} HRP, MPO and HOCl potentials were adapted from Ref 184. Structures of HRP and MPO possible binding positions with carboxylated SWCNTs (right) were adapted from Ref 156 and Ref 143, respectively. The density of states diagrams (left) was adapted from Ref 19, indicating the valence and conduction band of the semiconducting and metallic SWCNTs.

While this model works well for pristine SWCNTs, they are often p-doped by acid treatment,¹⁸⁸ which further increases their redox potential and theoretically lowers their reactivity compared with the pristine SWCNTs by drawing their valence band closer to the redox potential of the reactive species. This may not be the case, however, as pristine SWCNTs were shown not to be degradable by enzymatic oxidation.^{156,158} Therefore, certain functionalities are required for the SWCNTs to undergo the peroxidase cycle. Carboxyl and hydroxyl (phenol) groups have labile hydrogen atoms that assist the peroxidase cycle, in which Compound I oxidizes a substrate by two sequential one-electron oxidation steps to form water. In pristine SWCNTs that have

neither functional groups nor labile hydrogen atoms, the biodegradation of pristine SWCNTs cannot be initiated.

On the basis of our results, HRP/H₂O₂ oxidation results in restoration of the fluorescence of SWCNTs, indicating a chemical pathway in which functional groups are eliminated in order to restore the sp² lattices of the nanotubes. Such a pathway was not observed for the MPO/H₂O₂/NaCl and NaOCl systems. From the degradation of pristine SWCNTs by NaOCl, it appears that the hypochlorite ions directly attack the sidewalls of the SWCNTs.

2.2.5 Conclusion

HRP/H₂O₂ can oxidize highly defective, carboxylated SWCNTs and restore their optical properties. To this end, SWCNTs that were oxidized by a strong acid mixture and demonstrated weak absorption bands with no photoluminescence were further oxidized using HRP/H₂O₂ to yield shorter, less defective CNTs with well-defined absorption bands and a strong PL signal. HRP may be capable of oxidizing only carboxylic acid groups, which would be removed from the CNT lattice as CO₂.^{145,158,159} It is possible that other oxygen-containing functional groups such as hydroxyl, epoxide, and peroxides groups are not as easily removed from the lattice as carboxylic groups because of the numbers of bonds between the carbon in the oxygen functional group and the lattice.¹⁹¹ In contrast, when treated with MPO/H₂O₂/NaCl, the oxidized HiPco SWCNTs underwent complete oxidation (i.e., degradation) as a result of the highly oxidative reagent, OCl⁻. The shortened, fluorescent SWCNTs produced by HRP/H₂O₂ may find applications as NIR imaging agents or nanocarriers for use in medical diagnostics and therapeutics.

2.2.6 Experimental

2.2.6.1 Chemical Oxidation

Purified HiPco SWCNTs^{36,50} were purchased from NanoIntegris, Inc. (Skokie, IL; Lot # P2172). SWCNTs (10 mg) were sonicated in sulfuric acid (Fisher Scientific)/nitric acid (J.T. Baker) solution (15 mL of H₂SO₄, 5 mL of HNO₃) for 3 h 50 min at 40 °C. The oxidized SWCNT sample was diluted with deionized (DI) water, vacuum-filtered, washed with DI water several times, and collected on separate polytetrafluoroethylene (PTFE) filter papers to form thin films, known in the literature as buckypaper.¹⁹⁸ Pieces of the buckypaper were cut and redispersed in DI water by sonication for 40 min at room temperature. The resulting suspensions were centrifuged (3500 rpm, 20 min), and the supernatant was collected for enzymatic oxidation.

2.2.6.2 Enzymatic Oxidation of SWCNTs Using HRP

The procedure for the enzymatic oxidation of SWCNTs with HRP/H₂O₂ has been described elsewhere.^{145,156,158} Briefly, 8 mL of the supernatant containing oxidized SWCNTs was combined with 1.5 mg of HRP (Sigma-Aldrich). The sample was incubated for 24 h at room temperature on a shaker in the absence of light. After the incubation period, 4 μL of H₂O₂ (0.089 M, Sigma-Aldrich) was added daily to the oxidized SWCNT sample for 35 days. The sample was incubated with continuous shaking during this period. In a separate control experiment, non-oxidized SWCNTs were treated with 1.5 mg of HRP/H₂O₂ employing the same method. Both samples were characterized after 35 days using UV–vis–NIR spectroscopy, TEM, Raman spectroscopy, and PL mapping.

2.2.6.3 Enzymatic Oxidation of SWCNTs Using MPO

The protocol for enzymatic oxidation catalyzed by MPO was adopted from Kagan et al.,¹⁴³ with the total volume scaled for spectrometer requirements. Lyophilized purified native human MPO was purchased from Athens Research and Technology, Inc. (Athens, GA) and reconstituted with 350 μL of nanopure water to give a final concentration of 2.0 μM . Sodium chloride, diethylenetriaminepentaacetic acid (DTPA), and 0.1 M phosphate buffer were purchased from Sigma-Aldrich. A 100 μL aliquot of the oxidized SWCNT supernatant solution was mixed with 21 μL of 5 M NaCl, 45 μL of 5 mM DTPA, 12 μL of MPO solution, 4 μL of 18.75 mM H_2O_2 , and 568 μL of 0.1 M phosphate buffer. Every hour, 4 μL of 18.75 mM H_2O_2 was added for a total of seven additions a day for 5 days. The MPO solution was added to the mixture at a rate of 12 $\mu\text{L}/\text{day}$ to compensate for the loss of enzyme activity in the incubation system. The sample was characterized after 5 days using UV-vis-NIR spectroscopy, TEM, Raman spectroscopy, and PL mapping. In a separate control experiment, non-oxidized SWCNTs were treated with MPO/ H_2O_2 /NaCl under the same conditions. In a different control experiment, pristine SWCNTs were incubated with 0.20 M NaOCl for 1 day to explore the effect of high NaOCl concentrations on SWCNT degradation.

2.2.6.4 Raman Spectroscopy

SWCNTs were excited with a 633 nm laser, and measurements were performed using a Renishaw InVia Raman microscope (Wotton-under-Edge, UK). Aliquots (~ 0.1 mL) of suspended SWCNTs were drop-cast on a glass slide and allowed to dry under ambient conditions overnight, thereby forming aggregates of SWCNTs. Scans were carried out at a laser power of 1.7 mW with an accumulation time of 10 s over the range from 100 to 3200 cm^{-1} . Spectra were

acquired from multiple locations on the SWCNT aggregates, and the results were normalized to the most intense peak and averaged in accordance with published procedures.⁷⁵

2.2.6.5 TEM Imaging and Histogram Determination

A suspension of dispersed SWCNTs (6 μL) was diluted by a factor of 100, drop-cast onto carbon-coated lacey copper grids (Pacific Grid-Tech, San Francisco, CA), and allowed to dry overnight. The analysis was performed using a Morgagni transmission electron microscope (FEI, Hillsboro, OR) with an 80 keV electron beam. The mean SWCNT length distributions were derived from the TEM micrographs for ~ 100 nanotubes per sample.

2.2.6.6 HRTEM Imaging

HRTEM images were obtained with a JEOL 2100F microscope at an accelerating voltage of 200 kV. TEM samples were evenly dispersed in aqueous solution. A 10 μL aliquot of each sample was drop-cast on an ultrathin carbon film/copper TEM grid (Ted Pella) and dried at room temperature overnight before being imaged.

2.2.6.7 UV–Vis–NIR Spectroscopy and PL Mapping

Sodium cholate was added to the SWCNT suspensions (pristine, acid-oxidized, HRP treated, and MPO-treated) at a concentration of 1% (w/v), and the suspensions were sonicated for 2 h. UV–vis–NIR measurements of dispersed SWCNTs were acquired using a PerkinElmer Lambda 900 spectrophotometer over the wavelength range 200–1300 nm. PL maps were obtained using a Fluorolog 322 spectrofluorometer (HORIBA Jobin Yvon, Kyoto, Japan) equipped with a DSS-IGA020 L detector (Electro-Optical Systems, Phoenixville, PA). The excitation wavelength was scanned from 580 to 800 nm in 5 nm increments, and the emission was detected from 900 to

1300 nm in 2 nm increments. Spectra were corrected for variation in lamp intensity and monochromator response.

2.2.6.8 DFT Calculations

The quantum-chemical calculations of equilibrium geometries were carried out using the self-consistent charge density-functional-based tight-binding (SCC-DFTB) method,¹⁹⁹ which has been successfully applied to a wide class of systems of interest, including CNTs.²⁰⁰ As a validity check on our calculations, we found that the adsorption energy of COOH on (11,0) CNTs was 1.47 eV, which is in good agreement with the value of 1.42 eV obtained previously using standard DFT calculations. The minimum-energy paths were determined using the NEB method.²⁰¹ The calculations were carried out using a periodic supercell approach with three repeat units of a (14,0) SWCNT sampled at the Γ point of the Brillouin zone.

2.2.6.9 Modified Boehm's Titration

A modified Boehm's titration procedure was utilized to determine the density of oxygen-containing functional groups on the surface of the acid-oxidized SWCNTs.^{158,194} Approximately 3 mg of oxidized SWCNTs was dispersed in 6 mL of NaOH (Mallinckrodt) at 10 mM concentration. The sample was sealed with a septum stopper, sonicated, and degassed for 1.5 min under vacuum. The samples were incubated for 72 h. After the incubation process, the solutions were filtered through a 0.22 μm Teflon membrane. A small amount of the filtrate (0.25 mL) was transferred to a separate vial, to which was added 10 μL of aqueous indicator solution containing 3:2 (v/v) 0.1% bromocresol green and methyl red (Sigma-Aldrich). The solution was titrated with 0.0082 M HCl (Fisher) using a pipet (Eppendorf). A blank control consisting of only NaOH was also treated using the same procedure to determine the concentration of NaOH. All of the

titrations were repeated at least three times. The defect density (in units of $\mu\text{mol}/\text{mg}$) was calculated from the NaOH uptake by the SWCNTs divided by the mass. SWCNTs with larger diameters (~ 1.4 nm) were purchased from Carbon Solutions, Inc. (Riverside, CA) and oxidized for 4 h using the same acid oxidation method. This sample was also characterized by defect density.

2.3 NANO EMITTERS AND INNATE IMMUNITY: THE ROLE OF SURFACTANTS AND BIO-CORONAS IN MYELOPEROXIDASE-CATALYZED OXIDATION OF PRISTINE SINGLE-WALLED CARBON NANOTUBES

2.3.1 Preface

In this section, we examined the effect of CNT coatings on biooxidation. SWCNTs application as NIR emitters was discussed in Section 1.4.1.4. As mentioned, in vivo imaging application requires pristine semiconducting SWCNTs for their NIR emitting property and the CNTs are often coated by surfactants to improve their solubility and biodistribution. In this work, we searched for SWCNT chirality and coating conditions that would prevent/suppress biodegradation by the innate immune system (i.e., MPO enzyme and neutrophil cells). Our results showed the CNT coatings could significantly affect the effectiveness of MPO-catalyzed biooxidation. We identified surfactants and biomolecules that protect SWCNTs, protect SWCNTs with smaller diameters selectively, and those do not protect against the enzymatic oxidation. Our findings provide an important insight into the enzymatic degradation of coated-SWCNTs and can be applied and extended to other carbon nanomaterials and nano-emitters.

The material contained within Chapter 2.3 was published as an original research paper in the journal, *Nanoscale*. The figures have been reproduced with permission from Ref ²⁰².

List of Authors: C. F. Chiu, H. H. Dar, A. A. Kapralov, R. A. S. Robinson, V. E. Kagan, and A. Star

2.3.2 Introduction

Carbon nanotubes and graphene have unique electronic, optical and mechanical properties enabling many applications in materials and life sciences.^{203,204} Some of the promising medical applications are in the field of drug delivery and in-vivo imaging, where single-walled carbon nanotubes (SWCNTs) have their intrinsic bandgap photoluminescence (PL) in the near-infrared (NIR) region.⁵⁶ The excitations and emissions of the SWCNTs often lay in the range of the “biological window”, 650 nm to 1350 nm, whereby tissue-light interaction is minimal.²² The NIR photoactivity of SWCNTs has minimal photobleaching,²³ and avoids autofluorescence from biological molecules, which are typically excited by ultraviolet-visible light coinciding with small molecule dyes. The in-vivo imaging of tumors has been widely studied because of its medical values. The “search and destroy” approaches are of particular interest by coupling imaging with drug-release or thermal destruction to target cancer cells.^{24,25} The intensity of the emitted luminescence from the SWCNTs is critical for imaging, as well as for in-vivo chemical sensing.²⁷

Carbon nanotubes utilized in optical imaging are pristine (not chemically modified or functionalized) as defect sites can quench their bandgap luminescence.⁵⁸ Study has shown that even as-produced SWCNTs have structural growth defects and covalent derivatization of the CNT surface, which quench the PL of SWCNTs from their maximal brightness.¹⁰⁵ It has been determined that excitons in SWCNTs have a diffusional length of about 100 nm and are subjected to be attacked by reversible and irreversible reaction.¹⁸² In order to preserve the luminescence properties, and to increase water solubility, pristine hydrophobic SWCNTs are

often coated by surfactants,⁵⁸ polymers,^{70,205,206} DNA,^{206–209} and/or proteins.¹⁷⁰ These coatings had been shown to alter the cellular uptake and biodegradability of oxidized nanomaterials.^{70,170}

Enzymatic oxidative degradation of carbon nanomaterials has been demonstrated with different mammalian peroxidase systems such as neutrophil myeloperoxidase (MPO)^{143,147,158,159,164,170,172} (Figure 32a), eosinophil peroxidase (EPO),¹⁴⁶ and lactoperoxidase (LPO)¹⁴⁷. This degradation can cause structural modification and destruction of carbon nanotubes.^{143,147} This enzymatic oxidation is irreversible as opposed to a reversible protonation at low pH.¹⁸² MPO is an important enzyme in neutrophil antimicrobial responses and can undergo peroxidase and halogenation cycles to oxidize a substrate (Figure 32b). For nanomaterials, it has been shown that hypochlorite (OCl^-) is the major oxidant and an important initiating factor in the MPO system.^{143,147} We have previously proposed that the OCl^- produced from MPO can oxidize the pristine SWCNT surface first, followed by MPO peroxidase cycle to further degrade the nanomaterials at defect sites.¹⁴³ Cell study with neutrophils had also been conducted for oxidized CNTs with evidence of degradation.^{143,170}

While the enzymatic oxidation is efficient at degrading carbon nanomaterials with high defect densities, its effect on pristine SWCNTs has not been fully studied. The MPO-catalyzed reaction could oxidize the sidewalls of SWCNTs, generating defect sites which quench the luminescence of SWCNTs needed in NIR imaging. In this work, we analyzed the initial MPO-catalyzed oxidation of SWCNTs coated with common surfactants such as sodium cholate (SC) and sodium deoxycholate (SDC), as well as cytosine—phosphate—guanine (CpG) oligonucleotides, bovine serum albumin (BSA), phosphatidylserine (PS), and a branched phospholipid-polyethylene glycol (PL-PEG).

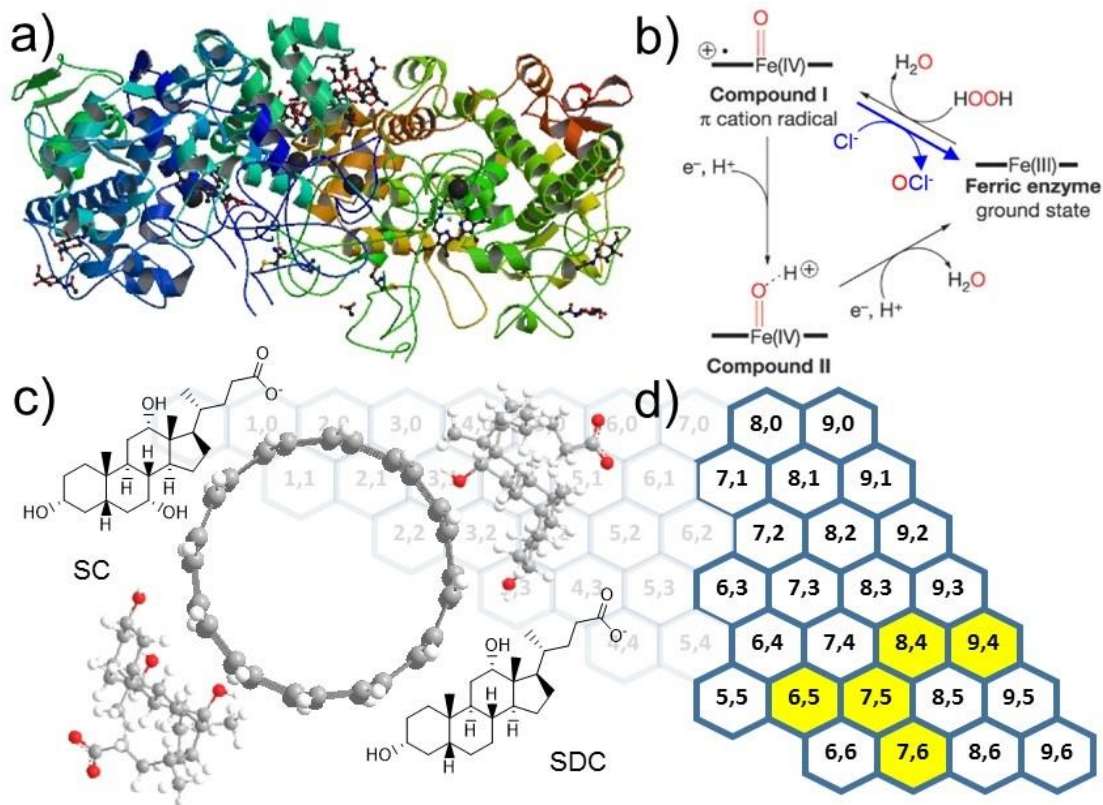


Figure 32. a) Crystal structure of MPO (Reproduced with permission from Ref 210. © 2009 American Society for Biochemistry and Molecular Biology). b) Peroxidase and halogenation cycles of MPO. (Reproduced with permission from Ref 151. Copyright 2002 Nature Publishing Group). c) Molecule structures of the surfactants, sodium cholate (SC) and deoxycholate (SDC), used in this study. d) Chiralities of SWCNTs investigated in this work are highlighted in yellow.

2.3.3 Results

Figure 33 shows the excitation-emission maps (EE map) of sodium cholate protected SWCNTs (SC-SWCNTs) before and after oxidation with MPO (Figure 33a,b). SWCNTs chiralities on the EE maps were assigned according to literature.⁵ For controls, various reagents, including MPO (Figure 33c), H₂O₂ or both (Figure 52 in Appendix B), had been taken out or replaced with equal volumes of water. Hydrogen peroxide (H₂O₂) concentrations were tested by colorimetric test

strips. With MPO/H₂O₂/NaCl (Figure 33b), the H₂O₂ was undetectable 30 mins after each addition, suggesting that MPO was actively consuming H₂O₂. In the absence of MPO (Figure 33c), H₂O₂ concentration increased with the additions.

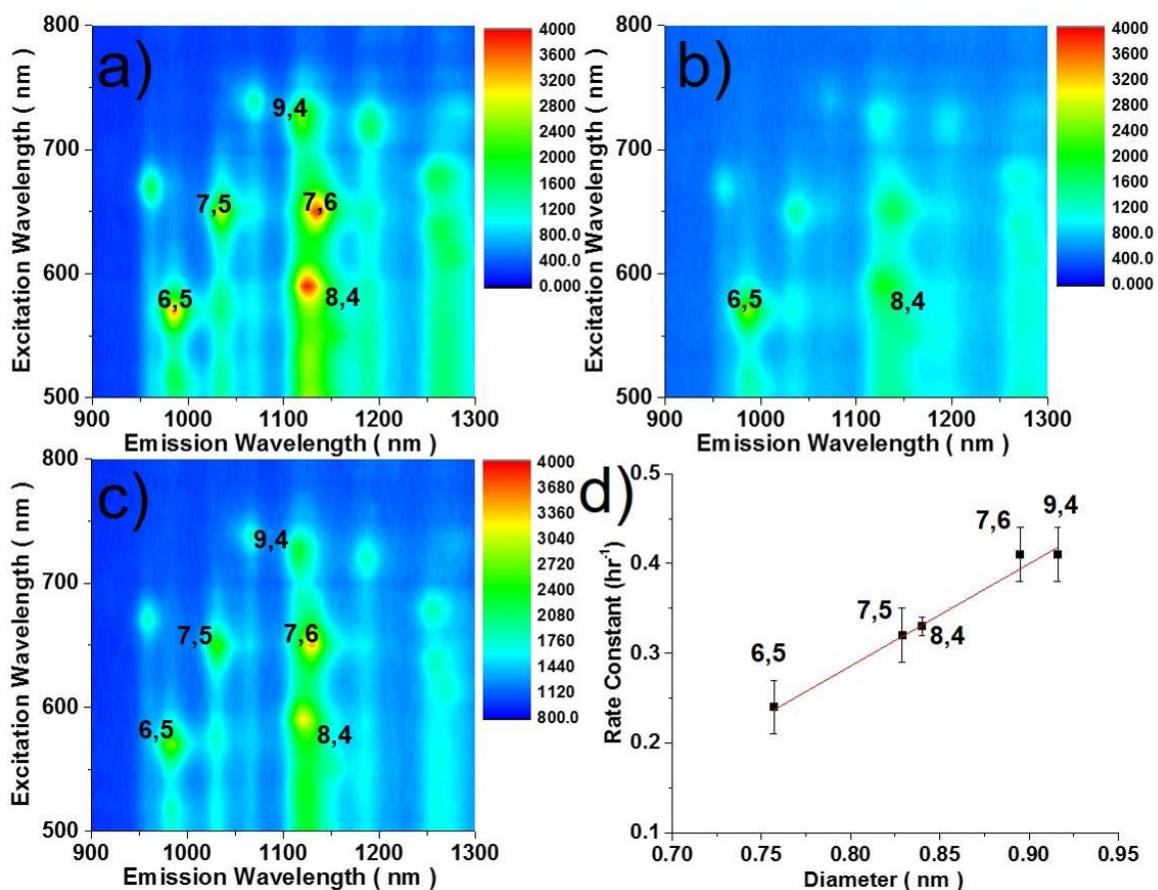


Figure 33. The excitation-emission (EE) maps of SC-SWCNTs a) before activation of the halogenation cycle of MPO and b) after five additions of H₂O₂ into the reaction mixture (MPO/NaCl). c) EE map for SC-SWCNTs treated with H₂O₂/NaCl (without MPO). d) Calculated rate constants of different SWCNTs versus their diameters.

Figure 33b depicts the EE map of SC-SWCNTs after five additions of H₂O₂ into the reaction mixture (MPO/NaCl). After these additions, PL intensities of SWCNTs have significantly decreased. Interestingly, the emission of (6,5) SWCNTs remained of a higher intensity relative to (9,4) and (7,6). The SWCNT distribution changes in EE maps were not

observed in any of the controls. In the absence of MPO halogenation cycle, EE maps exhibit similar chirality distributions, i.e., no changes of emission intensities relative to (6,5) CNT, revealing that the ratio between different SWCNTs remains constant (Figure 52). Doorn and co-workers demonstrated similar diameter-dependent changes in the contour plots with SDS-SWCNTs by the addition of NaCl salt.²¹¹ Our control experiments in Figure 33 and 52 reveal that salt was not the cause as all samples contained the same NaCl concentrations.

A more detailed progress of the myeloperoxidase oxidation of SC-SWCNTs over a total of 14 H₂O₂ additions is summarized as a time-lapse figure in the supporting information (Figure 53). The bandgap emission of the SWCNTs was quenched in diameter-dependent order. Figure 53d summarizes the changes in emission for different nanotube chiralities in comparison to the (6,5) SWCNTs. It reveals the order of quenching in the sequence of (9,4), (7,6), (8,4), (7,5), and (6,5) SWCNTs, which have diameters of 0.916, 0.895, 0.840, 0.829 and 0.757 nm, respectively.¹² The data from Figure 53 are further fitted to different rate law equations (Figure 53e-f). The reaction is verified to be first order to SWCNTs. Rate constant values for different CNT chiralities were extrapolated by applying first-order rate equation to the data (Figure 53h). The result is presented in Figure 33d and shows that larger diameter SWCNTs have a higher rate constant than smaller diameter ones. Values from Figure 33d are available in Table 7 in Appendix B.

To test if the SWCNTs were oxidized in the process, SWCNTs samples were subjected to Raman spectroscopy, and their D/G ratio was analyzed (Figure 34). The changes in Raman D/G signals at various reaction stages were not significant. We attribute this to the fact that photoluminescence spectroscopy is much more sensitive to low defect levels than Raman spectroscopy.^{54,112,212} Our observation here is in agreement with the reported photoluminescence

quenching in diazonium ion reaction, where severe quenching was observed with slight changes (+0.03) in Raman D/G ratio.⁵⁸

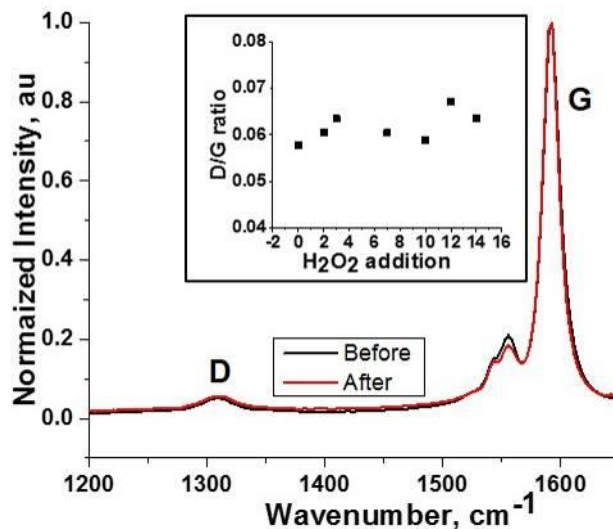


Figure 34. Raman spectra of SWCNT before and after the reaction. Inset shows the change of D/G ratio over H₂O₂ additions.

Sodium cholate is often compared to other bile salt derivatives such as sodium deoxycholate and sodium taurodeoxycholate for their similarity in chemical structure.^{58,59} When sodium cholate was replaced by sodium deoxycholate, SWCNTs peaks on the EE maps were intense before and after the MPO/H₂O₂/NaCl reaction (Figure 54), suggesting that SDC-SWCNTs were well dispersed and well protected from any quenching or oxidation. In comparison to SC, SDC provided better protection for SWCNTs under the same oxidative environment and could be the result of a thicker coating layer formed by SDC than SC.⁵⁹

The observed changes in SWCNT emissions during MPO/H₂O₂/NaCl incubation could be rationalized by either nanotube oxidation or removal of the surfactant coating. In the previous work, “stripping” of PEG coating from the SWCNT surface was observed when PEG-modified SWCNTs were exposed to activated neutrophils.⁷⁰ Surfactant desorption could reduce the

solubility of SWCNTs, which reduces the PL emission intensity by SWCNT bundling.²¹³ To stimulate surfactant desorption, removal of surfactant from SC-SWCNTs and SDC-SWCNTs was implemented by dialysis.^{214,215} Figure 55 shows the EE maps before and after dialysis. After overnight dialysis, the emission intensities were quenched by 24% in SC-SWCNTs (Figure 55a and 55b) and by 17% in SDC-SWCNTs (Figure 55d and 55e). The quenching was uniform for all nanotubes, suggesting that the diameter-dependence observed in MPO oxidation was not a direct result of surfactant desorption. Another dialysis experiment was performed in the presence of MPO. Other proteins, such as Concanavalin-A²¹⁵ and horseradish peroxidase,²¹⁴ had been adsorbed to SWCNTs using a surfactant exchange method developed by Graff et al.²¹⁵ SWCNTs were first suspended in a solution of sodium cholate and subsequently dialyzed in the presence of protein to remove the surfactant and form a protein-SWCNT complex.²¹⁵ We used the dialysis membrane with a molecular weight cut-off at ~5 kDa. The pores of this membrane are big enough for SC or SDC micelles, but not for MPO enzyme molecules. SC-SWCNT and SDC-SWCNT samples were incubated with MPO for 3 h and dialyzed overnight. EE maps from samples dialyzed with MPO are depicted in Figure 55c and 55f. In the presence of MPO, the quenching was more severe. We attribute this dialysis result to MPO binding onto SWCNT surface. As the surfactants were removed by dialysis, SWCNT surface became more accessible to MPO causing further quenching. It is worth noting that the quenching with MPO present was less severe in SDC-SWCNTs (36%) than in SC-SWCNTs (47%), pointing to the same conclusion that SDC provides better protection to SWCNTs than SC. More importantly, the observed quenching was not diameter dependent as in the case of the MPO/H₂O₂/NaCl oxidation.

The same diameter-dependence quenching from Figure 33b can be observed when the MPO/H₂O₂/NaCl oxidation components are replaced by the halogenation product, hypochlorite (OCl⁻). In Figure 35, SC-SWCNTs were exposed to sodium hypochlorite at 0.81 M, a quantity equivalent to 1080 additions of H₂O₂ and perfect efficiency in the MPO halogenation cycle, to illustrate that early stage oxidation by the MPO/H₂O₂/NaCl system in Figure 33 will eventually lead to complete degradation. EE maps on Figure 35b show similar diameter-dependence comparing to those produced by MPO/H₂O₂/NaCl system. As the reaction progressed (Figure 35c), all SWCNT peaks disappeared and a new broad emission band near 900 nm appeared. The origin of this new peak is unclear but is expected to be related to light-scattering or luminescence by the newly-formed by-products. The sample in Figure 35c was also investigated by Raman spectroscopy and transmission electron microscopy (TEM), from which the disappearance of D and G bands on Raman spectrum and the loss of tubular structures on TEM images indicate the complete degradation of SWCNTs.^{143,172,184} In Figure 56, SC-SWCNTs were exposed to the equivalent amount of OCl⁻ produced by H₂O₂ in Figure 33b. Together, Figure 35 and 56 provide evidence that the chirality-dependent quenching was caused by OCl⁻, and that given a high OCl⁻ concentration or longer reaction time, early oxidation altering the PL spectra will be followed by complete degradation of SWCNTs shown by Raman and TEM.

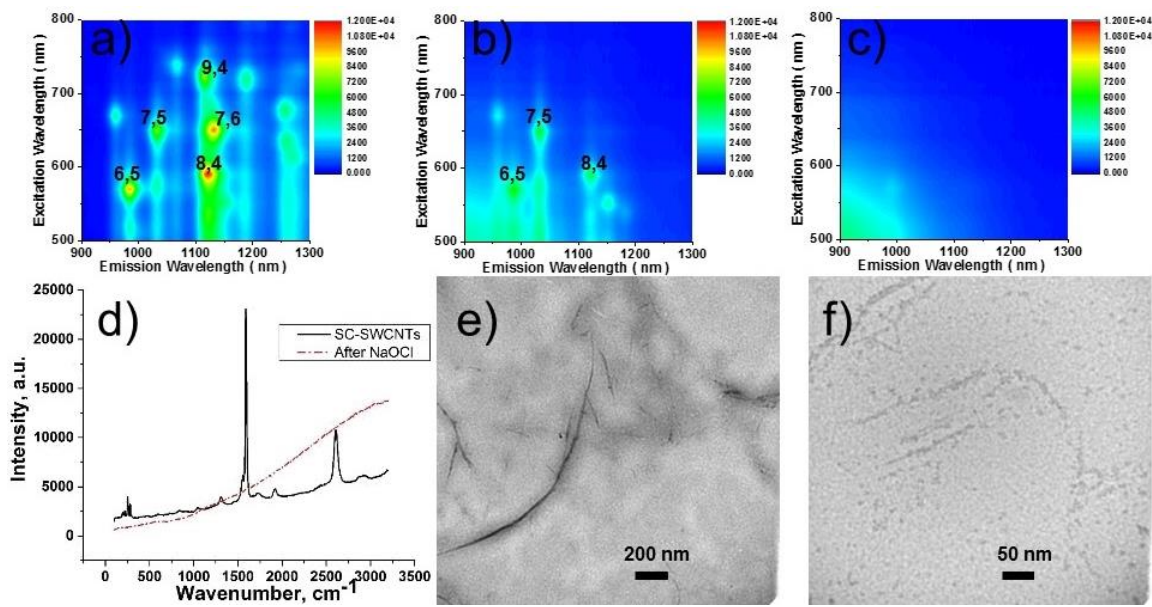


Figure 35. Complete degradation of SC-SWCNTs by NaOCl. EE maps of SC-SWCNTs a) before the addition of NaOCl, b) 1 day, and c) 3 days after. d) Raman spectra and TEM images of SC-SWCNTs e) before and f) after the reaction.

Our results with SC-SWCNTs and SDC-SWCNTs indicate that surfactant/protecting micelle affects the biodegradation of SWCNTs. We extended our work to other previously investigated biomolecule-based coatings such as DNA strands, phospholipid-polyethylene glycol, bovine serum albumin, and phosphatidylserine. CpG oligonucleotides are selected for this work due to their immunostimulatory properties.²¹⁶ Although CpG DNA does not activate neutrophils directly, it can induce an enhanced in-flux of neutrophil to the site of infection, increasing the production of reactive oxygen species and overall effectiveness.²¹⁶ CpG oligonucleotides have been coupled with SWCNTs (CpG DNA-SWCNTs) and have been demonstrated to have a photo-hyperthermic effect for cancer treatment in mice.²⁰⁹ Branched PL-PEG coated SWCNTs (PL-PEG-SWCNTs) have been utilized for circulation studies in mice.¹⁴⁰ BSA-coated SWCNTs (BSA-SWCNTs) and phosphatidylserine-coated SWCNTs (PS-SWCNTs) were analyzed for cellular uptake.^{67,217} Solutions of CpG DNA-SWCNTs, PL-PEG-SWCNTs,

BSA-SWCNTs, and PS-SWCNTs were prepared according to the literature procedures through sonication and centrifugation.^{67,165,209,217} The samples were subjected to MPO-catalyzed oxidation and their EE maps are presented in Figure 36. Changes in intensity values and control experiment are available in Figure 57 and 58 in Appendix B.

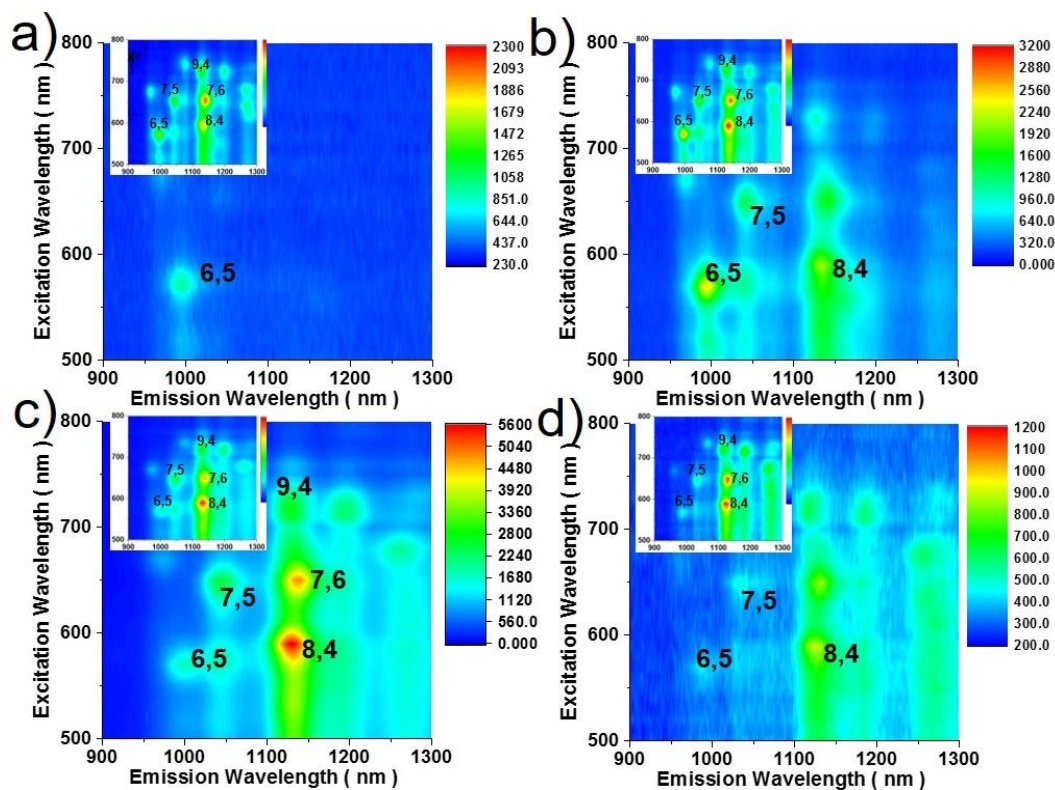


Figure 36. EE maps of a) CpG DNA-SWCNTs, b) BSA-SWCNTs, c) PL-PEG-SWCNTs, and d) PS-SWCNTs after oxidation with MPO/H₂O₂/NaCl. Inserts are EE maps before the reactions.

CpG DNA-SWCNTs after the MPO reaction showed a dominant (6,5) signal upon MPO oxidation comparable to SC-SWCNTs (Figure 36a). BSA-SWCNTs also shared the diameter dependent trend. SWCNTs of (7,6) and (8,4) chiralities were about 1.2 times brighter than (6,5) SWCNTs before and became ~70% of the brightness of (6,5) SWCNTs after the MPO oxidation (Figure 36b). Not all tested biological coatings shared the same diameter dependence quenching behavior. PL-PEG-SWCNTs showed excellent protection like those observed with SDC-SWCNTs. The intensity of the PL-PEG-SWCNTs was not quenched by the MPO reaction

(Figure 36c). Finally, PS-SWCNTs showed some degree of quenching, but not diameter dependent. Over the course of the MPO oxidation, all PS-SWCNTs emissions were quenched and resembled the same distribution as the initial EE map (Figure 36d). These results demonstrate that the diameter-dependence of MPO-catalyzed oxidation of SWCNTs is not restricted to surfactants and can also occur with DNA or protein coatings and can potentially extend to the biodegradation of opsonized SWCNTs in vivo, where SWCNTs are coated with different biomolecules (coronas) such as proteins and lipids.²¹⁸

With these results on MPO-catalyzed oxidation of protected SWCNTs, neutrophil oxidation of coated SWCNTs was attempted. Upon activation by N-formyl-methionyl-leucyl-phenylalanine (fMLP) and cytochalasin B (CyB), neutrophils had been shown to degrade oxidized SWCNTs through the MPO oxidation pathway.¹⁴³ Here, we incubated the SDC-SWCNTs, CpG DNA-SWCNTs, and BSA-SWCNTs with activated and non-activated neutrophils. Incubations with mouse embryonic fibroblast (MEF) cells were also performed as non-oxidative controls. Figure 37 summarizes our results with the normalized emission intensities of (7,6) SWCNTs. EE maps of these results are available in Figure 59.

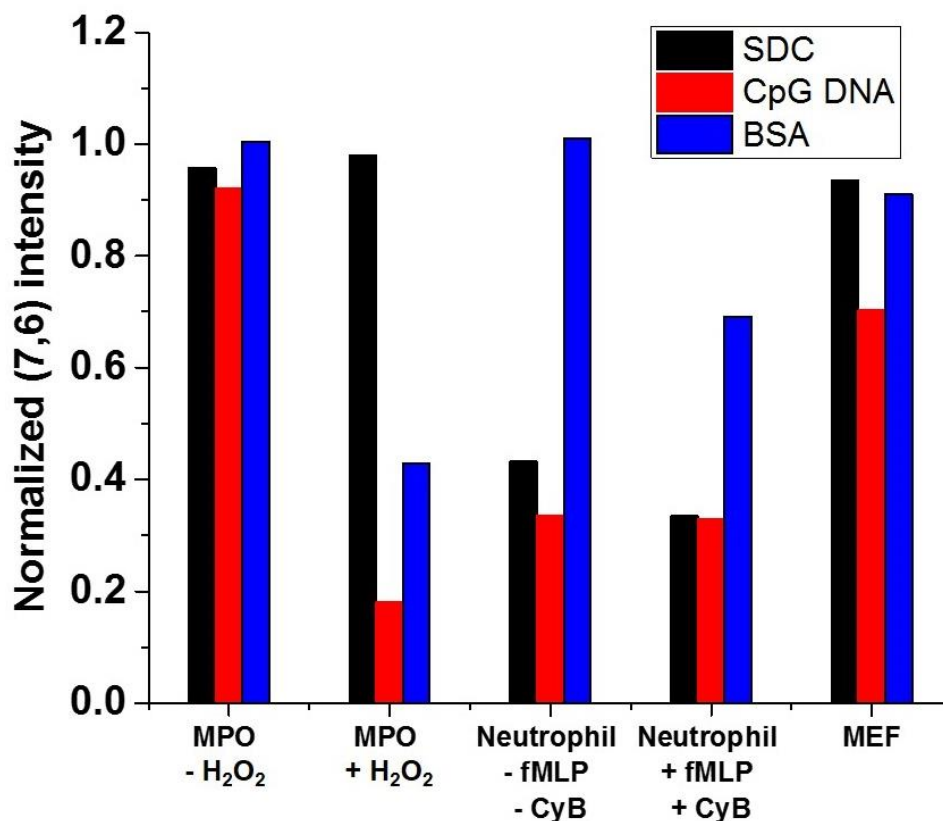


Figure 37. Normalized intensity of (7,6) SWCNTs after incubation with MPO, neutrophils, and MEF.

SDC-SWCNTs were chosen for their resistance towards OCl^- from our MPO experiments. The different results from active neutrophils, non-active neutrophils and EMF cells indicate that the spectral changes were not due to surfactant displacement by cell media. NIR emission from SDC-SWCNTs was 93% of the initial intensity after MEF incubation, showing similar resistance towards MEF cells and cell media. When incubated with neutrophils, however, the emission dropped to 30-40% regardless of whether the neutrophils were activated or not. It is possible that SWCNTs triggered the neutrophils activation without the specific agents (fMLP and CyB), which could explain the similar results in activated vs. non-activated neutrophils.¹⁶⁹ As mentioned above, SDC-SWCNTs can prevent the MPO oxidation, implying that the observed quenching with neutrophils might be due to other non-MPO pathways. The effects of activated neutrophils are realized via three major synergistically interacting mechanisms: i) oxidative

burst, ii) release of granules and iii) formation of neutrophil extracellular traps (NETs). While MPO is the major contributor to SWCNT modification through oxidative reactions of MPO, the other factors such as antibacterial serine proteases (neutrophil elastase, proteinase 3 and cathepsin G of the azurophilic granules), plasma membrane and cytosolic proteins and lipids as well as DNA are also likely candidates for the SWCNT modification.²¹⁹ These secreted from the activated neutrophils factors – acting together – can potentially affect the SWCNT wrapping, facilitate its displacement from the SWCNT surface and enhance the MPO-driven oxidative degradation process thus explain more efficient SWCNT degradation by neutrophils as compared to MPO alone.²²⁰

CpG DNA- and BSA- were chosen for their diameter dependence shown in MPO oxidation. It is important to note that such diameter dependence was not observed when incubated with either neutrophils or MEF cells (Figure 59). CpG DNA-SWCNTs fluorescence was quenched to 33% of the initial intensity in both activated and non-activated neutrophils and to 70% in MEF cells. As CpG DNA does not activate neutrophils, the similarity between activated and non-activated neutrophils suggests that the observed spectral changes were not a result of the oxidative burst.²¹⁶ The reduction in emission might be due to interactions between CpG DNA-SWCNTs with neutrophils and, to a lesser extent, MEF cells. Incidentally, BSA-SWCNTs were not affected by non-activated neutrophils, had 90% emission with MEF cells and 69% emission with activated neutrophils, making BSA-SWCNTs the least affected among the three coatings tested in the cell experiments.

2.3.4 Discussion

We and others have previously suggested diameter dependence in MPO-catalyzed oxidation by analyzing radial breathing modes (RBM) in SWCNT Raman spectra.^{164,170} While Raman RBM modes can be correlated to nanotube diameters,¹² our new PL data reveal the relative changes in nanotube chiralities. Our data shows the selective oxidation beginning from the larger diameter SWCNTs, as the quenching of SC-SWCNT progressed from the top right corner of the EE map to the bottom left, corresponding to nanotube with (9,4) chirality (0.916 nm) to (6,5) (0.757 nm).¹² Our data with chirality precision confirmed that MPO-catalyzed oxidation could be selective in SWCNTs.

The impact of the observed PL selectivity in the MPO-catalyzed oxidation of SWCNTs is two-fold. From a materials chemistry standpoint, our results suggest that (6,5) SWCNTs are more resistant to oxidation in comparison to nanotubes of other chiralities as in the case for SC-SWCNTs, CpG DNA-SWCNTs, and BSA-SWCNTs. Since the emission signal from (6,5) SWCNTs was less affected by oxidation than the other nanotubes, it would be reasonable to track the emission of (6,5) SWCNTs for NIR imaging purpose. However, from a biological imaging standpoint, (6,5) SWCNTs absorb light at 566 nm which is outside the range of “biological window”. Within our sample pool, (7,6) SWCNTs have the closest match to the biological window, with excitation at 642 nm and emission at 1115 nm. We have demonstrated sodium deoxycholate is excellent in protecting this band from MPO oxidation. Among the biological coatings we tested, PL-PEG-SWCNTs appeared to be the most efficient in protecting SWCNTs from the MPO-catalyzed oxidation.

We have attributed the diameter dependent spectral changes in fluorescence to the MPO halogenation cycle. Non-activated MPO ($-H_2O_2$) showed no reduction in SWCNTs emission and

dialysis experiments showed quenching with no diameter dependence. Therefore, we concluded that our observation was not the result of MPO binding to SWCNTs. In fact, we identified OCl^- oxidation to be the reason, as we have demonstrated in experiments with sodium hypochlorite (Figure 35).

The observed differences in the effects of coatings might be related to OCl^- ion diffusion to the coated nanotubes through the surfactant layers. SC-SWCNT layers were calculated by Fagan et al. to be ~ 1 nm thinner than those of the SDC-SWCNTs.⁵⁹ Our results here also indicate that SC-SWCNTs are worse at excluding quenchers than SDC. Diameter dependence with SC was illustrated by Hilmer et al. in diazonium reactions.⁵⁸ SDC showed more resistance to a given concentration of diazonium ions than SC,⁵⁸ just as we observe in this enzymatic oxidation.

The OCl^- diffusion argument can also be applied to DNA-coated SWCNTs. Taylor and co-workers had modeled DNA wrapping on SWCNTs. They showed an average 0.34 nm between DNA and SWCNTs, a typical π - π stacking distance, which was independent of the CNT chirality and the DNA sequence.²²¹ Furthermore, they indicated that larger diameter SWCNTs have a longer helical wrapping periodic distance along the tube. With wrapping period of 3.2 nm for (6,5) SWCNTs and 4.2 nm for larger (11,10) SWCNTs, it implies that all DNA wrapped SWCNTs have a gap that can be attacked by OCl^- . Moreover, larger diameter CNTs have a wider gap between helical wrapped DNA. In fact, this matches with our observed diameter dependence from CpG DNA-SWCNTs. CpG DNA was selected for this work because of its biological relevance.²¹⁶ As Zheng et al. demonstrated, the length and the sequence of DNA can affect its binding to SWCNTs, leading to SWCNTs separation by chirality using ion exchange chromatography.⁶⁹ It was hypothesized that each specific sequence of DNA can form an ordered DNA barrel structure only on one particular (n,m) CNT.⁶⁹ Such specific interaction would result

in the protection of SWCNTs of particular chirality. The interactions between specific ssDNA and their corresponding SWCNTs were demonstrated by Strano et al. in their study of fluorescence modulation of DNA-wrapped SWCNT to multiple biomolecules.²²²

Our results illustrate that the choice of the coating is the primary factor in the observed diameter dependence of the MPO oxidation. However, it is also possible that larger diameter SWCNTs have a higher reactivity in OCl^- oxidation. We have previously suggested diameter reactivity based on redox potentials.¹⁷² The electrochemical potentials of SWCNTs have been previously determined, and the bandgaps of SWCNTs were showed to increase as the nanotube diameter decreases.¹⁷² In this model, electron transfer takes place from the top of the valence band of SWCNT to the oxidizing species. Since the potential difference between hypochlorite and SWCNTs is larger with larger diameter SWCNTs, the reaction between large diameter SWCNTs and OCl^- should be more energetically favorable.¹⁷²

Previous studies have shown that oxidized SWCNTs can be degraded by both halogenation cycle and peroxidase cycle of the MPO. Without NaCl, MPO undergoes only peroxidase cycle and is markedly less effective in degrading oxidized SWCNTs.¹⁴³ It was suggested that the carboxyl sites resulted from OCl^- oxidation would lead to better binding of MPO and subsequent biodegradation through both peroxidase and halogenation cycles.¹⁴³ As the fluorescence emission required pristine SWCNTs, our nanotubes had a low density of functional groups for MPO to bind. Our study here focused on the early stages of SWCNT oxidation by MPO, and therefore we focused on the OCl^- pathway. Although we showed OCl^- can degrade SWCNTs using Raman spectroscopy and TEM, also previously demonstrated by Vlasova et al.,¹⁴⁷ the debate on the efficiency of a single-pathway degradation (halogenation only) versus a

dual-pathway degradation (using both peroxidase and halogenation cycles) is beyond the scope of this paper.

It is worth noting that sodium cholate used in this work is only physisorbed to the nanotube surfaces. The physisorbed surfactants are much more likely to be stripped off in comparison to the covalently attached molecules, as was recently demonstrated for PEG functionalized SWCNTs by Bhattacharya et al.⁷⁰ Our dialysis data showed universal quenching of nanotubes with all chiralities, suggesting that stripping or desorption is not the cause of the diameter dependence in MPO-catalyzed oxidation. However, these results do not rule out the possibility that the diameter-dependent quenching is a two-step process, where surfactants detach from the SWCNTs first, followed by OCl^- attack on the exposed surface.

Our understanding from experiments with surfactant protected SWCNTs can be extended to other biologically-relevant coatings, as demonstrated with CpG DNA, BSA, PL-PEG, and PS. Diameter-dependent quenching was observed from CpG DNA-SWCNTs and BSA-SWCNTs upon MPO-catalyzed oxidation, but not from PL-PEG-SWCNTs or PS-SWCNTs. These results indicate that coatings can alter the biological behavior of the SWCNTs.

From our neutrophil experiments, it appears that other factors are contributing to the nanotube fluorescence quenching in addition to MPO halogenation. Particularly, SDC-SWCNTs and CpG DNA-SWCNTs showed some unexpected results. The resistance of SDC-SWCNTs towards MPO oxidation was not observed with neutrophils. Diameter dependence with CpG DNA-SWCNTs in MPO-containing system was also not observed as emission signals were quenched uniformly by neutrophils. As the reduction of signals was detected for both activated and non-activated neutrophils, the cause of quenching could be related to the stripping of coatings by neutrophils and the activation of neutrophils by SWCNTs. Controlled incubations

with MEF cells indicated that the observed spectral changes were not a result of the cell culture media.

2.3.5 Conclusion

In this work, we demonstrated the MPO-catalyzed oxidation of surfactant-protected SWCNTs. Photoluminescence data show that at the early stages of oxidation, there is a diameter selectivity, where larger diameter SWCNTs undergo oxidation first, similar to results previously reported using Raman spectroscopy.^{164,170} We also show that surfactant desorption and MPO binding was not the cause, but OCl^- produced in MPO halogenation cycle oxidizes SWCNTs resulting in diameter-dependent quenching. The difference between SC-SWCNTs and SDC-SWCNTs suggests that surfactants can strongly influence the reactivity of SWCNTs. Similar diameter dependence was also observed with CpG DNA-SWCNTs and BSA-SWCNTs, but not with PL-PEG-SWCNTs or PS-SWCNTs. These findings underline how coatings bring an extra degree of complexity to the nanomaterials and how biodegradation or other reactions would be affected. This work provides an understanding of the enzymatic degradation of pristine but protected SWCNTs, and can be applied and extended to other carbon nanomaterials and nanocomposites.

2.3.6 Experimental

High-Pressure CO Conversion (HiPco) synthesized SWCNTs were purchased from NanoIntegris, Inc. (Skokie, IL; Lot # P2172). Sodium cholate (SC), sodium deoxycholate (SDC), sodium hypochlorite (NaOCl), and bovine serum albumin (BSA) were purchased from Sigma-Aldrich. SWCNTs were dispersed in 1% wt. SC or SDC at concentrations of 0.1 mg/mL. The

solutions were sonicated for 2 h. BSA-SWCNTs were prepared by dispersing SWCNTs with BSA in water using bath sonication, at a SWCNT: BSA ratio of 1:10 for a final SWCNT concentration of 0.1 mg/mL.²¹⁷ Branched PL-PEG was synthesized by an amide coupling with (Methyl-PEG₁₂)₃-PEG-NHS ester (Thermo Scientific) and N-(aminopropylpolyethyleneglycol) carbamyl-distearyl phosphatidylethanolamine (DSPE-050PA, NOF Corporation) in anhydrous dichloromethane.¹⁶⁵ N, N-Dicyclohexylcarbodiimide (DMAP) and 4-dimethylaminopyridine were added after 12 h. The resulting PL-PEG has a molecular mass of ~8k Da.¹⁶⁵ PL-PEG was stirred for 24 h and collected by vacuum filtration. PL-PEG-SWCNTs were prepared by sonicating SWCNTs with PL-PEG at a ratio of 1:10 for a final SWCNT concentration of 0.1 mg/mL. CpG oligonucleotides (5'-TCGACGTTTTGACGTTTTGACGTTTT-3') were purchased from Integrated DNA Technologies. CpG DNA-SWCNTs were prepared by sonicating SWCNTs with CpG DNA at SWCNT: CpG ratio of 1:5 for a final SWCNT concentration of 0.1 mg/mL.²⁰⁹ Phosphatidylserine (Fisher, NC9474115) SWCNT solutions were prepared at a SWCNT: phosphatidylserine mass ratio of 1:5. All SWCNT solutions were centrifuged at 3500 rpm for 15 minutes. The top 90% of the supernatant solutions were transferred and used as stock solutions for later experiments.

Lyophilized purified native human MPO was purchased from Athens Research and Technology, Inc. (Athens, GA) and reconstituted with 350 μ L of nanopure water to give a final concentration of 2.0 μ M. For the MPO reactions, 150 μ L of the dispersed SWCNTs stock solution were mixed with 500 μ L of distilled water, 12 μ L of MPO solution and 20 μ L of 5 M NaCl (EM Science, Germany). The solutions were incubated for 1 h before the first EE map was obtained. The reaction was initiated by the addition of 4 μ L of 18.75 mM H₂O₂ (Fisher), rested for 30 minutes before sequential EE mapping. A total of five H₂O₂ additions were applied unless

stated otherwise. H₂O₂ test strips (Quantofix®) were used to monitor the consumption of H₂O₂ and to verify the activity of the enzyme. In the NaOCl control, MPO solutions were not added and 4 μL H₂O₂ was replaced by 4 μL 18.75 nM NaOCl (Figure 56).

For the dialysis experiments, 300 μL of the surfactant protected SWCNTs were diluted with 1 mL of distilled water for the first EE map. The solutions were then dialyzed in 1 L of water with Float-A-Lyzer G2 dialysis device overnight before EE mapping. For dialysis in the presence of MPO, 300 μL of SWCNTs were diluted with 1 mL of distilled water. MPO solution (24 μL) was added and incubated for 3 h before dialysis. The solution was EE-mapped before and after the dialysis. EE maps with MPO before the reaction resemble the maps without MPO (data not shown).

Neutrophils were isolated from human buffy coat (Central blood bank, Greentree, PA) by density gradient centrifugation utilizing Histopaque (1.077 g/mL) (Sigma, St. Louis, MO). The pellet containing neutrophils was collected, and contaminated erythrocytes were removed using RBC (Red Blood Cells) lysis buffer. Neutrophils were washed twice with calcium and magnesium free PBS, and suspended in RPMI-1640 (no phenol red; GLICO) medium, with a concentration of 5×10^6 cells/mL. Neutrophil suspensions were incubated with SWCNTs at a ratio of 1 million cells/1 μg of SWCNTs. The dilution resulted with a 0.01 wt % of the corresponding SWCNT coatings. In a separate control experiment, neutrophils were subjected to 0.01 wt % of SDC to examine their survivability. Living cells can be observed after 3 h. Neutrophils were activated by the addition of N-formyl-methionyl-leucyl-phenylalanine (fMLP) and cytochalasin B (CyB) at final concentration of 100 nM and 5 μg/mL, respectively. The solutions were incubated for 3 h, with SWCNT emissions monitored every 30 mins. Mouse

embryonic fibroblasts (MEF) cells were used as a control with RPMI (no phenol red; GLICO) medium.

Photoluminescence excitation-emission (EE) maps were obtained using a Fluorolog 322 spectrofluorometer (HORIBA Jobin Yvon, Kyoto, Japan) equipped with a DSS-IGA020 L detector (Electro-Optical Systems, Phoenixville, PA). The excitation wavelength was scanned from 580 to 800 nm in 5 nm increments, and the emission was detected from 900 to 1300 nm in 2 nm increments. A second spectrofluorometer (Nanolog, Horiba Jobin Yvon) was also used with excitation wavelength scanned from 300 nm to 800 nm and emission detected between 820 nm to 1580 nm with 1.5 nm increments.

Raman measurements were performed using a Renishaw InVia Raman microscope (Wotton-under-Edge, UK) with a 633 nm laser. Samples were drop-casted on a glass slide and allowed to dry under ambient conditions overnight. Scans were carried out at a laser power of 1.7 mW with an accumulation time of 10 seconds over the range from 100 to 3200 cm^{-1} . Spectra were acquired from multiple locations and were normalized to the most intense peak and averaged.

TEM images were obtained using a Morgagni transmission electron microscope (FEI, Hillsboro, OR) with an 80 keV electron beam. Sample (10 μL) was diluted by a factor of 100 and sonicated for 10 mins. 10 μL of the diluted sample was drop-casted onto carbon-coated lacey copper grids (Pacific Grid-Tech, San Francisco, CA), and allowed to dry overnight at ambient conditions.

3.0 DEFECT-INDUCED NEAR-INFRARED PHOTOLUMINESCENCE OF SINGLE-WALLED CARBON NANOTUBES TREATED WITH POLYUNSATURATED FATTY ACIDS

3.1 CHAPTER PREFACE

In this chapter, we demonstrate that polyunsaturated fatty acids (PUFAs) undergo a chemical reaction with single-walled carbon nanotubes (SWCNTs) under certain conditions. Our photochemical reaction produces functionalized SWCNTs that have a downshifted near-infrared emission and suppress the intrinsic bandgap emission from pristine SWCNTs. Our data demonstrate that PUFAs and phospholipids can react with SWCNTs, raising concern for carbon nanotubes safety in vivo.

The material contained within Chapter 3.1 was published as an original research paper in the journal, *Journal of the American Chemical Society*, and the figures have been reproduced with permission from Ref ²²³.

List of Authors: C. F. Chiu, W. A. Saidi, V. E. Kagan, and A. Star

3.1.1 Introduction

Since its discovery in 2002, the bandgap luminescence of single-walled carbon nanotubes (SWCNTs) has been an important analytical tool for characterizing semiconducting SWCNTs.^{5,56} SWCNT species of specific diameters and chiralities have distinct first (E_{11}), second (E_{22}), and third (E_{33}) excitonic transitions, allowing for their relative concentrations to be correlated from their emission intensities using an excitation–emission map (EE map).⁵ The photoemission properties of SWCNTs have been investigated for applications in cancer diagnostics,^{224,225} cell recognition,^{138,225} and chemical sensing.^{226,227} The bandgap luminescence is often quenched by the surrounding environment and chemical reactions,^{206,228,229} in many cases making SWCNTs a turn-off sensor, thereby limiting its dynamic range.

A new SWCNTs emission band has been reported in recent years. Named E_{11}^- , or E_{11}^* , this emission band has a turn-on mechanism that requires activation by a small degree of functionalization.^{111–113} This “defect-induced” activation has been achieved by ozone,¹¹¹ diazonium,¹¹² alkylcarboxylation,¹¹³ hydrogen peroxide,¹⁰⁸ and other oxidants. Matsuda et al. compared the oxygen- and diazonium-based defects with respect to the E_{11}^- bands they produced. The researchers have concluded that the local electronic states generated from the defects are nearly independent of the origin.¹¹⁴ Meanwhile, recent findings revealed that different functional groups on diazonium adducts could generate E_{11}^- peaks on (6,5) SWCNTs at a range of 1110 to 1148 nm.¹¹² For oxygen-based defects, Ghosh et al. deduced the product of their ozone-functionalized SWCNTs to be ethers perpendicular to nanotube axis (ether-perpendicular) rather than epoxides.¹¹¹ This ether-related E_{11}^- peak was reported at 1120 nm on a (6,5) SWCNT.¹¹¹ Ma et al. demonstrated that different oxygen functional groups on (6,5) SWCNTs

could generate different emission peaks, with ether-perpendicular and epoxide causing peaks downshifted from the E_{11} band gap by ~ 135 (at 1115 nm) and 310 meV (at 1250 nm), respectively.²³⁰ This E_{11}^- peak could be utilized in a turn-on sensor as opposed to the bandgap-based turn-off sensors. A recent utilization of this defect-induced peak was demonstrated by Wang and co-workers as a pH sensor and nanothermometer.¹¹⁶

Lipids, especially those containing polyunsaturated fatty acids (PUFAs), can be oxidized to form lipid hydroperoxides.^{231–234} The resulting peroxides can damage cell membranes, resulting in cell death, and could be mutagenic and carcinogenic.²³⁵ Enzymatic oxidation, by lipoxygenases, is also important in cell signaling.²³⁶ We have previously functionalized SWCNTs with phospholipids, particularly phosphatidylserine, to make them recognizable by different phagocytic cells.⁶⁷ We have also reported that SWCNTs selectively adsorbed two types of the most abundant surfactant phospholipids: phosphatidylcholines (PC) and phosphatidylglycerols (PG).²¹⁸

In this work, we investigated photoluminescence (PL) emission of lipid-coated SWCNTs and observed the decrease in their E_{11} signal and formation of a new E_{11}^- emission under illumination conditions. In addition to PL spectroscopy, the nanotube samples were studied using Raman, X-ray photoelectron spectroscopy (XPS), diffuse reflectance infrared Fourier transform spectroscopy (DRIFTS), and density functional theory (DFT) calculations. Our results suggest that lipid hydroperoxides react with the sidewalls of SWCNTs and form oxygen-containing defects.

3.1.2 Result

Figure 38 shows EE maps of (6,5) purified high-pressure carbon monoxide (HiPco) SWCNTs before and after reaction with linoleic acid (LA, C18:2) under illumination at 566 nm. A typical bandgap luminescence from the (6,5) SWCNTs (E_{11}) was observed before the reaction (Figure 38a) and a new E_{11}^- peak, centered at ~ 1120 nm, dominated the EE map after the reaction (Figure 38b). Figure 38c shows the spectral changes during the reaction, revealing the decrease in the bandgap emission (E_{11}) and the increase in the defect-induced peak (E_{11}^-) over a reaction time of 60 min. Figure 38d compares the UV-vis-NIR absorption of LA/SWCNTs with linoleic acid. Linoleic acid autoxidizes in air via a free radical chain reaction and forms linoleic acid hydroperoxide (LA-OOH), which gives a characteristic absorption at 235 nm due to the conjugated diene structure.^{231–233} The shrinkage of this peak after reaction with SWCNTs indicates that LA-OOH was consumed in the process. The vis-NIR portion of the spectra also shows that bandgap absorptions of the SWCNTs, E_{11} and E_{22} , remain essentially unchanged after the reaction. The spectral changes in PL emission and UV-vis-NIR absorption are analogous to those observed during alkylcarboxylation and UV-ozone treatments.^{111,113} The reaction between LA and SWCNTs was not specific to HiPco SWCNTs, as cobalt-molybdenum-catalyzed (CoMoCAT) SWCNTs also provided similar results (Figure 60 in Appendix C). Figure 38e shows the changes of emission intensity of E_{11} and E_{11}^- peaks of CoMoCAT SWCNTs over a reaction time of 6 h. The E_{11} emission decreased in the first 30 min of the reaction, whereas the E_{11}^- intensity increased to a maximum after 60 min and then subsequently decreased. The decline in the E_{11}^- peak was previously demonstrated by Wang and co-workers with diazonium functionalization.¹¹² The maximum emission at 1120 nm was reached by achieving optimal

defect density on the SWCNTs, with further reaction resulting in overfunctionalization of SWCNTs with excess defects, and diminishing the E_{11}^- emission.

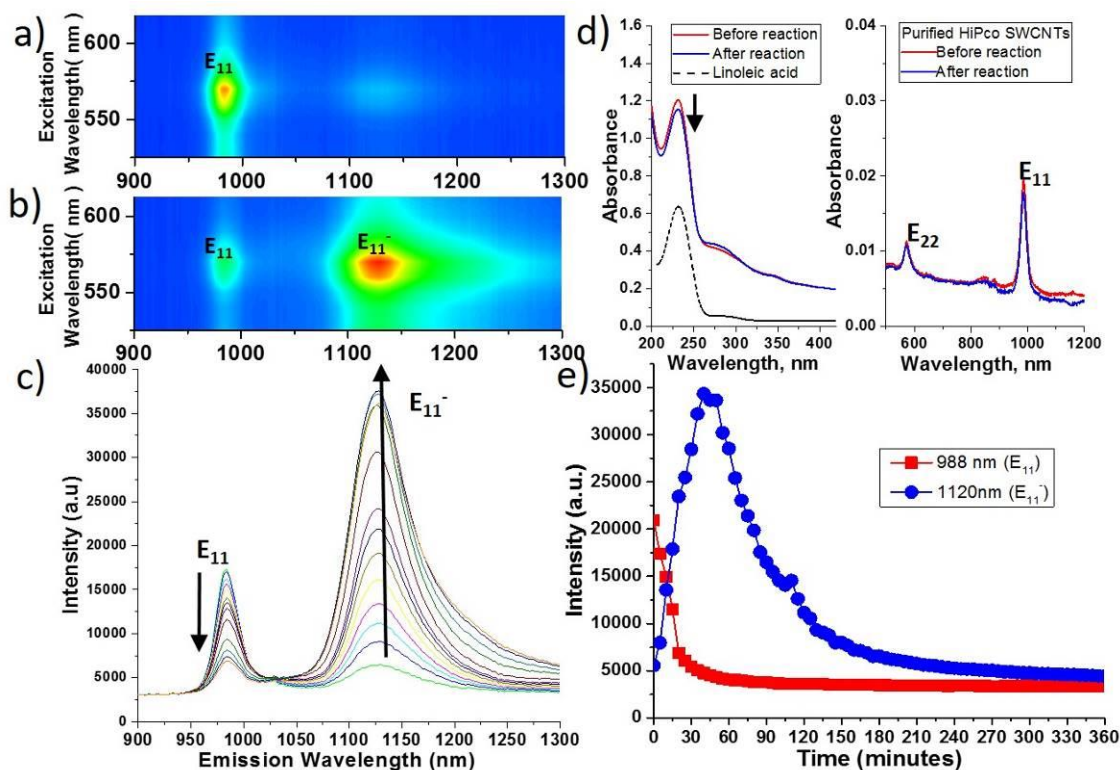


Figure 38. EE maps of (6,5) purified HiPco SWCNTs (a) before and (b) after reaction with linoleic acid. (c) Spectral changes over 60 min (spectra taken every 5 min). (d) UV-vis absorption spectra showing the presence of lipid hydroperoxide (235 nm) and its concentration decreasing after reaction with SWCNTs. SWCNTs vis-NIR absorptions were unshifted. (e) Emission intensities of E_{11}^- and E_{11} of CoMoCAT SWCNTs reacted with linoleic acid over 6 h.

To ensure the effects were caused by the reaction between LA-OOH and SWCNTs, different control experiments were conducted. Figure 61a (in Appendix C) shows the spectral changes with LA and SWCNTs in the absence of surfactant. The E_{11}^- peak was still clearly observable after the reaction despite the low signal level due to the poor dispersibility of pristine SWCNTs. SWCNT/sodium cholate (SC) produced a stable suspension with a non-photobleachable E_{11} photoluminescence, as documented in the literature,²²⁶ and no evolution of

the E_{11}^- band (Figure 61b). Sodium cholate/linoleic acid did not produce any NIR emission signal, as there were no NIR emitters in the solution (Figure 61c). To demonstrate that linoleic acid hydroperoxide was responsible for functionalizing the SWCNTs, a sample of linoleic acid was pretreated with morin to inhibit the LA-OOH formation via terminating the radical chain reactions.²³³ When SWCNTs were exposed to this pretreated linoleic acid, no enhancement in E_{11}^- emission was observed (Figure 61d). This is in agreement with our observation from Figure 38d, in which LA-OOH was consumed in the reaction process. From these control experiments, we conclude that the E_{11}^- peak was induced by photoinitiated reaction between LA-OOH and SWCNTs, and sodium cholate was merely acting as a surfactant, which improves the dispersibility of SWCNTs thus enhancing the emission signals.

The roles of surfactant type and concentration were investigated, and the results are summarized in Table 5. CoMoCAT SWCNTs were dispersed in sodium cholate (SC), sodium dodecyl sulfate (SDS), or sodium dodecylbenzenesulfonate (SDBS) at 0.1 and 1 wt % surfactant concentration, and reacted with linoleic acid. Emission spectra were collected before and after 1 h of reaction time, and the changes of E_{11}^- intensities are reported in Table 5. Using SC or SDS at 0.1% concentration, the E_{11}^- peak formation is apparent (Figure 62). The reaction is slower at higher surfactant concentrations. Better shielding effect is expected at higher concentrations, as the increase in surfactant density provided better coverage of nanotube surface, suggesting that the photochemical reaction between LA-OOH and SWCNTs was a surface event. Interestingly, the E_{11}^- formation reaction is inefficient when SDBS was used.

Table 5. Reaction Progression (ΔE_{11^-} Intensity) with Different Surfactants at Two Concentrations*

surfactant	concentration	
	0.1 %	1.0 %
sodium cholate (SC)	14975	-160
sodium dodecyl sulfate (SDS)	15506	578
sodium dodecylbenzenesulfonate (SDBS)	1015	-257

$$* \Delta E_{11^-} = (E_{11^-})_{\text{final}} - (E_{11^-})_{\text{initial}}$$

We investigated the effect of illumination wavelength on the reaction (Figure 39a). The emission spectra were analyzed using 566 nm wavelength before and after illumination at various wavelengths (235, 366, 466, 566, and 666 nm) for 60 min. The normalized E_{11^-} intensities were calculated using the changes of the defect-induced (E_{11^-}) emission peaks corrected by the photon flux of the wavelength used.²³⁷ The resulting values were normalized to the highest value for simplicity and are available in Table 8 in Appendix C. The normalized E_{11^-} intensities here were not normalized to the absorption of the SWCNTs and therefore should not be interpreted as the quantum yield of the reaction. We observed the furthest progression with 566 nm illumination, the wavelength which matches the absorption (E_{22} transition) band of (6,5) SWCNTs. This result suggests that the mechanism of the reaction involves the excited state of the SWCNTs, but not the excited state of lipid hydroperoxide as demonstrated by the lack of E_{11^-} formation at 235 nm excitation.

To further investigate the photochemical nature of the reaction between LA and SWCNTs, the samples were stored in the dark for 3 days, before being illuminated with 566 nm light for 1 h (Figure 39b). When the samples were stored in the dark, no evolution of the E_{11^-} peak was observed. The same solutions were subsequently activated by excitation with 566 nm light, showing E_{11^-} progression dependent on LA-OOH concentration. From our data, we calculated that the minimum ratio required is ~5 nmol of LA-OOH : 0.01 mg of SWCNTs. At

lower ratios, the spectral difference was not significant. We expect this ratio is efficient for in vivo detection of lipid hydroperoxide, though this is beyond the scope of this paper.

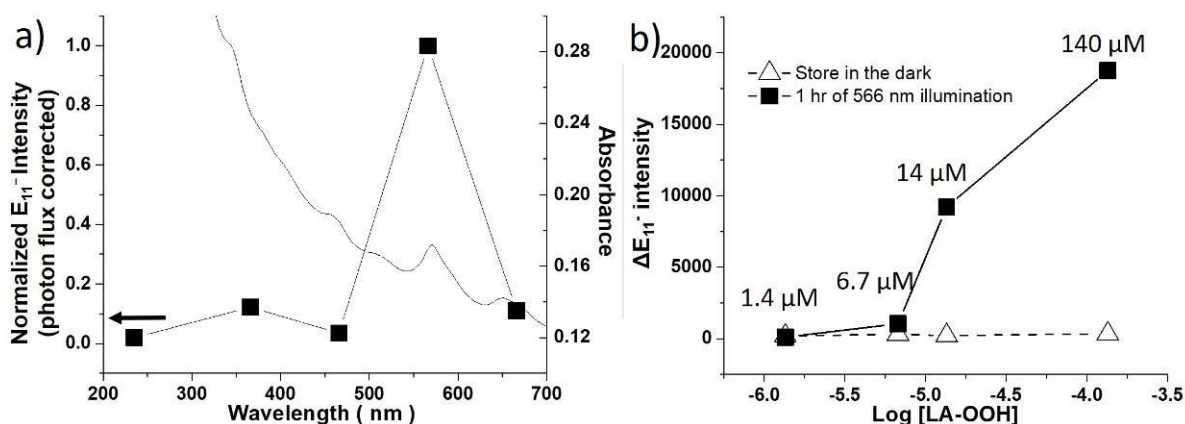


Figure 39 (a) Normalized E_{11}^- intensities of the reaction illuminated at different wavelengths (235, 366, 466, 566, and 666 nm). All data points were collected with 566 nm excitation and efficiency was corrected to photon flux. UV-vis absorption of SWCNTs suspension is shown on the right axis. (b) Effect of LA-OOH concentration on the SWCNT NIR emission. Samples were stored in the dark for 3 days and then activated with 566 nm illumination for 1 h.

The observed results are comparable to other defect-induced luminescence examples reported in the literature.¹¹¹⁻¹¹³ In all cases, the new E_{11}^- peaks were attributed to defects on the SWCNT sidewalls. Product analysis was performed on SWCNT samples reacted with linoleic acid for 6 h for a better signal response. Nanotube defect formation was confirmed by Raman spectroscopy. Figure 40a shows the Raman spectra of SWCNTs with a small increase of D/G ratio from 0.13 to 0.27 after the reaction, indicating a slight increase in defect density.

SWCNT samples were further analyzed using XPS and DRIFTS. Figure 40b shows low-resolution, or survey, XPS spectra and the high-resolution spectra of the oxygen peak. From the survey spectra, it is clear that SWCNTs were oxidized upon LA reaction as illustrated by the increase of the carbon:oxygen ratio from 1.00:0.10 to 1.00:0.32. High-resolution peaks were deconvoluted and showed an increase in C–O (~532 eV) in comparison to C=O (~531 eV) in the

oxygen spectra (Figure 40c).^{238–240} The increase of C–O bonding is also observed in the carbon spectra (Figure 63) and can be attributed to hydroxyl or ether bonds.^{230,240} The presence of nitrogen, silicon and chlorine in XPS survey might come from contaminants, which also explain the abnormally high content of oxygen. However, the increase of D/G ratio should not be affected by any non-graphitic contents and the increase of C–O bondings can also be detected by DRIFTS.

Figure 40d shows the DRIFTS spectra of LA/SWCNTs with and without light activation. The two samples showed similar intensities in hydroxyl (O–H) and alkyl (C–H) bonding. The major difference is at 1000–1200 cm^{-1} , attributed to ether (C–O–C) or hydroxyl (O–H) bonds.^{188,241} However, the hydroxyl band does not change significantly in the $\sim 3400 \text{ cm}^{-1}$ region, implying that the density of O–H groups does not increase on the CNT surface. Therefore, assignment of the $\sim 1100 \text{ cm}^{-1}$ band to ether or epoxide group (C–O–C) is more dependable.

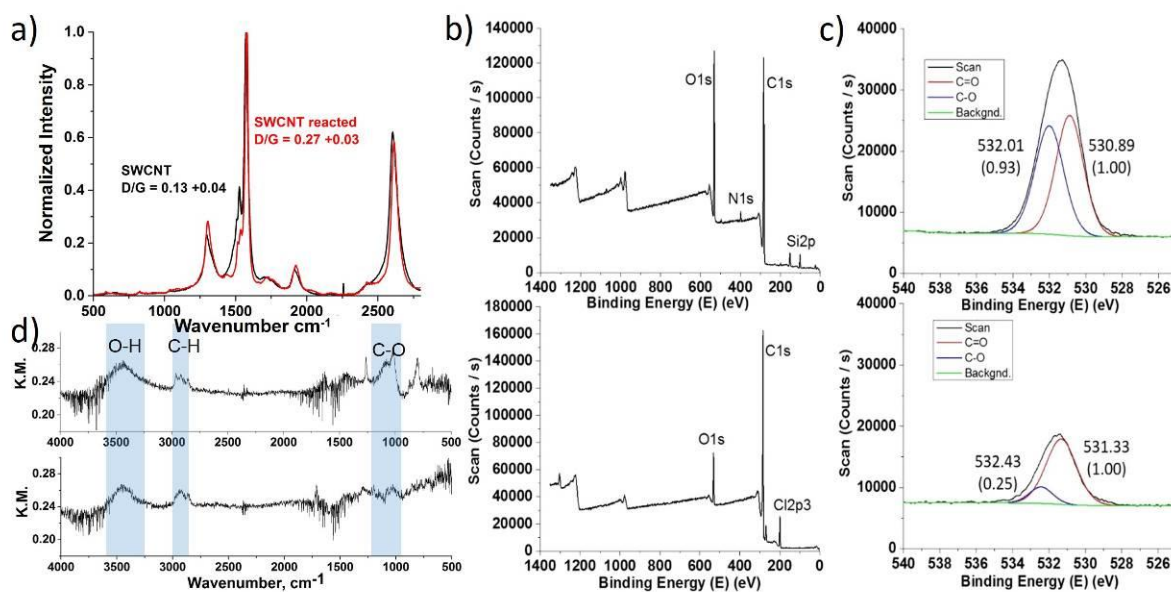


Figure 40. (a) Raman, (b) XPS survey and (c) high-resolution spectra of the oxygen peak. (d) DRIFTS spectra of LA-OOH/SWCNTs after (top) and before (bottom) illumination.

We further investigated the electronic structure of oxidized (6,5) SWCNTs using DFT calculations by examining different oxidizing agents namely, O, O₂ and O₃. For the oxygen-doped CNT, we find that the most favorable adsorption configuration is at the bridge site on a carbon bond that is nearly perpendicular to the tube axis. In this configuration, the C–C bond at which oxygen is adsorbed increases to 2.08 Å from its original length of 1.43 Å for the undoped CNT. Further, the C–O bond is nearly 1.39 Å. We will refer to this configuration as ether-perpendicular. The second most favorable adsorption site is the bridge site that is parallel to the tube axis with a binding energy that is nearly 1 eV higher than ether-perpendicular. We will refer to this configuration as epoxide-parallel as oxygen with the two carbon atoms that it bonds to form nearly an equilateral triangle (C–C bond is 1.52 Å, and C–O bond is 1.46 Å). These results are consistent with references.^{111,230} For O₂-doped CNT, we find that energetically it is nearly the same whether O₂ bonds to the two carbon atoms that are nearly parallel or perpendicular to the CNT tube axis. For O₃-doped CNT, we find that the ozone molecule can be stabilized only by bonding to C–C that is perpendicular to the tube axis.

The oxidation of the CNTs introduces new adsorption bands as can be seen from Table 6 and Figure 64. For ether-perpendicular configuration, the new absorption band E_{11}^- is located nearly ~200 meV lower in energy than that of the bright exciton E_{11} band of the pristine CNT. This is consistent with the results of Ma et al. where this model was investigated using B3LYP.²³⁰ In our calculations, we noticed that the exciton peaks at the B3LYP level are lower in energy than those at the CAM-B3LYP level.

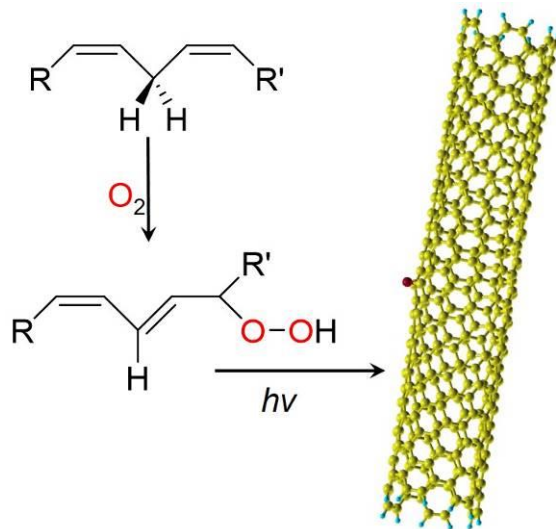
Table 6. Computation of Electronic Properties of Undoped and Oxygen-Doped (6,5) SWCNTs

	exciton peak (eV)	shifts (eV)
pristine CNT	2.180	-
ether-perpendicular	2.000	-0.180
epoxide-parallel	1.696	-0.484
O ₂ -parallel	1.906	-0.274
O ₂ -perpendicular	1.557	-0.622
O ₃ -perpendicular	1.877	-0.303

The functionalization reaction between SWCNTs and linoleic acid reported here can also be observed with other PUFAs and lipids. Figures 65 and 66 show the spectral changes of SWCNTs with γ -linolenic acid (18:3) and cardiolipin (18:2). The decrease in E_{11} and increase in E_{11}^- were observed in both cases. Saturated stearic acid (18:0) and stearyl-cardiolipin (14:0), on the other hand, did not produce any spectral changes. These results demonstrated that the reaction reported here requires unsaturated fatty acids/lipids and cannot be repeated with saturated ones. This is in agreement with our proposed mechanism that involves the formation of lipid hydroperoxides.

3.1.3 Discussion

Scheme 1. Proposed Reaction between Polyunsaturated Fatty Acids/Lipids and SWCNTs



Scheme 1 summarizes the photochemical reaction between SWCNT and linoleic acid reported in this work. Linoleic acid autoxidizes through radical chain reactions to form linoleic acid hydroperoxide.^{231–233} The linoleic acid hydroperoxide further reacts with photoexcited SWCNTs, forming ether defects on the nanotube surface.

The autoxidation of PUFAs is well documented in the literature and involves radical chain reaction to produce lipid hydroperoxide with conjugated diene structure.^{231–233} Our UV-vis-NIR absorption spectra reveal the characteristic 235 nm peak of lipid hydroperoxides and its reduction upon reaction with SWCNTs (Figure 38d). Using morin as an antioxidant to terminate the radical chain reaction,^{232,233} we have further demonstrated (Figure 61d) that the restricted formation of lipid hydroperoxide could limit the SWCNTs functionalization.

The photoreaction between linoleic acid hydroperoxide and SWCNTs is expected to take place on the nanotube surface as demonstrated by experiments with different surfactants (Table 5). The hydrophobic ends of fatty acids can interact with the hydrophobic surface of the

SWCNTs in a way similar to SDS. At higher surfactant concentrations, the SWCNTs are better protected by higher surfactant density, and hence E_{11}^- formations were less profound. Moreover, we speculate that the different result for SDS and SDBS was due to the different SWCNT surface coverage, in which SDBS arranged parallel to the nanotube surface to maximize π - π stacking and provided better shielding from oxidation.

Lipid hydroperoxides can be decomposed into peroxy radicals and alkoxy radicals.²⁴² The decomposition of lipid hydroperoxides can be catalyzed by transition metals, which pristine SWCNTs contain as residual catalysts from nanotube synthesis. The fact that the reaction can proceed with both CoMoCAT and HiPco SWCNTs suggests that metal catalyst should not be the factor, as the two SWCNTs contain different metals but give similar results. We further dismiss the effect of metal ions by adding diethylenetriaminepentaacetic acid (DTPA) to the reaction as a metal chelator (Figure 67).²⁴³ E_{11}^- emission from LA/SWCNTs was detected in the presence of DTPA, suggesting that the effect of metal is minimal. It is possible that excitons on SWCNTs are catalyzing the decomposition of lipid hydroperoxides like free electrons in metal. A similar argument was proposed by Wang and co-workers, in which the oxidation potential of SWCNTs was raised by the excited electrons.²³⁷ Such pathway might produce radicals that functionalized SWCNTs regardless of the presence of metal. To test this hypothesis, antioxidants were added to SWCNTs before subjected to linoleic acid hydroperoxide. In the presence of antioxidants, the E_{11}^- emission from SWCNTs was not observed, suggesting that the functionalization reaction might undergo via radical formation (Figure 68). Upon reaction, the linoleic acid hydroperoxide is expected to be reduced to form hydroxylated linoleic acid and other associated products, including 2-hydroxyheptanal and 4-hydroxy-2-nonenal (HNE).^{232,244,245} The results suggest that lipid peroxidation process, typically catalyzed in vivo by iron-containing enzymes and monitored

using chemiluminescence schemes, can be facilitated by SWCNTs, where their NIR fluorescence can be used to study the lipid peroxidation.

In principle, the oxidation of SWCNTs by LA-OOH could result in an addition of oxygen functional groups on the nanotubes (e.g., hydroxyl, ether, and epoxide) or the covalent grafting of fatty acid to SWCNTs through ether bonding (SWCNT-O-LA). The attachment of linoleic acid to SWCNT should generate a carboxyl signal in the HRXPS at ~ 534 eV in oxygen band²³⁸ and ~ 289 eV in the carbon band.²³⁹ The absence of these peaks suggests that the attachment of linoleic acid to SWCNTs is unlikely. Similar conclusions can be drawn from the DRIFTS spectra. The signature O-H bonds (3400 cm^{-1}) and carbonyl bonds (1700 cm^{-1}) from carboxyl groups were not detected. Instead, an increase at $1000\text{-}1300\text{ cm}^{-1}$ from C-O bonds was observed. Although there is a small peak at 2968 cm^{-1} and moderate ones at 1262 and 805 cm^{-1} , which can all be assigned to C-H bonding, their changes were relatively small compared to the C-O bonding.

Although HRXPS and DRIFTS can refute the grafting of linoleic acid on CNT surface, these techniques do not directly reveal the chemical identity of the functional groups. The observed increase in C-O bonding can be related to different oxygen-containing functional groups. In determining the origin of these induced defects, we compared the observed E_{11}^- peak with values calculated by DFT and previously reported by Ma et al.²³⁰ Our E_{11}^- peak, downshifted by 130 meV from the E_{11} bandgap, matches closely with the calculated and previously reported values for ether-perpendicular. This is also in agreement with earlier work by Ghosh et al., who associated ether functional groups perpendicular to the tube axis with their observed E_{11}^- emission from ozonation.¹¹¹ In our work, a radical reaction might involve the addition of OH or fatty acid, yet neither of them was detected in our characterization. The

formation of epoxide should generate a defect-induced peak at ~1250 nm in the emission spectrum, which was not detected in this work.²³⁰ Based on the position of the E_{11}^- peak at 1120 nm, assigning the functional group to ether is more dependable.²³⁰ The assignment of this defect-induced band to ether groups might also explain the low emission intensity at 1120 nm before the reaction. It was shown in the literature that as-produced SWCNTs contain defects,¹⁰⁵ some of which are oxygen moieties.²⁴⁶ A noticeable C-O bonding in the oxygen HRXPS from our starting SWCNTs could be evidence of a small amount of ether defects.

Our data from Figure 39 have shown that the reaction is photochemical. Additional experiments were conducted to show that reaction can be stopped and product harvested for doping purposes. SWCNTs/LA-OOH reaction can be ceased by removing the sample from light. A reacted sample was withdrawn from the illumination and stored in the dark for 7 days and showed similar spectral features before and after storage (Figure 69a,b). To illustrate the isolation of reacted SWCNTs, another sample was treated with LA-OOH (Figure 69c) and dialyzed overnight to remove surfactants and linoleic acid. The isolated SWCNTs were redispersed in bovine serum albumin and showed a similar emission profile before and after the isolation (Figure 69d).

Although our data indicate that the reaction has a higher efficiency when excited at a wavelength in resonance with the SWCNT bandgap, the reaction can be initiated using white light. SWCNTs were sonicated with linoleic acid under normal laboratory lighting condition, and the development of E_{11}^- band was observed (Figure 70 in Appendix C). The finding here is important when considering SWCNT-unsaturated fatty acid/liposome complexes prepared in the laboratory.⁸² We recommend that SWCNT-liposome complex be prepared in a dark and oxygen-free environment to prevent undesired CNT oxidation. While all our data point to a

photochemical reaction, we cannot rule out the possibility that the PUFA-SWCNTs reaction can proceed without light at an extremely slow rate and was only made possible to detect by excitation enhancement. As recently demonstrated by Wang et al., the reaction rate between SWCNTs and diazonium salts was enhanced by resonant light at nanotube E₂₂, E₃₃, and E₄₄ transitions.²³⁷ Such an effect at the E₃₃ transition was not observed in our work. We attribute this to the low absorbance at E₃₃ in our sample and the insufficient excitation at this wavelength due to low power density.

3.1.4 Conclusion

We demonstrate that PUFAs can oxidize SWCNTs under ambient conditions. We attribute this new reaction to the autoxidation of PUFAs capable of forming lipid hydroperoxides resulting in the formation of ether functional groups on the sidewall of SWCNTs. The reaction is photochemical and is more efficient when the illuminating light matches the resonance wavelength of the nanotubes. More importantly, the functionalization dramatically changes the optical and electronic properties of the SWCNTs, resulting in a new E₁₁⁻ band emission. Our data also suggest that the photoexcited nanotube surface might be catalyzing the decomposition of lipid hydroperoxide. These findings, in addition to providing a new understanding of SWCNT-lipid interactions, can be potentially used for in vivo lipid peroxidation detection.

3.1.5 Experimental

Linoleic acid (Sigma L1376) was autoxidized in air. The concentration of lipid hydroperoxide produced was determined by UV-vis absorption at 235 nm at which the linoleic acid

hydroperoxide (LA-OOH) has a molar attenuation coefficient of $25000 \text{ L mol}^{-1} \text{ cm}^{-1}$.^{231,236}

Morin and ascorbic acid were purchased from Sigma-Aldrich.

Purified high-pressure carbon monoxide (HiPco) produced SWCNTs with (6,5) chirality was obtained from Atom NanoElectronics. Cobalt-molybdenum-catalyzed (CoMoCAT) single-walled (6,5) carbon nanotubes were purchased from Sigma-Aldrich (Lot # MKBG5771V). SWCNT suspension was prepared at 0.02 mg/mL concentration with 0.1 wt % sodium cholate (SC, Sigma-Aldrich) as a surfactant unless otherwise stated. The HiPco SWCNTs stock solution was dispersed in 2 wt % mixture of SC and SDS and was diluted 10 times before use. The suspension was sonicated for 1 h and centrifuged to remove large bundles. The top 90% of the supernatant was transferred to a separate container and used as stock. Sodium dodecyl sulfate (SDS) and sodium dodecylbenzenesulfonate (SDBS) were purchased from Sigma-Aldrich and used without further purification. The SWCNT supernatant (500 μL) was exposed to 1.4–140 μM of linoleic acid hydroperoxide. Samples were illuminated with 566 nm light for 60 min unless stated otherwise. Emission spectra were obtained every 5 min during this period. Excitation–emission maps (EE maps) and absorption spectra were obtained both before and after the reaction.

Photoluminescence measurements were obtained using a Nanolog spectrofluorometer (HORIBA Jobin Yvon) equipped with a xenon lamp (400 W) light source, double excitation monochromators, and Symphony II InGaAs array (NIR) detector. For the EE maps, the excitation wavelength was scanned from 300 to 800 nm in 5 nm increments, and the emission was detected between 820 to 1580 nm with 1.5 nm increments. Spectra were obtained using 566 nm excitation wavelength, which is in resonance with the second absorption band of the (6,5) SWCNTs. Slit widths were set at 10 nm for both excitation and emission. All measurements

were obtained with an 830 nm long-pass filter at ambient temperature. Power density was measured independently with an optical power meter (Thorlabs PM200) and detector (Thorlabs S120VC). The power density at 566 nm was 7.49 mW/cm². Power densities at other wavelengths are available in Table 8.

UV–vis–NIR measurements were acquired using a PerkinElmer Lambda 900 spectrophotometer over the wavelength range of 200–1200 nm.

Raman measurements were performed using a XploRA plus Raman microscope with a 532 nm laser (HORIBA). SWCNTs were drop-cast on a glass slide and allowed to dry under ambient conditions overnight, thereby forming aggregates of SWCNTs. Scans were carried out at a laser power of 2.5 mW with an accumulation time of 15 s over the range from 200 to 3200 cm⁻¹. Spectra were acquired from multiple locations, and the results were normalized to the most intense peak. D/G ratios were calculated by integrating the area under the peaks.

X-ray photoelectron spectroscopy (XPS) was performed on a Thermo Scientific ESCALAB 250xi spectrometer using monochromated Al K α X-rays as the source. SWCNTs were reacted with LA-OOH for ~6 h to increase the defect density for a better signal response. Samples were collected from multiple runs to obtain the amount required for XPS analysis. The SWCNT samples were dialyzed with 1 kD membrane (Spectra/Por 7 MWCO) for 3 days to remove the surfactant and linoleic acid. The aggregated SWCNTs were collected in water and solvent-extracted using ethyl acetate. Samples in ethyl acetate were drop-cast on a glass slide and dried at 60 °C in vacuum for 6 h prior to measurements.

Diffuse-reflectance Infrared Fourier transform spectroscopy (DRIFTS) was performed employing an IR-Prestige spectrophotometer (Shimadzu Scientific) outfitted with an EasiDiff accessory (Pike Technologies). Samples were mixed with KBr and vacuum-dried for 3 h prior to

measurement. Spectra were averaged from 160 scans per sample over the range of 500–4000 cm^{-1} with a resolution of 2 cm^{-1} . Kubelka–Munk conversion was applied.

DFT calculations were performed using FHI-aims²⁴⁷ and Gaussian 09 program.²⁴⁸ The (6,5) CNT was modeled using a cluster model with one repeat unit of the primitive unitcell with 386 atoms, amounting to a tube segment with a length of ~ 40 Å. The carbon atoms at both ends were replaced with hydrogen to eliminate the dangling bonds and any spurious end-effects such as having edge-states. This approach has been applied in several studies.^{230,249–251} The CNT oxidation was carried out using atomic oxygen, O_2 , and O_3 where the functionalization is done in the middle of the group to avoid spurious edge state effects. The optimum structures of the CNTs were obtained by relaxing the atomic position of all atoms using a convergence threshold of 0.01 eV/Å. For this, we used PBE as implemented in FHI-aims using a tier-1 basis set. Using the optimum structures, the excited states and the absorption spectra of the pristine and functionalized CNTs were investigated CAM-BLYP functional.²⁵² The CAM-B3LYP is a hybrid long-range order corrected functional, which in particular improves the description of charge-transfer states. For comparison with previous study by Ma et al.,²³⁰ we also computed the absorption spectra profile using B3LYP. All of our calculations were done using STO-3G consistent with previous studies.

4.0 STATISTIC AND REPRODUCIBILITY

Experiments were done in triplicate whenever possible. Due to the complexity of the three dimension EE maps, only one set of data is presented at a time. Many of these repeated data are available in the Appendix. Neutrophil study was not repeated due to the short lifespan of the isolated neutrophils.

For Raman spectroscopy, the spectra were averaged from at least 5 different spots on the samples. Length distribution from TEM was calculated from ~100 measurements. Modified Boehm's titration were done in triplicate. Linoleic acid reaction on SWCNTs were reproduced with SWCNTs from two different sources (HiPco and CoMoCAT). XPS were averaged from multiple slots on the sample. DRIFTS spectra were averaged from 160 scans per sample.

5.0 OUTLOOK AND FUTURE DIRECTIONS

5.1 CHAPTER PREFACE

In this concluding chapter, an outlook of the current field including real-time SWCNTs imaging will be explored. This technique is intriguing for *in vivo* imaging and can be applied for immunity system study from Chapter 2.3 and fatty acid reactions from Chapter 3.1. Furthermore, thin film SWCNT luminescence for chemical detection is summarized in Section 4.1.2.

5.1.1 Real Time in vivo Imaging of SWCNTs

In a recent study, Lefebvre has demonstrated a hyperspectroscopy method for SWCNT imaging.²⁵³ The method utilized a supercontinuum (SC) light source that produces light from 450 to 2100 nm. The beam is filtered to remove unwanted infrared wavelengths and focused to well-defined slit illumination with each point along the slit becomes one excitation wavelength. This new method speeds up the time required to obtain individual EE maps from minutes to subsecond time scales. Dopant-induced quenching presents a simple dependence on nanotube diameter, similar to what is presented in Chapter 2.3 with a much faster acquisition time.

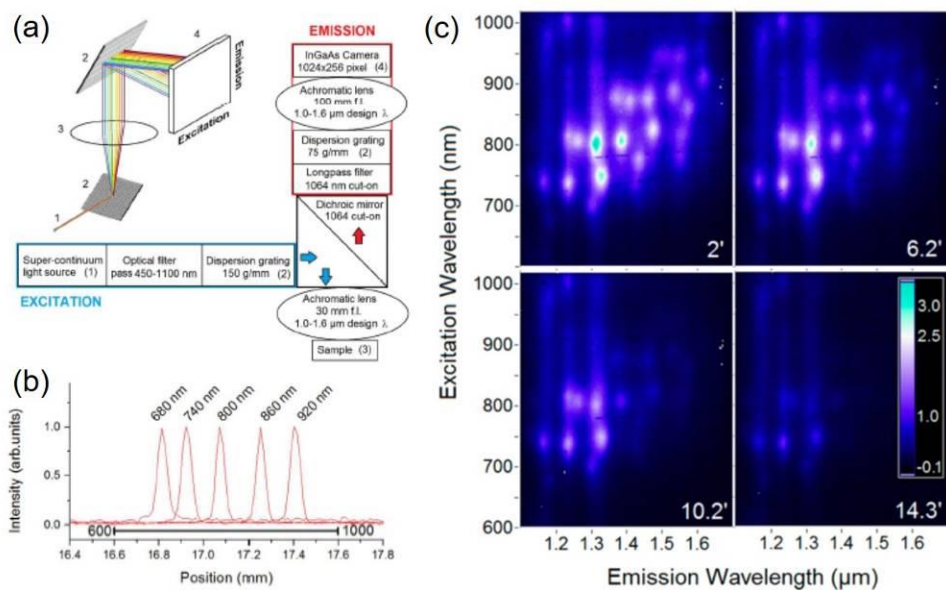


Figure 41. (a) Schematic of the hyperspectroscopy method using supercontinuum light source. (b) Spatial extent of the excitation source at the sample focus. The 600-1000 nm excitation range covers a 1 mm width. (c) Four PLE maps taken from a time series, where F4-TCNQ is successively added to a SWCNT dispersion after 2, 6, 10, and 14 min. Integration time was 200 ms, averaged over four frames. (Reproduced with permission from Ref 253. © 2016 American Chemical Society)

This method is different from other real-time imaging technique in that the various excitation wavelengths were applied to the sample and a full-scale EE map of the SWCNTs can be collected.¹³⁶ If the technique were adapted to in vivo imaging, it would be beneficial for an in vivo animal imaging extension of Chapter 2.3, or any similar diameter/chirality dependent SWCNTs reactions.

For the in vivo study of PUFAs induced functionalization of carbon nanotubes (extension to Chapter 3.1), current imaging technique with a single excitation wavelength is capable of real-time imaging as both E_{11} and E_{11}^- shares the same excitation wavelength at 566 nm. The two emissions can be detected using a 2D InGaAs array and spectrum to be obtained.¹³⁶ The limitation is that the 566 nm excitation wavelength is out of the near-infrared window in biological tissue and cannot penetrate deeply.²² The E_{11}^- functionalization can be extended to SWCNTs with larger diameters that have their bandgap transition within the biological window. SWCNTs with (9,4) chirality, for example, have E_{22} and E_{11} transitions at 719 nm and 1098 nm, and the expected E_{11}^- is at 1241 nm, making it more suitable for in vivo applications from the wavelength penetration perspective. A study on PUFAs functionalized SWCNTs using continuum light source is also interesting, as the reaction is photochemical to the E_{22} of the SWCNTs.

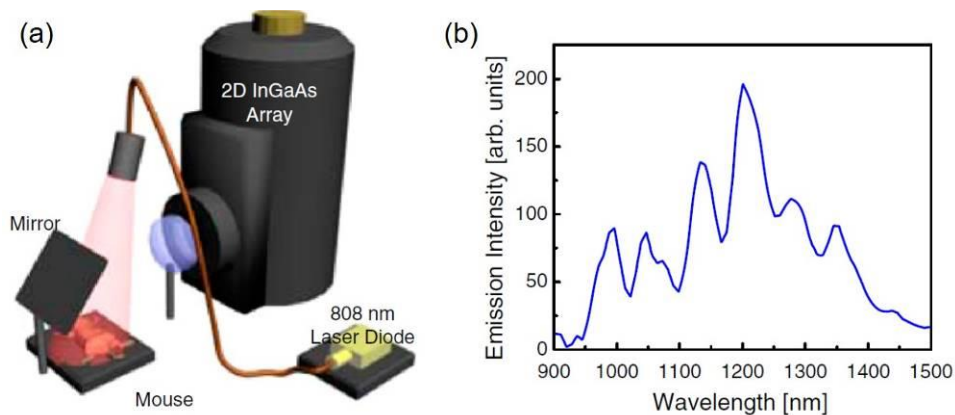


Figure 42. (a) Schematic of NIR II imaging setup. Anesthetized mice are illuminated from above with 808-nm light. NIR fluorescence (1,100–1,700 nm) is filtered and imaged onto a 2D InGaAs array. (b) Fluorescence spectrum of functionalized SWNTs excited at 808 nm showing several emission peaks. (Adapted from Ref 136. © 2011 National Academy of Sciences)

5.1.2 Thin-film SWCNT Luminescence and Chemical Detection

Although most of the work in this dissertation is in solution phase, solid/thin-film SWCNT luminescence are possible and create opportunities for research for optical and sensing applications.

Htoon et al. have shown that individual SWCNT can be embedded in a SiO₂ matrix and its emission spectrum detected.²⁵⁴ A top layer of SiO₂ was deposited by electron-beam deposition, a process that induced a low concentration of oxygen dopants to the sidewalls of SWCNTs. The resulting ethers and epoxides on the CNT sidewall generate new emission peaks similar to what was reported in Chapter 3.1 but in the solid phase. The encapsulation of these oxygen-doped SWCNTs in a SiO₂ matrix can be applied to single-tube field-effect transistor structures and photonic/dielectric metamaterial waveguides.²⁵⁴

Other SWCNT thin films of interest are transparent conducting films for electronic applications²⁵⁵ and biocompatible polymers films^{256–259}. Their applications include solar cells²⁵⁵, liquid crystal displays²⁵⁵, organic light-emitting diodes²⁵⁵, scaffolds for neuron growth²⁵⁶, and chemical sensor²⁶⁰.

The optical properties of these SWCNTs thin-films have shown to be affected by their physical conditions. Stretching of the film would align the embedded nanotubes and change the angle between nanotube axis and incident light polarization, therefore affecting absorption⁷¹ and Raman spectra²⁶¹. Photoluminescence from E₁₁ bandgap transition can also be detected from SWCNT thin films.^{71,257} A recent study showed that the drying processes of CMC-SWCNTs film can shift the emission peak by ~15 nm and was attributed to the uniaxial compression strain.²⁵⁷ The strain can be released by stretching the CMC film and wetting of the CMC surface.²⁵⁷

We have been extending our research to SWCNTs thin-film. Our preliminary result shows that SWCNTs dispersed in sodium carboxymethylcellulose (CMC) have a different optical behavior in solution phase and in thin-film. Well-dispersed SWCNTs have dominating E_{22→11} transitions and these transitions were used to identify their chiralities as discussed in Section 1.3.5.1. It is commonly understood that individually dispersed SWCNTs prefer the E_{22→11} relaxation route, leading to an intense primary PL peak.⁹⁹ E_{33→11} transition is also possible from individualized SWCNTs. Chen et al studied the effect of aggregation on PL sidebands and showed bundling of SWCNTs can suppress the E_{33→11} sidebands while enhancing the effect of exciton energy transfer (EET).⁹⁹ Figure 43a and 43b show the EE maps of CMC/SWCNTs in solution and a drop-casted sample on quartz slide. The E₃₃ to E₁₁ transition is much stronger from the thin-film sample than the one in solution. The observed change is reversible and can be

achieved by dissolving the dried film in water. Our preliminary result also shows that the thin-film is sensitive to humidity. Figure 43c shows the ratio of $E_{22 \rightarrow 11}$ and $E_{33 \rightarrow 11}$ peaks at different relative humidity. Our hypothesis is that CMC-SWCNTs interaction might have limited the E_{22} or enhanced the E_{33} relaxation route. The drying process dehydrates the CMC/SWCNTs thin film and increases CMC/SWCNTs contacts. The change is reversible as the polymer swells at higher humidity. This CMC/SWCNTs ink can also produce CNT thin-film on paper, on Si/SiO₂ chip (Figure 43d), as well as freestanding substrate free thin-film (Figure 43e) with detectable PL emissions. With printed electrodes, IV curve can also be obtained from the CMC/SWCNTs thin film on Si/SiO₂ chip. This creates a new opportunity for dual sensing using optical and electrical measurements. Cellulose/CNT films had been used for NO₂ and ammonia detection by measuring the changes in conductance.²⁶⁰ Future work should include exploring the mechanism for the spectral changes and applying that to targeted analytes.

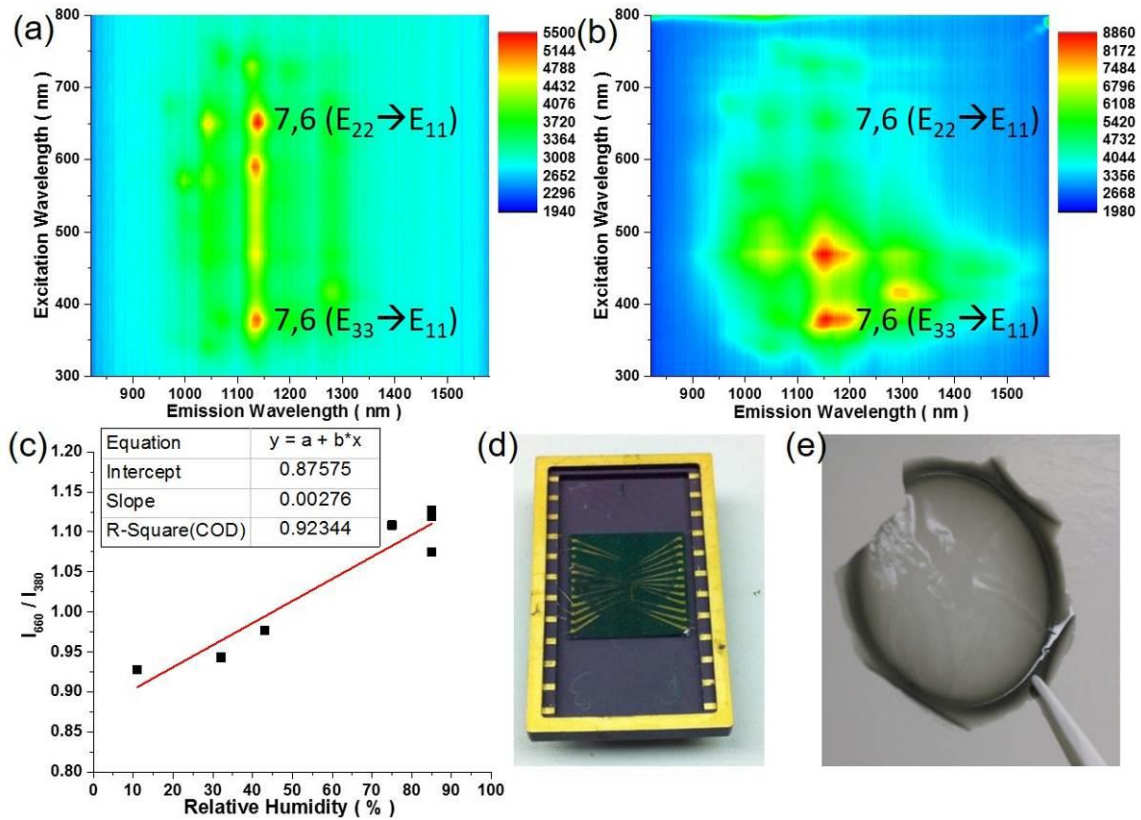


Figure 43. SWCNTs dispersed in sodium carboxymethylcellulose (a) as a solution, and (b) drop casted on quartz slide. (c) Peak ratio of $E_{22} \rightarrow E_{11}$ / $E_{33} \rightarrow E_{11}$ of (7,6) SWCNTs in CMC film exposed to different humidity. (d) CMC/SWCNTs film drop-casted on Si/SiO₂ chip with printed gold electrodes. (e) Free standing CMC/SWCNTs film.

6.0 PUBLICATIONS

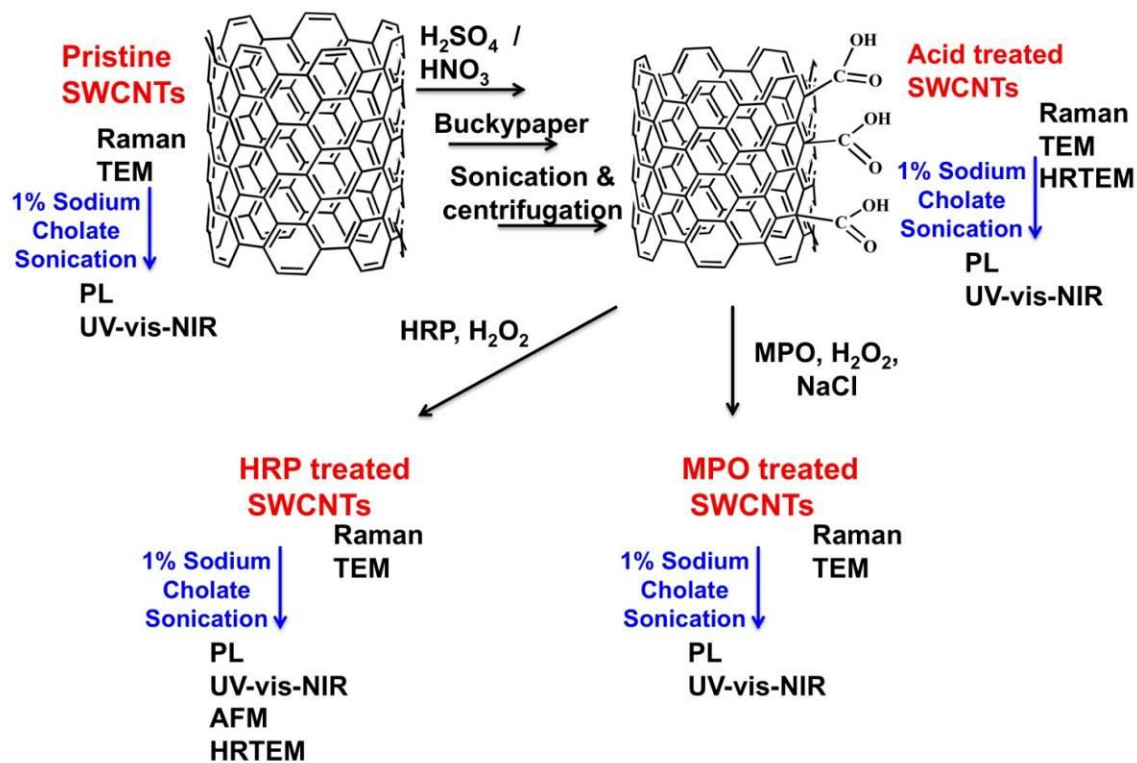
- (3) Chiu, C. F.; Dar, H. H.; Kapralov, A. A.; Robinson, R. A. S.; Kagan, V. E.; Star, A. Nanoemitters and Innate Immunity: The Role of Surfactants and Bio-Coronas in Myeloperoxidase-Catalyzed Oxidation of Pristine Single-Walled Carbon Nanotubes. *Nanoscale* **2017**, *9*, 5948–5956.
- (2) Chiu, C. F.; Saidi, W. A.; Kagan, V. E.; Star, A. Defect-Induced Near-Infrared Photoluminescence of Single-Walled Carbon Nanotubes Treated with Polyunsaturated Fatty Acids. *J. Am. Chem. Soc.* **2017**, *139*, 4859–4865.
- (1) Chiu, C. F.; Barth, B. A.; Kotchey, G. P.; Zhao, Y.; Gogick, K. A.; Saidi, W. A.; Petoud, S.; Star, A. Enzyme-Catalyzed Oxidation Facilitates the Return of Fluorescence for Single-Walled Carbon Nanotubes. *J. Am. Chem. Soc.* **2013**, *135*, 13356–13364.

APPENDIX A

ENZYME-CATALYZED OXIDATION FACILITATES THE RETURN OF FLUORESCENCE FOR SINGLE-WALLED CARBON NANOTUBES

This Appendix contains the Supplementary Information (SI) for Chapter 2.2. The content includes experimental procedure (Scheme 2), Raman RBM section of the pristine SWCNTs (Figure 44), control experiments with acid oxidized SWCNTs (Figure 45), and PL maps and Raman spectra of the oxidized SWCNTs incubated with 0.1 mg of HRP and 1.5 mg of HRP (Figure 46). Characterizations of pristine SWCNTs before and after HRP/H₂O₂, and additional control experiments (Figure 47), non-oxidized HiPco SWCNTs before and after MPO/H₂O₂/NaCl treatment (Figure 48), and pristine SWCNTs after NaClO treatment (Figure 49) are also available. DFT calculation for defective CNTs (Figure 50) and AFM image of the surfactant-wrapped, oxidized SWCNTs after HRP/H₂O₂ for 35 days (Figure 51) are also available.

Scheme 2. Experimental Procedure for the Enzymatic Oxidations of Oxidized SWCNTs



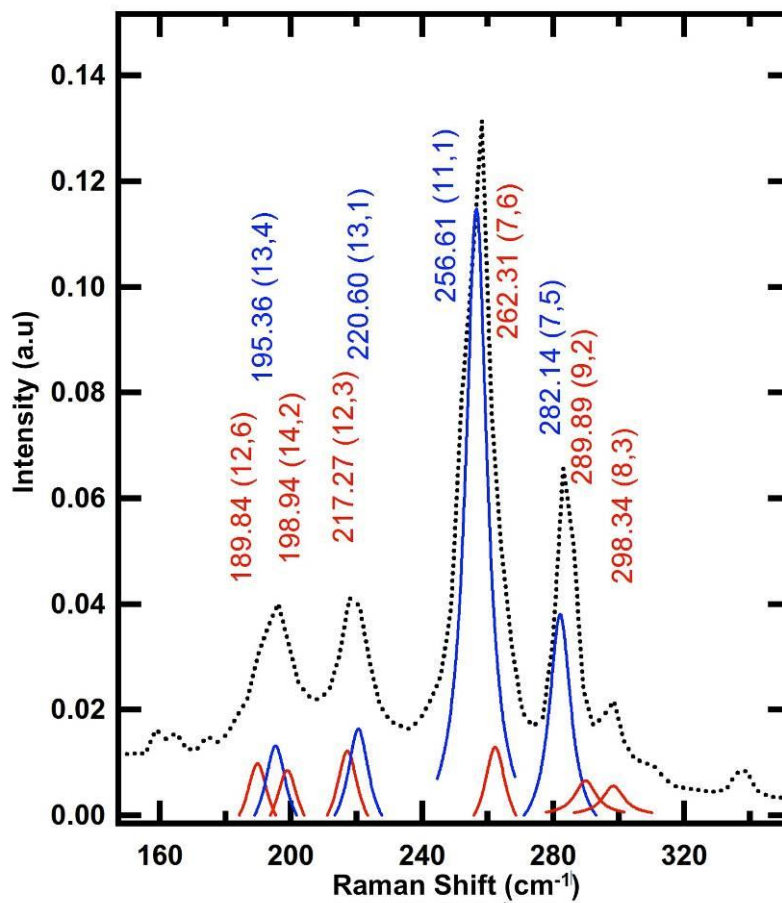
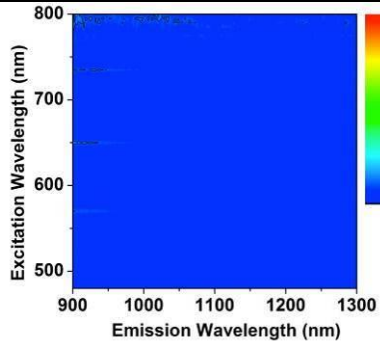
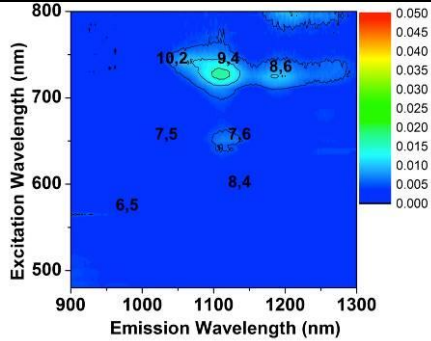


Figure 44. Raman RBM section of the pristine SWCNTs fitted with reported literature values using Lorentzian function.¹² The Raman shift in wavenumbers can be corresponded to the chiral indices of SWCNTs (in parentheses). The major components of the peaks are highlighted in blue.

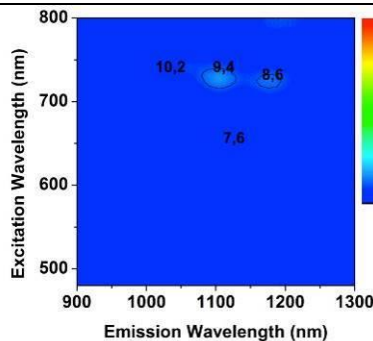
Acid oxidized
SWCNTs
samples with
HRP/H₂O₂



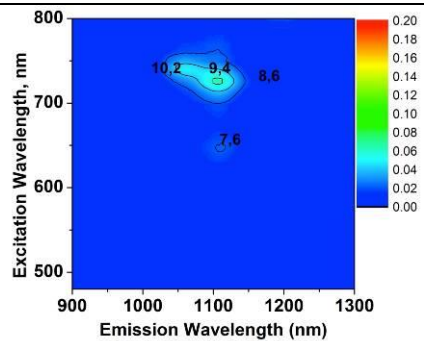
(a) 1.5 mg HRP/H₂O₂ 35 days, (-) SC



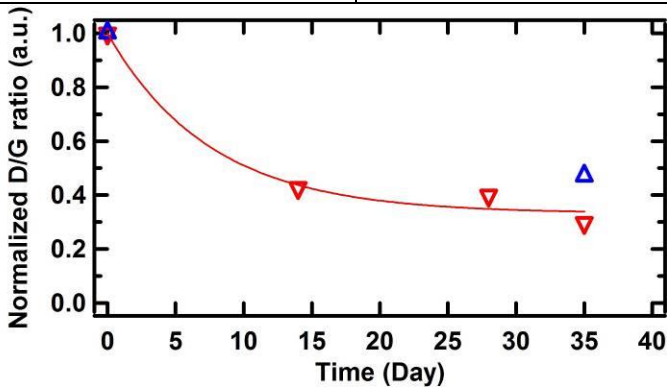
(b) 1.5 mg HRP/H₂O₂ 35 days, (+) SC



(c) 0.1 mg HRP/H₂O₂ 14 days, (+) SC



(d) 0.1 mg HRP/H₂O₂ 35 days, (+) SC



(e) 0.1 mg HRP/H₂O₂

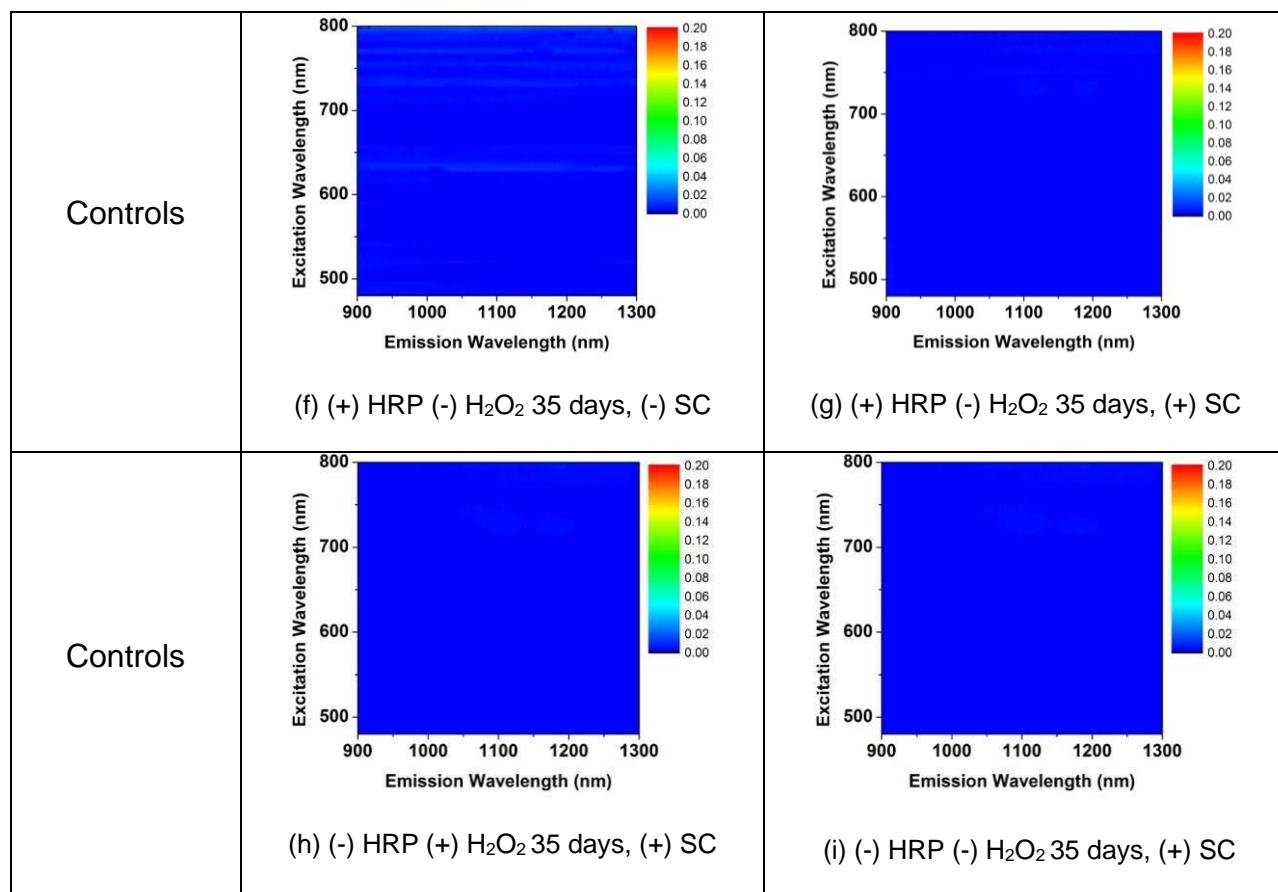


Figure 45. Control Experiments with acid oxidized SWCNTs

PL maps of acid-treated SWCNTs: incubated with 1.5 mg HRP/H₂O₂ after 35 days (a) before and (b) after wrapping with sodium cholate; incubated with 0.1 mg HRP/H₂O₂ for (c) 14 days and (d) 35 days after wrapping with sodium cholate; (e) Normalized D/G ratio over time using (blue) 1.5 mg and (red) 0.1 mg HRP; incubated with 1.5 mg HRP (no H₂O₂) for 35 days (f) before and (g) after wrapping with sodium cholate; (h) treated with H₂O₂ (no HRP) for 35 days after wrapping with sodium cholate; and (i) incubated in water for over 35 days without HRP and H₂O₂ after wrapping with sodium cholate.

Figure 45a and 45b show that sodium cholate is needed for individualizing SWCNTs in solution for the PL mapping. SWCNTs with chiralities (9,4), (8,6) and (7,6) are clearly present after the addition of sodium cholate.

To test if the process is controllable by reaction time or dose dependent, the enzymatic

reaction was performed at a lower dose (0.1 mg) HRP/H₂O₂. Figure 45c demonstrated the return of some photoluminescence signals after 14 days suggesting that the process could be time and dose dependent. After 35 days, the result (Figure 45d) is similar to the 1.5 mg HRP run shown in Figure 26 in the main text. Figure 45e indicates that the D/G ratio decreased by ~50% in the first 14 days and then flattened afterward.

Figure 45f-i show that both HRP and H₂O₂ are necessary for the signal to return. No SWCNTs peaks were observed with HRP alone, H₂O₂ alone, and without both HRP and H₂O₂.

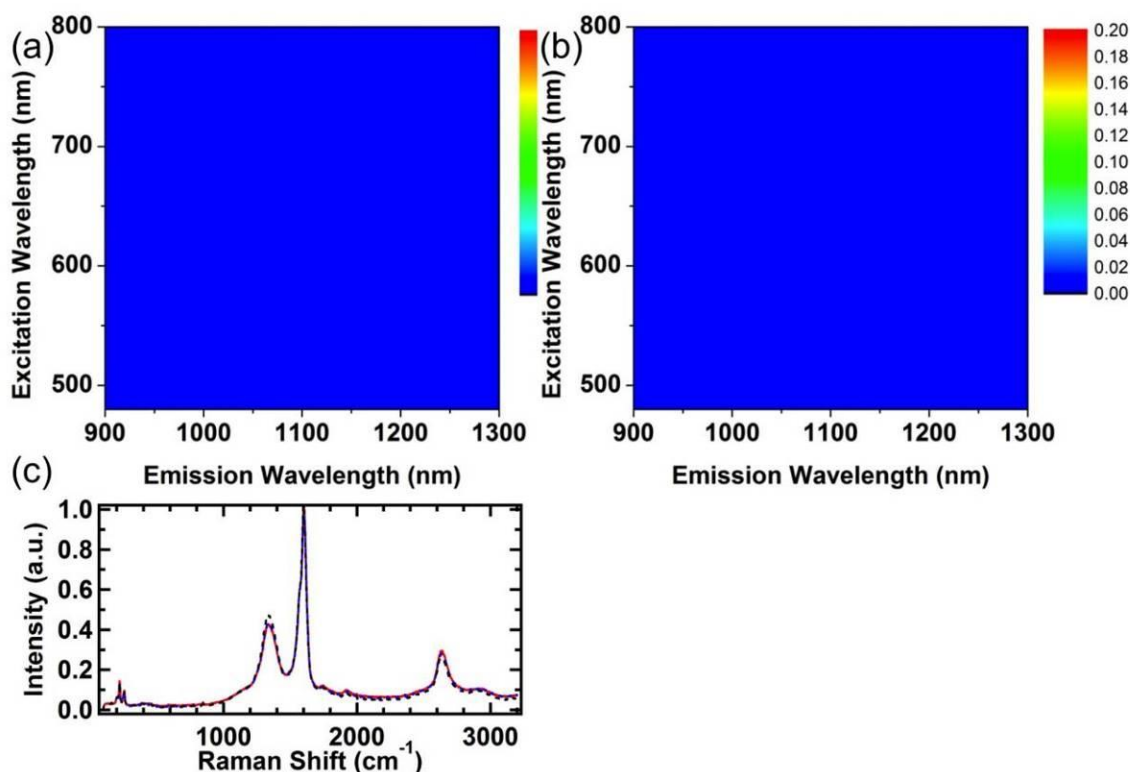


Figure 46. PL maps of the oxidized SWCNTs incubated with (a) 0.1 mg of HRP and (b) 1.5 mg of HRP for 35 days. (c) Raman spectra of the oxidized SWCNTs (black, dotted), 0.1 mg HRP treated SWCNTs (blue) and 1.5 mg HRP treated SWCNTs (red).

No SWCNTs luminescence signals were detected for both HRP concentrations, indicating that the peroxidase alone without H₂O₂ cannot return fluorescence of the oxidized SWCNTs by reducing oxygen functional groups via the oxidase cycle.

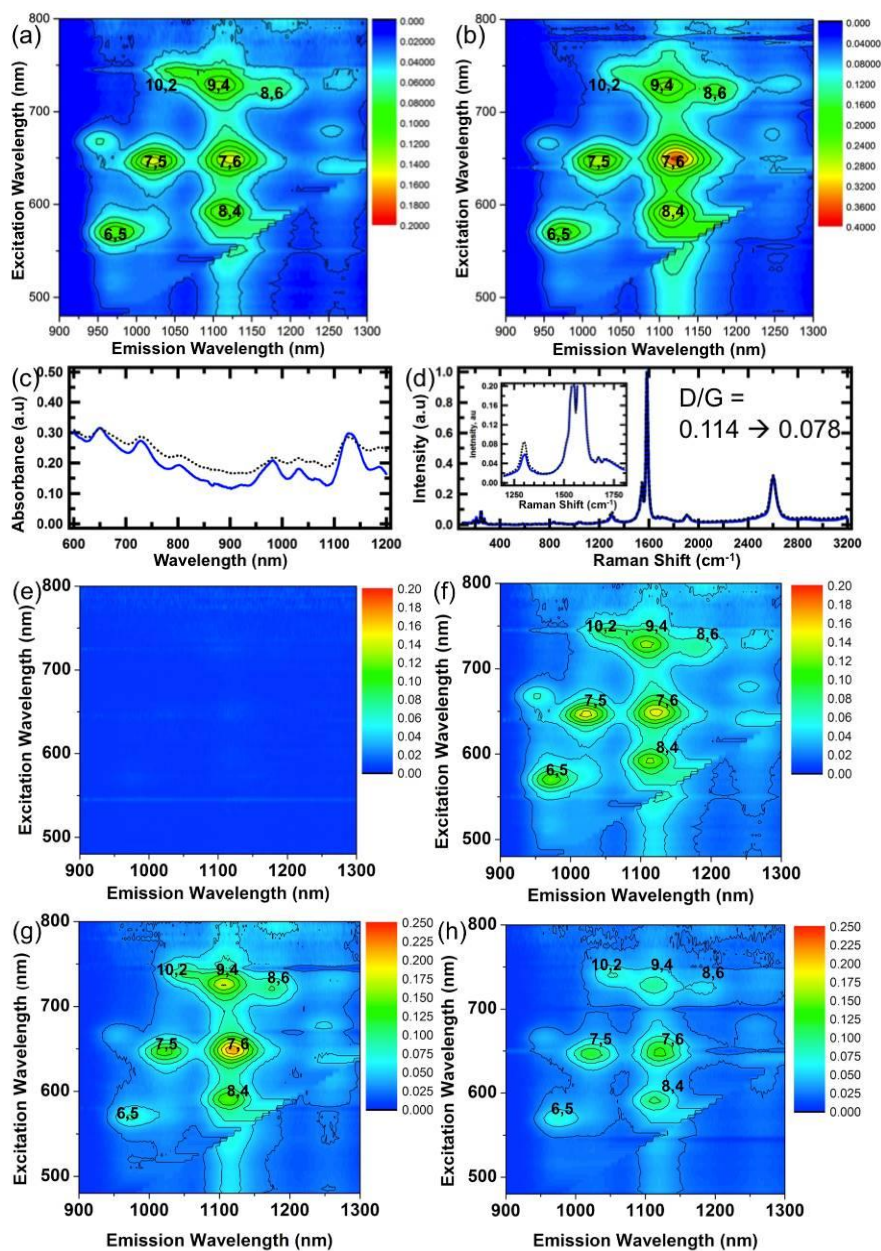


Figure 47. Photoluminescence (PL) maps of SWCNTs (a) before oxidation and (b) non-oxidized sample after treatment with HRP/H₂O₂. (c) UV-vis-NIR absorption and (d) Raman spectrum of non-oxidized HiPco SWCNTs (black, dotted) after HRP/H₂O₂ treatment (blue). Inset depicts enlarged Raman spectrum of the D and G peak region. Additional control experiments: Pristine SWCNTs dispersed in (e) HRP and (f) 1%wt sodium cholate. Results from 47e, 47f, and Figure 45 demonstrated HRP could not individualize SWCNTs. Sodium cholate-wrapped SWCNTs (g) before and (h) after the addition of HRP, showing that HRP is not an enhancer in SWCNT luminescence.

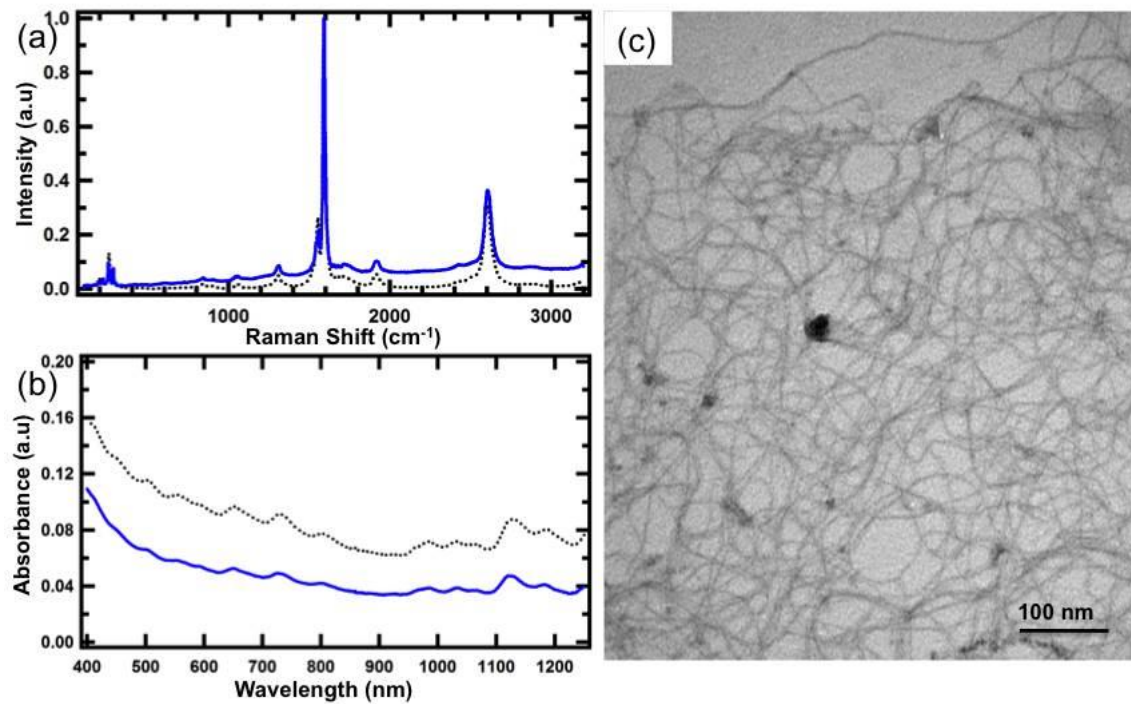


Figure 48. (a) Raman and (b) UV-vis-NIR absorption spectra of the non-oxidized HiPco SWCNTs (black, dotted) after MPO/H₂O₂/NaCl treatment (blue). (c) TEM micrograph of the pristine SWCNTs after MPO/H₂O₂/NaCl treatment.

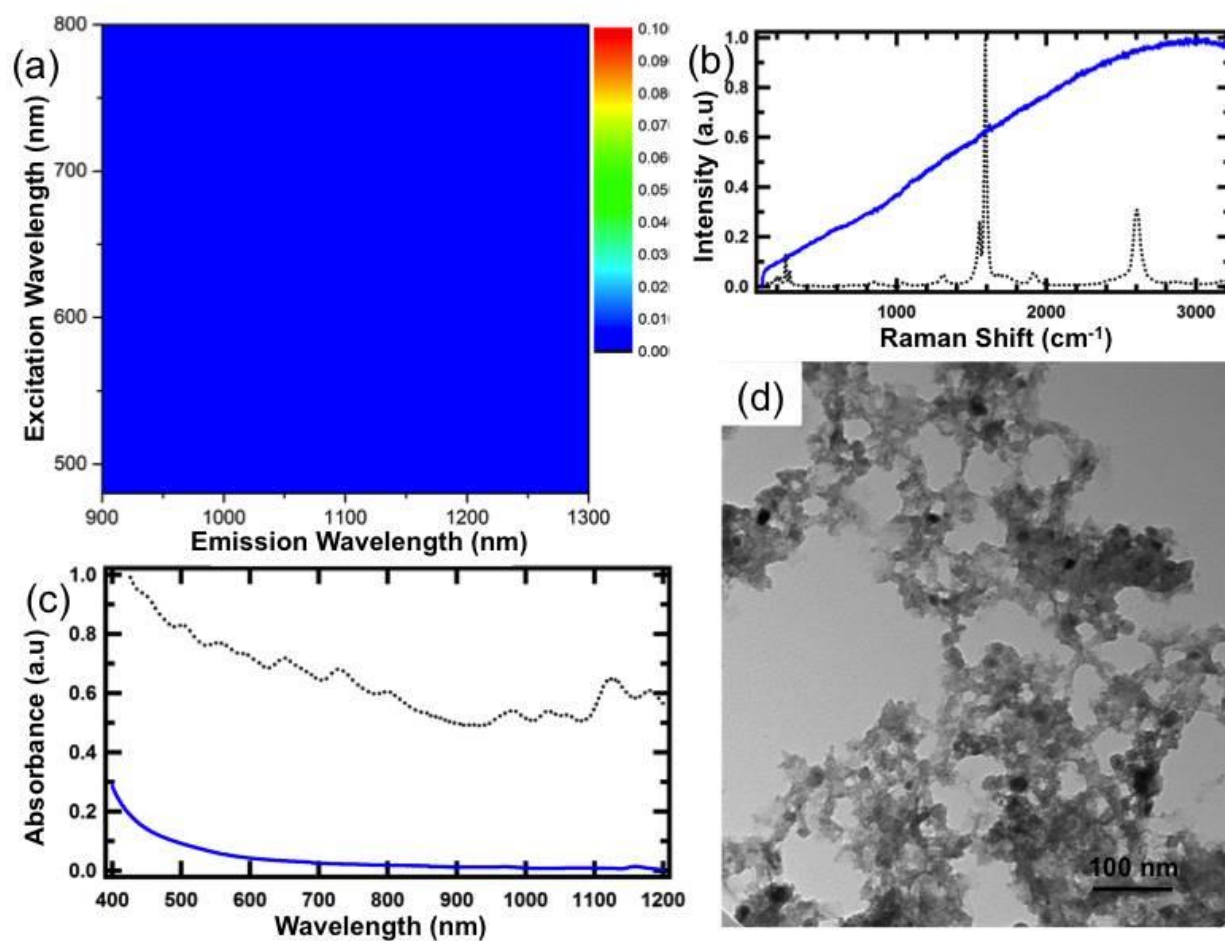


Figure 49 (a) Photoluminescence map of the pristine SWCNTs after NaOCl treatment. (b) Raman and (c) UV-vis-NIR absorption spectra of the non-oxidized HiPco SWCNTs (black, dotted) after NaOCl treatment (blue). (d) TEM micrograph of the pristine SWCNTs after NaOCl treatment.

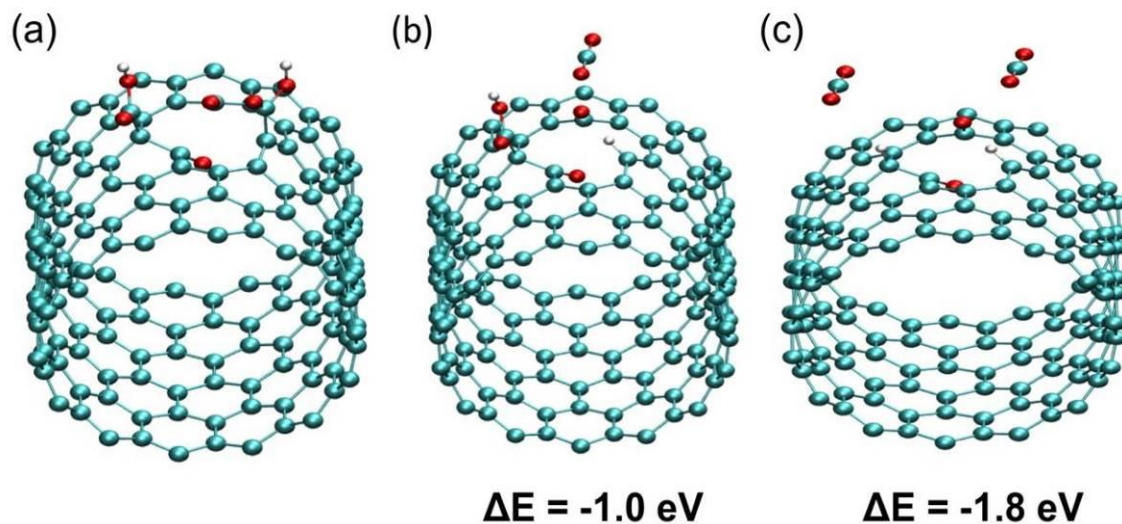


Figure 50. (a) Defective CNT (14,0) functionalized with two ketone and two carboxyl groups. (b) Partially decarboxylated CNT associated with a release of one CO₂ molecule in the gas phase. Compared to (a), the energy of this structure is lower by 1 eV. (c) Full decarboxylation of the CNT with the release of two CO₂ molecules in the gas phase. This process is exothermic by 1.8 eV compared to (a).

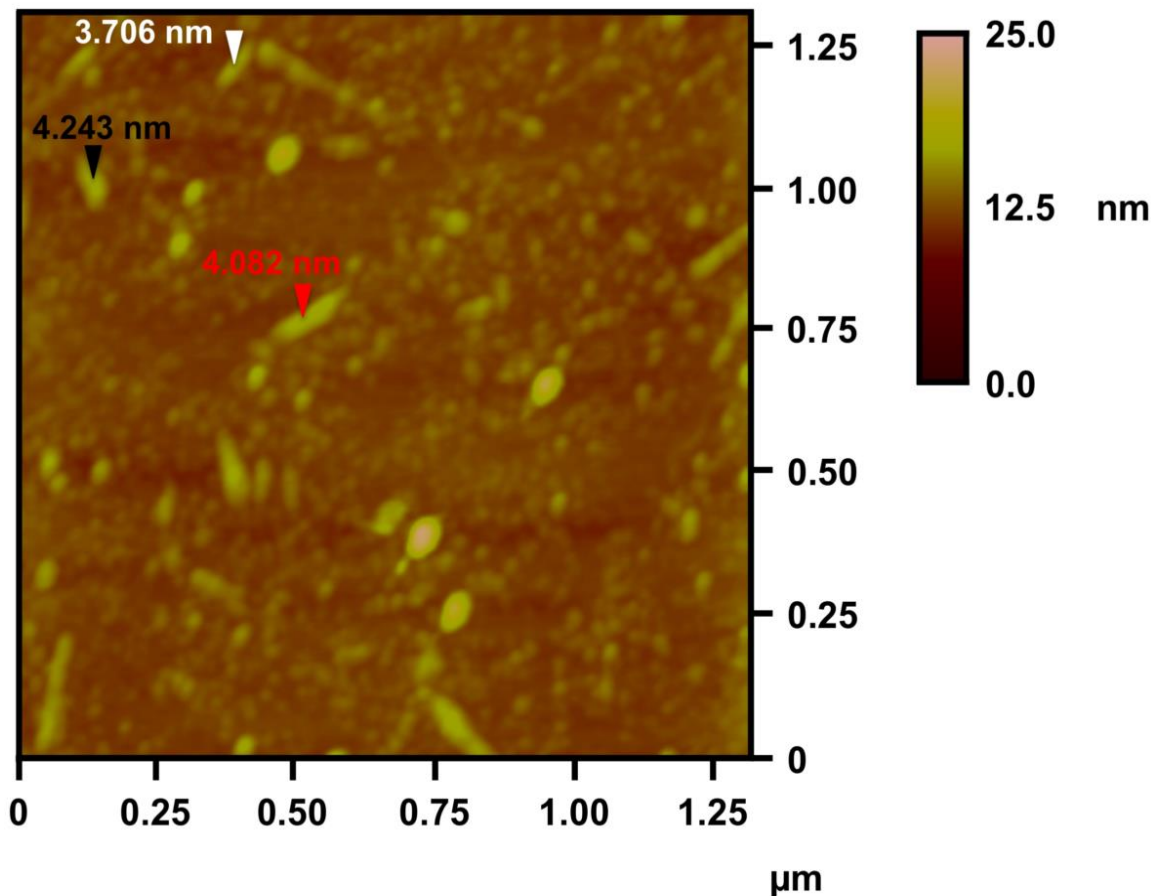


Figure 51. AFM image of the surfactant-wrapped, oxidized SWCNTs that were treated with HRP/H₂O₂ for 35 days (from Figure 26c)

Atomic Force Microscopy (AFM)

To obtain the height image and sectional analysis of the CNT sample, a multimode scanning probe microscope (Veeco) was employed in tapping mode. Sample preparation entailed: (1) treatment with approximately 20 μL of 0.1% (w/w) poly-L-Lysine (aq) deposited on freshly cleaved mica through spin coating at 1,400 revolution per minute (r.p.m.) followed by (2) spin coating approximately 10 μL of sample (aq) at 1,400 r.p.m. The sample was allowed to dry in ambient for 45 minutes prior to imaging. Using a “supersharpest” Si probe (tip radius <5nm, AppNano), tapping mode was performed at a drive frequency of 181.289 Hz, an amplitude set point of 0.2465 V, and a drive amplitude of 216 mV. Images were initially scanned in a 13.1 μm area prior to the magnification of relevant areas. Post-imaging processing included image flattening and section analysis for quantifying cross-sectional heights of samples.

APPENDIX B

NANO EMITTERS AND INNATE IMMUNITY: THE ROLE OF SURFACTANTS AND BIO-CORONAS IN MYELOPEROXIDASE-CATALYZED OXIDATION OF PRISTINE SINGLE-WALLED CARBON NANOTUBES

This Appendix contains the Supplementary Information (SI) for Chapter 2.3. The content includes: EE maps and emission profile of SC-SWCNTs controls (Figure 52), 3D view for MPO/H₂O₂/NaCl treated SC-SWCNTs EE maps and relative emission intensity plot (Figure 53), EE maps of SDC-SWCNTs under MPO oxidation (Figure 54), EE maps for dialysis experiment with SC- and SDC-SWCNTs (Figure 55), EE maps of NaOCl oxidation on SC-SWCNTs (Figure 56), Intensity plot for SWCNTs with bio-coating during oxidation with MPO/H₂O₂/NaCl. (Figure 57), EE maps of CpG DNA-SWCNTs and BSA-SWCNTs controls (Figure 58), and EE maps for neutrophils and MEF cells experiments (Figure 59).

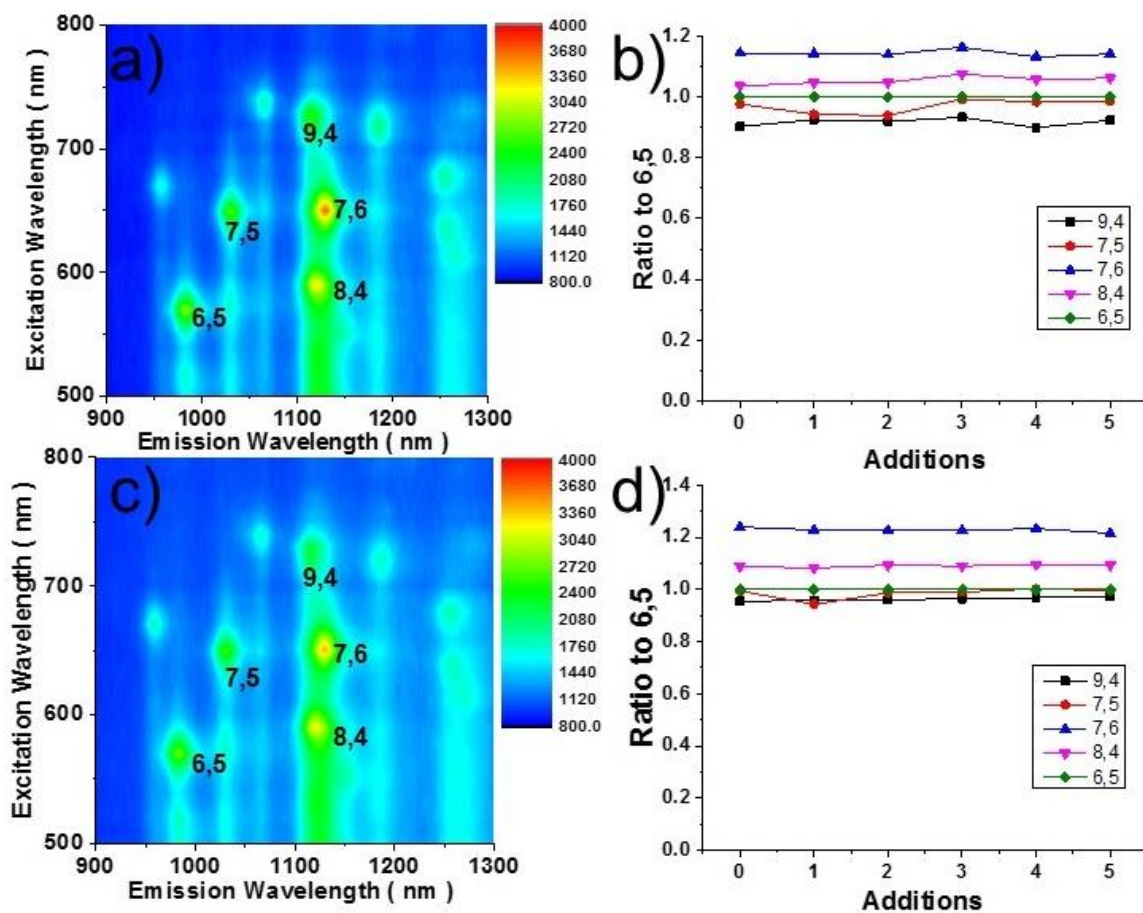


Figure 52. EE maps and relative intensity plots for control experiments: (a, b) MPO/NaCl without H₂O₂, and (c, d) NaCl without neither MPO nor H₂O₂.

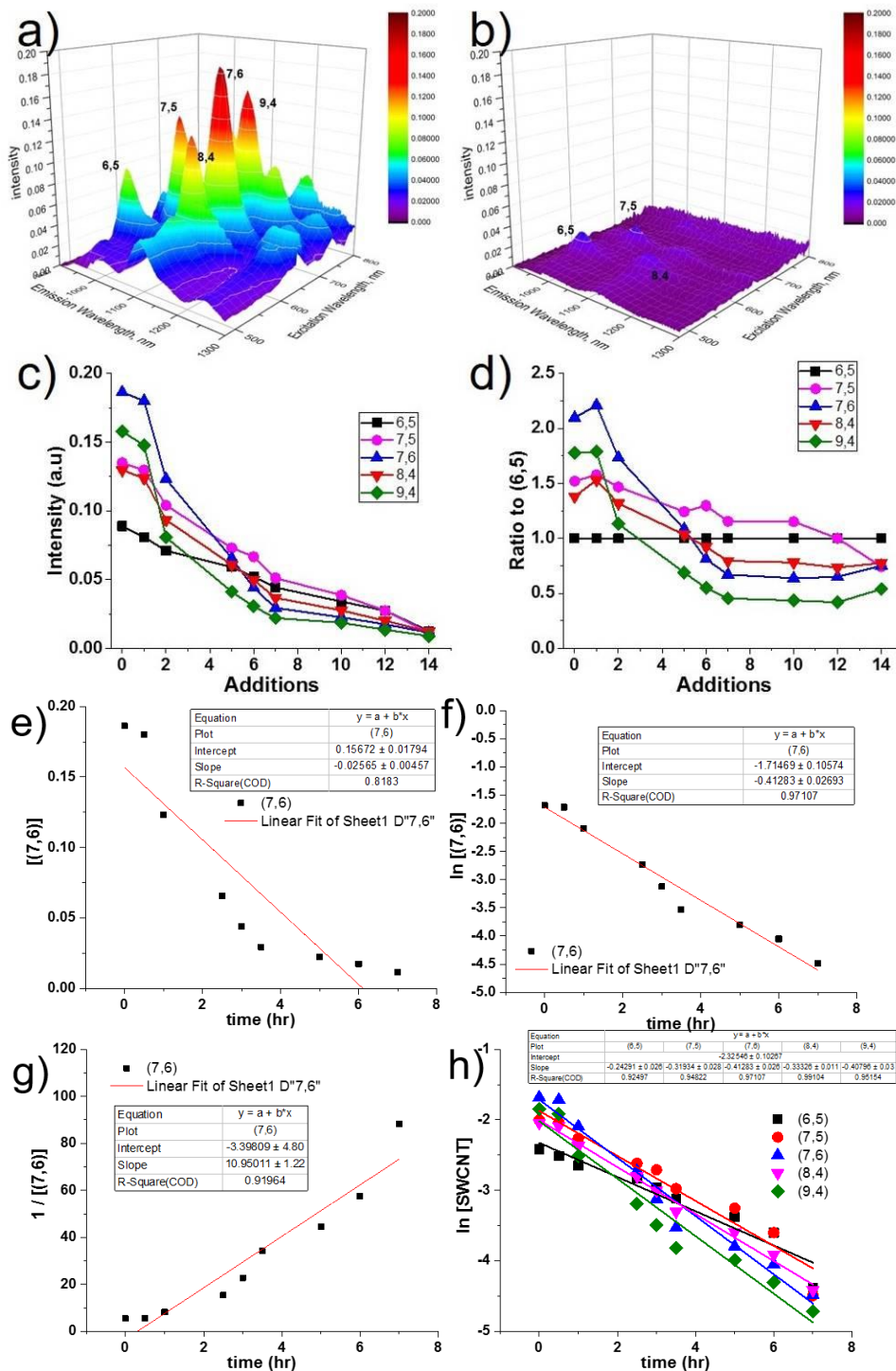


Figure 53. 3D plot for MPO/H₂O₂/NaCl treated SC-SWCNTs EE maps a) before and b) after 14 additions of H₂O₂ in MPO/H₂O₂/NaCl oxidation. c) Intensity values from the EE maps, and d) Relative emission intensity plot. Animated EE map is available as gif file. Data from (7,6) SWCNTs were fitted to (e) zero, (f) first, and (g) second order rate law. h) First order reaction equation applied to all SWCNTs

Table 7. Calculated Rate Constant of Different SWCNTs for MPO/H₂O₂/NaCl Reaction

SWCNTs	(6,5)	(7,5)	(8,4)	(7,6)	(9,4)
Diameter (nm)	0.757	0.829	0.840	0.895	0.916
Rate Constant (/hr)	0.24 ± 0.03	0.32 ± 0.03	0.33 ± 0.01	0.41 ± 0.03	0.41 ± 0.03

Values were obtained from Figure 53h, applied to Figure 33d in the main text and resulted in the linear fitting equation

Equation	$y = a + b*x$
Intercept	-0.63 ± 0.07
Slope	1.14 ± 0.09
R-Square	0.98327

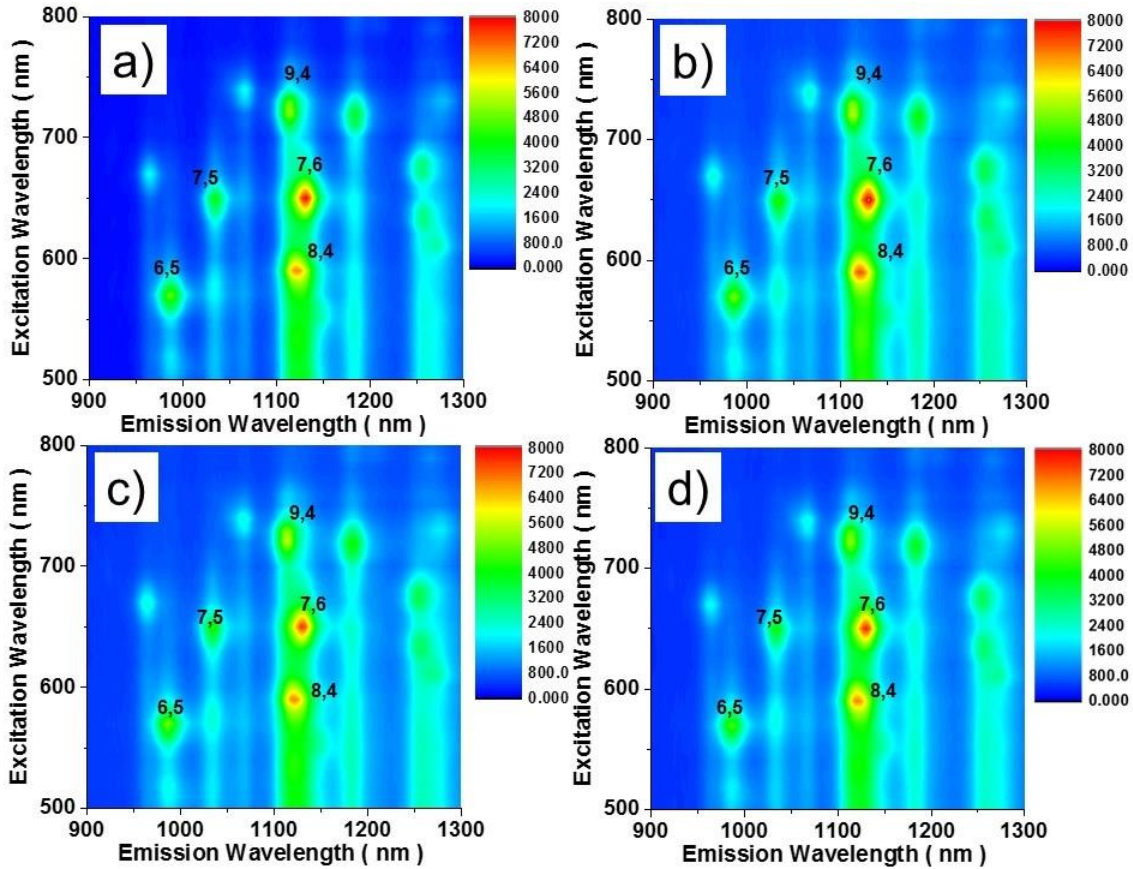


Figure 54. EE maps of SDC-SWCNTs a) before and b) after oxidation with MPO/H₂O₂/NaCl. EE maps for controls, c) with MPO/NaCl (without H₂O₂), and d) with H₂O₂/NaCl (without MPO).

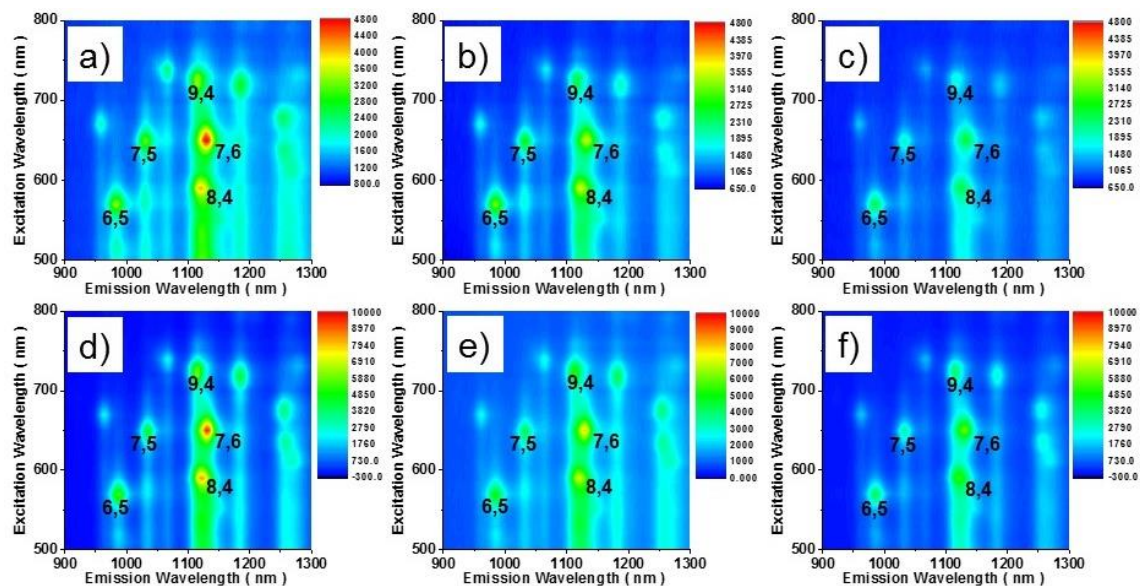


Figure 55. EE maps for SC-SWCNTs a) before dialysis, b) after dialysis, and c) dialyzed in the presence of MPO. EE maps for SDC-SWCNTs d) before dialysis, e) after dialysis, and f) dialyzed in the presence of MPO.

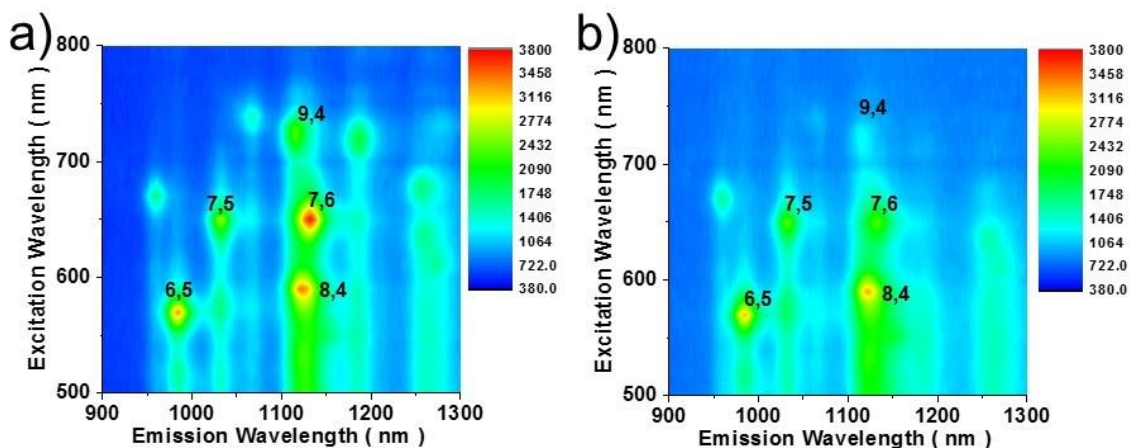


Figure 56. EE maps a) before and b) after NaOCl oxidation of SC-SWCNTs.

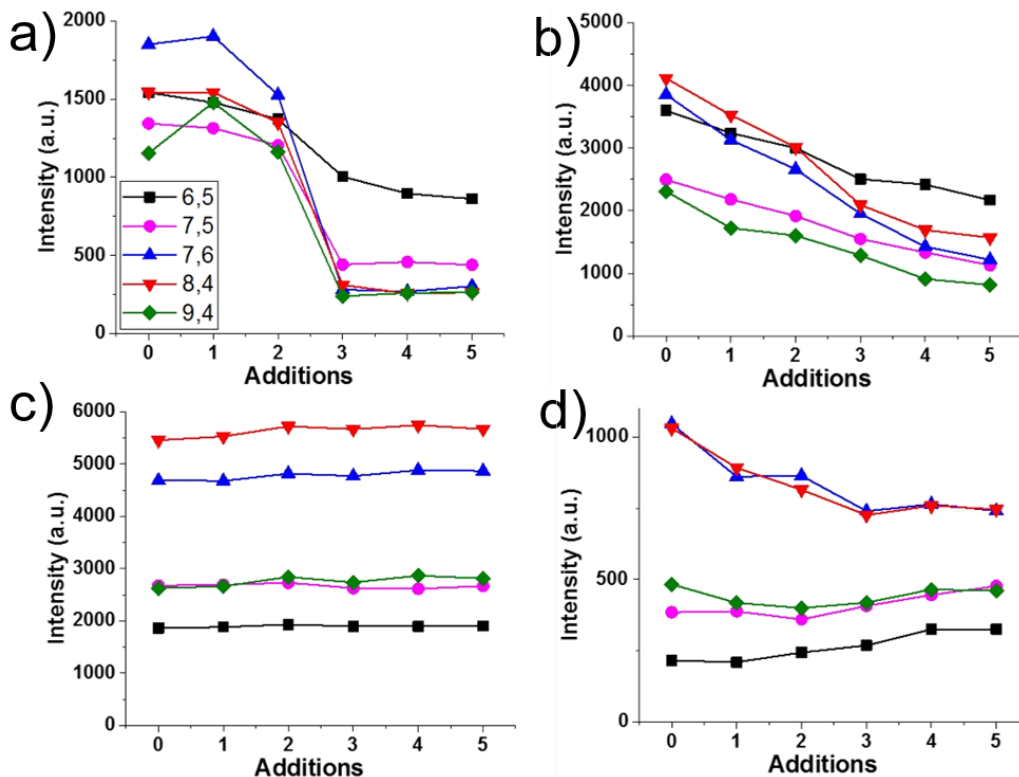


Figure 57. Intensity plot for a) CpG DNA-SWCNTs, b) BSA-SWCNTs, c) PL-PEG-SWCNTs, and d) PS-SWCNTs during oxidation with MPO/H₂O₂/NaCl.

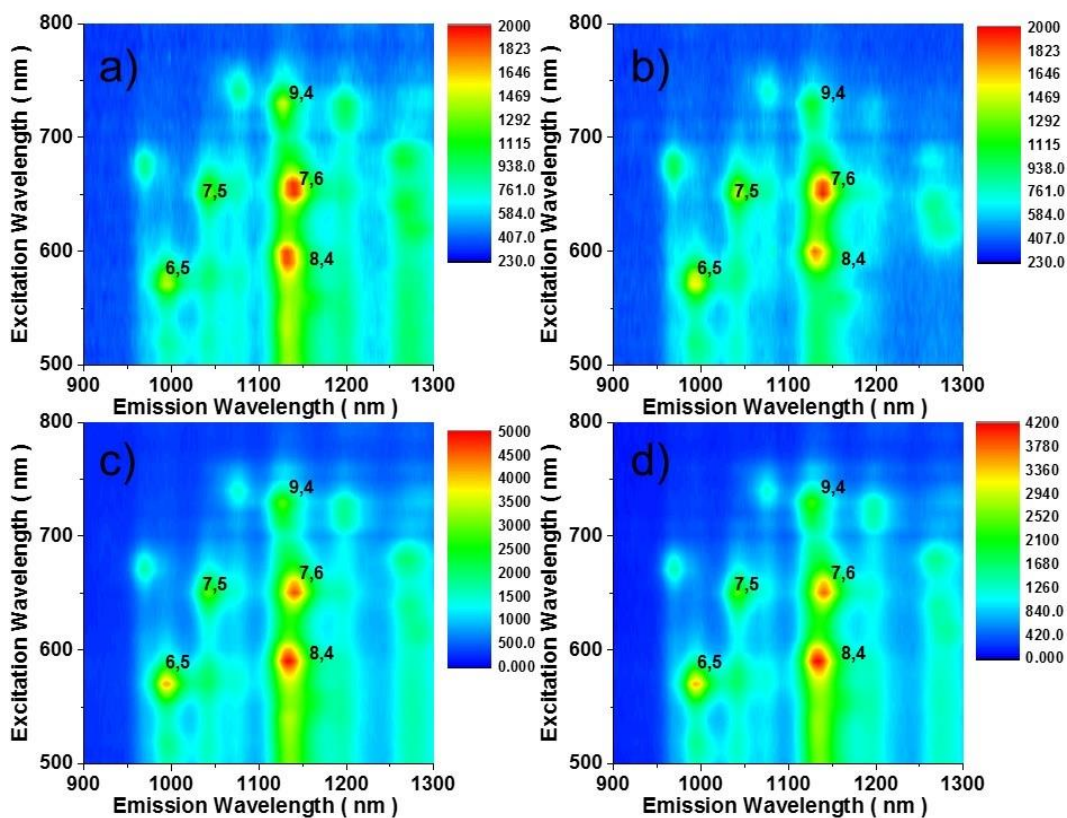


Figure 58. Controls for CpG DNA-SWCNTs oxidation with MPO/H₂O₂/NaCl: (a) MPO/NaCl without H₂O₂, and (b) H₂O₂/NaCl without MPO. Controls for MPO-catalyzed oxidation of BSA-SWCNTs: (c) MPO/NaCl without H₂O₂, and (d) H₂O₂/NaCl without MPO.

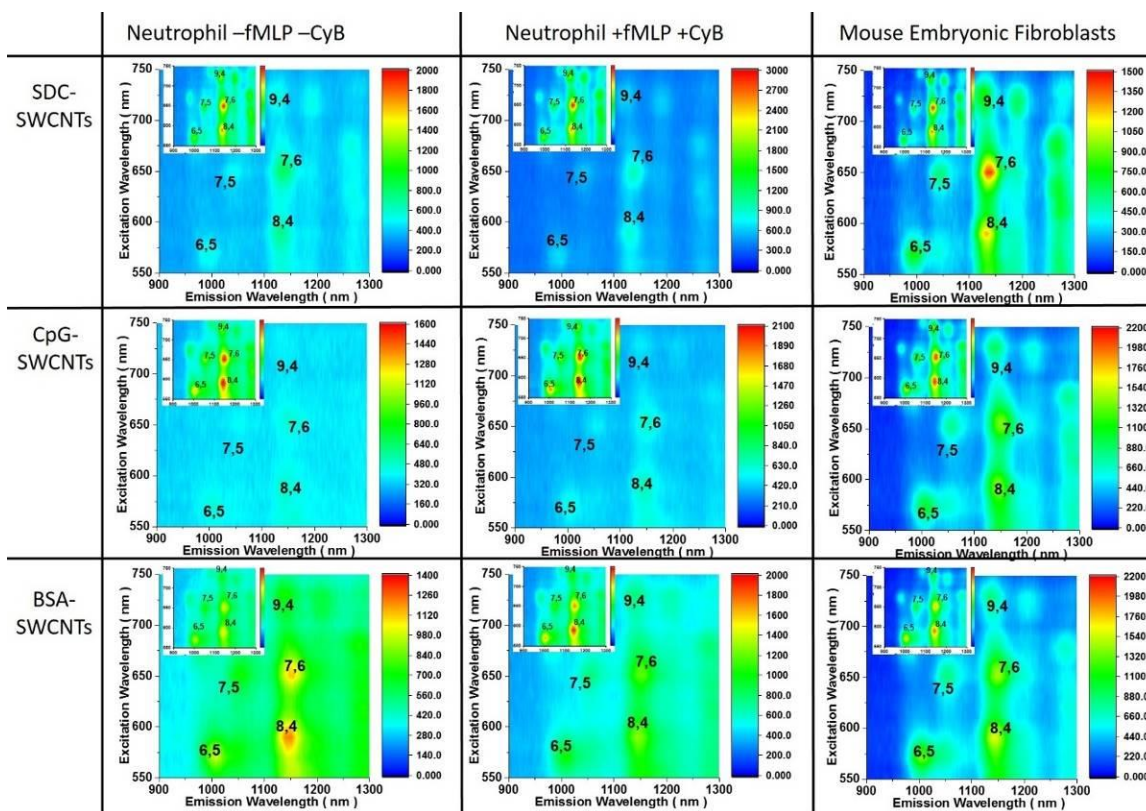


Figure 59. EE maps of SDC-SWCNTs (top), CpG DNA-SWCNTs (middle) and BSA-SWCNTs (bottom) subjected to non-activated neutrophils (left), activated neutrophils (center) and mouse embryonic fibroblasts (right). Inserts are EE maps before the reactions.

APPENDIX C

DEFECT-INDUCED NEAR-INFRARED EMISSION OF SINGLE-WALLED CARBON NANOTUBES BY POLYUNSATURATED FATTY ACIDS

This Appendix contains the Supplementary Information (SI) for Chapter 3.0. The content includes, characterization of CoMoCAT SWCNTs a) before and b) after reaction with linoleic acid (Figure 60), control experiments with various components and antioxidant (Figure 61), data from surfactant experiment (Figure 62), HRXPS spectra of the carbon peak (Figure 63), DFT calculation of absorption spectra and optimum adsorption configuration of oxygen-doped CNTs (Figure 64), reaction with other PUFAs and saturated fatty acid (Figure 65), reaction with autoxidized and non-oxidized cardiolipin (Figure 66), control experiment with diethylenetriaminepentaacetic acid (DTPA) (Figure 67), control experiments with antioxidant (Figure 68), product isolation (Figure 69), control experiment under normal laboratory lighting conditions (Figure 70), and EE maps of raw SWCNTs starting material (Figure 71).

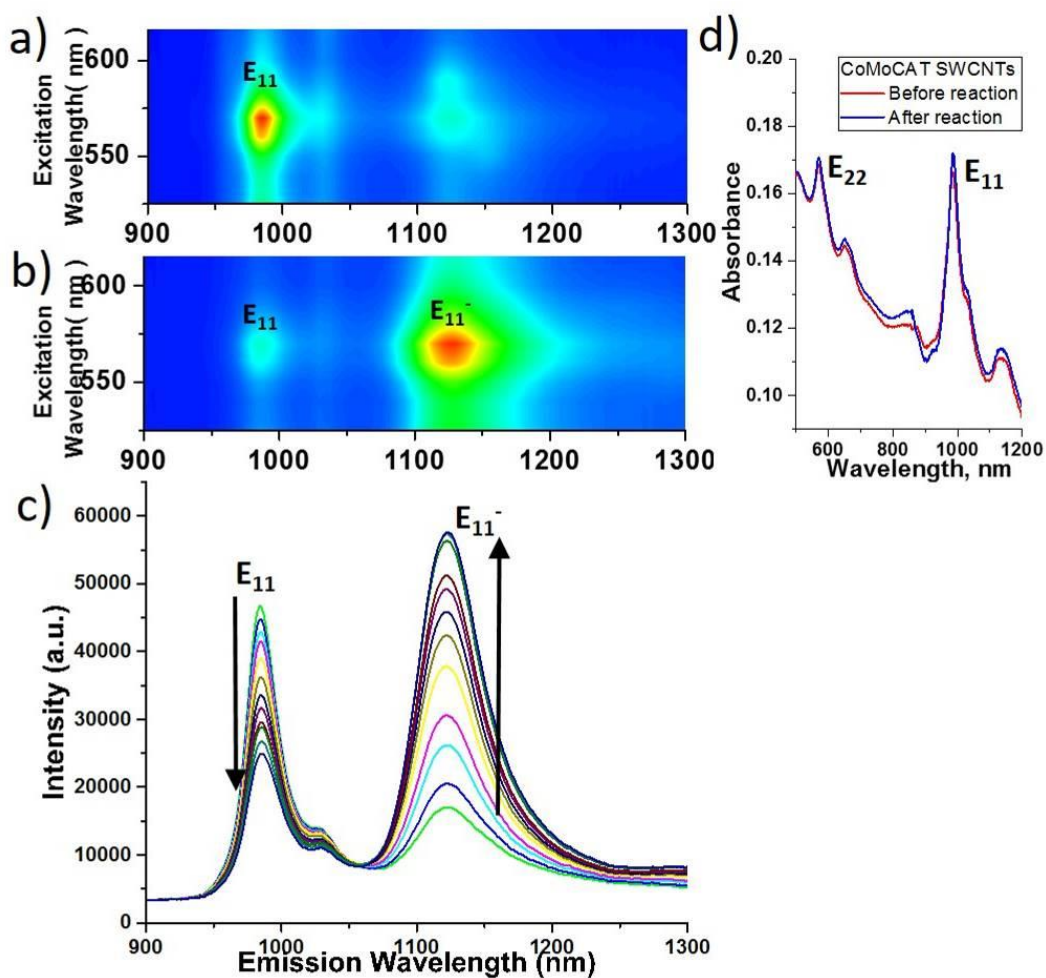


Figure 60. EE maps of CoMoCAT SWCNTs a) before and b) after reaction with linoleic acid. Panel c) shows the spectral changes over 60 mins (spectra taken every 5 mins). d) vis-NIR absorption spectra of SWCNTs before and after the reaction.

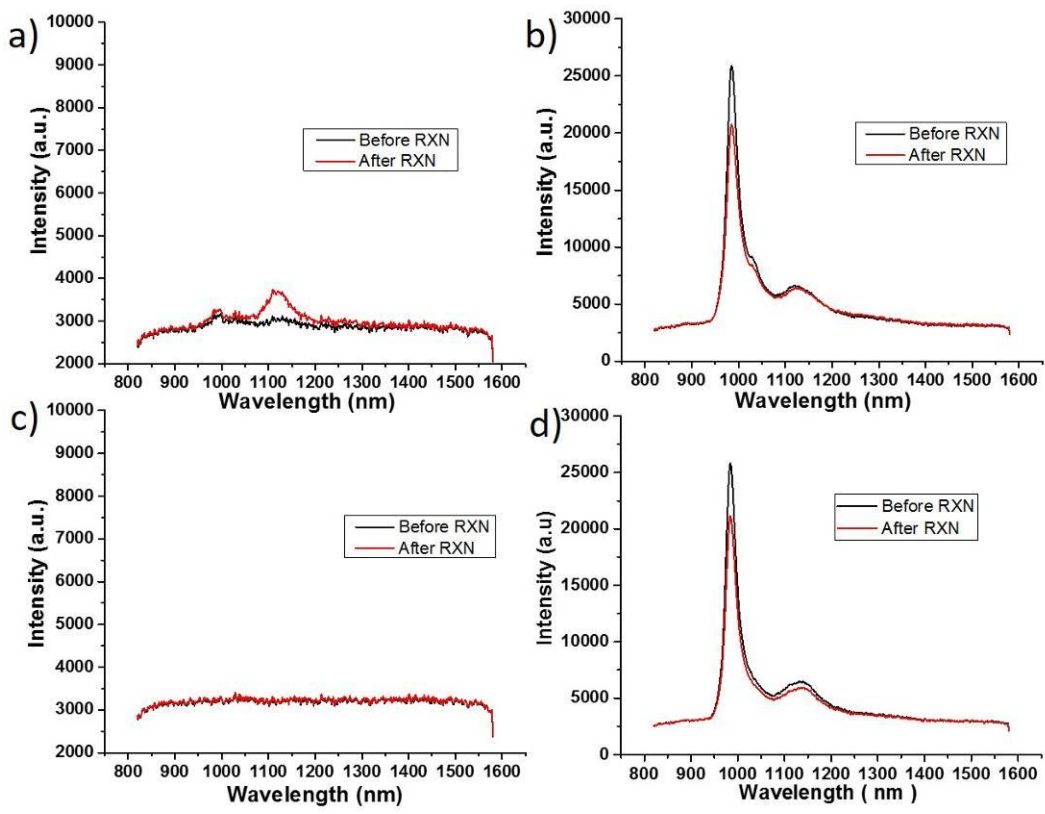


Figure 61. Control reactions with a) only SWCNTs and linoleic acid (no surfactant), b) SWCNTs and sodium cholate (no linoleic acid), and c) sodium cholate and linoleic acid (no SWCNTs). d) Linoleic acid pretreated with morin (250 $\mu\text{g} / \text{mL}$) to inhibit the autoxidation by terminating the radical chain reactions. SWCNTs exposed to pretreated linoleic acid showed no increase in E_{11}^- emission.

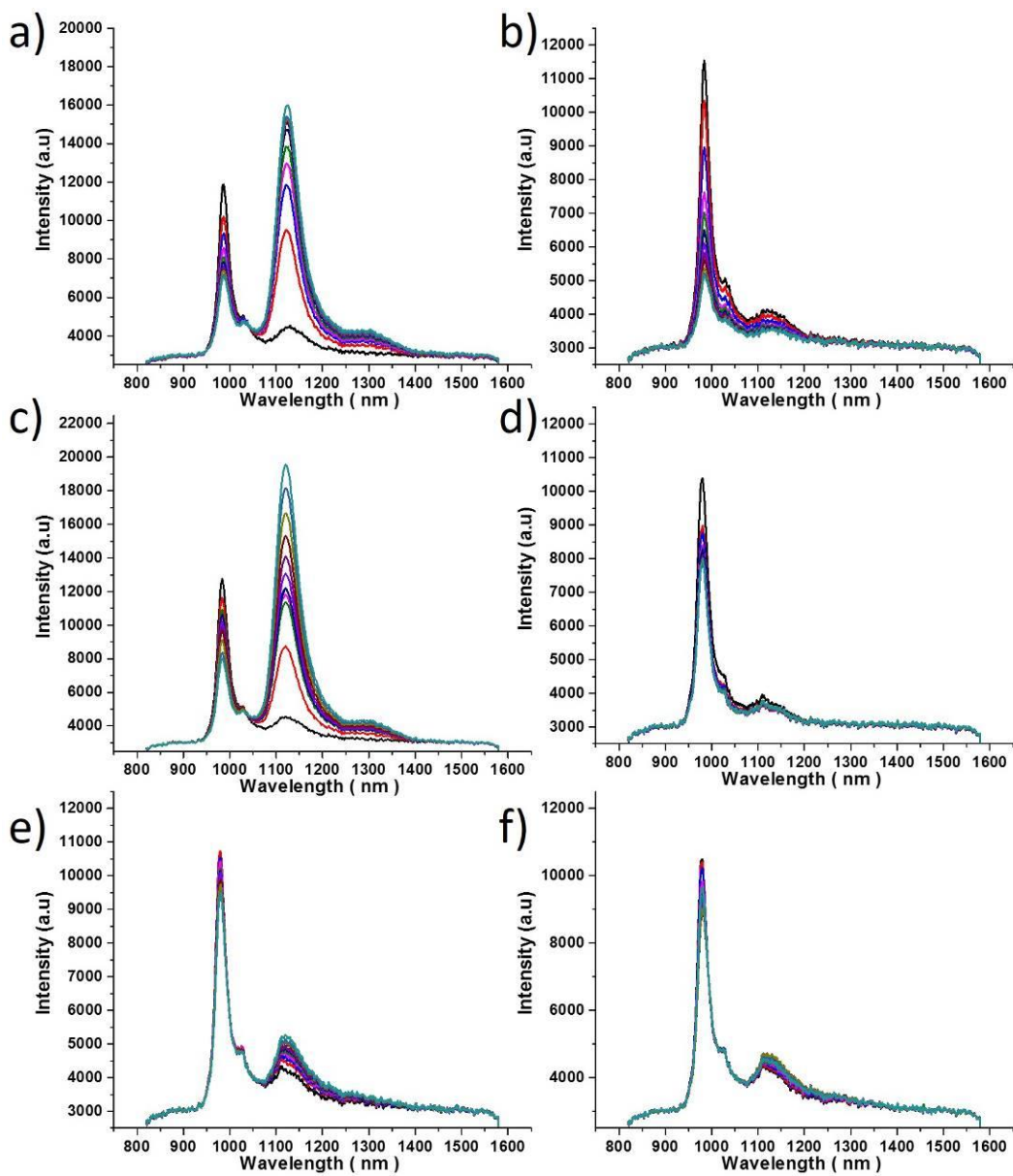


Figure 62. Spectra of SWCNTs / LA-OOH reaction using different surfactants. Sodium cholate (SC) at a) 0.1 wt % and b) 1 wt %, sodium dodecyl sulfate (SDS) at c) 0.1 wt % and d) 1 wt %, and dodecylbenzene sulfonate (SDBS) at e) 0.1 wt % and f) 1 wt %.

Table 8. Reaction Conditions and Calculations for Wavelength-Dependence Experiment.

Wavelength	Power density	Photon flux	ΔE_{11}^-	Photon Flux Corrected Intensity	Normalized Intensity (Photon Flux Corrected)
(nm)	(mW/cm ²)	(photons per second)			
666	2.93	9.82E+15	1329	1.35E-13	0.11
566	7.49	2.13E+16	26111	1.22E-12	1.00
466	14.22	3.34E+16	1420	4.26E-14	0.03
366	5.18	9.54E+15	1431	1.50E-13	0.12
235	3.14	3.71E+15	89	2.40E-14	0.02

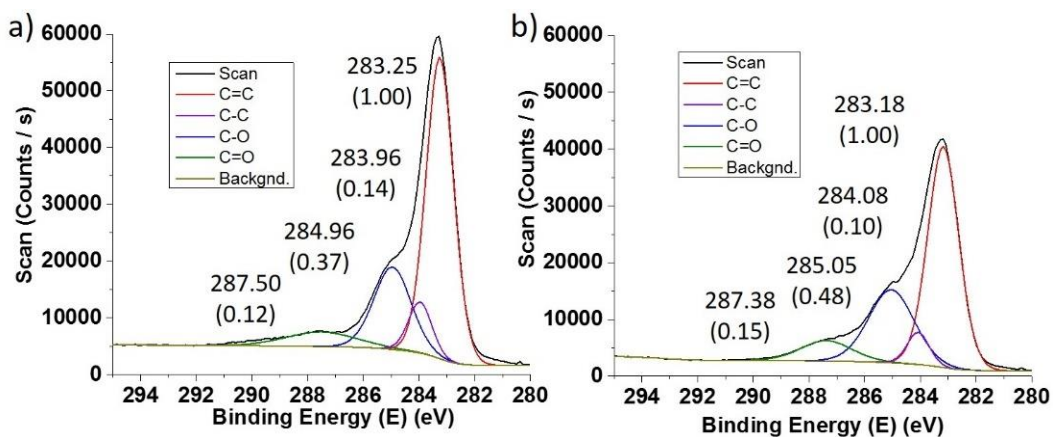


Figure 63. HRXPS spectra of carbon peak of the SWCNTs (a) before and (b) after LA-OOH reaction.

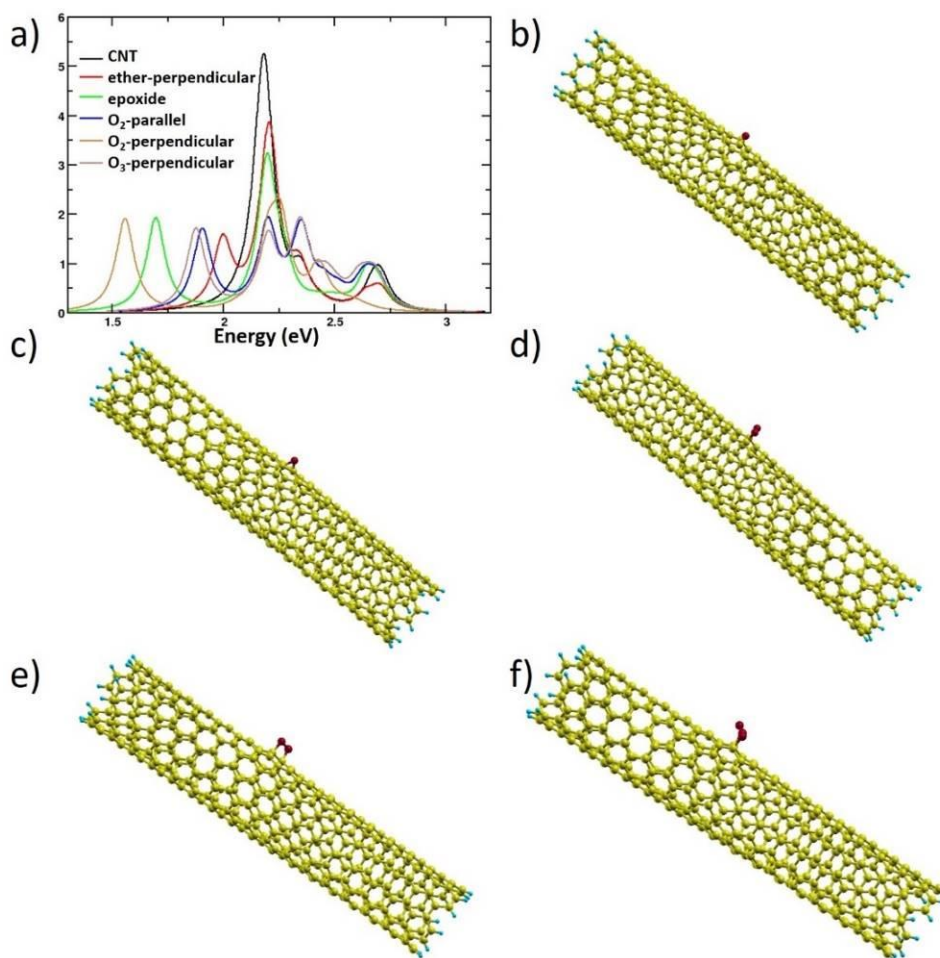


Figure 64. a) The absorption spectra of the pristine and the oxygen-doped CNTs. Optimum adsorption configuration of the CNT with b) ether-perpendicular c) epoxide-parallel, d) O₂-parallel, e) O₂-perpendicular, and f) O₃-perpendicular.

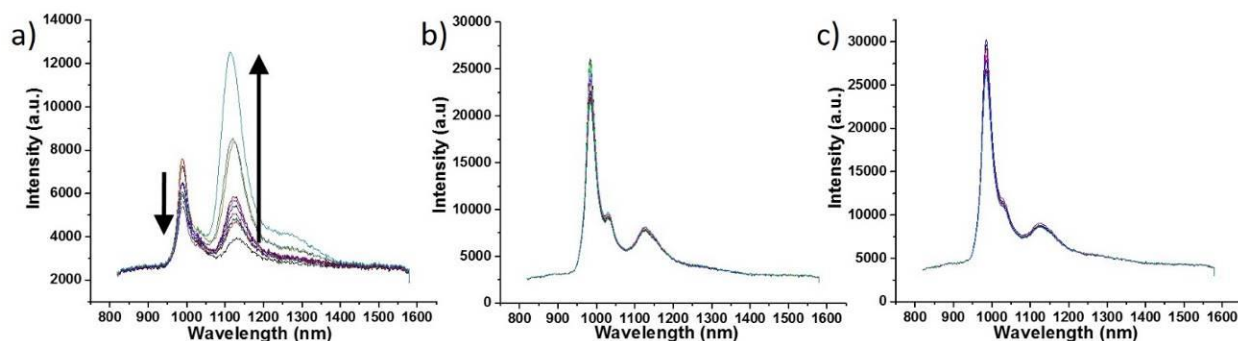


Figure 65. Emission spectra of SWCNTs reacted with a) γ -linolenic acid (18:3), b) stearic acid (18:0), and c) stearyl-cardiolipin (14:0).

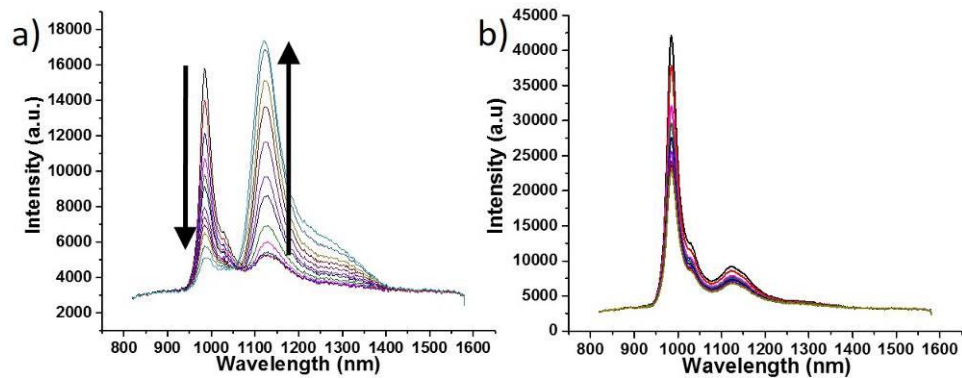


Figure 66. Emission spectra of SWCNTs reacted with a) autoxidized cardiolipin (18:2), and b) non-oxidized cardiolipin (18:2).

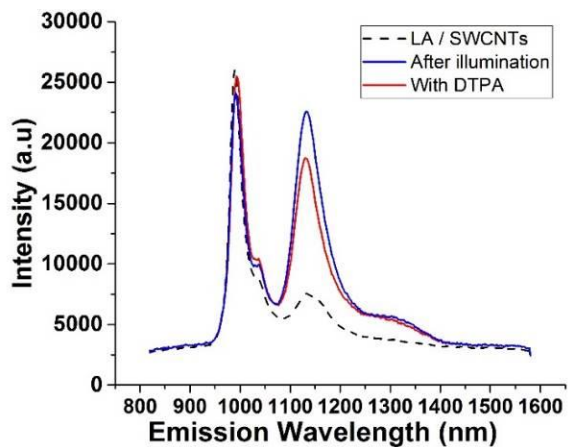


Figure 67. Emission spectra of SWCNTs treated with linoleic acid before, after illumination, and in the presence of diethylenetriaminepentaacetic acid (DTPA).

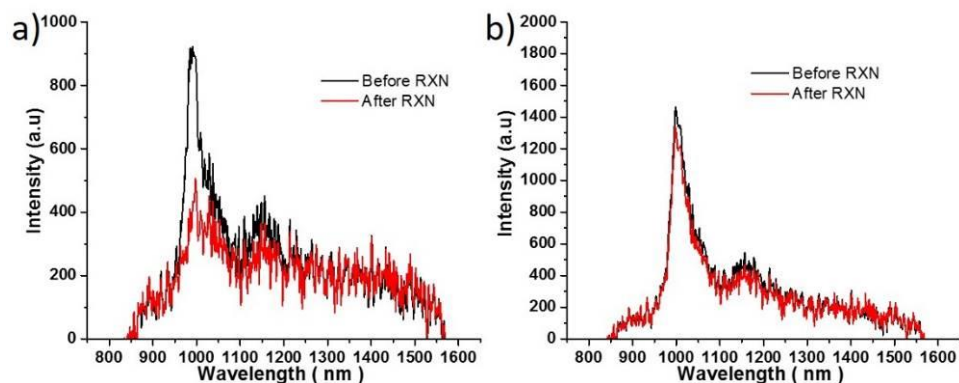


Figure 68. SWCNTs treated with antioxidants, a) ascorbic acid (250 mM) and b) morin (250 µg / mL), before subjected to linoleic acid hydroperoxide and 566 nm excitation light for one hour. No evolvment of the E_{11}^- emission was observed.

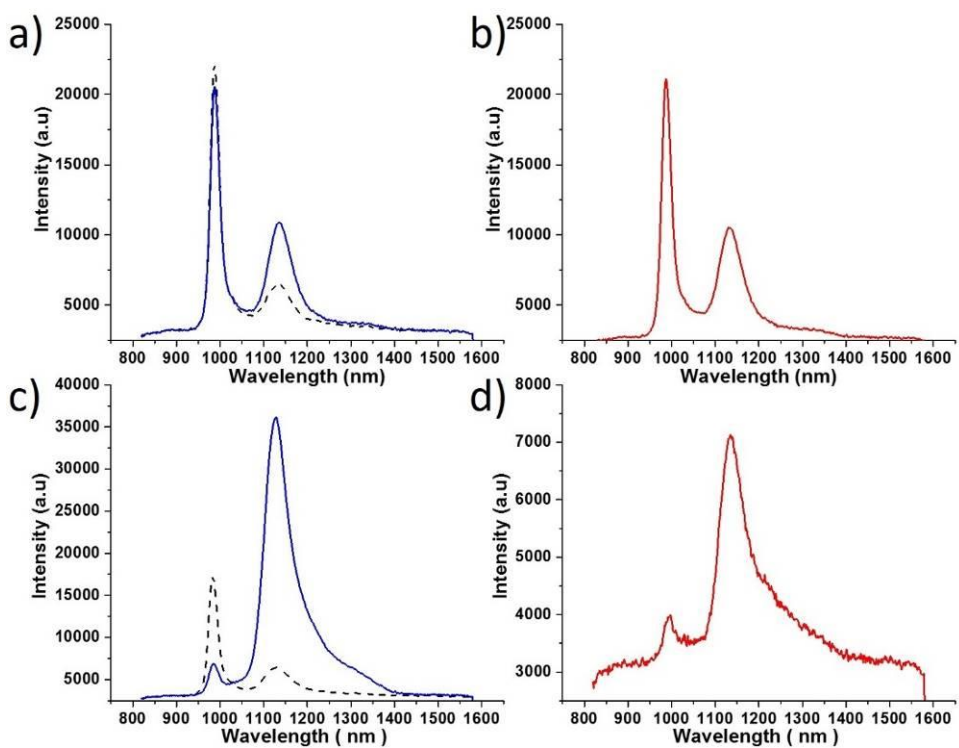


Figure 69. Reaction control and product isolation. SWCNTs were a) reacted with LA-OOH, and b) analyzed again after being stored in the dark for 1 week. Another sample was c) reacted with LA-OOH, and d) dialyzed to remove linoleic acids and surfactants, and re-dispersed in bovine serum albumin (1 wt %) in water.

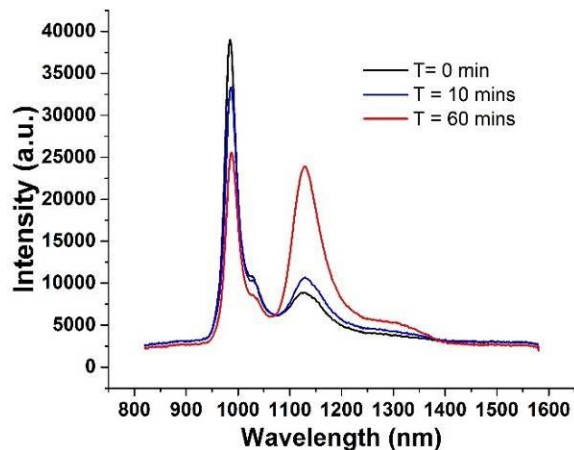


Figure 70. Emission spectra of sodium cholate coated SWCNTs/LA taken after sonication for 0, 10 and 60 minutes under normal laboratory lighting conditions.

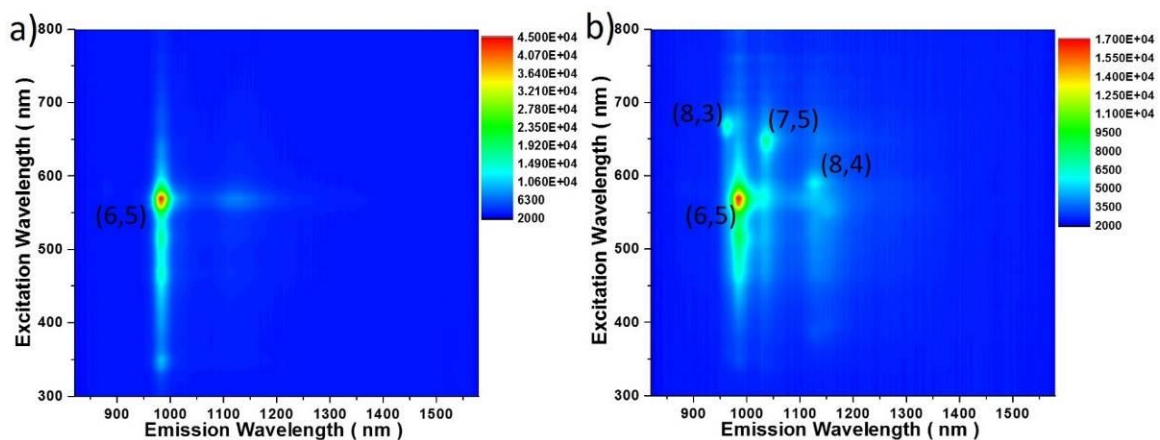


Figure 71. EE maps of raw a) (6,5) purified HiPco and b) CoMoCAT (6,5) SWCNTs.

BIBLIOGRAPHY

- (1) Kroto, H. W.; Heath, J. R.; O'Brien, S. C.; Curl, R. F.; Smalley, R. E. *Nature* **1985**, *318* (6042), 162–163.
- (2) Iijima, S. *Nature* **1991**, *354* (6348), 56–58.
- (3) Novoselov, K. S.; Geim, A. K.; Morozov, S. V.; Jiang, D.; Zhang, Y.; Dubonos, S. V.; Grigorieva, I. V.; Firsov, A. A. *Science* **2004**, *306* (5696), 666–669.
- (4) Balasubramanian, K.; Burghard, M. *Small* **2005**, *1* (2), 180–192.
- (5) Bachilo, S. M.; Strano, M. S.; Kittrell, C.; Hauge, R. H.; Smalley, R. E.; Weisman, R. B. *Science* **2002**, *298* (5602), 2361–2366.
- (6) Geim, A. K.; Novoselov, K. S. *Nat. Mater.* **2007**, *6* (3), 183–191.
- (7) Weisman, R. B. *Anal. Bioanal. Chem.* **2010**, *396* (3), 1015–1023.
- (8) Eklund, P. C.; Holden, J. M.; Jishi, R. A. *Carbon* **1995**, *33* (7), 959–972.
- (9) Dresselhaus, M. S.; Dresselhaus, G.; Jorio, A.; Souza Filho, A. G.; Pimenta, M. A.; Saito, R. *Acc. Chem. Res.* **2002**, *35* (12), 1070–1078.
- (10) Qin, L.-C. *Phys. Chem. Chem. Phys.* **2007**, *9* (1), 31–48.
- (11) Kim, S. N.; Rusling, J. F.; Papadimitrakopoulos, F. *Adv. Mater.* **2007**, *19* (20), 3214–3228.
- (12) Strano, M. S. *J. Am. Chem. Soc.* **2003**, *125* (51), 16148–16153.
- (13) Iijima, S. *Phys. B Condens. Matter* **2002**, *323* (1–4), 1–5.
- (14) Zhang, R.; Zhang, Y.; Zhang, Q.; Xie, H.; Qian, W.; Wei, F. *ACS Nano* **2013**, *7* (7), 6156–6161.
- (15) Hirsch, A. *Angew. Chem. Int. Ed.* **2002**, *41* (11), 1853.
- (16) Dervishi, E.; Li, Z.; Xu, Y.; Saini, V.; Biris, A. R.; Lupu, D.; Biris, A. S. *Part. Sci. Technol.* **2009**, *27* (2), 107–125.

- (17) Lu, J. P. *Phys. Rev. Lett.* **1997**, *79* (7), 1297–1300.
- (18) De Volder, M. F. L.; Tawfick, S. H.; Baughman, R. H.; Hart, A. J. *Science* **2013**, *339* (6119), 535–539.
- (19) Sgobba, V.; Guldi, D. M. *Chem. Soc. Rev.* **2009**, *38* (1), 165–184.
- (20) Battie, Y.; Ducloux, O.; Thobois, P.; Dorval, N.; Lauret, J. S.; Attal-Trétout, B.; Loiseau, A. *Carbon* **2011**, *49* (11), 3544–3552.
- (21) Allen, B. L. L.; Kichambare, P. D. D.; Star, A. *Adv. Mater.* **2007**, *19* (11), 1439–1451.
- (22) Robinson, J. T.; Hong, G.; Liang, Y.; Zhang, B.; Yaghi, O. K.; Dai, H. *J. Am. Chem. Soc.* **2012**, *134* (25), 10664–10669.
- (23) Heller, D. A.; Baik, S.; Eurell, T. E.; Strano, M. S. *Adv. Mater.* **2005**, *17* (23), 2793–2799.
- (24) Reilly, R. M. *J. Nucl. Med.* **2007**, *48* (7), 1039–1042.
- (25) Choi, K. Y.; Liu, G.; Lee, S.; Chen, X. *Nanoscale* **2012**, *4* (2), 330.
- (26) Shi Kam, N. W.; O’Connell, M.; Wisdom, J. A.; Dai, H. *Proc. Natl. Acad. Sci.* **2005**, *102* (33), 11600–11605.
- (27) Kim, J.-H.; Heller, D. A.; Jin, H.; Barone, P. W.; Song, C.; Zhang, J.; Trudel, L. J.; Wogan, G. N.; Tannenbaum, S. R.; Strano, M. S. *Nat. Chem.* **2009**, *1* (6), 473–481.
- (28) Lacerda, L.; Bianco, A.; Prato, M.; Kostarelos, K. *Adv. Drug Deliv. Rev.* **2006**, *58* (14), 1460–1470.
- (29) Liu, Z.; Tabakman, S.; Welsher, K.; Dai, H. *Nano Res.* **2009**, *2* (2), 85–120.
- (30) Hirata, E.; Ménard-Moyon, C.; Venturelli, E.; Takita, H.; Watari, F.; Bianco, A.; Yokoyama, A. *Nanotechnology* **2013**, *24* (43), 435101.
- (31) Resende, R.; Tonelli, F. M. P.; Santos, A. K.; Gomes, K. N.; Lorençon, E.; Ladeira, L. O.; Guatimosim, S. *Int. J. Nanomedicine* **2012**, *7*, 4511.
- (32) Liu, Z.; Sun, X.; Nakayama-Ratchford, N.; Dai, H. *ACS Nano* **2007**, *1* (1), 50–56.
- (33) Kuzmany, H.; Kukovecz, A.; Simon, F.; Holzweber, M.; Kramberger, C.; Pichler, T. *Synth. Met.* **2004**, *141* (1–2), 113–122.
- (34) Zhao, B.; Hu, H.; Mandal, S. K.; Haddon, R. C. *Chem. Mater.* **2005**, *17* (12), 3235–3241.
- (35) Lee, B.; Baek, Y.; Lee, M.; Jeong, D. H.; Lee, H. H.; Yoon, J.; Kim, Y. H. *Nat. Commun.* **2015**, *6* (May 2014), 7109.
- (36) Nikolaev, P.; Bronikowski, M. J.; Bradley, R. K.; Rohmund, F.; Colbert, D. T.; Smith, K.

- .; Smalley, R. E. *Chem. Phys. Lett.* **1999**, *313* (1–2), 91–97.
- (37) Kitiyanan, B.; Alvarez, W. E.; Harwell, J. H.; Resasco, D. E. *Chem. Phys. Lett.* **2000**, *317* (3–5), 497–503.
- (38) Merchan-Merchan, W.; Saveliev, A. V.; Kennedy, L.; Jimenez, W. C. *Prog. Energy Combust. Sci.* **2010**, *36* (6), 696–727.
- (39) Kolosnjaj-Tabi, J.; Just, J.; Hartman, K. B.; Laoudi, Y.; Boudjemaa, S.; Alloyeau, D.; Szwarc, H.; Wilson, L. J.; Moussa, F. *EBioMedicine* **2015**, *2* (11), 1697–1704.
- (40) Guo, T.; Nikolaev, P.; Rinzler, A. G.; Tomanek, D.; Colbert, D. T.; Smalley, R. E. *J. Phys. Chem.* **1995**, *99* (27), 10694–10697.
- (41) Liu, H.; Nishide, D.; Tanaka, T.; Kataura, H. *Nat. Commun.* **2011**, *2* (May), 309.
- (42) Lolli, G.; Zhang, L.; Balzano, L.; Sakulchaicharoen, N.; Tan, Y.; Resasco, D. E. *J. Phys. Chem. B* **2006**, *110* (5), 2108–2115.
- (43) Duan, H. M.; McKinnon, J. T. *J. Phys. Chem.* **1994**, *98* (49), 12815–12818.
- (44) Richter, H.; Treska, M.; Howard, J. B.; Wen, J. Z.; Thomasson, S. B.; Reading, A. A.; Jardim, P. M.; Vander Sande, J. B. *J. Nanosci. Nanotechnol.* **2008**, *8* (11), 6065–6074.
- (45) Haddon, R. C.; Sippel, J.; Rinzler, A. G.; Papadimitrakopoulos, F. *MRS Bull.* **2004**, *29* (4), 252–259.
- (46) Ansón-Casaos, A.; González, M.; González-Domínguez, J. M.; Martínez, M. T. *Langmuir* **2011**, *27* (11), 7192–7198.
- (47) Itkis, M. E.; Perea, D. E.; Niyogi, S.; Rickard, S. M.; Hamon, M. A.; Hu, H.; Zhao, B.; Haddon, R. C. *Nano Lett.* **2003**, *3* (3), 309–314.
- (48) Datsyuk, V.; Kalyva, M.; Papagelis, K.; Parthenios, J.; Tasis, D.; Siokou, A.; Kallitsis, I.; Galiotis, C. *Carbon* **2008**, *46* (6), 833–840.
- (49) Chiang, I. W.; Brinson, B. E.; Smalley, R. E.; Margrave, J. L.; Hauge, R. H. *J. Phys. Chem. B* **2001**, *105*, 1157–1161.
- (50) Chiang, I. W.; Brinson, B. E.; Huang, A. Y.; Willis, P. A.; Bronikowski, M. J.; Margrave, J. L.; Smalley, R. E.; Hauge, R. H. *J. Phys. Chem. B* **2001**, *105* (35), 8297–8301.
- (51) Liu, J.; Rinzler, A. G.; Dai, H.; Hafner, J. H.; Bradley, R. K.; Boul, P. J.; Lu, A.; Iverson, T.; Shelimov, K.; Huffman, C. B.; Rodriguez-Macias, F.; Shon, Y.-S.; Lee, T. R.; Colbert, D. T.; Smalley, R. E. *Science* **1998**, *280* (5367), 1253–1256.
- (52) Wang, Y.; Shan, H.; Hauge, R. H.; Pasquali, M.; Smalley, R. E. *J. Phys. Chem. B* **2007**, *111* (6), 1249–1252.

- (53) Yang, C.-M.; Park, J. S.; An, K. H.; Lim, S. C.; Seo, K.; Kim, B.; Park, K. A.; Han, S.; Park, C. Y.; Lee, Y. H. *J. Phys. Chem. B* **2005**, *109* (41), 19242–19248.
- (54) Strano, M. S.; Dyke, C. A.; Usrey, M. L.; Barone, P. W.; Allen, M. J.; Shan, H. W.; Kittrell, C.; Hauge, R. H.; Tour, J. M.; Smalley, R. E. *Science* **2003**, *301* (5639), 1519–1522.
- (55) Banerjee, S.; Hemraj-Benny, T.; Wong, S. S. *Adv. Mater.* **2005**, *17* (1), 17–29.
- (56) O’Connell, M. J.; Bachilo, S. M.; Huffman, C. B.; Moore, V. C.; Strano, M. S.; Haroz, E. H.; Rialon, K. L.; Boul, P. J.; Noon, W. H.; Kittrell, C.; Ma, J.; Hauge, R. H.; Weisman, R. B.; Smalley, R. E. *Science* **2002**, *297* (5581), 593–596.
- (57) Moore, V. C.; Strano, M. S.; Haroz, E. H.; Hauge, R. H.; Smalley, R. E.; Schmidt, J.; Talmon, Y. *Nano Lett.* **2003**, *3* (10), 1379–1382.
- (58) Hilmer, A. J.; McNicholas, T. P.; Lin, S.; Zhang, J.; Wang, Q. H.; Mendenhall, J. D.; Song, C.; Heller, D. A.; Barone, P. W.; Blankschtein, D.; Strano, M. S. *Langmuir* **2012**, *28* (2), 1309–1321.
- (59) Fagan, J. A.; Zheng, M.; Rastogi, V.; Simpson, J. R.; Khripin, C. Y.; Silvera Batista, C. A.; Hight Walker, A. R. *ACS Nano* **2013**, *7* (4), 3373–3387.
- (60) Flavel, B. S.; Kappes, M. M.; Krupke, R.; Hennrich, F. *ACS Nano* **2013**, *7* (4), 3557–3564.
- (61) Britz, D. A.; Khlobystov, A. N. *Chem. Soc. Rev.* **2006**, *35* (7), 637.
- (62) Chen, R. J.; Zhang, Y.; Wang, D.; Dai, H. *J. Am. Chem. Soc.* **2001**, *123* (16), 3838–3839.
- (63) Ehli, C.; Rahman, G. M. A.; Jux, N.; Balbinot, D.; Guldi, D. M.; Paolucci, F.; Maccaccio, M.; Paolucci, D.; Melle-Franco, M.; Zerbetto, F.; Campidelli, S.; Prato, M. *J. Am. Chem. Soc.* **2006**, *128* (34), 11222–11231.
- (64) Rahman, G. M. A.; Guldi, D. M.; Campidelli, S.; Prato, M. *J. Mater. Chem.* **2006**, *16* (1), 62–65.
- (65) Peng, X.; Komatsu, N.; Bhattacharya, S.; Shimawaki, T.; Aonuma, S.; Kimura, T.; Osuka, A. *Nat. Nanotechnol.* **2007**, *2* (6), 361–365.
- (66) Peng, X.; Komatsu, N.; Kimura, T.; Osuka, A. *ACS Nano* **2008**, *2* (10), 2045–2050.
- (67) Konduru, N. V.; Tyurina, Y. Y.; Feng, W.; Basova, L. V.; Belikova, N. A.; Bayir, H.; Clark, K.; Rubin, M.; Stolz, D.; Vallhov, H.; Scheynius, A.; Witas, E.; Fadeel, B.; Kichambare, P. D.; Star, A.; Kisin, E. R.; Murray, A. R.; Shvedova, A. A.; Kagan, V. E. *PLoS One* **2009**, *4* (2), e4398.
- (68) Gonzalez-Dominguez, J. M.; Tesa-Serrate, M. A.; Anson-Casaos, A.; Diez-Pascual, A.

- M.; Gomez-Fatou, M. A.; Martinez, M. T. *J. Phys. Chem. C* **2012**, *116* (13), 7399–7408.
- (69) Tu, X.; Manohar, S.; Jagota, A.; Zheng, M. *Nature* **2009**, *460* (7252), 250–253.
- (70) Bhattacharya, K.; Sacchetti, C.; El-Sayed, R.; Fornara, A.; Kotchey, G. P.; Gaugler, J. A.; Star, A.; Bottini, M.; Fadeel, B. *Nanoscale* **2014**, *6* (24), 14686–14690.
- (71) Minami, N.; Kim, Y.; Miyashita, K.; Kazaoui, S.; Nalini, B. *Appl. Phys. Lett.* **2006**, *88* (9), 93123.
- (72) Khripin, C. Y.; Fagan, J. A.; Zheng, M. *J. Am. Chem. Soc.* **2013**, *135* (18), 6822–6825.
- (73) Komatsu, N.; Wang, F. *Materials* **2010**, *3* (7), 3818–3844.
- (74) Zhou, W.; Ooi, Y. H.; Russo, R.; Papanek, P.; Luzzi, D. E.; Fischer, J. E.; Bronikowski, M. J.; Willis, P. A.; Smalley, R. E. *Chem. Phys. Lett.* **2001**, *350* (1–2), 6–14.
- (75) Ziegler, K. J.; Gu, Z. N.; Peng, H. Q.; Flor, E. L.; Hauge, R. H.; Smalley, R. E. *J. Am. Chem. Soc.* **2005**, *127* (5), 1541–1547.
- (76) Arnold, M. S.; Green, A. A.; Hulvat, J. F.; Stupp, S. I.; Hersam, M. C. *Nat. Nanotechnol.* **2006**, *1* (1), 60–65.
- (77) Ghosh, S.; Bachilo, S. M.; Weisman, R. B. *Nat. Nanotechnol.* **2010**, *5* (6), 443–450.
- (78) Fagan, J. A.; Becker, M. L.; Chun, J.; Hobbie, E. K. *Adv. Mater.* **2008**, *20* (9), 1609–1613.
- (79) Hornyak, G. L.; Dutta, J.; Tibbals, H. F.; Rao, A. K. *Introduction to Nanoscience*; CRC Press: Danvers, 2008.
- (80) Pumera, M. *Chem. Asian J.* **2009**, *4* (2), 250–253.
- (81) Rinzler, A. G.; Liu, J.; Dai, H.; Nikolaev, P.; Huffman, C. B.; Rodríguez-Macías, F. J.; Boul, P. J.; Lu, A. H.; Heymann, D.; Colbert, D. T.; Lee, R. S.; Fischer, J. E.; Rao, A. M.; Eklund, P. C.; Smalley, R. E. *Appl. Phys. A* **1998**, *67* (1), 29–37.
- (82) Tunuguntla, R. H.; Allen, F. I.; Kim, K.; Belliveau, A.; Noy, A. *Nat. Nanotechnol.* **2016**, *11* (April), 639–644.
- (83) Warner, J. H.; Young, N. P.; Kirkland, A. I.; Briggs, G. A. D. *Nat. Mater.* **2011**, *10* (12), 958–962.
- (84) Dresselhaus, M. S.; Dresselhaus, G.; Jorio, A.; Souza Filho, A. G.; Saito, R. *Carbon* **2002**, *40* (12), 2043–2061.
- (85) Saito, R.; Takeya, T.; Kimura, T.; Dresselhaus, G.; Dresselhaus, M. S. *Phys. Rev. B* **1998**, *57* (7), 4145–4153.
- (86) Graupner, R. *J. Raman Spectrosc.* **2007**, *38* (6), 673–683.

- (87) Dresselhaus, M. S.; Eklund, P. C. *Adv. Phys.* **2000**, *49* (6), 705–814.
- (88) Piscanec, S.; Lazzeri, M.; Mauri, F.; Ferrari, A. C. *Eur. Phys. J. Spec. Top.* **2007**, *148* (1), 159–170.
- (89) Thomsen, C.; Reich, S. In *Light Scattering in Solid IX*; Springer Berlin / Heidelberg, 2007; Vol. 232, pp 115–232.
- (90) Dresselhaus, M. S.; Dresselhaus, G.; Saito, R.; Jorio, A. *Phys. Rep.* **2005**, *409* (2), 47–99.
- (91) Dyke, C. A.; Tour, J. M. *J. Am. Chem. Soc.* **2003**, *125* (5), 1156–1157.
- (92) Dresselhaus, M. S.; Jorio, A.; Souza Filho, A. G.; Saito, R. *Philos. Trans. R. Soc. A Math. Phys. Eng. Sci.* **2010**, *368* (1932), 5355–5377.
- (93) Dong, L.-X.; Chen, Q. *Front. Mater. Sci. China* **2010**, *4* (1), 45–51.
- (94) Fantini, C.; Jorio, A.; Souza, M.; Strano, M. S.; Dresselhaus, M. S.; Pimenta, M. A. *Phys. Rev. Lett.* **2004**, *93* (14), 147406.
- (95) Rance, G. A.; Marsh, D. H.; Nicholas, R. J.; Khlobystov, A. N. *Chem. Phys. Lett.* **2010**, *493* (1–3), 19–23.
- (96) Suzuki, S.; Mizusawa, T.; Okazaki, T.; Achiba, Y. *Eur. Phys. J. D* **2009**, *52* (1–3), 83–86.
- (97) Kawai, M.; Kyakuno, H.; Suzuki, T.; Igarashi, T.; Suzuki, H.; Okazaki, T.; Kataura, H.; Maniwa, Y.; Yanagi, K. *J. Am. Chem. Soc.* **2012**, *134* (23), 9545–9548.
- (98) Tan, P. H.; Rozhin, A. G.; Hasan, T.; Hu, P.; Scardaci, V.; Milne, W. I.; Ferrari, A. C. *Phys. Rev. Lett.* **2007**, *99* (13), 137402.
- (99) Wei, L.; Li, L. J.; Chan-Park, M. B.; Yang, Y.; Chen, Y. *J. Phys. Chem. C* **2010**, *114* (14), 6704–6711.
- (100) Miyauchi, Y.; Oba, M.; Maruyama, S. *Phys. Rev. B* **2006**, *74* (20), 205440.
- (101) Hwang, J.-Y.; Nish, A.; Doig, J.; Douven, S.; Chen, C.-W.; Chen, L.-C.; Nicholas, R. J. *J. Am. Chem. Soc.* **2008**, *130* (11), 3543–3553.
- (102) Larsen, B. A.; Deria, P.; Holt, J. M.; Stanton, I. N.; Heben, M. J.; Therien, M. J.; Blackburn, J. L. *J. Am. Chem. Soc.* **2012**, *134* (30), 12485–12491.
- (103) Ohno, Y.; Iwasaki, S.; Murakami, Y.; Kishimoto, S.; Maruyama, S.; Mizutani, T. *Phys. Rev. B* **2006**, *73* (23), 235427.
- (104) Haggemueller, R.; Rahatekar, S. S. S.; Fagan, J. a; Chun, J.; Becker, M. L.; Naik, R. R.; Krauss, T.; Carlson, L.; Kadla, J. F.; Trulove, P. C.; Fox, D. F.; Delong, H. C.; Fang, Z.; Kelley, S. O.; Gilman, J. W. *Langmuir* **2008**, *24* (9), 5070–5078.

- (105) Cherukuri, T. K.; Tsyboulski, D. A.; Weisman, R. B. *ACS Nano* **2012**, *6* (1), 843–850.
- (106) Fagan, J. A.; Simpson, J. R.; Bauer, B. J.; Lacerda, S. H. D. P.; Becker, M. L.; Chun, J.; Migler, K. B.; Walker, A. R. H.; Hobbie, E. K. *J. Am. Chem. Soc.* **2007**, *129* (34), 10607–10612.
- (107) Knorr, F. J.; Hung, W.-C.; Wai, C. M. *Langmuir* **2009**, *25* (18), 10417–10421.
- (108) McDonald, T. J.; Blackburn, J. L.; Metzger, W. K.; Rumbles, G.; Heben, M. J. *J. Phys. Chem. C* **2007**, *111* (48), 17894–17900.
- (109) Reuel, N. F.; Dupont, A.; Thouvenin, O.; Lamb, D. C.; Strano, M. S. *ACS Nano* **2012**, *6* (6), 5420–5428.
- (110) Hong, G.; Wu, J. Z.; Robinson, J. T.; Wang, H.; Zhang, B.; Dai, H. *Nat. Commun.* **2012**, *3*, 700.
- (111) Ghosh, S.; Bachilo, S. M.; Simonette, R. a; Beckingham, K. M.; Weisman, R. B. *Science* **2010**, *330* (6011), 1656–1659.
- (112) Piao, Y.; Meany, B.; Powell, L. R.; Valley, N.; Kwon, H.; Schatz, G. C.; Wang, Y. *Nat. Chem.* **2013**, *5* (10), 840–845.
- (113) Zhang, Y.; Valley, N.; Brozena, A. H.; Piao, Y.; Song, X.; Schatz, G. C.; Wang, Y. *J. Phys. Chem. Lett.* **2013**, *4* (5), 826–830.
- (114) Iwamura, M.; Akizuki, N.; Miyauchi, Y.; Mouri, S.; Shaver, J.; Gao, Z.; Cognet, L.; Lounis, B.; Matsuda, K. *ACS Nano* **2014**, *8* (11), 11254–11260.
- (115) Yim, W. L.; Johnson, J. K. *J. Phys. Chem. C* **2009**, *113* (41), 17636–17642.
- (116) Kwon, H.; Kim, M.; Meany, B.; Piao, Y.; Powell, L. R.; Wang, Y. *J. Phys. Chem. C* **2015**, *119* (7), 3733–3739.
- (117) Lam, C. W.; James, J. T.; McCluskey, R.; Hunter, R. L. *Toxicol. Sci.* **2003**, *77* (1), 126–134.
- (118) Warheit, D. B.; Laurence, B. R.; Reed, K. L.; Roach, D. H.; Reynolds, G. A. M.; Webb, T. R. *Toxicol. Sci.* **2003**, *77* (1), 117–125.
- (119) Ge, C.; Meng, L.; Xu, L.; Bai, R.; Du, J.; Zhang, L.; Li, Y.; Chang, Y.; Zhao, Y.; Chen, C. *Nanotoxicology* **2012**, *6* (5), 526–542.
- (120) Liu, Y.; Zhao, Y.; Sun, B.; Chen, C. *Acc. Chem. Res.* **2013**, *46* (3), 702–713.
- (121) Kagan, V. E.; Tyurina, Y. Y.; Tyurin, V. A.; Konduru, N. V.; Potapovich, A. I.; Osipov, A. N.; Kisin, E. R.; Schwegler-Berry, D.; Mercer, R.; Castranova, V.; Shvedova, A. A. *Toxicol. Lett.* **2006**, *165* (1), 88–100.

- (122) Pulskamp, K.; Diabaté, S.; Krug, H. F. *Toxicol. Lett.* **2007**, *168* (1), 58–74.
- (123) Sato, Y.; Yokoyama, A.; Shibata, K.; Akimoto, Y.; Ogino, S.; Nodasaka, Y.; Kohgo, T.; Tamura, K.; Akasaka, T.; Uo, M.; Motomiya, K.; Jeyadevan, B.; Ishiguro, M.; Hatakeyama, R.; Watari, F.; Tohji, K. *Mol. Biosyst.* **2005**, *1* (2), 176.
- (124) Yamashita, K.; Yoshioka, Y.; Higashisaka, K.; Morishita, Y.; Yoshida, T.; Fujimura, M.; Kayamuro, H.; Nabeshi, H.; Yamashita, T.; Nagano, K.; Abe, Y.; Kamada, H.; Kawai, Y.; Mayumi, T.; Yoshikawa, T.; Itoh, N.; Tsunoda, S.; Tsutsumi, Y. *Inflammation* **2010**, *33* (4), 276–280.
- (125) Poland, C. A.; Duffin, R.; Kinloch, I.; Maynard, A.; Wallace, W. A. H.; Seaton, A.; Stone, V.; Brown, S.; MacNee, W.; Donaldson, K. *Nat. Nanotechnol.* **2008**, *3* (7), 423–428.
- (126) Palomäki, J.; Välimäki, E.; Sund, J.; Vippola, M.; Clausen, P. A.; Jensen, K. A.; Savolainen, K.; Matikainen, S.; Alenius, H. *ACS Nano* **2011**, *5* (9), 6861–6870.
- (127) Wick, P.; Manser, P.; Limbach, L. K.; Dettlaff-Weglikowska, U.; Krumeich, F.; Roth, S.; Stark, W. J.; Bruinink, A. *Toxicol. Lett.* **2007**, *168* (2), 121–131.
- (128) Bottini, M.; Bruckner, S.; Nika, K.; Bottini, N.; Bellucci, S.; Magrini, A.; Bergamaschi, A.; Mustelin, T. *Toxicol. Lett.* **2006**, *160* (2), 121–126.
- (129) Porter, A. E.; Gass, M.; Bendall, J. S.; Muller, K.; Goode, A.; Skepper, J. N.; Midgley, P. A.; Welland, M. *ACS Nano* **2009**, *3* (6), 1485–1492.
- (130) Shi Kam, N. W.; Jessop, T. C.; Wender, P. a; Dai, H. *J. Am. Chem. Soc.* **2004**, *126* (22), 6850–6851.
- (131) Williams, K. A.; Veenhuizen, P. T. M.; de la Torre, B. G.; Eritja, R.; Dekker, C. *Nature* **2002**, *420* (6917), 761.
- (132) Sayes, C. M.; Liang, F.; Hudson, J. L.; Mendez, J.; Guo, W.; Beach, J. M.; Moore, V. C.; Doyle, C. D.; West, J. L.; Billups, W. E.; Ausman, K. D.; Colvin, V. L. *Toxicol. Lett.* **2006**, *161* (2), 135–142.
- (133) Cherukuri, P.; Bachilo, S. M.; Litovsky, S. H.; Weisman, R. B. *J. Am. Chem. Soc.* **2004**, *126* (48), 15638–15639.
- (134) Yang, S. T.; Wang, X.; Jia, G.; Gu, Y.; Wang, T.; Nie, H.; Ge, C.; Wang, H.; Liu, Y. *Toxicol. Lett.* **2008**, *181* (3), 182–189.
- (135) Schipper, M. L.; Nakayama-Ratchford, N.; Davis, C. R.; Kam, N. W. S.; Chu, P.; Liu, Z.; Sun, X.; Dai, H.; Gambhir, S. S. *Nat. Nanotechnol.* **2008**, *3* (4), 216–221.
- (136) Welsher, K.; Sherlock, S. P.; Dai, H. *Proc. Natl. Acad. Sci. U. S. A.* **2011**, *108* (22), 8943–8948.

- (137) Antaris, A. L.; Robinson, J. T.; Yaghi, O. K.; Hong, G.; Diao, S.; Luong, R.; Dai, H. *ACS Nano* **2013**, *7* (4), 3644–3652.
- (138) Welsher, K.; Liu, Z.; Daranciang, D.; Dai, H. *Nano Lett.* **2008**, *8* (2), 586–590.
- (139) Welsher, K.; Liu, Z.; Sherlock, S. P.; Robinson, J. T.; Chen, Z.; Daranciang, D.; Dai, H. *Nat. Nanotechnol.* **2009**, *4* (11), 773–780.
- (140) Liu, Z.; Davis, C.; Cai, W.; He, L.; Chen, X.; Dai, H. *Proc. Natl. Acad. Sci. U. S. A.* **2008**, *105* (5), 1410–1415.
- (141) Yang, S.; Guo, W.; Lin, Y.; Deng, X.; Wang, H.; Sun, H.; Liu, Y.; Wang, X.; Wang, W.; Chen, M.; Huang, Y.; Sun, Y.-P. *J. Phys. Chem. C* **2007**, *111* (48), 17761–17764.
- (142) Shvedova, A. A.; Kisin, E. R.; Mercer, R.; Murray, A. R.; Johnson, V. J.; Potapovich, A. I.; Tyurina, Y. Y.; Gorelik, O.; Arepalli, S.; Schwegler-Berry, D.; Hubbs, A. F.; Antonini, J.; Evans, D. E.; Ku, B.-K.; Ramsey, D.; Maynard, A.; Kagan, V. E.; Castranova, V.; Baron, P. *Am. J. Physiol. Lung Cell. Mol. Physiol.* **2005**, *289* (5), L698-708.
- (143) Kagan, V. E.; Konduru, N. V.; Feng, W.; Allen, B. L.; Conroy, J.; Volkov, Y.; Vlasova, I. I.; Belikova, N. A.; Yanamala, N.; Kapralov, A.; Tyurina, Y. Y.; Shi, J.; Kisin, E. R.; Murray, A. R.; Franks, J.; Stolz, D.; Gou, P.; Klein-Seetharaman, J.; Fadeel, B.; Star, A.; Shvedova, A. A. *Nat. Nanotechnol.* **2010**, *5* (5), 354–359.
- (144) Shvedova, A. A.; Kapralov, A. A.; Feng, W. H.; Kisin, E. R.; Murray, A. R.; Mercer, R. R.; St Croix, C. M.; Lang, M. A.; Watkins, S. C.; Konduru, N. V.; Allen, B. L.; Conroy, J.; Kotchey, G. P.; Mohamed, B. M.; Meade, A. D.; Volkov, Y.; Star, A.; Fadeel, B.; Kagan, V. E. *PLoS One* **2012**, *7* (3), e30923.
- (145) Allen, B. L.; Kichambare, P. D.; Gou, P.; Vlasova, I. I.; Kapralov, A. A.; Konduru, N.; Kagan, V. E.; Star, A. *Nano Lett.* **2008**, *8* (11), 3899–3903.
- (146) Andón, F. T.; Kapralov, A. A.; Yanamala, N.; Feng, W.; Baygan, A.; Chambers, B. J.; Hultenby, K.; Ye, F.; Toprak, M. S.; Brandner, B. D.; Fornara, A.; Klein-Seetharaman, J.; Kotchey, G. P.; Star, A.; Shvedova, A. A.; Fadeel, B.; Kagan, V. E. *Small* **2013**, *9* (16), 2721–2729.
- (147) Vlasova, I. I.; Sokolov, A. V.; Chekanov, A. V.; Kostevich, V. A.; Vasilyev, V. B. *Russ. J. Bioorganic Chem.* **2011**, *37* (4), 453–463.
- (148) Lalwani, G.; Xing, W.; Sitharaman, B. *J. Mater. Chem. B* **2014**, *2* (37), 6354.
- (149) Zhang, C.; Chen, W.; Alvarez, P. J. J. *Environ. Sci. Technol.* **2014**, *48* (14), 7918–7923.
- (150) Kawaoka, A.; Kawamoto, T.; Ohta, H.; Sekine, M.; Takano, M.; Shinmyo, A. *Plant Cell Rep.* **1994**, *13–13* (3–4), 149–154.
- (151) Berglund, G. I.; Carlsson, G. H.; Smith, A. T.; Szöke, H.; Henriksen, A.; Hajdu, J.; Szoke,

- H.; Henriksen, A.; Hajdu, J. *Nature* **2002**, *417* (6887), 463–468.
- (152) Adediran, S. A.; Lambeir, A.-M. *Eur. J. Biochem.* **1989**, *186* (3), 571–576.
- (153) Weinryb, I. *Biochemistry* **1966**, *5* (6), 2003–2008.
- (154) Ali, M.; Tahir, M. N.; Siwy, Z.; Neumann, R.; Tremel, W.; Ensinger, W. *Anal. Chem.* **2011**, *83* (5), 1673–1680.
- (155) Wang, Y.; Du, J.; Li, Y.; Shan, D.; Zhou, X.; Xue, Z.; Lu, X. *Colloids Surf., B* **2012**, *90*, 62–67.
- (156) Allen, B. L.; Kotchey, G. P.; Chen, Y.; Yanamala, N. V. K.; Klein-Seetharaman, J.; Kagan, V. E.; Star, A. *J. Am. Chem. Soc.* **2009**, *131* (47), 17194–17205.
- (157) Russier, J.; Menard-Moyon, C.; Venturelli, E.; Gravel, E.; Marcolongo, G.; Meneghetti, M.; Doris, E.; Bianco, A.; Ménard-Moyon, C.; Venturelli, E.; Gravel, E.; Marcolongo, G.; Meneghetti, M.; Doris, E.; Bianco, A. *Nanoscale* **2011**, *3* (3), 893–896.
- (158) Zhao, Y.; Allen, B. L.; Star, A. *J. Phys. Chem. A* **2011**, *115* (34), 9536–9544.
- (159) Kotchey, G. P.; Allen, B. L.; Vedala, H.; Yanamala, N.; Kapralov, A. A.; Tyurina, Y. Y.; Klein-Seetharaman, J.; Kagan, V. E.; Star, A. *ACS Nano* **2011**, *5* (3), 2098–2108.
- (160) Sureshbabu, A. R.; Kurapati, R.; Russier, J.; Ménard-Moyon, C.; Bartolini, I.; Meneghetti, M.; Kostarelos, K.; Bianco, A. *Biomaterials* **2015**, *72*, 20–28.
- (161) Arnhold, J.; Furtmüller, P. G.; Regelsberger, G.; Obinger, C. *Eur. J. Biochem.* **2001**, *268* (19), 5142–5148.
- (162) Furtmüller, P. G.; Zederbauer, M.; Jantschko, W.; Helm, J.; Bogner, M.; Jakopitsch, C.; Obinger, C. *Arch. Biochem. Biophys.* **2006**, *445* (2), 199–213.
- (163) Klebanoff, S. J.; Kettle, A. J.; Rosen, H.; Winterbourn, C. C.; Nauseef, W. M. *J. Leukoc. Biol.* **2013**, *93* (2), 185–198.
- (164) Kotchey, G. P.; Gaugler, J. A.; Kapralov, A. A.; Kagan, V. E.; Star, A. *J. Mater. Chem. B* **2013**, *1* (3), 302–309.
- (165) Seo, W.; Kapralov, A. A.; Shurin, G. V.; Shurin, M. R.; Kagan, V. E.; Star, A. *Nanoscale* **2015**, *7* (19), 8689–8694.
- (166) Kurapati, R.; Russier, J.; Squillaci, M. A.; Treossi, E.; Ménard-Moyon, C.; Del Rio-Castillo, A. E.; Vazquez, E.; Samorì, P.; Palermo, V.; Bianco, A. *Small* **2015**, *11* (32), 3985–3994.
- (167) Zhao, Y.; Burkert, S. C.; Tang, Y.; Sorescu, D. C.; Kapralov, A. A.; Shurin, G. V.; Shurin, M. R.; Kagan, V. E.; Star, A. *J. Am. Chem. Soc.* **2015**, *137* (2), 675–684.

- (168) Zhang, M.; Yang, M.; Bussy, C.; Iijima, S.; Kostarelos, K.; Yudasaka, M. *Nanoscale* **2015**, 7 (7), 2834–2840.
- (169) Vlasova, I. I.; Vakhrusheva, T. V.; Sokolov, A. V.; Kostevich, V. A.; Gusev, A. A.; Gusev, S. A.; Melnikova, V. I.; Lobach, A. S. *Toxicol. Appl. Pharmacol.* **2012**, 264 (1), 131–142.
- (170) Lu, N.; Li, J.; Tian, R.; Peng, Y. *Chem. Res. Toxicol.* **2014**, 27 (6), 1070–1077.
- (171) Yang, S.; Wang, H.; Meziani, M. J.; Liu, Y.; Wang, X.; Sun, Y.-P. *Biomacromolecules* **2009**, 10 (7), 2009–2012.
- (172) Chiu, C. F.; Barth, B. A.; Kotchey, G. P.; Zhao, Y.; Gogick, K. A.; Saidi, W. A.; Petoud, S.; Star, A. *J. Am. Chem. Soc.* **2013**, 135 (36), 13356–13364.
- (173) Collins, P. G.; Avouris, P. *Sci. Am.* **2000**, 283 (6), 62–69.
- (174) Fadel, T. R.; Look, M.; Staffier, P. A.; Haller, G. L.; Pfefferle, L. D.; Fahmy, T. M. *Langmuir* **2010**, 26 (8), 5645–5654.
- (175) Guldi, D. M.; Rahman, G. M. A.; Prato, M.; Jux, N.; Qin, S. H.; Ford, W. *Angew. Chem. Int. Ed.* **2005**, 44 (13), 2015–2018.
- (176) Lam, C.-W. W.; James, J. T.; McCluskey, R.; Arepalli, S.; Hunter, R. L. *Crit. Rev. Toxicol.* **2006**, 36 (3), 189–217.
- (177) Shi, X.; von dem Bussche, A.; Hurt, R. H.; Kane, A. B.; Gao, H. *Nat. Nanotechnol.* **2011**, 6 (11), 714–719.
- (178) Ali-Boucetta, H.; Nunes, A.; Sainz, R.; Herrero, M. A.; Tian, B.; Prato, M.; Bianco, A.; Kostarelos, K. *Angew. Chem. Int. Ed.* **2013**, 52 (8), 2274–2278.
- (179) Kolosnjaj-Tabi, J.; Hartman, K. B.; Boudjemaa, S.; Ananta, J. S.; Morgant, G.; Szwarc, H.; Wilson, L. J.; Moussa, F. *ACS Nano* **2010**, 4 (3), 1481–1492.
- (180) Murphy, F. A.; Poland, C. A.; Duffin, R.; Al-Jamal, K. T.; Ali-Boucetta, H.; Nunes, A.; Byrne, F.; Prina-Mello, A.; Volkov, Y.; Li, S.; Mather, S. J.; Bianco, A.; Prato, M.; MacNee, W.; Wallace, W. A.; Kostarelos, K.; Donaldson, K. *Am. J. Pathol.* **2011**, 178 (6), 2587–2600.
- (181) Chen, J.; Chen, S.; Zhao, X.; Kuznetsova, L. V.; Wong, S. S.; Ojima, I. *J. Am. Chem. Soc.* **2008**, 130 (49), 16778–16785.
- (182) Cognet, L.; Tsyboulski, D. a; Rocha, J.-D. R.; Doyle, C. D.; Tour, J. M.; Weisman, R. B. *Science* **2007**, 316 (5830), 1465–1468.
- (183) Dukovic, G.; White, B. E.; Zhou, Z. Y.; Wang, F.; Jockusch, S.; Steigerwald, M. L.; Heinz, T. F.; Friesner, R. A.; Turro, N. J.; Brus, L. E. *J. Am. Chem. Soc.* **2004**, 126 (46),

15269–15276.

- (184) Kotchey, G. P.; Hasan, S. A.; Kapralov, A. A.; Ha, S. H.; Kim, K.; Shvedova, A. A.; Kagan, V. E.; Star, A. *Acc. Chem. Res.* **2012**, *45* (10), 1770–1781.
- (185) Matousek, P.; Towrie, M.; Parker, A. W. *J. Raman Spectrosc.* **2002**, *33* (4), 238–242.
- (186) Maultzsch, J.; Telg, H.; Reich, S.; Thomsen, C. *Phys. Rev. B* **2005**, *72* (20), 205438.
- (187) O’Connell, M. J.; Sivaram, S.; Doorn, S. K.; O’Connell, M. J.; Sivaram, S.; Doorn, S. K. *Phys. Rev. B* **2004**, *69* (23), 235415.
- (188) Barros, E. B.; Filho, A. G. S.; Lemos, V.; Filho, J. M.; Fagan, S. B.; Herbst, M. H.; Rosolen, J. M.; Luengo, C. A.; Huber, J. G. *Carbon* **2005**, *43* (12), 2495–2500.
- (189) Martínez, M.; Martinez, M. T.; Callejas, M. A.; Benito, A. M.; Cochet, M.; Seeger, T.; Anson, A.; Schreiber, J.; Gordon, C.; Marhic, C.; Chauvet, O.; Fierro, J. L. G.; Maser, W. K. *Carbon* **2003**, *41* (12), 2247–2256.
- (190) Huang, L. S.; Colas, C.; de Montellano, P. R. O. *J. Am. Chem. Soc.* **2004**, *126* (40), 12865–12873.
- (191) Liu, X.; Hurt, R. H.; Kane, A. B. *Carbon* **2010**, *48* (7), 1961–1969.
- (192) Hou, W. C.; He, C. J.; Wang, Y. S.; Wang, D. K.; Zepp, R. G. *Environ. Sci. Technol.* **2016**, *50* (7), 3494–3502.
- (193) Qu, X.; Alvarez, P. J. J.; Li, Q. *Environ. Sci. Technol.* **2013**, *47* (24), 14080–14088.
- (194) Boehm, H. P. *Carbon* **2002**, *40* (2), 145–149.
- (195) O’Connell, M. J.; Eibergen, E. E.; Doorn, S. K.; O’Connell, M. J.; Eibergen, E. E.; Doorn, S. K. *Nat. Mater.* **2005**, *4* (5), 412–418.
- (196) Kim, K. K.; Yoon, S.-M.; Park, H. K.; Shin, H.-J.; Kim, S. M.; Bae, J. J.; Cui, Y.; Kim, J. M.; Choi, J.-Y.; Lee, Y. H. *New J. Chem.* **2010**, *34* (10), 2183.
- (197) Tanaka, Y.; Niidome, Y.; Nakashima, N. *Chem. Lett.* **2009**, *38* (8), 864–865.
- (198) Muramatsu, H.; Hayashi, T.; Kim, Y. A.; Shimamoto, D.; Kim, Y. J.; Tantrakarn, K.; Endo, M.; Terrones, M.; Dresselhaus, M. S. *Chem. Phys. Lett.* **2005**, *414* (4–6), 444–448.
- (199) Elstner, M.; Porezag, D.; Jungnickel, G.; Elsner, J.; Haugk, M.; Frauenheim, T.; Suhai, S.; Seifert, G. *Phys. Rev. B* **1998**, *58* (11), 7260–7268.
- (200) Lee, S. M.; An, K. H.; Lee, Y. H.; Seifert, G.; Frauenheim, T. *J. Am. Chem. Soc.* **2001**, *123* (21), 5059–5063.
- (201) Henkelman, G.; Uberuaga, B. P.; Jonsson, H. *J. Chem. Phys.* **2000**, *113* (22), 9901–9904.

- (202) Chiu, C. F.; Dar, H. H.; Kapralov, A. A.; Robinson, R. A. S.; Kagan, V. E.; Star, A. *Nanoscale* **2017**, *9* (18), 5948–5956.
- (203) Baughman, R. H. *Science* **2002**, *297* (5582), 787–792.
- (204) Sun, Y.-P.; Fu, K.; Lin, Y.; Huang, W. *Acc. Chem. Res.* **2002**, *35* (12), 1096–1104.
- (205) Lin, Y.; Mezziani, M. J.; Sun, Y.-P. *J. Mater. Chem.* **2007**, *17* (12), 1143.
- (206) Iverson, N. M.; Barone, P. W.; Shandell, M.; Trudel, L. J.; Sen, S.; Sen, F.; Ivanov, V.; Atolia, E.; Farias, E.; McNicholas, T. P.; Reuel, N.; Parry, N. M. A.; Wogan, G. N.; Strano, M. S. *Nat. Nanotechnol.* **2013**, *8* (11), 873–880.
- (207) Fantini, C.; Jorio, A.; Santos, A. P.; Peressinotto, V. S. T.; Pimenta, M. A. *Chem. Phys. Lett.* **2007**, *439* (1–3), 138–142.
- (208) Zhang, J.; Boghossian, A. A.; Barone, P. W.; Rwei, A.; Kim, J. H.; Lin, D.; Heller, D. A.; Hilmer, A. J.; Nair, N.; Reuel, N. F.; Strano, M. S. *J. Am. Chem. Soc.* **2011**, *133* (3), 567–581.
- (209) Zhou, S.; Hashida, Y.; Kawakami, S.; Mihara, J.; Umeyama, T.; Imahori, H.; Murakami, T.; Yamashita, F.; Hashida, M. *Int. J. Pharm.* **2014**, *471* (1–2), 214–223.
- (210) Carpena, X.; Vidossich, P.; Schroettner, K.; Calisto, B. M.; Banerjee, S.; Stampfer, J.; Soudi, M.; Furtmuller, P. G.; Rovira, C.; Fita, I.; Obinger, C. *J. Biol. Chem.* **2009**, *284* (38), 25929–25937.
- (211) Niyogi, S.; Boukhalfa, S.; Chikkannavar, S. B.; McDonald, T. J.; Heben, M. J.; Doorn, S. K. *J. Am. Chem. Soc.* **2007**, *129* (7), 1898–1899.
- (212) Jorio, A.; Lucchese, M. M.; Stavale, F.; Achete, C. A. *Phys. Status Solidi* **2009**, *246* (11–12), 2689–2692.
- (213) Tabakman, S. M.; Welsher, K.; Hong, G.; Dai, H. *J. Phys. Chem. C. Nanomater. Interfaces* **2010**, *114* (46), 19569–19575.
- (214) Palwai, N. R.; Martyn, D. E.; Neves, L. F. F.; Tan, Y.; Resasco, D. E.; Harrison, R. G. *Nanotechnology* **2007**, *18* (23), 235601.
- (215) Graff, R. A.; Swanson, J. P.; Barone, P. W.; Baik, S.; Heller, D. A.; Strano, M. S. *Adv. Mater.* **2005**, *17* (8), 980–984.
- (216) Krieg, A. M. *Annu. Rev. Immunol.* **2002**, *20* (1), 709–760.
- (217) Holt, B. D.; Dahl, K. N.; Islam, M. F. *Small* **2011**, *7* (16), 2348–2355.
- (218) Kapralov, A. A.; Feng, W. H.; Amoscato, A. A.; Yanamala, N.; Balasubramanian, K.; Winnica, D. E.; Kisin, E. R.; Kotchey, G. P.; Gou, P.; Sparvero, L. J.; Ray, P.; Mallampalli, R. K.; Klein-Seetharaman, J.; Fadeel, B.; Star, A.; Shvedova, A. A.; Kagan,

- V. E. *ACS Nano* **2012**, *6* (5), 4147–4156.
- (219) Korkmaz, B.; Horwitz, M. S.; Jenne, D. E.; Gauthier, F. *Pharmacol. Rev.* **2010**, *62* (4), 726–759.
- (220) Farrera, C.; Bhattacharya, K.; Lazzaretto, B.; Andón, F. T.; Hultenby, K.; Kotchey, G. P.; Star, A.; Fadeel, B. *Nanoscale* **2014**, *6* (12), 6974.
- (221) Yarotski, D. A.; Kilina, S. V.; Talin, A. A.; Tretiak, S.; Prezhdo, O. V.; Balatsky, A. V.; Taylor, A. J. *Nano Lett.* **2009**, *9* (1), 12–17.
- (222) Salem, D. P.; Landry, M. P.; Bisker, G.; Ahn, J.; Kruss, S.; Strano, M. S. *Carbon* **2016**, *97*, 147–153.
- (223) Chiu, C. F.; Saidi, W. A.; Kagan, V. E.; Star, A. *J. Am. Chem. Soc.* **2017**, *139* (13), 4859–4865.
- (224) Robinson, J. T.; Welsher, K.; Tabakman, S. M.; Sherlock, S. P.; Wang, H.; Luong, R.; Dai, H. *Nano Res.* **2010**, *3* (11), 779–793.
- (225) Welsher, K.; Liu, Z.; Sherlock, S. P.; Robinson, J. T.; Chen, Z.; Daranciang, D.; Dai, H. *Nat. Nanotechnol.* **2009**, *4* (11), 773–780.
- (226) Barone, P. W.; Baik, S.; Heller, D. A.; Strano, M. S. *Nat. Mater.* **2004**, *4* (1), 86–92.
- (227) Kruss, S.; Landry, M. P.; Vander Ende, E.; Lima, B. M. A.; Reuel, N. F.; Zhang, J.; Nelson, J.; Mu, B.; Hilmer, A.; Strano, M. *J. Am. Chem. Soc.* **2014**, *136* (2), 713–724.
- (228) Jain, A.; Homayoun, A.; Bannister, C. W.; Yum, K. *Biotechnol. J.* **2015**, *10* (3), 447–459.
- (229) Hong, G.; Diao, S.; Antaris, A. L.; Dai, H. *Chem. Rev.* **2015**, *115* (19), 10816–10906.
- (230) Ma, X.; Adamska, L.; Yamaguchi, H.; Yalcin, S. E.; Tretiak, S.; Doorn, S. K.; Htoon, H. *ACS Nano* **2014**, *8* (10), 10782–10789.
- (231) Jussila, M.; Sundberg, S.; Hopia, A.; Mäkinen, M.; Riekkola, M. L. *Electrophoresis* **1999**, *20* (1), 111–117.
- (232) Wanasundara, P. K. J. P. D.; Shahidi, F. In *Bailey's Industrial Oil and Fat Products*; John Wiley & Sons, Inc.: Hoboken, NJ, USA, 2005.
- (233) Torel, J.; Cillard, J.; Cillard, P. *Phytochemistry* **1986**, *25* (2), 383–385.
- (234) Wisastra, R.; Dekker, F. J. *Cancers* **2014**, *6* (3), 1500–1521.
- (235) Marnett, L. J. *Mutat. Res. Res., Fundam. Mol. Mech. Mutagen.* **1999**, *424* (1–2), 83–95.
- (236) Vick, B. A.; Zimmerman, D. C. *Plant Physiol.* **1987**, *85* (4), 1073–1078.

- (237) Powell, L. R.; Piao, Y.; Wang, Y. *J. Phys. Chem. Lett.* **2016**, *7* (18), 3690–3694.
- (238) Arrigo, R.; Hävecker, M.; Wrabetz, S.; Blume, R.; Lerch, M.; McGregor, J.; Parrott, E. P. J.; Zeitler, J. A.; Gladden, L. F.; Knop-Gericke, A.; Schlögl, R.; Su, D. S. *J. Am. Chem. Soc.* **2010**, *132* (28), 9616–9630.
- (239) Tien, H. W.; Huang, Y. L.; Yang, S. Y.; Wang, J. Y.; Ma, C. C. M. *Carbon* **2011**, *49* (5), 1550–1560.
- (240) Zhang, W.; Zhang, H.; Xiao, J.; Zhao, Z.; Yu, M.; Li, Z. *Green Chem.* **2014**, *16* (1), 211–220.
- (241) Jiang, T.; Xu, K.; Ji, S. *J. Chem. Soc. Faraday Trans.* **1996**, *92* (18), 3401.
- (242) Gardner, H. W. *Free Radical Biol. Med.* **1989**, *7* (1), 65–86.
- (243) Llobet, J. M.; Domingo, J. L.; Corbella, J. *Arch. Toxicol.* **1986**, *58* (4), 278–281.
- (244) Loidl-Stahlhofen, A.; Hannemann, K.; Spiteller, G. *Biochim. Biophys. Acta - Lipids Lipid Metab.* **1994**, *1213* (2), 140–148.
- (245) Wilcox, A. L.; Marnett, L. J. *Chem. Res. Toxicol.* **1993**, *6* (4), 413–416.
- (246) Dementev, N.; Feng, X.; Borguet, E. *Langmuir* **2009**, *25* (13), 7573–7577.
- (247) Blum, V.; Gehrke, R.; Hanke, F.; Havu, P.; Havu, V.; Ren, X.; Reuter, K.; Scheffler, M. *Comput. Phys. Commun.* **2009**, *180* (11), 2175–2196.
- (248) Frisch, M. J.; Trucks, G. W.; Schlegel, H. B.; Scuseria, G. E.; Robb, M. A.; Cheeseman, J. R.; Scalmani, G.; Barone, V.; Mennucci, B.; Petersson, G. A.; Nakatsuji, H.; Caricato, M.; Li, X.; Hratchian, H. P.; Izmaylov, A. F.; Bloino, J.; Zheng, G.; Sonnenberg, J. L.; Hada, M.; Ehara, M.; Toyota, K.; Fukuda, R.; Hasegawa, J.; Ishida, M.; Nakajima, T.; Honda, Y.; Kitao, O.; Nakai, H.; Vreven, T.; Montgomery, J. A., Jr; Peralta, J. E.; Ogliaro, F.; Bearpark, M. J.; Heyd, J.; Brothers, E. N.; Kudin, K. N.; Staroverov, V. N.; Kobayashi, R.; Normand, J.; Raghavachari, K.; Rendell, A. P.; Burant, J. C.; Iyengar, S. S.; Tomasi, J.; Cossi, M.; Rega, N.; Millam, N. J.; Klene, M.; Knox, J. E.; Cross, J. B.; Bakken, V.; Adamo, C.; Jaramillo, J.; Gomperts, R.; Stratmann, R. E.; Yazyev, O.; Austin, A. J.; Cammi, R.; Pomelli, C.; Ochterski, J. W.; Martin, R. L.; Morokuma, K.; Zakrzewski, V. G.; Voth, G. A.; Salvador, P.; Dannenberg, J. J.; Dapprich, S.; Daniels, A. D.; Farkas, Ö.; Foresman, J. B.; Ortiz, J. V.; Cioslowski, J.; Fox, D. J. Gaussian, Inc.: Wallingford, CT, USA 2009.
- (249) Tretiak, S. *Nano Lett.* **2007**, *7* (8), 2201–2206.
- (250) Saidi, W. A.; Norman, P. *Phys. Chem. Chem. Phys.* **2014**, *16* (4), 1479–1486.
- (251) Saidi, W. A.; Norman, P. *Carbon* **2014**, *67*, 17–26.

- (252) Yanai, T.; Tew, D. P.; Handy, N. C. *Chem. Phys. Lett.* **2004**, *393* (1–3), 51–57.
- (253) Lefebvre, J. *ACS Nano* **2016**, *10* (10), 9602–9607.
- (254) Ma, X.; Hartmann, N. F.; Baldwin, J. K. S.; Doorn, S. K.; Htoon, H. *Nat. Nanotechnol.* **2015**, *10* (8), 671–675.
- (255) Yu, L.; Shearer, C.; Shapter, J. *Chem. Rev.* **2016**, *116* (22), 13413–13453.
- (256) Singh, N.; Chen, J.; Koziol, K.; Hallam, K. R.; Janas, D.; Patil, A.; Strachan, A.; Hanley, J.; Rahatekar, S. S. *Nanoscale* **2016**, 8288–8299.
- (257) Ito, M.; Yajima, H.; Homma, Y. *Jpn. J. Appl. Phys.* **2016**, *55* (7), 75101.
- (258) Riou, I.; Bertoncini, P.; Bizot, H.; Mevellec, J. Y.; Buléon, A.; Chauvet, O. *J. Nanosci. Nanotechnol.* **2009**, *9* (10), 6176–6180.
- (259) Mol Menamparambath, M.; Arabale, G.; Nikolaev, P.; Baik, S.; Arepalli, S. *Appl. Phys. Lett.* **2013**, *102* (17), 1–6.
- (260) Karthigeyan, A.; Minami, N.; Iakoubovskii, K. *Jpn. J. Appl. Phys.* **2008**, *47* (9 PART 1), 7440–7443.
- (261) Arutyunyan, N. R.; Obraztsova, E. D. *J. Nanoelectron. Optoelectron.* **2013**, *8* (1), 67–70.